An advanced microstructured semiconductor radiation detector for neutron imaging and oil well logging

by

Sanchit Sharma

M.Tech., Pandit Deendayal Petroleum University, India, 2017

AN ABSTRACT OF A DISSERTATION

submitted in partial fulfillment of the
requirements for the degree

DOCTOR OF PHILOSOPHY

Alan Levin Department of Mechanical and Nuclear Engineering
Carl R. Ice College of Engineering

KANSAS STATE UNIVERSITY
Manhattan, Kansas

2022

Abstract

The work presented in this dissertation will serve as an essential tool for modern nuclear engineers to perform radiation transport with import of complex computer aided design (CAD) models efficiently. Performing radiation transport with complex CAD geometries and obtaining accurate detector response functions has been a major challenge. For micro-structured semiconductor detectors, results obtained from radiation transport alone are not enough to provide a clear picture of expected performance. Hence, the work presented in this dissertation is divided into two major research areas (RAs). RA 1 describes methods for sensor response modelling with hybrid Geant4 geometries consisting of both conventional C++ based models and complex CAD based models in a single simulation. This RA will address the methods developed for radiation transport models and benchmarking experimental detector responses. Additionally, this RA will further discuss how these models were later utilized for finalizing design parameters of a semiconductor radiation detection system (Timepix3 coupled with Dual-Sided Microstructured Semiconductor Neutron Detector). Multiple bugs were identified in Geant4 source code as a result of the work presented in RA 1. RA 2 of this dissertation will provide detailed analysis of the existing boundary conditions of the DS-MSND and MSND detectors. Finite Element Analysis based semiconductor physics modeling was performed to investigate various parameters of the Si-SiO_2 interface.

The radiation transport models were developed for simulating the Kansas State University Materials Interrogation (KSUMI) test facility that was set up to enable bulk-material irradiation experiments that replicate similar oil-well logging scenarios. These experiments were conducted with an aim to address the problem of replacement of conventional radioisotope sources commonly used in oil-well logging industries. An exploration tool similar to an oil-well logging tool was used to conduct experiments with water and sand as testing materials. The facility includes a 2500-gallon concrete test chamber to be filled with testing material with an aluminum pipe going horizontally through it, permitting placement of a neutron source and radiation sensors. A machine-based

14.1 MeV deuterium-tritium neutron source was used to irradiate the 2500-gallon testing material. Experiments were performed with tap water and sand as bulk testing materials. Irradiation was performed for one hour and results were obtained from a $BF_3/^3He$ neutron sensor, a BF_3 neutron sensor, and two NaI gamma sensors placed at different locations within the exploration tool. Geant4, a Monte-Carlo based toolkit, was deployed on a high-performance computing system to simulate the entire experiment in order to benchmark the experimental responses obtained from the photon and neutron sensors. The facility was modeled in detail with accurate dimensions and material compositions. Materials such as tap water, high-density polyethylene, and aluminum metal were modeled with thermal neutron scattering cross-sections. The reference physics list QGSP_BIC_HP along with G4NDL and $S(\alpha,\beta)$ cross-sections were found to be appropriate for simulation of neutron interrogation experiments with neutron energies lower than 20 MeV. The experimental results obtained were successful in characterizing the bulk testing materials, and results obtained from Geant4 were found to be in good agreement with the experimental results in most cases.

The source code developed for the above method was then utilized to design the physical parameters for an X-DS-MSND system. These detectors have the benefit of doubling neutron detection efficiency as compared to single-sided devices (X-MSND) by staggering ^{6}LiF-filled trenches between the top and bottom surface of a silicon diode. This produces a more complex electric field distribution and depletion characteristics in the diode and creates an indirect path for signal carrier transport between device electrodes. Geant4 was extensively utilized for radiation transport and interaction modeling, and Allpix Squared was used for mobile charge carrier transport and total charge collection. The results of this simulation work provided an estimate of charge cluster shape and intensity for a pixel array configuration corresponding to Timepix3 read-out system. In addition, imaging performance for transmission radiography was demonstrated with a simple two-dimensional shape in a Gaussian beam of thermal neutrons. The simulated neutron detection efficiency was 57.6%.

It was discovered that the Allpix Squared is not optimal for simulation of complex boundary conditions and charge carrier transport inside the DS-MSND. To understand the behavior of charge carriers in the presence of a complex electric field and boundary conditions, a simpler non-conformally doped MSND geometry was fabricated and analyzed. This sensor geometry produced a complex electric field distribution and depletion characteristics within the diode. The fixed oxide charge present at the trench walls and its effects on the depletion characteristics and electric field were analyzed. The capacitance-voltage and current-voltage curve characterizations were performed for these prototypes and compared with the COMSOL Multiphysics simulations. An ^{241}Am alpha particle source was further utilized to perform spectral analysis. Geant4 was utilized for radiation transport, interaction modeling, and benchmarking the spectral data. The results of this simulation work provided a reasonable confidence in capability to obtain and benchmark electric fields and spectral data for complex micro-structured semiconductor radiation detectors. Further, COMSOL Multiphysics was used to account for time-dependent charge carrier motion and detector response for these boundary conditions.

As a result of work presented in RA 1 and RA 2, important features in the MSND/DS-MSND geometry were discovered that could significantly impact the device's performance. These features were incorporated in the updated Monte-Carlo model of the DS-MSND sensor. Simulated response of the updated DS-MSND sensor as a replacement of BF_3/^{3}He was then analyzed for the oil-well logging irradiation environment using Geant4 simulations. The results obtained from these simulations establish DS-MSND as a strong contender for replacing BF_3/^{3}He sensors for oil well logging experiments.

An advanced microstructured semiconductor radiation detector for neutron imaging and oil well logging

by

Sanchit Sharma

M.Tech., Pandit Deendayal Petroleum University, India, 2017

A DISSERTATION

submitted in partial fulfillment of the
requirements for the degree

DOCTOR OF PHILOSOPHY

Alan Levin Department of Mechanical and Nuclear Engineering
Carl R. Ice College of Engineering

KANSAS STATE UNIVERSITY
Manhattan, Kansas

2022

Approved by:

Co-Major Professor
Amir A. Bahadori

Approved by:

Co-Major Professor
Walter J. McNeil

Copyright

Abstract

The work presented in this dissertation will serve as an essential tool for modern nuclear engineers to perform radiation transport with import of complex computer aided design (CAD) models efficiently. Performing radiation transport with complex CAD geometries and obtaining accurate detector response functions has been a major challenge. For micro-structured semiconductor detectors, results obtained from radiation transport alone are not enough to provide a clear picture of expected performance. Hence, the work presented in this dissertation is divided into two major research areas (RAs). RA 1 describes methods for sensor response modelling with hybrid Geant4 geometries consisting of both conventional C++ based models and complex CAD based models in a single simulation. This RA will address the methods developed for radiation transport models and benchmarking experimental detector responses. Additionally, this RA will further discuss how these models were later utilized for finalizing design parameters of a semiconductor radiation detection system (Timepix3 coupled with Dual-Sided Microstructured Semiconductor Neutron Detector). Multiple bugs were identified in Geant4 source code as a result of the work presented in RA 1. RA 2 of this dissertation will provide detailed analysis of the existing boundary conditions of the DS-MSND and MSND detectors. Finite Element Analysis based semiconductor physics modeling was performed to investigate various parameters of the Si-SiO_2 interface.

The radiation transport models were developed for simulating the Kansas State University Materials Interrogation (KSUMI) test facility that was set up to enable bulk-material irradiation experiments that replicate similar oil-well logging scenarios. These experiments were conducted with an aim to address the problem of replacement of conventional radioisotope sources commonly used in oil-well logging industries. An exploration tool similar to an oil-well logging tool was used to conduct experiments with water and sand as testing materials. The facility includes a 2500-gallon concrete test chamber to be filled with testing material with an aluminum pipe going horizontally through it, permitting placement of a neutron source and radiation sensors. A machine-based

14.1 MeV deuterium-tritium neutron source was used to irradiate the 2500-gallon testing material. Experiments were performed with tap water and sand as bulk testing materials. Irradiation was performed for one hour and results were obtained from a BF_3/^{3}He neutron sensor, a BF_3 neutron sensor, and two NaI gamma sensors placed at different locations within the exploration tool. Geant4, a Monte-Carlo based toolkit, was deployed on a high-performance computing system to simulate the entire experiment in order to benchmark the experimental responses obtained from the photon and neutron sensors. The facility was modeled in detail with accurate dimensions and material compositions. Materials such as tap water, high-density polyethylene, and aluminum metal were modeled with thermal neutron scattering cross-sections. The reference physics list QGSP_BIC_HP along with G4NDL and S(α,β) cross-sections were found to be appropriate for simulation of neutron interrogation experiments with neutron energies lower than 20 MeV. The experimental results obtained were successful in characterizing the bulk testing materials, and results obtained from Geant4 were found to be in good agreement with the experimental results in most cases.

The source code developed for the above method was then utilized to design the physical parameters for an X-DS-MSND system. These detectors have the benefit of doubling neutron detection efficiency as compared to single-sided devices (X-MSND) by staggering ^{6}LiF-filled trenches between the top and bottom surface of a silicon diode. This produces a more complex electric field distribution and depletion characteristics in the diode and creates an indirect path for signal carrier transport between device electrodes. Geant4 was extensively utilized for radiation transport and interaction modeling, and Allpix Squared was used for mobile charge carrier transport and total charge collection. The results of this simulation work provided an estimate of charge cluster shape and intensity for a pixel array configuration corresponding to Timepix3 read-out system. In addition, imaging performance for transmission radiography was demonstrated with a simple two-dimensional shape in a Gaussian beam of thermal neutrons. The simulated neutron detection efficiency was 57.6%.

It was discovered that the Allpix Squared is not optimal for simulation of complex boundary conditions and charge carrier transport inside the DS-MSND. To understand the behavior of charge carriers in the presence of a complex electric field and boundary conditions, a simpler non-conformally doped MSND geometry was fabricated and analyzed. This sensor geometry produced a complex electric field distribution and depletion characteristics within the diode. The fixed oxide charge present at the trench walls and its effects on the depletion characteristics and electric field were analyzed. The capacitance-voltage and current-voltage curve characterizations were performed for these prototypes and compared with the COMSOL Multiphysics simulations. An ^{241}Am alpha particle source was further utilized to perform spectral analysis. Geant4 was utilized for radiation transport, interaction modeling, and benchmarking the spectral data. The results of this simulation work provided a reasonable confidence in capability to obtain and benchmark electric fields and spectral data for complex micro-structured semiconductor radiation detectors. Further, COMSOL Multiphysics was used to account for time-dependent charge carrier motion and detector response for these boundary conditions.

As a result of work presented in RA 1 and RA 2, important features in the MSND/DS-MSND geometry were discovered that could significantly impact the device's performance. These features were incorporated in the updated Monte-Carlo model of the DS-MSND sensor. Simulated response of the updated DS-MSND sensor as a replacement of BF_3/^{3}He was then analyzed for the oil-well logging irradiation environment using Geant4 simulations. The results obtained from these simulations establish DS-MSND as a strong contender for replacing BF_3/^{3}He sensors for oil well logging experiments.

Table of Contents

List of Figures xiii

List of Tables xxii

Acknowledgements xxiii

Dedication xxiv

1 Introduction 1

1.1 Distinguished Research Objectives 5

1.2 Structure of Dissertation 6

2 Background Literature 7

2.1 Radiation Transport 7

2.2 Background 10

2.2.1 Oil Well Logging Experiment 10

2.2.2 MSND Sensor Details 11

2.2.3 DS-MSND Sensor Details 12

2.2.4 Previous X-MSND device details 12

2.2.5 Existing competition to X-DS-MSND 13

2.2.6 Semiconductor Physics Modeling 16

2.2.7 Boundary Conditions 18

2.3 Charge Carrier Transport 20

3 Radiation Interactions and Simulated Geometries 24

3.1 Neutron Sources 24
3.2 Neutron Interactions in Oil Well Logging Experiments 25
3.2.1 Neutron Absorption 28
3.2.2 Neutron Scattering 29
3.3 Neutron Interactions in Trenched Silicon Neutron Sensors 30
3.4 Gamma-Ray Interactions in Oil Well Logging Experiments 30
3.4.1 Photoelectric Effect 31
3.4.2 Compton Scattering 32
3.4.3 Pair Production 33
3.5 Gamma-Ray Interactions in Trenched Silicon Neutron Sensors 34
3.6 Simulation Details: The Oil Well Logging Experiment 34
3.6.1 Selection of Physics List 35
3.6.2 Modeled Materials and Geometry 35
3.7 Simulation Details: Trenched Microstructured Neutron Detector 41

4 Semiconductor physics models of DS-MSND sensor 47
4.1 COMSOL Multiphysics 48
4.2 Preliminary Simulation of Induced Current Profiles from COMSOL and Allpix Squared 59
4.3 Summary 62

5 Experiments and High Fidelity Simulations 63
5.1 Fixed Oxide Charge 67
5.2 Signal Formation 67
5.3 Experiment Details 68
5.3.1 CV and IV Curve Details 68
5.3.2 ^{241}Am Source Spectroscopy Details 69
5.4 Modeling Methodology 69

5.4.1 Geant4 Radiation Transport Toolkit Simulation Details 69
5.4.2 COMSOL Multiphysics Models for Steady State Analysis 73
5.4.3 COMSOL Multiphysics Models for Transient Analysis 75
5.5 Modeling Charge Carrier Injection 77
5.5.1 Electric Fields Within the Sensor 77
5.5.2 Charge Injection Method 78
5.6 Charge Cloud Motion 83
5.7 Modeling Realistic Boundary Conditions 85
6 Results and Discussions 95
6.1 Radiation Transport Oil Well Logging Experiments 95
6.1.1 Uncertainty in Source Output 96
6.1.2 Comparison of Simulated Results 97
6.1.3 Error Analysis in Simulations 100
6.2 Sensor Response Simulation and Analysis 105
6.2.1 Electric Field Calculations 105
6.2.2 CV Plot Calculations 108
6.2.3 Spectral Data Calculations 111
6.2.4 Electric Field Solutions 114
6.2.5 Induced Current Profile 116
6.2.6 Experimental Results and Analysis 120
6.3 Application of X-DS-MSND sensor as a neutron radiation counter 133
7 Conclusions 138
Bibliography 142

List of Figures

1.1 An overview of the presented work representing the fusion of two different research areas. 3

2.1 A generalized representation of the effects of the formation of fixed oxide charge due to the formation of a SiO_2 mask on a *n*-type (Left) and *p*-type (Right) silicon substrate. 19

2.2 Representation of charge cloud motion inside a semiconductor device in the presence of an applied electric field. 21

3.1 A representation of the total neutron microscopic interaction cross section for hydrogen obtained from the Evaluated Nuclear Data File (ENDF) Database Version ENDF/B-VII.0[1]. 27

3.2 A representation of the inelastic scattering interaction cross section for iron obtained from the Evaluated Nuclear Data File (ENDF) Database Version ENDF/B-V 27

3.3 A representation of possible neutron interactions with matter 29

3.4 A representation of the total neutron microscopic interaction cross-section for ^{6}Li obtained from Evaluated Nuclear Data File (ENDF) database[1]. 31

3.5 A representation of the gamma-ray interaction cross-sections for ^{82}Pb obtained from NIST-XCOM[2]. 32

3.6 A view of exploration tool and source placement 37

3.7 A comparison of modeled and experimental exploration tool 37

3.8 Detailed NaI sensor model in Geant4 38

3.9 Outer view representation of the experimental facility in Geant4 39

3.10 Internal view representation of the experimental facility in Geant4. A secondary gamma-ray scattering trajectory is demonstrated in green. 40
3.11 A representation of exploration tool and sensor placement in Geant4 40
3.12 A representative geometry for the DS-MSND sensor demonstrating parameters under investigation. 42
3.13 A representation of DS-MSND sensor imported in Geant4 and the 25.3 meV thermal neutron source placement. This simulation setup was used for optimizing the design parameters for the DS-MSND sensor. 43
3.14 A representation of DS-MSND spectral results obtained due to irradiations simulated with a 25.3 meV thermal neutron source and a 662 keV gamma-ray source, and an energy based threshold at 0.54 MeV. 44
3.15 A representation of (left) Energy deposited by neutron reaction products in the Si diode of the DS-MSND sensor; note the large signal that can be obtained over (right) gamma-ray induced signals due to the geometry of the DS-MSND-type structure and large energy reaction products. 44
3.16 A representation of (left) Geant4 simulation of neutron detection efficiency for various trench widths and Packing Fractions (P.F.) of the DS-MSND sensor. (right) Final Geant4 simulated neutron detection efficiencies of the X-DS-MSND with 28 µm trench width. 46

4.1 A representation of the COMSOL FEM model (left) and the associated unstructured mesh (right) for the highlighted regions. 50
4.2 A comparison of the peak doping profile obtained from COMSOL Multiphysics and from ion implant analytical calculation. 51
4.3 A representation of the dual-sided trenched, DS-MSND doping profile. Dashed region represents phosphorous doped (n-type) region, dotted region represents boron doped (p-type) region, green colour represents LiF nano-powder and blue colour represents bulk high-resistive silicon. Figure is not to scale. 52

4.4 A representation of the dual-sided trenched, X-DS-MSND depletion profiles obtained at 264 V(Left) and 350 V(right). 53
4.5 A representation of the dual-sided trenched, DS-MSND depletion profiles obtained at 264 V(Left) and 350 V(right). 54
4.6 Analysis of the effects of variation of *p*-type peak doping concentrations on the peak electric field magnitude present inside the device at a constant junction depth of 1 µm. 55
4.7 COMSOL Simulation results to obtain peak electric field magnitude around p-type implant at (left) 1 µm and (right) 2 µm junction depth. This result is for a 350 V bias (complete depletion). 56
4.8 Electric field magnitude profile for a 25 µm gap in between pixels in y-direction. The size of the pixel is 20 µm-by-30 µm. This result is for a 350V bias (complete depletion). 57
4.9 Electric field magnitude profile for a 20 µm gap in between pixels in y-direction. The size of the pixel is 20 µm-by-30 µm. This result is for a 350V bias (complete depletion). 57
4.10 Electric field magnitude profile for a 15 µm gap in between pixels in y-direction. The size of the pixel is 20 µm-by-30 µm. This result is for a 350V bias (complete depletion). 58
4.11 Electric field magnitude profile for a 10 µm gap in between pixels in y-direction. The size of the pixel is 20 µm-by-30 µm. This result is for a 350V bias (complete depletion). 58
4.12 Electron (blue)-Hole (orange) pair tracks simulated in Allpix Squared from a single neutron absorption event in a LiF-filled trench, producing ionization from an alpha particle (α) and triton (t) in silicon. Each track represents 500 individual charge carriers. 61

4.13 Induced current obtained from Allpix Squared. The current pulse was extracted from bottom electrode is a case where holes and traveling downwards. 62

5.1 A representation of effects of FOC on the prototype MSND device and the doping scheme used for fabrication. 64

5.2 Calculated effects of realistic boundary conditions on the depletion depths achieved for the X-DS-MSND diode. Solid lines represent values when FOC is 5×10^9 cm^{-2}. Dashed lines represent values when FOC is 5×10^{10} cm^{-2} 65

5.3 A SEM image of the fabricated single-sided MSND device. 66

5.4 IV curve data obtained for all the fabricated diodes. Top plot is for MSNDs with 50 nm thick SiO_2 layer. While, the bottom plot is for chips with 250 nm thick SiO_2 layer. A leakage current of 218 nA was observed at the breakdown voltage of 539 V for the best performing diode (Chip 4 with 250 nm thick SiO_2 layer). Measurements performed by Radiation Detection Technologies, Inc. 70

5.5 CV curve data obtained for all the fabricated diodes. Top plot is for MSNDs with 50 nm thick SiO_2 layer. While, the bottom plot is for chips with 250 nm thick SiO_2 layer. Diodes with 250 nm thick oxide observes consistency in the measured data. Measurements performed by Radiation Detection Technologies, Inc. 71

5.6 Experimental setup to obtain alpha particle irradiation response. 72

5.7 Geant4 simulated model of the experimental setup. 1: Overall geometry; 2: zoomed view of the sensor and oxide layer; 3: entire sensor structure with the trenches; 4: zoomed view of trenches with the dead layer. 73

5.8 A representation of the COMSOL FEM model (left) and the associated unstructured mesh (right). 74

5.9 (Left) A representation of simulated 3D geometry in COMSOL. (Right) A representation of Electron Concentration at 200 V reverse bias. 76

5.10 Electric field magnitude inside the sensor along the cutline. The plot shows location of charge carrier injection and maximum electric fields faced by the 'drifting' charge carriers in motion. 78
5.11 A comparison of energy charge deposition profiles for a 4.7 MeV alpha particle incident perpendicularly on a Si surface, calculated from Geant4 and SRIM. 79
5.12 Unstructured Mesh Profile used for calculating the solutions for the COMSOL Multiphysics model. 80
5.13 Cumulative free electron-hole pairs injected in the simulated model with respect to time extracted from COMSOL Multiphysics. 81
5.14 Profile of electron-hole pairs at 8 ns instant in the simulated model (at 200V reverse bias) with respect to depth inside the sensor extracted from COMSOL Multiphysics. 82
5.15 Electric field profile within the MSND sensor at 200 V external bias. A zoomed-in view at the left shows an arrow plot obtained by plotting x, y, & z components of the electric field. 84
5.16 Models for holes transport for a reverse external bias of 200 V. The snapshots of transient time-dependent simulations are provided for 25 ns, 40 ns, 100 ns, 200 ns, and 215 ns 85
5.17 One dimension Models for holes transport for a reverse external bias of 200 V plotted along the cutline within the device. 86
5.18 A representation of diode's depletion depth achieved for various FOC values. 87
5.19 A representation of electric field magnitude plotted along the cutline for various values of FOC in the Si-SiO_2 interface. 88
5.20 Electric field profile within the MSND sensor at 200 V external bias. A zoomed-in view at the left shows an arrow plot obtained by plotting x, y, & z components of the electric field. 90

5.21 Models for holes transport for a reverse external bias of 200 V on a Simulated MSND modeled with the Si-SiO_2 interface boundary condition. The snapshots of transient time-dependent simulations are provided for 25 ns to 13 001 ns 91
5.22 One dimensional simulated holes transport model for a reverse external bias of 200 V plotted along the cutline within the MSND device modeled with Si-SiO_2 interface boundary condition. 92
5.23 Experimental setup to obtain alpha detection pulses from an MSND sensor. 93

6.1 A representation of anisotropy in the output of the D-T generator 96
6.2 Optimization of Geant4 results. Unoptimized Geant4 model consists of only active region of the NaI sensors. Optimized Geant4 model includes all the realistic components of the NaI detector, for e.g. PMT tube, light shield, oxide layer, etc. . . 101
6.3 Comparison of MCNP and Optimized Geant4 results. 101
6.4 Comparison of Geant4 and experimental results of NaI sensors with water as a testing material 102
6.5 Comparison of Geant4 and experimental results of NaI sensors with sand as a testing material 102
6.6 Relative error calculated for Gamma spectra obtained from Geant4 simulations . . 103
6.7 Comparison of log of electron concentration at 200 V reverse bias for a planar diode (left), an MSND diode with zero FOC & SRV (middle), and an MSND diode with FOC = $5 \times 10^{10}\,cm^{-2}$ & SRV = $10\,cm\,s^{-1}$ (right). 106
6.8 Calculated electric field magnitude plotted along the cutline (shown in the figure) at a 200 V reverse bias for a planar diode and an MSND diode (with zero FOC & SRV, and with FOC = $5 \times 10^{10}\,cm^{-2}$ & SRV = $10\,cm\,s^{-1}$). 107
6.9 A comparison of simulated and experimental CV curve data for an MSND diode. The y-axis is normalized for plate area to compare simulated and experimental results. 108

6.10 A plot demonstrating increment in the capacitance values observed in simulated (C) values as compared to the experimental values (E). 109
6.11 A plot of log of electron concentration representing the depletion region widths achieved at 100 V, 120 V, and 200 V external reverse bias. 111
6.12 Experimental spectral data obtained from the alpha irradiation of the fabricated MSND detector. 112
6.13 Particle energy deposition in the MSND device's active volume from simulating the alpha irradiation experiment in Geant4. 113
6.14 A representation of regions of interest for the explanation of three distinct peaks in the alpha energy spectrum. 114
6.15 Variation of electric field magnitude along the line of charge injection at various times. 115
6.16 A comparison between the induced currents (at 200 V reverse bias) when the simulated charge cloud is in a generalized Gaussian profile and an imported profile with Bragg distribution. The figure further shows the amount of total induced charge in the bottom electrode. 117
6.17 Methodology to determine realistic Si-SiO_2 boundary conditions. 118
6.18 A comparison between the simulated induced currents for an MSND device modeled with Si-SiO_2 interface obtained for various reverse bias values. A artificial cutoff is implemented as the simulations are resource and time expensive. No current is induced initially for a few hundred nanoseconds as the charge carriers are diffusing in all the directions inside the fins, cancelling each other's effects. The artificial cutoff for the induced currents from COMSOL was removed and replaced with extrapolated values for processing in LTspice 142A preamplifier model. 119
6.19 A representation of regions of interest for the explanation of three distinct group of pulses observed in the experimental data. 123

6.20 Experimental pulses observed from oscilloscope's persistence mode. The pulses emerge from 142A preamplifier due to alpha particle irradiation at 200 V detector bias. 124
6.21 Intensity plots demonstrating the mutation of correlation between pulses heights and rise times for the preamplifier's pulses collected from one hour of alpha particle irradiation at 40 V, 50 V, 60 V, 70 V, 80 V, and 120 V reverse bias. 125
6.22 Intensity plot for one hour irradiation obtained from analysis of preamplifier pulses at 200 V external reverse bias. 126
6.23 (LEFT) Rise time histogram obtained from alpha irradiation of an MSND diode reverse biased at 200 V reverse bias. (RIGHT) Pulse height spectrum obtained from alpha irradiation of an MSND diode reverse biased at 200 V reverse bias. . . . 127
6.24 (LEFT) Curve fit performed on rise time histogram obtained from alpha irradiation of an MSND diode reverse biased at 200 V reverse bias for Group 1, 2, and 3 pulses. (RIGHT) Rise time distribution of measured pulses in Group 1, 2, and 3 pulses obtained from alpha particle irradiation of reverse MSND at different reverse biases. 128
6.25 LTspice model of the Ortec 142A preamplifier. 129
6.26 A visual representation of comparison of simulated and experimental pulses of Group 1, obtained from the MSND at 200 V reverse bias. 130
6.27 A visual representation of comparison of simulated and experimental pulses of Group 3, obtained from MSND at 200 V reverse bias. 131
6.28 Spectral response from a realistic DS-MSND model. 133
6.29 Neutron and Gamma-ray spectrum obtained from ^{3}He detector in oil well logging setup with water as a testing material. 134
6.30 Six 2-by-2 X-DS-MSND tiles placement in oil-well logging experiment. 135
6.31 Neutron and Gamma-ray spectrum obtained from X-DS-MSND as a replacement of ^{3}He detector in oil well logging setup with water as a testing material. 135

6.32 Shape features used to perform cluster morphological analysis. 136

6.33 Proof of concept describing results for machine learning processing of simulated training data. 136

List of Tables

2.1 Technology Summary Table 16

4.1 Peak electric field magnitude obtained for various simulated junction depths with a 5 µm and 10 µm fillet at the corners of p-type implants in COMSOL 56

5.1 Updepleted regions/region with no electric field obtained for various simulated FOC values at 200 V reverse bias 88

6.1 Analysis of neutron sensor experimental results from the sand experiment 99

6.2 Analysis of neutron sensor experimental results from the water experiment 99

Acknowledgments

I am extremely grateful to my dissertation supervisors, Professor Amir A. Bahadori and Professor Walter J. McNeil for their invaluable advice and continuous support during my PhD research work. Their immense knowledge and plentiful experience have encouraged me towards excellence in academic research. I would also like to thank the honorable members of my dissertation committee for their technical support on my studies. I would like to thank all the members in the Radiological Engineering Analysis Laboratory (REAL), Radiological Systems Integration Lab (RSIL), Semiconductor Materials and Radiological Technologies (S.M.A.R.T.) Laboratory, and the employees of Radiation Detection Technologies, Inc., for helpful discussions. I consider myself extremely lucky that I had a chance to attend various courses provided by Professor J. Kenneth Shultis and Professor Douglas S. McGregor. The fundamentals I build because of their coursework and their guidance will be a solid foundation for the type of scientific contributions I aim to make in future. I extend my apologies to those who may not have been mentioned but contributed to the presented work.

A majority of this work was funded by the U.S. Department of Energy STTR Contract DE-SC0019676. I am incredibly grateful to the sponsors as well for their support and understanding during delays caused due to COVID.

Dedication

It is with genuine gratitude and warm regard that I dedicate this work to my family and ancestors.

Chapter 1

Introduction

The objective of this dissertation is analyze the possibility of utilizing the existing microstructured semiconductor neutron detector (MSND)[3]/ dual-sided microstructured semiconductor neutron detector (DS-MSND)[4–6] detectors and electrically coupling them with a state-of-the-art fast detector readout system, the Timepix[7], to design a solid-state radiation imager (designated as X-DS-MSND) and to test its validity as a replacement for commercially available BF_3/^{3}He tubes to be used in large-scale neutron irradiation experiments. The work presented in this dissertation will begin with the details of work accomplished in the radiation transport area to incorporate computer aided design (CAD) import functionality for analyzing the conventional detector responses usually deployed in oil well logging experiments. This will be followed by much more detailed studies to design and develop a solid-state radiation imager that can be used as a potential replacement for BF_3/^{3}He tubes. The imager will provide capability to efficiently discriminate gamma-ray and neutron counts on the basis on cluster shape morphology. Efficient import methods and models are provided that will help future engineers analyze and develop newer detector models with different geometries.

The development of solid-state radiation detectors and their accurate response analysis has been an essential area of interest for nuclear engineers for a long time. A high fidelity and detailed analysis of these detectors would include analysis of radiation interaction probabilities directly coupled with the analysis of charge carrier transport inside the semiconductor detector volume.

This would provide details about two following fundamental properties of the device performance:

1. Detection efficiency of the sensor for investigating the target radiation field, and
2. Ability of the sensor to promptly sweep out the free charge carriers (due to detection event) from the active region of the sensor, i.e., ability of the sensor to process a detection event as fast as possible.

Analysis of the probabilities of radiation interaction within the sensor is accomplished by performing radiation transport simulations. The most common way to perform radiation transport is with Monte Carlo methods. Multiple softwares have already been developed to assist engineers in performing these analyses in detail. MCNP[8] is controlled software and, for those not employed at Los Alamos National Laboratory, must be obtained from the Radiation Safety Information Computational Center (RSICC). Although this code is straightforward to use, it has serious limitations when it comes to importing complex CAD models and directly coupling it with other available open source softwares. On the other hand, Geant4[9] is an open source C++-based radiation analysis toolkit that can be used to import CAD geometries readily coupled with other open source charge transport codes. Additionally, obtaining MCNP source code from RSICC is difficult for foreign nationals, while the Geant4 source code is open and readily available from its website. Hence, for this dissertation, Geant4 will be utilized for performing and demonstrating almost all of the radiation transport simulation methods and analysis.

Although radiation transport provides radiation propagation information such as interaction location and energy deposition, these results must be linked to the charge transport codes, which is the next crucial step in the solid-state detector physics analysis. Two options are investigated to carry out charge transport:

- 1) Allpix Squared[10]: A Monte Carlo-based transport code that is directly coupled with Geant4. The default code provides the capability to simulate charge transport for a pixelated planar semiconductor device. Significant edits will be made to the source code to incorporate the proposed sensor configuration into this software.

- 2) COMSOL Multiphysics[11]: A finite element methods (FEM)-based commercial software that provides capability to model and simulate complex semiconductor physical properties and perform high-fidelity detector simulations on a per-event basis. The simulations are costly in terms of time and memory, but are extremely accurate.

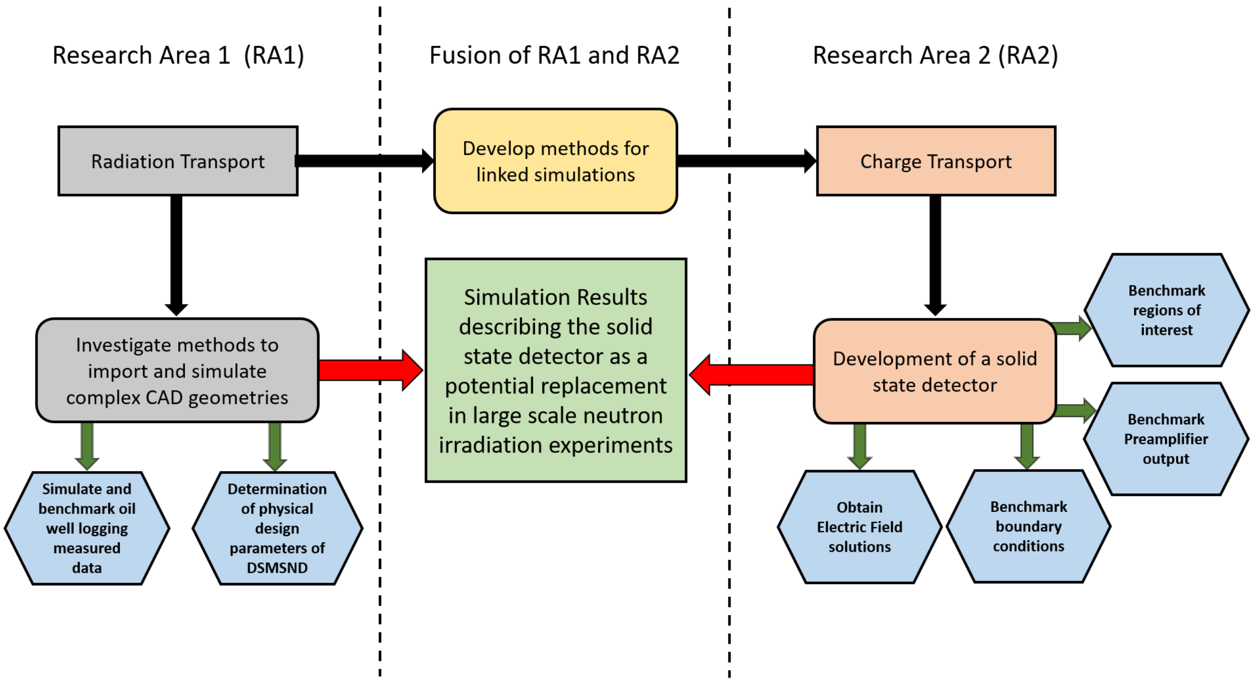

Figure 1.1: *An overview of the presented work representing the fusion of two different research areas.*

The structure and approach of this dissertation are summarized in Figure 1.1, where two different research focus areas are investigated. Research Area 1 (RA 1) will entail investigations related to methods of effective CAD-based geometry import. This will be done by simulating and benchmarking sensor responses from a large-scale oil well logging experiment. Various bugs related to simulation of CAD-based models in a high performance cluster were resolved in Geant4. Experimental analysis of neutron detector dead times will then be discussed, justifying a need for development and analysis of a fast and efficient solid state radiation detector. It will also be shown that Geant4 provides much better detector responses as compared to the responses obtained from MCNP. Further, the methods developed will then be used to perform a detailed parametric study to design and develop a dual sided microstructured neutron detector (DS-MSND) with modified features as per Timpix3 requirements. These modified features of the DS-MSND will further ensure that the detector provides around 60% thermal neutron detection efficiency, a spatial resolution close to 100 μm, and a gamma-ray rejection ratio of 10^{-6} [12]. Geant4 will be utilized for the simulations, and a CAD based accurate replication of DS-MSND geometry will be utilized to obtain the DS-MSND design parameters and perform other related studies.

Research Area 2 involved semiconductor physics modeling of the designed detector during RA1. This was the first time a solid-state structure like a MSND/DS-MSND was analyzed for its timing properties. This section is focused towards obtaining the much needed answers regarding the behavior of induced charge cloud inside the fins of the sensor. The semiconductor physics modeling of the microstructured detectors proceeded with an accurate estimation of the electric field profile inside the sensor. To accomplish this task, it was vitally important that the peak doping profiles and the background doping profiles represent the actual fabricated device. The shape of the pixels, i.e., the ohmic metal contact on the bottom electrode, was also a key parameter that was investigated. This was followed by the analysis of Si-SiO_2 interface boundary conditions. The effects of these Si-SiO_2 interface boundary conditions on the charge cloud behavior inside the fin are widely unknown, and almost no information is available in the present literature. The work presented in this dissertation answered a series of these questions in detail. For efficient investigation of these thrust areas, multiple prototype MSNDs with various thermally grown oxide thicknesses were fabricated by Radiation Detection Technologies, Inc., and detailed experimental studies were conducted using these devices. The validation of the experimental measurement results for these devices was then performed by preparing high-fidelity FEM models and performing multiple transient simulations in COMSOL Multiphysics. The results and observations made in this research area determined the regions of interest (ROI) that needed to be modeled with the final DS-MSND sensor to obtain an accurate simulated response.

Methods and models of the developed MSND/DS-MSND detector assisted in providing key ROIs for the updated DS-MSND detector model. This was updated and several Geant4 simulations were performed with the updated DS-MSND sensor model as a replacement for the BF_3/^{3}He sensor in oil well logging experiments. This effectively concluded major research objectives of this dissertation that are also described below.

1.1 Distinguished Research Objectives

The work presented in this dissertation aims to provide future researchers with a simulation infrastructure to efficiently perform Monte Carlo radiation transport for complex CAD-based geometries to validate the responses of neutron and gamma ray sensors. The same method will be connected to the FEM-based codes to perform charge carrier transport to obtain simulated current pulses for microstructured semiconductor radiation detectors with challenging boundary conditions.

1. The objective was to utilize hybrid geometries in Geant4 to simulate complex CAD based geometries in High Performance Computing (HPC) systems. These geometries will enable user to benchmark neutron and gamma-ray signatures of common radiation detectors like BF_3/^{3}He and NaI(Tl). The methods developed can be readily used to validate the sensor responses in complex pulsating neutron field environments present in oil-well logging experiments.

2. The Geant4 methods developed and described in objective 1 will then be utilized to determine the physical parameters a DS-MSND sensor that can provide a thermal neutron detection efficiency of around 60%. A CAD model of the sensor will be imported in Geant4 and simulated on Beocat, Kansas State University's high performance computing (HPC) system, in multi-threading mode. Initial induced current and neutron imaging estimates will be presented by utilizing the designed sensor geometry in Allpix Squared [10].

3. COMSOL Multiphysics software will be utilized to perform steady state simulations to design the implant shapes and sizes for the X-DS-MSND. Multiple COMSOL Multiphysics simulations are needed to estimate the junction doping profile, resistivity of the substrate, and peak electric field within the designed sensor. These details are significantly important for the fabrication team to proceed with the sensor fabrication.

4. To assist the fabrication team in determining the response times of the DS-MSND sensors, a few reverse MSNDs were fabricated with 250 nm thick thermally grown oxide and multiple experiments and characterizations were performed. Transient simulations in COMSOL

Multiphysics are needed to simulate accurate charge deposition and transport in the designed sensor. These simulation results will be instrumental for the fabrication team to work on a different passivisation schemes for the future generations of the DS-MSND diodes.

1.2 Structure of Dissertation

This work presentation in this dissertation is divided into seven chapters. The basic concepts of radiation transport are covered in Chapter 2, along with detailed background literature on oil-well logging experiments, the DS-MSND sensor, FEA modeling of semiconductor physics, and existing boundary conditions of Si-SiO_2. These details will be followed by a brief discussion of charge carrier transport. Chapter 3 begins with details of expected neutron and gamma-ray interactions for oil-well logging experiment and DS-MSND sensor and finalizing appropriate reference physics list for Geant4 simulations. This is followed by detailed representation of Geant4 simulated geometry and materials for both research areas. Chapters 4 and 5 contain methods and modeling procedures for microstructured silicon devices with appropriate boundary conditions. Details of charge transport in COMSOL and Allpix Squared are also provided to validate the estimated Si-SiO_2 boundary conditions with experimental results. This is followed by Chapter 6, which consists of discussions of results obtained from methods and models described in the preceding chapters. Finally, Chapter 7 contains conclusions from the content presented, followed by suggestions for future work.

Chapter 2

Background Literature

2.1 Radiation Transport

To analyze the responses of radiation detectors in various complex radiation environments, rigorous radiation transport is required[13]. The propagation of radiation through a medium is affected by absorption, emission, and scattering processes. The elementary quantity used to characterize how a radiation field propagates in matter is the differential number dN of the transported radiation particles in a position within dr about r, with momentum within dp about p, at time t, given by the following equation:

$$dN = f(r, p, t, \alpha) \times d^3 r \times d^3 p \times dt \times d^n \alpha \tag{2.1}$$

Here, α includes n other variables like particle species, spin, etc., and $f(r, p, t, \alpha)$ is the radiation particle-number density. Assume that an initial source density $f_{\mathrm{src}}(r_0, p_0, t_0, \alpha_0)$ is provided for a mono-energetic point source, the particle density $f_{\mathrm{det}}(r, p, t, \alpha)$ obtained in a detector after the radiation field propagates through a material is found by considering a point source of, say, protons at r_0 emitted at t_0 with momentum p_0 traversing a material M, with a detector D placed after it. Thus, the detector response for a simple mono-energetic point source is obtained by equation:

$$f_{det}(r, p, t, \alpha) = G(r, p, t, \alpha; r_0, p_0, t_0, \alpha_0) \times f_{src}(r_0, p_0, t_0, \alpha_0) \tag{2.2}$$

In the above equation, $G(r, p, t, \alpha; r_0, p_0, t_0, \alpha_0)$ is called a "propagator", which accounts for geometry boundary conditions, scattering through various interaction mechanisms, generation of secondary particles, and effects of external fields. For a more general source, extended in space and with some momentum and energy spectrum, the above equation will be modified as:

$$f_{det}(r, p, t, \alpha) = \int d^3r_0 \times \int d^3p_0 \times \int dt_0 \times \int d\alpha_0 \times G(r, p, t, \alpha; r_0, p_0, t_0, \alpha_0) \times f_{src}(r_0, p_0, t_0, \alpha_0) \tag{2.3}$$

This is a schematic formal way of representing a Boltzmann transport equation, which is generally a multidimensional (>6) integro-differential equation. Unfortunately, for this equation, general analytical or closed-form solutions are extremely time-consuming and difficult. Thus, a stochastic method is often utilized to achieve viable solutions [14].

The Monte Carlo (MC) radiation transport method is a mathematical tool that provides a numerical solution to a problem. The solution provided by this method is based on random statistical trials. This transport method represents a probabilistic model for radiation interactions with matter. It provides the ability to predict many quantities of interest to the nuclear engineering community, e.g., volumetric/surface flux, reaction rates, energy deposited, which are difficult to achieve with manual mathematical calculation. The huge advancements obtained in these methods and their applications in almost every major scientific area are due to their ability to solve difficult mathematical problems with tremendous computational speed provided due to the capability of modern digital computers. Furthermore, due to the stochastic nature of the calculations, simulation of a large number of particle histories is required to achieve the desired statistical accuracy [15]. A number of general-purpose MC-based simulation codes are currently available to today's nuclear engineers for the radiation transport applications, e.g., MCNP [8], Geant4 [9], EGSnrc [16], and PENELOPE [17].

For the work presented in this dissertation, the Geant4 Radiation Transport Toolkit [9] was utilized because it is an open source code available to all. This toolkit can be deployed to efficiently simulate the passage of particles through matter. The functionality provided by this toolkit includes:

1. Tracking: Keeping records of trajectories of radiation particle traversing through matter.

2. Hits: Provides details related to radiation particle interaction with matter.

3. Physics Models: Multiple pre-built physics models are available to the user for various specific applications.

The physics processes simulated include a wide range of radiation particle interaction processes, including electromagnetic, hadronic, and optical processes. An extensive Radioactive Decay module is also available to simulate a large set of long-lived particles, materials, and elements. This toolkit was the result of a dedicated collaboration of software engineers and physicists. Application development with object-oriented C++ language is needed to operate this tool efficiently. This software has found applications in particle and nuclear physics, nuclear and space engineering, and medical physics [18–22].

A sensitive volume is used to declare existing volume as detectors. A particle that enters the detector volume is treated as a point object with a well characterized instantaneous momentum. The space time position of the position of the particle inside the detector is (x,y,z,t) while its energy-momentum is (P_x,P_y,P_z,E). The developers of Geant4 deemed that this is a reasonable approximation, considering that in almost all of the practical simulation cases particles are seen as "*tracks*" in macroscopic detectors. Geant4 employs a semi-classical approach, since the radiation particles are treated classically throughout the simulation, but their interactions - cross sections and final states - take into account the results of quantum-mechanical effects. The basic unit of simulation in Geant4 toolkit is called an "*event*". Initialization of every simulation in Geant4 begins with loading all the necessary physics lists to simulate radiation interaction processes. The C++ based stacking concept is used to track a particle. A run or a process in the simulations begins by generation of primary tracks. The details of these tracks are pushed into a *std::stack*. A track of the radiation particle is processed from the *std::stack* one by one, as per last in first out basis (LIFO). The resulting secondary tracks are pushed into the *std::stack* and this tracking lasts as long as the stack has a track in its memory. When the stack becomes empty, the processing of the event is concluded.

2.2 Background

2.2.1 Oil Well Logging Experiment

The first section of the dissertation will discuss the details of the Geant4 benchmarks performed for a bulk irradiation experiment. Oil-well logging industries around the world utilize inspection tools that typically contain multi-curie level AmBe and ^{137}Cs sources identified by the National Academy of Sciences as Category 1 dangerous radiological sources[23]. The challenge is to find suitable machine-based sources as replacements for these conventional radioisotope sources. Existing radioisotope sources in oil-well logging tools are fairly long-lived and exist in thousands of tools used around the world. In the past, there have been incidents involving these sources that have created great safety and security risks. Past accidents include sources that got stuck down a well and eventually get lost; lost (misplaced) sources during or after well logging; lost or stolen sources (in storage or transport); physical damage (fishing); transportation accidents, including fire; suspected exposure of persons; and leaking sources[24]. Cases like these make the use of conventional sources in well logging an environmental safety and security concern. The preliminary goal was to promote the utilization of powerful machine-based sources as a replacement for radioisotope sources with a more transparent and experimental approach. The major objective of this project was to develop a version of the Monte Carlo Library Least Squares (MCLLS) to invert data from multiple neutron and photon sensors.

A deuterium-tritium (D-T) generator was considered as a replacement neutron source because higher-energy neutrons can generate high-energy inelastic scatter gamma rays from a number of elements, providing useful information on a larger volume of substrate composition. To validate the MCLLS model, it was necessary to design and construct a prototype exploration tool and the Kansas State University Materials Interrogation (KSUMI) testing facility[25]. The purpose of this experimental facility is to provide validation for the simulated responses to benchmark the MCLLS data and to perform experiments demonstrating the effectiveness of powerful pulsed neutron generators as an apparent replacement for conventional radioisotope sources. The skeleton of the designed exploration tool was similar to that of the tool used in oil-well logging industries;

simplicity in design ensured easy modeling in Solidworks[26]. The test facility consists of a large concrete enclosure built around an aluminum pipe of 8 in diameter, representing a borehole. The interrogating source is a pulsed 14.1 MeV neutron source with a 10% duty cycle generating 1000 pulses of high-energy neutrons every second. Geant4[27], was utilized to develop a source code to simulate the complex experimental setup and achieve the results for two experiments with water and sand, respectively. The aim of this study was to compare the experimental data obtained with Geant4 simulations to validate the simulation results, which is important for the future design of fieldable oil well logging tools that utilize machine sources of neutrons.

Methods were developed to define a hybrid geometry in Geant4 where the complicated geometries can be directly imported from CAD and basic structures of the geometry can be defined using conventional C++ object-oriented code. The methods developed during this section of the study were instrumental for the second section of the presented study.

2.2.2 MSND Sensor Details

The silicon-based, single-sided, trenched microstructured semiconductor neutron detector (MSND) is a state-of-the-art semiconductor thermal neutron detector, designed and developed by the S.M.A. R.T. Lab at Kansas State University[4;5;28–36]. The MSND geometry consists of trenches etched along the top surface of the sensor that are back-filled with LiF enriched in ^{6}Li to provide neutron sensitivity. Previous research has been performed at Kansas State University to integrate neutron-sensitive conformally doped MSNDs with Timepix chip for neutron imaging[37–39], with the final product designated as piXelated MSND (X-MSND). It was determined that planar doping geometry, instead of conformal doping in trenches, would help to achieve greater neutron counting rates. In the absence of doping on the trench side-walls, fixed oxide charge (FOC) may impact depletion and electric field characteristics in the device. This work is the first to observe and characterize multiple rise times for microstructured Si devices irradiated with alpha particles. It is also the first reported observation of the effects of FOC in the microstructured sensors. The research presented in this dissertation provides a deeper insight into the impact of Si-SiO_2 interface boundary conditions on signal from a novel semiconductor detector.

2.2.3 DS-MSND Sensor Details

To design and analyze microstructured detectors, MCNP[8] has been utilized in the past, and the simulated geometry was constructed with universes. The Monte Carlo radiation transport source codes and methods developed for the work discussed in previous sections were utilized to import CAD models in Geant4[8] and simulate the precise sensor geometry in multithreading mode in a HPC system. The advanced sensor addresses the need for a compact, high-efficiency, and high spatial-resolution neutron imager. Improvements in neutron detectors for use at high-flux pulsed neutron sources are required for materials research involving neutron scattering experiments conducted in DOE laboratories, including single-crystal diffractometers, neutron reflectometers, and time-of-flight (TOF) measurements. Generally, the requirements for neutron detectors used in these facilities include spatial resolution of the order of 100 μm or less, neutron-detection efficiency exceeding 60% for 1-2 Å wavelength neutrons, ability to operate at rates exceeding 20,000,000 CPS with minimal dead time, and gamma-ray rejection ratios of less than 10^{-6}[12]. Advances in sensor design, readout technology, and data processing algorithms are required to meet these challenging requirements. These requirements will be met by integrating a DS-MSND[4;5;28–31] with the Timepix3[7] read-out chip to create a detection assembly (the X-DS-MSND) and software, capable of being tiles into large imaging arrays.

Geant4 was extensively used to calculate various physical parameters such as trench depth, fin height, and packing fraction of neutron conversion material for the detector that meets some of the requirements mentioned above such as thermal neutron detection efficiency and gamma-ray rejection ratio. There are other properties of the DS-MSND sensor such as charge collection efficiency, response to a detection event, boundary conditions, depletion profile. that are extremely essential for a proper device operation and cannot be evaluated using Geant4 alone. For determination of these properties, detailed semiconductor physics modeling is needed.

2.2.4 Previous X-MSND device details

Significant work has been previously performed and reported with a single sided X-MSND imager[36–38;40]. Here, a single sided conformally doped MSND was coupled to the Timepix readout device. These devices, although slow, were able to successfully demonstrate thermal neutron and x-ray imaging capabilities. The simulation framework for this work consisted of extraction of steady state simulation results (electric field and weighting potential) from COMSOL Multiphysics. These results were then imported to Allpix Squared[10] for charge transport. The X-MSND simulation framework did not consider charge carrier interactions like recombination and repulsion, which are significant, considering that the majority of charge carriers are injected in a region with negligible electric field. Allpix Squared cannot account for accurate FOC and SRV on the Si-SiO_2 interface. High density charge transport in Si devices involves accurate representation of plasma effects[41–44], which was not considered in the X-MSND simulation framework either. These shortcomings of X-MSND framework are addressed and resolved in the new simulation framework presented in this dissertation.

2.2.5 Existing competition to X-DS-MSND

A prospective review of the capabilities of existing technology is needed to understand the state of the art. The proposed X-DS-MSND technology is based on a well-characterized DS-MSND fabrication process with enhancements to make the sensor compatible with Timepix3 pixelated readout application-specific integrated circuits (ASICs). The implementation of a silicon-based microstructured neutron imager has significant advantages over other competing technologies, a few of which are enumerated below.

1. Deeply trenched DS-MSNDs have previously shown greater than 60% thermal neutron detection efficiency.

2. The high Q value of ^{6}Li neutron capture reaction ensures a large output signal and good signal-to-noise characteristics[12].

3. Silicon as a semiconductor substrate ensures the imagers will function well under diverse conditions; no vacuum is required and sensors operate at room temperature.

4. The low overall presence and low-Z number of the silicon substrate ensures that an excellent gamma rejection is possible.

5. The stable availability of high resistivity silicon ensures a consistent supply of substrate material for sensor fabrication.

6. Micro-fabrication of silicon substrates is a well characterized process and ensures repeatability, and bump bonding of silicon sensors to Timepix sensors has also been demonstrated to be repeatable by multiple commercial vendors.

Currently, two sensor technologies offer capabilities and performance similar to those of the X-DS-MSND: the doped microchannel plate (MCP) imagers and Li-In-Se semiconductor imagers. To that effect, a brief prospective comparison of the expected performance of X-DS-MSND against these currently available technologies is presented below.

Doped Micro-Channel Plates (MCP)

^{10}B doped micro-channel plate (MCP) based neutron imagers are commercially available[45–47], and high-resolution variants are currently in development. Variants of the technology have also used Timepix ASICs for read out, with arrays up to 2×2 found in publications[48]. The DS-MSND sensors do not require significant encapsulation (generally, only a metal light/RF shield is applied over the sensor), whereas MCP devices require large evacuated enclosures or vacuum conditions to operate. Neutron imaging with MCPs requires careful alignment of a forward-facing doped micro channel plate, and generally two other amplifying MCPs. This may introduce significant shock and vibration sensitivity. High resolution versions using narrow delay line anodes are also tensioned and aligned, exacerbating the problem. Biases of at least 1100 V are needed in the MCP with a forward face, with voltage division used to bias the secondary MCP planes. However, DS-MSNDS are expected to reach full depletion at 350 V. The high vacuum requirement limits the portability and increases the system footprint of MCP imagers compared to comparable semiconductor-based DS-MSND designs. Arrayed Medipix MCP neutron imaging is limited to 2×N array sizes due to incompatibility of the canted Medipix chips used in large area arrays. Timepix3-based X-DS-MSND assemblies can also be arrayed to produce large area sensors; Timepix3 readout chips are three-edge buttable, and edgeless semiconductor sensor arrays have been manufactured as large as 10x10 chips (14.3 cm × 14.3 cm). Larger MCP imagers are possible with proprietary cross-delay line anode readouts, though these increase readout complexity and limit system compatibility compared to the USB 3.0 based Timepix3 interface[49].

Li-In-Se$_2$

The newly developed sc-LISe semiconductor[50] has been explored as a ^{6}Li loaded semiconductor material for neutron detection and neutron imaging. Imagers have been made by bump bonding LISe wafers to Timepix sensors, similar to conventional planar sensors. However, the main reaction is ^{6} Li(n,α)t for both the X-DS-MSND and LISe detector. In LISe, the isotope ^{115}In has an exceptionally larger cross-section for radiative capture of around 202 b; that of natural indium is 195 b. Also, ^{79}Se has an appreciable n-γ cross-section of 50.0232 b. These materials compete with ^{6}Li for neutron absorption and decrease the neutron detection efficiency of the sensor. In case of LiF, the absorption cross section of ^{9}F is 9.57×10^{-3} b. Therefore, a greater neutron detection efficiency can be observed from X-DS-MSND. LISe sensors become activated via neutron capture. The decay of ^{116}In will release betas (isomer with a large end-point energy of 3.3 MeV). The range of a beta at this energy is 6 mm, over 100 times the pixel pitch, greatly distributing the charge in the sensor. These decays are accompanied by gamma-rays, which may interact with the sensor material. The band gap of the LISe material is 2.8 eV, compared to 1.1 eV for Si based DS-MSNDs. LISe operating voltage is 545 V mm^{-1}, comparable to the X-DS-MSNDs at 350 V mm^{-1}; considerably less leakage current is observed in DS-MSNDs. The articles on LISe devices further discuss performance concerns due to sample size limitations[50]. Because the sensors were grown to a diameter smaller than the Timepix ASIC, the sensor operated only on a subset of the available pixels. Materials like ^{79}Se and ^{115}In in LISe sensor have 5-6 b cross-sections for fast neutrons, whereas X-DS-MSNDs are mostly used for detection of thermal neutrons. MCNP simulations have been performed on LISe devices, but no advanced charged-drift simulations are available. The constituent elements of LISe have higher atomic number as compared to silicon, making them more susceptible to gamma and X-ray interactions. No gamma-ray rejection methods are discussed in published literature, and a single energy-based threshold reduces neutron detection efficiency. No publications are available on sc-LISe thicker than 1 mm, whereas X-DS-MSND sizes are limited

Table 2.1: *Technology Summary Table*

Properties	X-DS-MSND	MCP	LISe
Spatial Resolution	<55 μm	<50 μm (commercial) ∼10-15 μm (research)	∼34 μm
Temporal Resolution	50 ns	100 ns	N/A
Neutron Sensitivity	60%	∼45%	35-55%
Gamma-ray Sensitivity	$1{:}10^6$	1:100	N/A
Single Sensor Size	14 mm×14 mm	18 mm - 150 mm (dia)	8.25 mm×5.5 mm
Readout Interface	USB 3.0	USB 2.0	USB 2.0

only to the availability of high resistivity silicon. A brief parametric comparison of these technologies is provided in Table 2.1 [4;5;12;28–31;45–50].

2.2.6 Semiconductor Physics Modeling

COMSOL [11], a finite element solver, was utilized to simulate the semiconductor physics to investigate the effects of FOC on the trenches of the prototype MSND device. COMSOL's Semiconductor Module is a collection of interfaces and predefined models that are utilized for modeling and for addressing semiconductor device physics. It also includes a dedicated physics interface to solve the single-particle Schrödinger equation [51] for general quantum mechanical problems as well as quantum-confined semiconductor systems. The semiconductor module assumes a Maxwell-Boltzmann distribution for the carrier energies of nondegenerate semiconductors at a given temperature. This assumption reduces the non-linearity of the semiconductor equations. If degenerate semiconductors are present within the model, or at lower temperatures, it is necessary to use Fermi-Dirac statistics [52].

COMSOL's Semiconductor Module is well documented and includes detailed outline of the theory on which it is based. The software is uniquely transparent because the model equations are always visible. This interface solves the continuous Poisson equation related to electric field for charge carriers represented in equation 2.4.

$$\nabla \cdot \mathbf{E} = \nabla \cdot (-\varepsilon_r \nabla V) = q(p - n + N_d^+ - N_a^-) \tag{2.4}$$

Here, E is the electric field, the permittivity of silicon is represented by ε_r, q is the elementary charge, n is the electron concentrations, p is the hole concentration, N_d^+ is the donor concentration, and N_a^- is the acceptor concentration. Results obtained for this equation provide complex electric field, carrier concentration, and leakage current for the user defined semiconductor device geometry.

Another important aspect of the COMSOL based semiconductor simulations is the creation of an unstructured mesh. An extremely fine mesh would enhance the accuracy of the results; however, this would severely increase the simulation time. Furthermore, an extremely coarse mesh would fail to converge due to the high computational error per iteration. Thus, while solving for electrostatic fields in the presence of mobile charge carriers, it is important to consider the Debye length as shown in equation 2.5.

$$L_d = \sqrt{\frac{k_B T \varepsilon_0 \varepsilon_r}{q^2 N}} \tag{2.5}$$

Here, k_b is the Boltzmann constant, T is the temperature of the lattice, ε_0 is the permittivity of the free space, ε_r is the relative permittivity of the semiconductor, q is the elementary charge and N is the total concentration of holes and electrons. This length is the scale over which the electric field decays in the presence of mobile carriers; it is critically important to resolve this length scale with the unstructured mesh defined by the user in semiconductor models. To further optimize the simulation time, zero-Neumann boundary conditions were applied such that a one-quarter pixel geometry geometry was modeled and meshed. The COMSOL default silicon material was used to model the diode. The Charge Conservation node was deployed to use add air as a dielectric material; this node provides capability of modeling charge conservation properties according to Gauss's Law for the electric displacement field.

Fabrication work for this dissertation was performed by Radiation Detection Technologies, Inc. A set of well-characterized single- and double-sided MSNDs was fabricated to provide empirical data to validate the observations made from the simulated models. The DS-MSNDs were fabricated with trenches etched through a planar n-type contact and a planar p-type contact diffused into the backside of the diode. It was noticed that the KOH wet etching step drastically (> 10x) increased the lateral etch rate of the fins. This increased etch rate was probably due to the high concentration of dopant atoms on the tops of the fins. Therefore, to prevent lateral etch-out of the DS-MSNDs an undoped buffer region was masked by SiO_2 between the doped region on the fin and the edge of the trench. A new photomask with these features was obtained and used prior to implant pattering of the X-DS-MSND. The reverse MSND wafers were then separated to study the efficacy of different surface passivation techniques for exposed Si in the trenches: native oxide, 50 nm dry oxidation, 100 nm dry oxidation, 250 nm dry oxidation, and h-termination followed by 200 nm parylene coating. Following passivation, the IV and CV characteristics were measured. In general, 250 nm dry oxidation performed the best, demonstrating the highest average breakdown voltage while retaining a relatively low leakage current below breakdown. Thicker oxides may further reduce the leakage current but would negatively affect the neutron detection efficiency by reducing the neutron absorption efficiency and the reaction product escape probability. The maximum concentration of *n*-type dopant near the top of the device was around $5 \times 10^{17}\ \mathrm{cm}^{-3}$. The bottom of the detector was doped with a similar concentration of *p*-type dopant.

2.2.7 Boundary Conditions

Two main characteristics of the Si-SiO_2 interface are FOC and interface traps that could have a significant impact on charge transport. These boundary conditions will be analyzed and considered in this dissertation. The Si-SiO_2 interface will cover the entire fin structure of the DS-MSND diode, and since most of the charge carrier injection will occur in the fins, it is extremely essential that the effects of these boundary conditions are accurately modeled in the simulations. The analysis and implementation of boundary conditions present multiple challenges in setting up an optimum unstructured mesh for the simulations to converge with minimum iteration steps. Furthermore, high-fidelity modeling of these conditions drastically increases the simulation time.

Fixed Oxide Charge

The depletion profiles of the trenched devices are complicated by trapped charges in the thermally grown oxide layer during fabrication[53]. These charges are called oxide charges and are further classified into four types: surface states, FOCs, oxide-trapped charges, and mobile oxide charges.

Surface states are caused by structural defects and are typically removed by a low-temperature annealing process. Oxide-trapped charges are holes or electrons that are trapped near the oxide interface; these charge carriers are created in the semiconductor volume by the external incident ionizing radiation, and can be removed by low temperature annealing. Mobile oxide charges are contaminants from Na^+, Li^+, or K^+ ions that can occur during the fabrication process. These charges are often identified using a bias stress test. FOCs are typically positive charges located near the semiconductor-oxide interface and are the result of the thermal oxidation process[53;54]. FOCs are of primary interest for the trenched sensors discussed in this dissertation. A positive space charge is formed inside the oxide film as a result of these FOCs during the thermal oxidation process. This induces a negative image charge in the Si substrate. The accumulation of *n*-type carriers near the Si-SiO_2 interface on an *n*-type substrate further decreases the resistivity of the substrate around the Si-SiO_2 interface, increasing the bias required for complete depletion of the diode as represented in Figure 2.1[55].

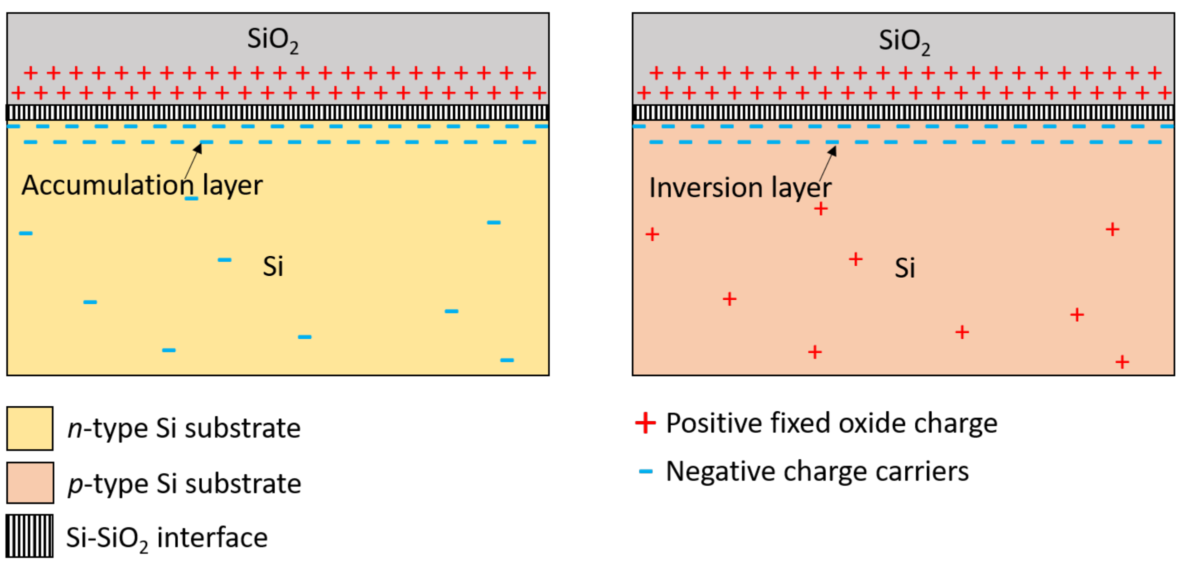

Figure 2.1: *A generalized representation of the effects of the formation of fixed oxide charge due to the formation of a SiO_2 mask on a n-type (Left) and p-type (Right) silicon substrate.*

FOCs are stable under moderate temperature and bias conditions and are not affected by changes in surface potential[56]. The density of FOC is dependent on the surface orientation of the substrate. For DS-MSND / MSND sensors, the effects of FOC need to be investigated on the trench walls ($< 111 >$ orientation) of the fabricated detector.

Charge Recombination Velocity

Charge carrier recombination is a phenomenon that can severely affect the amplitude of the output current signal of the sensor. Defects or impurities present at the Si-SiO_2 interface enhance recombination rates and severely decrease the lifetimes of the charge carriers around the interface. Since the Si-SiO_2 interface represents a severe disruption of the crystal lattice, the surface of the fin is a site of particularly high recombination. Due to the high recombination rates, the region around the Si-SiO_2 interface is further depleted of minority charge carriers. A localized area of low charge carrier concentration causes charge carriers to flow into this region from the surrounding higher charge carrier concentration regions. Therefore, the surface recombination rate is limited by the rate at which minority charge carriers move towards the Si-SiO_2 interface. A parameter called surface recombination velocity (SRV) is used to characterize the recombination at a Si-SiO_2 interface. Furthermore, changes in the SRV value are expected due to the substrate resistivity and the FOC value. The work presented in this dissertation will provide an approximation of the SRV value to accurately estimate the DS-MSND/MSND response.

2.3 Charge Carrier Transport

Understanding the depletion region, including the direction and magnitude of the electric field, is key for detailed analysis of a modern semiconductor radiation detector. It is known that any motion of charge carriers in an electric field causes an induced current. The motion of the charge cloud in the presence of a substantial electric field is often dominated by drift. Charge carriers typically do not follow straight line paths, as they encounter velocity changes due to thermal scattering. In the absence of a substantial electric field inside the semiconductor material, such as that found in the undepleted region, diffusion dominates the charge carrier motion. In many circumstances, charge carrier diffusion and drift are both important for predicting the corresponding current pulse. There is an average net motion of the charge cloud along the direction of the applied electric field, and the charge cloud diffuses as it drifts. These phenomena are depicted in Figure 2.2. The diffusion of charge carriers with respect to time[57] is given by:

$$\sigma = \sqrt{2Dt} \tag{2.6}$$

Here, σ is the root mean square (rms) width of the charge cloud diffusion, t is the time and D is the diffusion constant, linked to the charge mobility (μ_q) by the Einstein relation:

$$D = \frac{kT}{q}\mu_q \tag{2.7}$$

In the above equation, k is the Boltzmann constant, T is the absolute temperature, and q is the elementary charge.

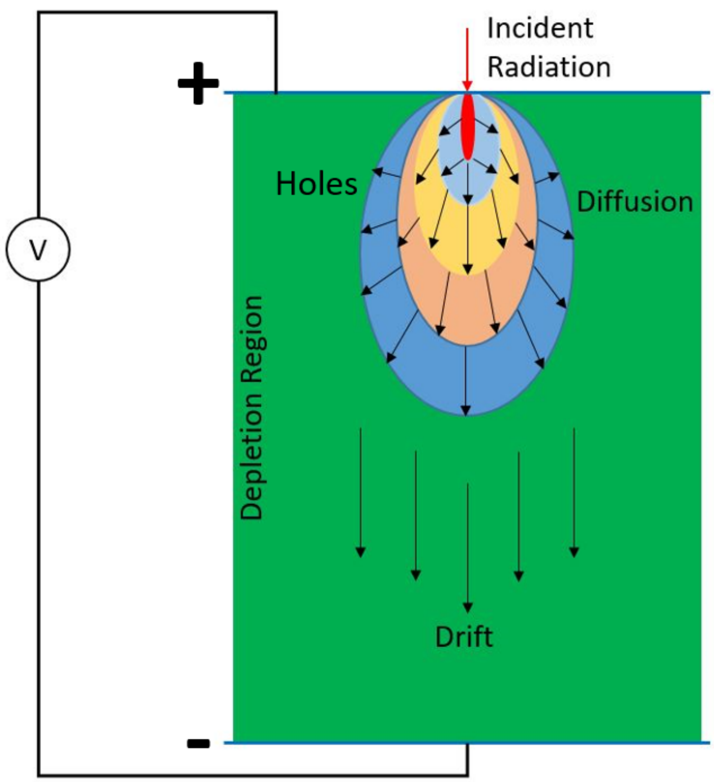

Figure 2.2: *Representation of charge cloud motion inside a semiconductor device in the presence of an applied electric field.*

There is a tremendous need for simulation methods and models to accurately predict the charge carrier motion and account for the detector response current corresponding to the radiation particle interaction in the active region of the sensor. The current literature lacks details about the charge cloud behavior and resulting induced currents in a planar-doped microstructured solid-state detector, which are provided in this dissertation. If the injected charge cloud is a result of a densely ionizing particle, and if the electric field is not strong enough to penetrate the charge cloud completely, charge collection takes much longer than estimated using simple theoretical estimations. This phenomenon is called the "plasma effect" and was discovered in 1960 by Miller[41]. In addition, analytical results were provided by Tove in 1966[42]. Tove suggested that in order for the plasma effect to take place, the ionization density of the particle track must be sufficient to introduce a conductive channel inside the active semiconductor volume along its path, justifying the existence of plasma conditions that would cause a comparable delay in the separation of injected charge carriers due to shielding from the existing external field. Tove's article provided one-dimensional approximations for plasma effects that greatly overestimated experimental plasma time results, as this problem requires three-dimensional analysis. In 1973, Tove published a follow-up article[43], which provided better agreement with the experimental results for particle tracks longer than 15 μm and for the alpha particles of energies between 5.3-8.8 MeV.

Plasma effects also cause inefficient collection of charge carriers at respective electrodes because of the presence of traps and recombination inside the dense injected charge cloud. Further, the aforementioned theoretical estimations include a serious uncertainty in the calculation of the charge carrier transit time, since the last group of carriers to be collected move in an electric field that is modified by the charge carriers moving in front of them. The aforementioned articles further describe the plasma time as the time needed to bring all the charge carriers inside the injected charge cloud under the influence of an external electric field. More relevant terms "Peak Time" (T_P) and "Knee Time" (T_K) were used by Williams[44] to describe the key features of induced current or space charge limited currents due to motion of injected high density charge cloud. Similar terminologies will be used to describe the work presented in this dissertation as well. Furthermore, the aforementioned studies assume a simple planar device with a linearly varying electric field profile. The work presented in the dissertation provides detailed insights on plasma time effects, by describing and benchmarking charge-cloud behavior in a non-planar device by utilizing high-fidelity finite element method (FEM) based COMSOL Multiphysics simulations. The previously cited articles could only provide estimations for an over-depleted semiconductor sensor. This dissertation will address the complexities of charge cloud motion inside a partially depleted microstructured solid state radiation detector.

Section Summary

A through background of the present literature justifies that there is a serious need for coupled radiation-charge transport simulations. There is no literature available that describes the behavior of the injected charge in the vicinity of the Si-SiO_2 interface.

Chapter 3

Radiation Interactions and Simulated Geometries

3.1 Neutron Sources

The interrogating source for the oil well logging experiment is an accelerator-based D-T neutron generator that produces neutrons with 14.1 MeV kinetic energy. It is a B-322 model developed by ThermoFisher Scientific; this model is not currently in production, but the output of B-322 is similar to the B-320 model[58]. The generator produces a nearly isotropic distribution of mono-energetic neutrons with a maximum yield of 1.6×10^8 neutrons per second, with a pulse repetition frequency of 1 kHz and a 10% duty cycle. For this experiment, the accelerator was housed in a cylindrical metallic structure with a diameter of 2 in and length of 40 in. An external electrical supply of 200 V and 24 µA was required to power a control board that interfaced with the accelerator assembly. To generate the desired neutron output from the generator, separate internal voltage bias and tube current are applied; for these experiments, the generator was operated at 40 kV and 40 µA. In this setting, the generator produced approximately 2×10^6 to 3.5×10^6 neutrons per second. This source can be remotely operated through a desktop using a graphical user interface provided by the manufacturer.

For the development of the X-DS-MSND, simulations were performed with a mono-energetic thermal neutron source of 0.0253 eV kinetic energy, as per the requirement of the funding agency [12]. Thus, it is important that the developed Geant4 source code accounts for all the primary and secondary interactions caused by thermal neutrons as described below.

3.2 Neutron Interactions in Oil Well Logging Experiments

As neutrons are indirectly ionizing particles, they interact with matter via physical collisions with the target atomic nuclei. On the basis of the probability of interaction, depending on the incoming neutron's kinetic energy, the neutron might scatter off the target atomic nucleus or combine with it. The aforementioned probability of interaction between a neutron and an individual or nucleus is characterized by the microscopic cross-section, σ [59]. Based on the type of interactions, various microscopic cross sections values can be obtained for a neutron traveling with the same kinetic energy [60]. The important microscopic cross sections are provided in the following.

- σ_{es} is elastic scattering cross section,
- σ_{is} is inelastic scattering cross section,
- σ_{γ} is radiative capture cross-section,
- σ_{f} is fission cross section,
- σ_{p} is (n, p) reaction cross section,
- σ_{T} is (n, T) reaction cross section, and
- σ_{α} is (n, α) reaction cross-section.

The sum of the microscopic cross sections of reactions in which a neutron is completely absorbed in matter is called the total absorption cross section. Mathematically, it is given by:

$$\sigma_a = \sigma_\gamma + \sigma_f + \sigma_p + \sigma_T + \sigma_\alpha \tag{3.1}$$

Here, σ_{a} is the absorption cross section of the incident neuron as a function of its kinetic energy. Similarly, the sum of the microscopic interaction cross sections for interactions in which neutrons scatter is called a scattering cross section and is given by:

$$\sigma_s = \sigma_{es} + \sigma_{is} \tag{3.2}$$

Here, σ_{s} is the scattering cross section of the incident neuron as a function of its kinetic energy. σ_{es} and σ_{is} is the elastic and inelastic scattering cross section, respectively. Finally, the sum of all reaction interaction cross sections is known as the total neutron cross section.

$$\sigma_t = \sigma_a + \sigma_s \tag{3.3}$$

The SI unit for the microscopic interaction cross section is the barn, which is equal to 1×10^{-28} m^{-2}. The macroscopic cross section is defined as the probability that a neutron interacts with a material per unit travelled path length, i.e., the probability of neutron-nucleus interaction per centimeter of neutron travel[61]. The macroscopic interaction cross section is also known as total neutron cross section $\sum_{\mathrm{t}}$ given by:

$$\sum = N\sigma \tag{3.4}$$

N is the atomic density of the target material in cm^{-3}, and is given by:

$$N = \frac{\rho}{A} N_A \tag{3.5}$$

Here, ρ is the mass density, A is the atomic weight, $\mathrm{N_A}$ is Avogadro's number, $6.022\,140\,76 \times 10^{23}$ mol^{-1}. The cross section variables discussed in the above equations are freely available and can be obtained from the Evaluated Nuclear Data File (ENDF) database[1]. The variation of the total neutron microscopic interaction cross section as a function of incoming neutron energy for hydrogen is represented in Figure 3.1. Figure 3.2 represents the variation of the inelastic scattering interaction cross section as a function of incoming neutron energy for iron.

There are several possibilities of neutron interactions with matter, as shown in Figure 3.3. As

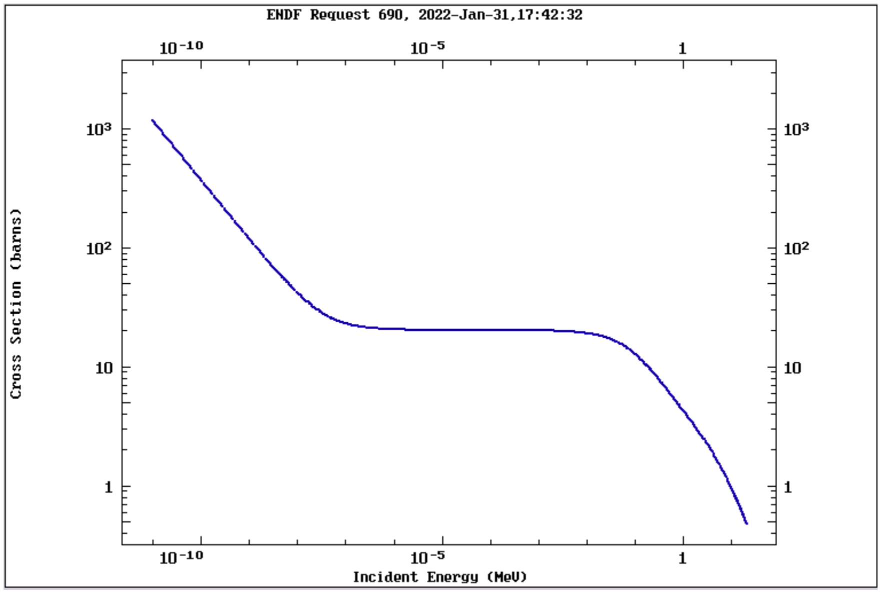

Figure 3.1: *A representation of the total neutron microscopic interaction cross section for hydrogen obtained from the Evaluated Nuclear Data File (ENDF) Database Version ENDF/B-VII.0* [1].

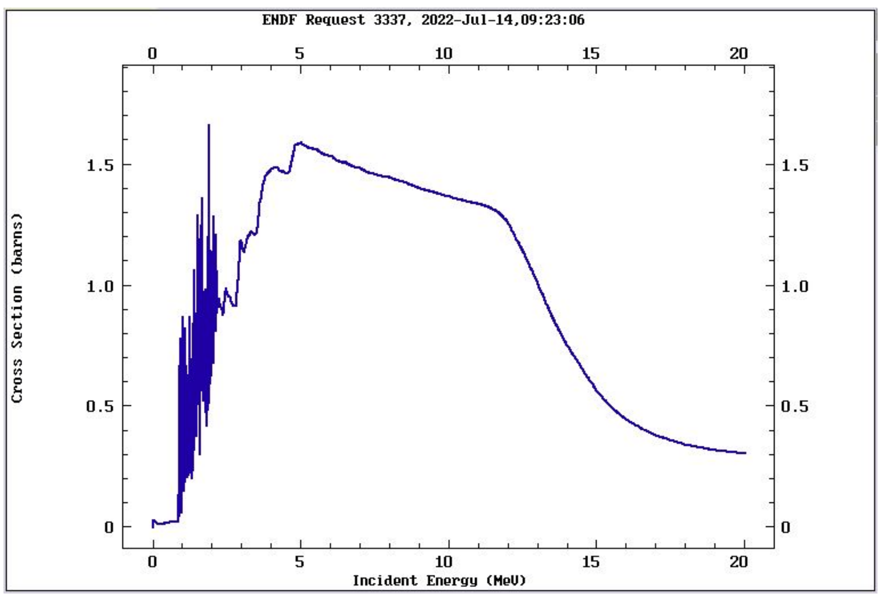

Figure 3.2: *A representation of the inelastic scattering interaction cross section for iron obtained from the Evaluated Nuclear Data File (ENDF) Database Version ENDF/B-V*

mentioned above, there are two main categories of neutron interactions with matter, scattering and absorption [62].

3.2.1 Neutron Absorption

The incoming neutron is completely absorbed by the target nucleus in these types of interaction and, as a result, a compound nucleus is formed.

Electromagnetic

Type of nuclear reaction in which a target nucleus absorbs a neutron and then emits a discrete quantity of electromagnetic energy, i.e., a gamma photon. The target nucleus and the product nucleus are different isotopes of the same element. These reactions are also designated as (n,γ) reactions. Some examples are ^{19}F(n,γ)^{20}F and ^{12}C(n,γ)^{13}C.

Charged

These type of reactions include the absorption of the incoming neutron, resulting in an unstable compound nucleus. This compound nucleus obtains stability after releasing a charged particle. These reactions are designated by (n,p), (n,α), (n,d), etc.

Neutral

These type of reactions include absorption of incoming neutrons, thus resulting in an unstable compound nucleus. This compound nucleus obtains stability after releasing one or more neutrons. These reactions are designated by (n, n), (n, 2n), (n, 3n), etc.

Fission

This is a special case, especially for materials with a heavier nucleus, such as ^{235}U. The incoming neutron is absorbed and the compound nucleus breaks apart, resulting in a high net energy yield because of the difference in the sum of the masses of the products and reactants.

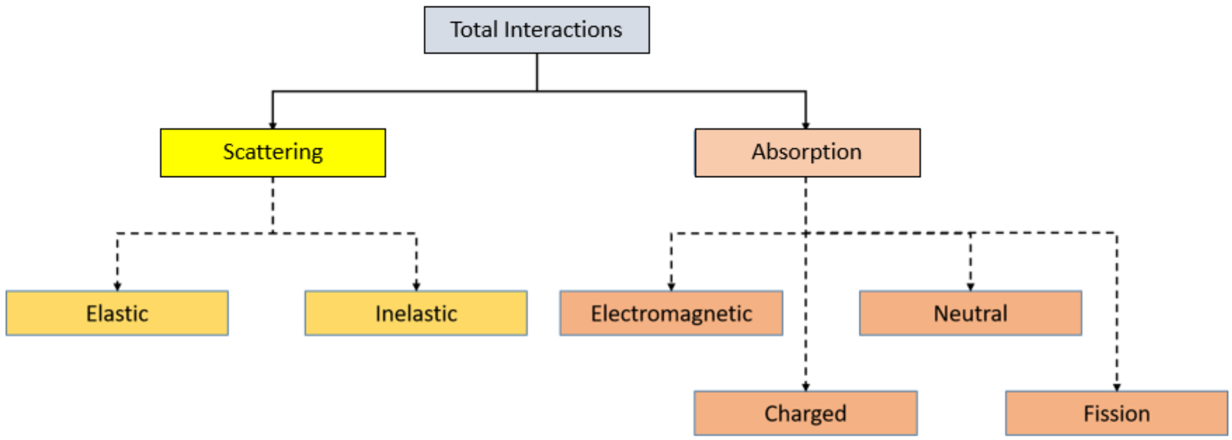

Figure 3.3: *A representation of possible neutron interactions with matter*

3.2.2 Neutron Scattering

Elastic Scattering

Elastic scattering is a neutron scattering process in which the kinetic energy of the incoming neutron particle is conserved in the center-of-mass frame; however, its direction of propagation is modified due to interaction with the target nucleus. Furthermore, while the particle's kinetic energy in the center-of-mass frame is constant, its energy in the laboratory frame is not. Generally, elastic scattering describes a process in which the total kinetic energy of the system is conserved.

Inelastic Scattering

Inelastic neutron scattering is a process in which the kinetic energy of an incident neutron is not conserved. This process is largely observed for fast neutron interactions that result in a short lived activated target radionuclide. This activated target radionuclide immediately stabilizes by release of a prompt gamma-ray. For irradiation experiments with a fast neutron source, prompt gamma signals from inelastic neutron scattering are an important consideration. An example of activation gamma rays resulting from fast neutron interactions is one involving aluminum, which is a commonly used structural material. The reaction ^{27}Al(n, α)^{24}Na yields two gamma rays of energies 1.37 and 2.75 MeV following the radioactive decay via cascade of ^{24}Na ($t_{\frac{1}{2}}$ = 14.96 h).

3.3 Neutron Interactions in Trenched Silicon Neutron Sensors

Fast neutrons interact with silicon by displacing atoms in the lattice, thus creating direct ionization due to displacement defects and other secondary radiation particles[63;64]. Thermal neutrons, on the other hand, have very low interaction cross sections with silicon and require a neutron conversion material. The conversion material has a high thermal neutron absorption cross section and a very short half-life. The final reaction products are heavy ions that deposit energy directly in the silicon material. For microstructured Si based sensors, the neutron conversion material is 96% enriched LiF nanopowder[4]. ^{6}Li has a very high cross-section of 938.818 b at 0.0253 eV neutron kinetic energy compared to that of ^{7}Li (1.085 14 b), ^{19}F ((3.747 39 b)), and ^{28}Si ((2.160 33 b))[65]. The variation of the absorption cross section of ^{6}Li with respect to the incoming neutron kinetic energy represented in Figure 3.4, showing a higher absorption probability for cold to thermal neutrons. The interaction probability decreases rapidly with respect to increasing neutron kinetic energy.

The primary reaction to obtain appreciable neutron sensitivity in the Si-based microstructured devices is shown below:

$$^{6}Li + n \longrightarrow {}^{3}H + {}^{4}He + 4.783\,\mathrm{MeV}, \tag{3.6}$$

In the above equation, the alpha and triton particles have energies of 2.055 MeV and 2.728 MeV, respectively. Monte Carlo simulations will be needed to determine the LiF packing fraction of the designed sensor. B_4C is another competitive candidate; however, it was rejected due to the fact that the reaction products of ^{10}B will undergo larger parasitic energy losses in the conversion material compared to the LiF material, as shown in Section 3.1.2 of the dissertation[38]. The alpha and triton particles are emitted anti-parallel to each other and originate almost instantly. The optimum enrichment of ^{6}Li is needed to be determined to achieve high detection efficiency in the DS-MSND sensors.

3.4 Gamma-Ray Interactions in Oil Well Logging Experiments

The photon is a type of elementary particle. Photons are chargeless and massless, moving at the speed of light in a vacuum environment. There are basically three types of photon interactions with

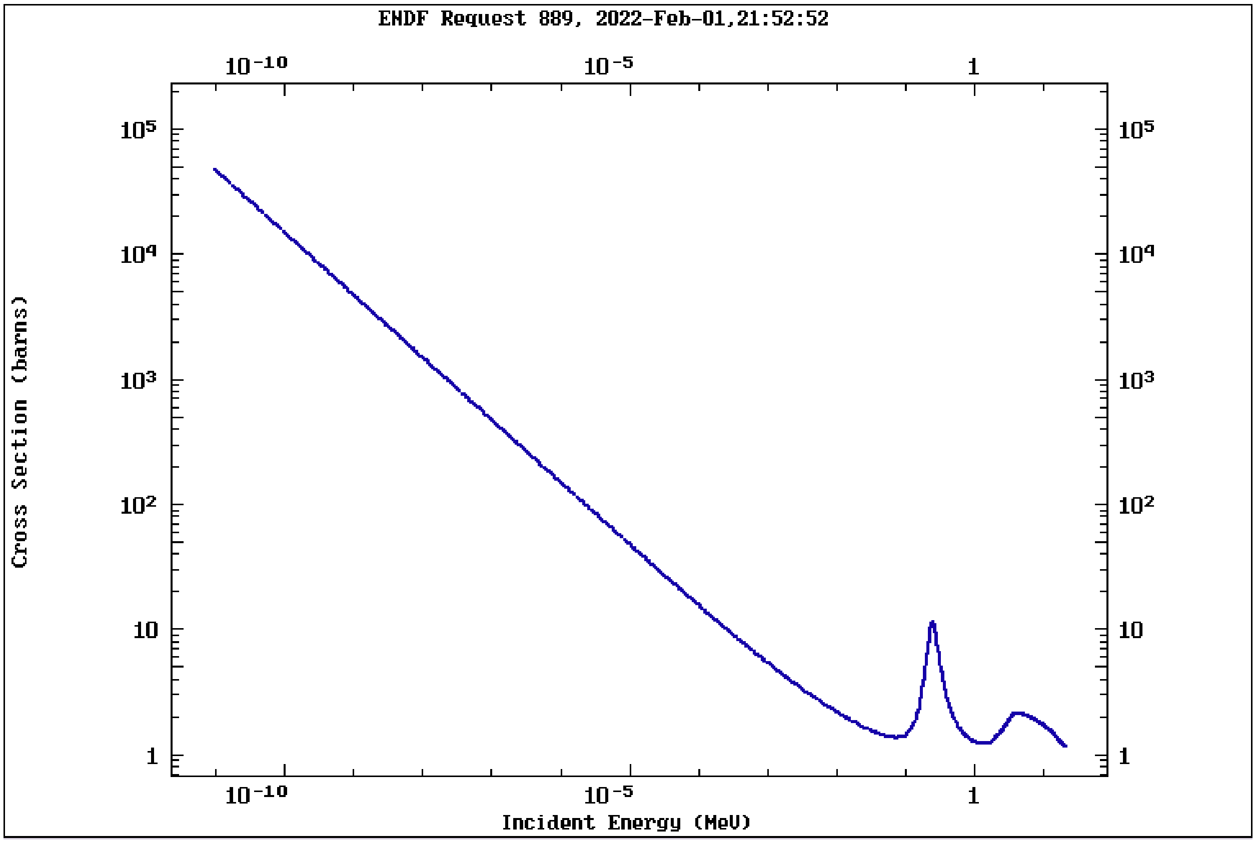

Figure 3.4: *A representation of the total neutron microscopic interaction cross-section for ^{6}Li obtained from Evaluated Nuclear Data File (ENDF) database*[1].

matter that need to be accounted for in the simulations. It is widely known that a fast neutron field is always accompanied by large number of gamma-rays due to inelastic interactions with air. As the neutrons are the primary source of irradiation for this work, it is essential for the simulation framework to account for all secondary interactions.

3.4.1 Photoelectric Effect

Historically, the photoelectric effect is defined as the emission of electrons from a material after the absorption of electromagnetic radiation. Physicist Albert Einstein was the first to describe the effect fully and received a Nobel Prize for his work[66] in 1921. The kinetic energy of the ejected electron is equal to the photon energy minus the binding energy of the electron for the specified atom. The energy of the incoming photon is partly used to liberate the electron from the atom. The

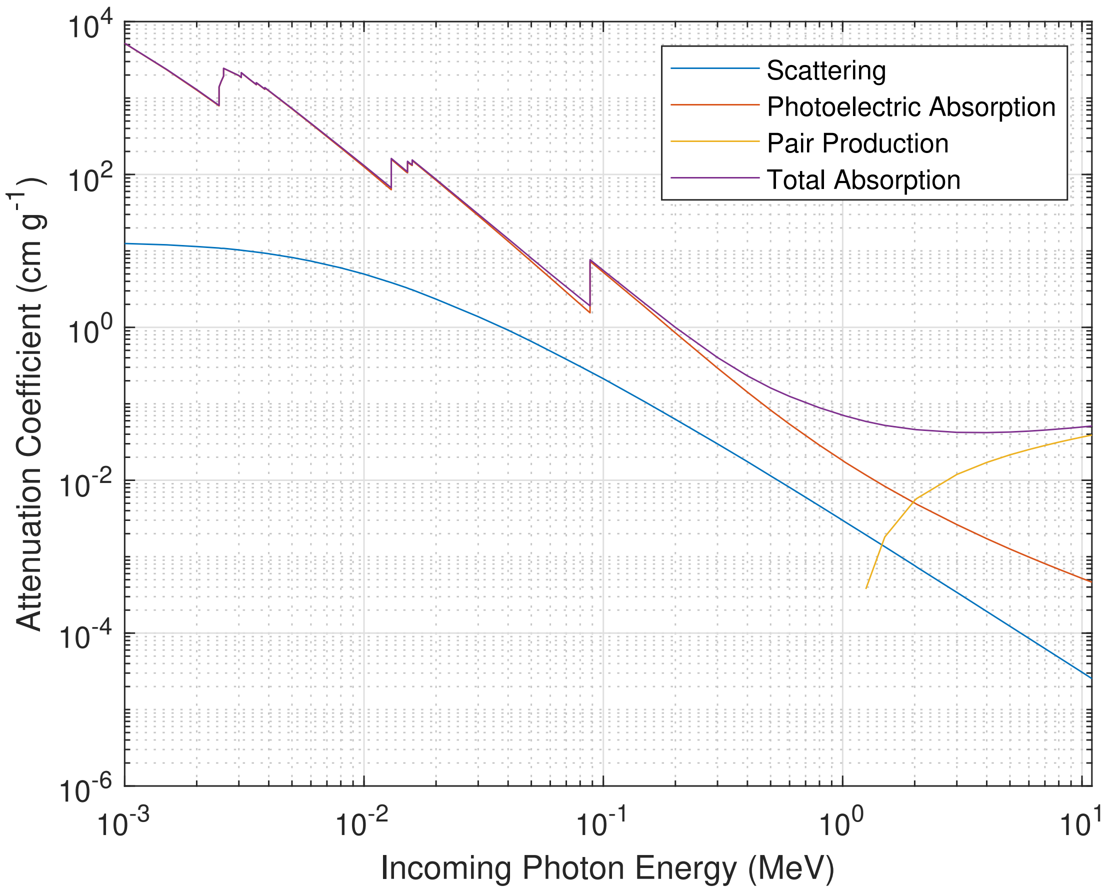

Figure 3.5: *A representation of the gamma-ray interaction cross-sections for ^{82}Pb obtained from NIST-XCOM*[2].

remainder is given to the kinetic energy of the ejected electron. In equation form,

$$KE_m = hf - BE \tag{3.7}$$

Here, KE_{m} is the kinetic energy of the ejected electron, hf is the energy of the incoming photon, and BE is the binding energy of the electron specific to the material of interaction.

3.4.2 Compton Scattering

Compton scattering is the inelastic scattering of a photon by a free electron. The incident photon is deflected through an angle with respect to its original direction. This deflection decreases the photon energy (decrease in the photon frequency). The photon transfers a portion of its energy to the recoil electron. The energy transferred to the recoil electron can vary from zero to a large fraction of the incident photon energy, since all scattering angles are possible. A. H. Compton observed the Compton scattering in 1923 at Washington University in St. Louis[67] and earned the Nobel Prize in Physics in 1927 for this new understanding of the particle nature of photons. The wavelength shift formula for the scattered photon is:

$$\Delta\lambda = \frac{h}{m_e c}(1 - \cos\theta) \tag{3.8}$$

where m_e is the mass of the electron, and θ is the angle between the incident and scattered photons. The final photon energy is obtained by modifying Equation 3.8 and is provided below:

$$E_f = \frac{1}{E_i^{-1} + E_e^{-1}(1 - \cos\theta)} \tag{3.9}$$

where E_i is kinetic energy of the incident photon and $E_e = m_e c^2$ is the rest energy of the electron.

3.4.3 Pair Production

Pair production is direct conversion of radiant energy to matter. It is one of the principal ways that high-energy gamma rays interact in matter. For pair production to occur, the photon energy must be at least 1.02 MeV. Photon energy in excess of this amount, when pair production occurs, undergoes conversion as per Equation 3.10. The positron quickly undergoes annihilation with another electron in matter. There exists an inverse process to pair production called pair annihilation, in which a particle and its antiparticle collide and annihilate; the total energy of the two particles is converted to electromagnetic radiation. In the case of an electron and positron, the energy balance can be represented as:

$$2m_0c^2 + K(-e) + K(+e) = hf \tag{3.10}$$

The first term represents the rest energy of both particles, the second and third terms are the kinetic energies just before the collision, and the term on the right-hand side of the equation represents the creation of two photons, each having the same frequency f and energy hf. The equation indicates that hf must be at least equal to m_0c^2=0.511 MeV.

3.5 Gamma-Ray Interactions in Trenched Silicon Neutron Sensors

Incident photons on a Si-based device may interact and deposit energy in the substrate. An energy deposition equivalent to 3.62 eV[68] results in the generation of one electron-hole. Once created, the carriers are free to move in the semiconductor lattice, where they are either quickly collected by pixel elements or electrodes or undergo recombination. Usually, silicon-based imagers are designed and fabricated so that the electrons are collected and the holes are discarded through a ground because of higher electron mobility. However, MSND-type sensors utilized for this dissertation are designed so that the holes are collected and the electrons are discharged to ensure that the free holes are prevented from falling in the Si-SiO_2 interface traps present at the fin walls. Particles other than photons are also capable of producing the free charge carriers by ionizing silicon atoms as they travel through the lattice. These particles could include high-energy electrons, alpha particles, and protons.

3.6 Simulation Details: The Oil Well Logging Experiment

Geant4[69;70], a widely used C++ based Monte Carlo radiation transport simulation toolkit that is capable of efficiently simulating complex radiation environments in any type of modeled experimental environment, was utilized to simulate the oil well logging experimental setup. To accurately model the setup, a hybrid geometry was prepared. The term "hybrid geometry" describes the fact that the entire geometry except the exploration skeleton tool was modeled with the usual C++ based conventional Geant4 code. The exploration skeleton tool that houses the machine-based D-T neutron generator was first designed in Solidworks and later imported into Geant4 in a Geometry Description Markup Language (GDML) format based on tessellated geometry[71]. Geant4 provides the user with a GDML parser that imports the GDML file as a *G4Solid*, and thus the *G4DisplacementSolid* object was used to place the solid in the simulated geometry. During this process, a new bug was reported in the multithreaded Geant4.10.5 version related to the GDML import functionality to the Geant4 development team[72]. The bug prevented the execution of the above-mentioned hybrid geometry on multiple threads. This was resolved in Patch 1 release of Geant4.10.5; here, protection was implemented to the internal *Write()* and *Read()* functions of the GDML parser to prevent worker threads from executing writing and restricting this to only the master thread (referenced as problem report #2156[73]). The resolution of this bug in the subsequent Geant4 version made the application capable of simulating the hybrid geometry on a high performance computing server in multithreaded mode.

3.6.1 Selection of Physics List

With Geant4, it is generally recommended that a pre-built reference physics list be used for the simulations as they are rigorously tested and validated for common radiation transport applications. The *QGSP* is a quark-gluon string model for high-energy interactions of protons, neutrons, pions, kaons, and nuclei. High energy interactions create an excited nucleus, which is passed to the precompound model for nuclear deexcitations[74;75]. For this work, both *QGSP_BIC_HP* (*QGSP* with binary cascade model) and *QGSP_BERT_HP* (*QGSP* with Bertini Intranuclear Cascade model) were considered. By applying *_HP* to *QGSP_BERT* and *QGSP_BIC* physics lists, the data-driven high-precision neutron package (*NeutronHP*) is applied to transport neutrons below 20 MeV, ensuring high accuracy results for neutron transport at lower energies. As the entire geometry mostly consisted of concrete, *QGSP_BIC_HP* reference physics list was finalized according to the recommendations provided in past studies[76]. The low-energy neutron cross section data in Geant4 utilized ENDF/B-VII.1 data libraries[1].

3.6.2 Modeled Materials and Geometry

The Kansas State University Materials Interrogation (KSUMI) test facility was modeled in Geant4 in great detail.

Simulated Materials

The first major material was concrete with an effective density of $2.35\,\mathrm{g\,cm^{-3}}$. This material model consists of approximately 50% oxygen, 8% calcium, and 31% silicon by weight; minor contributions to this composition were also from hydrogen, sulfur, aluminum, iron, potassium, sodium, and magnesium. In the Geant4 model, the roof, floor, facility walls, and tank walls were made of concrete.

The second major material was borated high density polyethylene (HDPE) with a density of $1.04\,\mathrm{g\,cm^{-3}}$. It is a plastic with a chemical composition consisting of carbon and hydrogen in $(C_2H_4)_n$ form and was enriched with 8% natural boron by weight. This material is commonly used for thermal neutron shielding due to its affinity for absorbing thermal neutrons because of the presence of boron (absorber) and moderation of fast neutrons because of its high hydrogen content.

The third major material for external components was HDPE with an effective density of $0.97\,\mathrm{g\,cm^{-3}}$. This is also plastic with a chemical composition consisting of carbon and hydrogen in $(C_2H_4)_n$ form. It is widely used for neutron shielding because of the high hydrogen content.

The fourth major material was high-purity aircraft grade aluminum metal with a density of $2.7\,\mathrm{g\,cm^{-3}}$. This material is composed of 96% aluminum by weight and minor traces ($<1\%$) of silicon, iron, copper, manganese, magnesium, chromium, zinc, titanium, and oxygen. The benchmarking tool, sensor casing, and borehole pipe were made of this material.

The first testing material was tap water (H_2O), modeled at room temperature and pressure, with a density of $0.998\,207\,\mathrm{g\,cm^{-3}}$. The second testing material was sand (SiO_2), with a density of $1.8\,\mathrm{g\,cm^{-3}}$, modeled as a mixture of 95% dry sand and 5% water (representing moisture) by weight. The simulated dry sand contained 98% silicon dioxide (SiO_2) and traces of aluminum oxide, titanium oxide, calcium oxide, magnesium oxide, ferric oxide, sodium monoxide and potassium oxide[77].

Exploration Tool (Skeleton)

An aluminum alloy (6061) was used to model the skeleton of the exploration tool. This alloy contained approximately 96% aluminum and traces of silicon, iron, copper, magnesium, manganese, chromium, zinc, and titanium. Although the cross section of aluminum is low for neutron interactions, it was important to implement the model of exploration tool due to its proximity to the neutron source and gamma spectrometers, as aluminum could contribute significantly to the annihilation peak at 0.511 MeV measured by the photon sensors. The exploration tool and its Geant4 equivalent are shown in Figures 3.6 and 3.7.

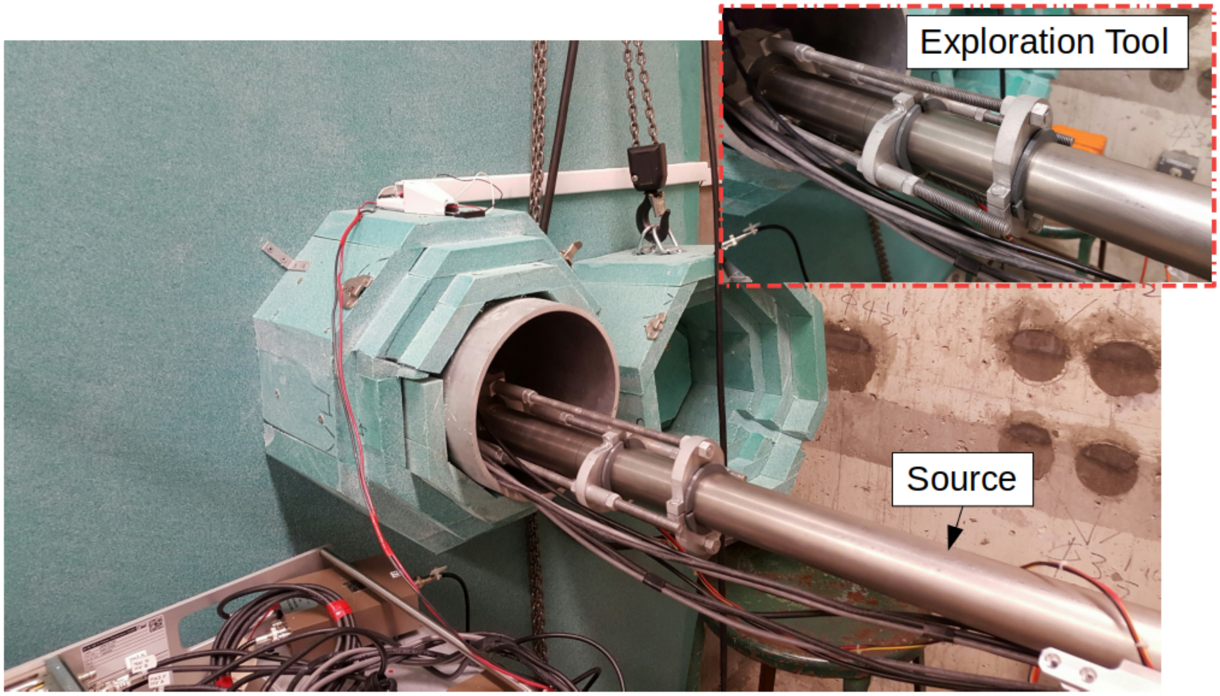

Figure 3.6: *A view of exploration tool and source placement*

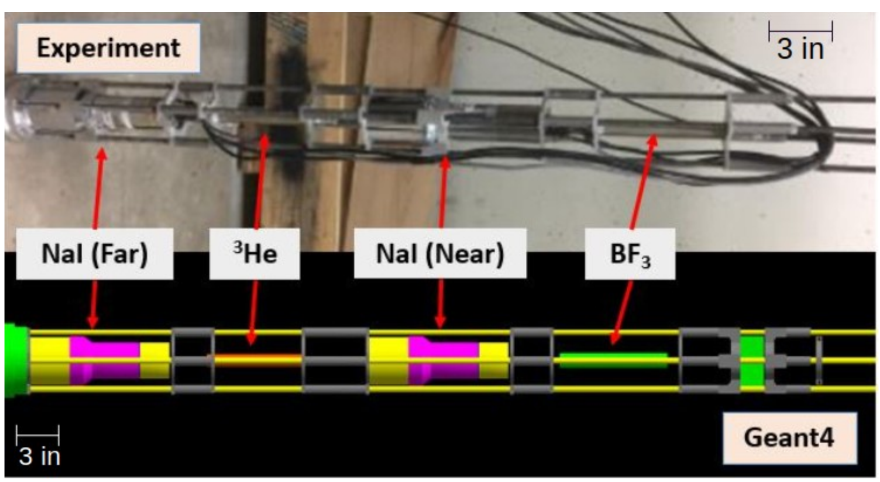

Figure 3.7: *A comparison of modeled and experimental exploration tool*

Radiation Sensors

The two photon sensors were Canberra Model 802, standard 3 in diameter and 3 in height, sodium iodide scintillator sensors with a density of 3.67 $g\,cm^{-3}$. Preliminary Geant4 simulations were performed with only the modeled NaI (Tl) crystal. It was found that it is critically important to model some external components of the sensor to obtain better agreement in spectral features of the simulated spectrum. The details of the external components were obtained mainly from the manufacturer's online article[78] and from personal communications with Hamamatsu[79] and Saint-Gobain[80].

The ^3He sensor was a 1 in diameter thermal neutron sensor filled with ^3He gas at 4 atm pressure. Similarly, the BF_3 sensor was also a 1 in diameter cylindrical sensor modeled with BF_3 gas filled at 1 atm pressure. Only the gaseous volume of the sensors were modeled in the Geant4. X-ray scanning was used to verify the active regions of the gas sensors.

A natural lead block with a density of 11.35 $g\,cm^{-3}$ was modeled between the source and the sensors to limit neutrons streaming through the sensors. These component models are also shown in Figure 3.11.

Neutron Source

The actual D-T source is a cylinder. However, according to the manufacturer's recommendations[81], this was modeled as a mono-energetic, isotropic, point source of 14.1 MeV neutrons.

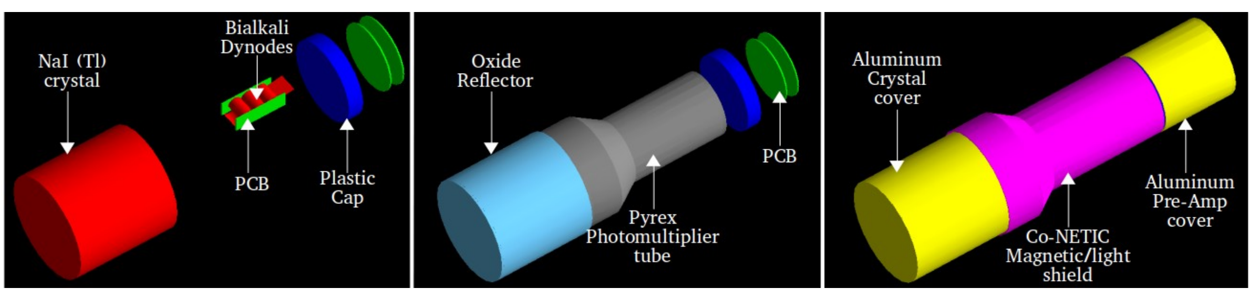

Figure 3.8: *Detailed NaI sensor model in Geant4*

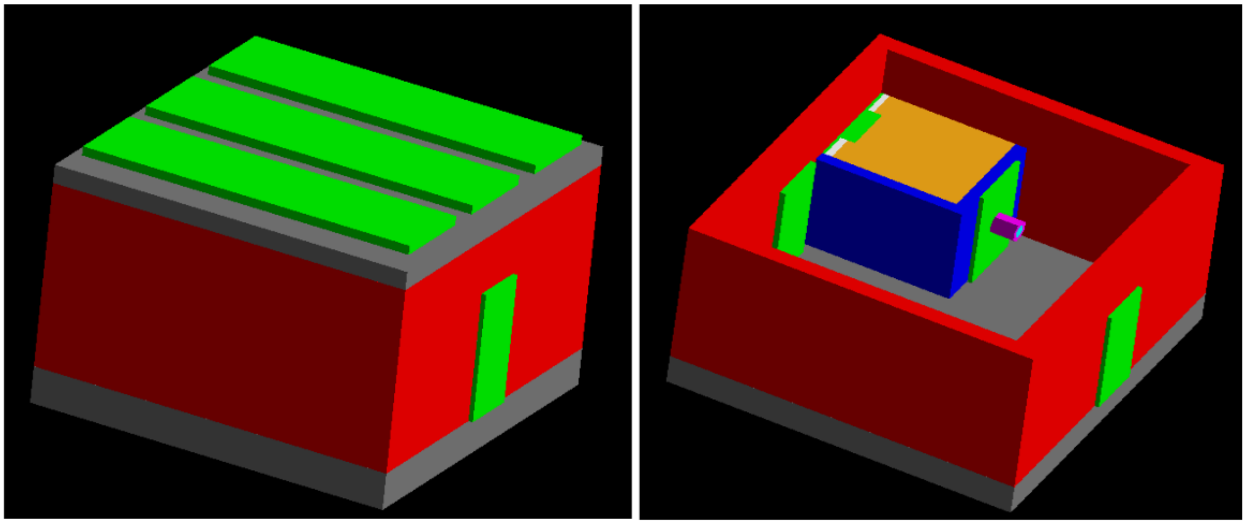

Figure 3.9: *Outer view representation of the experimental facility in Geant4*

External Support Structure

The modeled outer part of the facility is shown in the left part of Figure 3.9. Here, the red portion represents the walls of the facility. These walls range from 12 to 18 in thick. The three green slabs, each around 6 in thick, represent borated HDPE shielding on the roof. The roof is represented as a thin gray slab with a thickness of approximately 12 in. The thicker gray slab below the walls represents the floor of the facility and was about 24 in thick. The green slab on the wall is also borated HDPE shielding for doors with an approximate thickness of 3 in.

On the right side of Figure 3.9 and in Figure 3.10, the nodes of the roof and its shields were removed in the Geant4 visualization tool to demonstrate the internal structure of the modeled geometry. Here, the blue structure represents the concrete tank that was filled with the testing materials, with a wall thickness of around 8 in. The testing materials, sand, and water are represented in orange. The green slab beside the testing material is borated HDPE shielding about 12 in thick. The white slabs designate normal HDPE shields and are around 4-5 in thick. Two thin layers of borated HDPE of approximately 2 in each separate the HDPE layer from concrete walls. The green slab adjacent to the blue tank in Figure 3.9, is a 4 in thick borated HDPE shield for the main doors inside the facility. There is a 3 in thick slab of borated HDPE to protect around the source, as shown in Figure 3.10. In addition, an octagonal-shaped, magenta-colored structure presented in

Figure 3.9 (right) and Figure 3.10 is the borated HDPE shield around the source. The orange node for the testing material has been removed from Figure 3.10 (left) and the yellow aluminum tube is made transparent to visualize the placement of the exploration tool along with the sensors. Figure 3.11 represents the exploration tool, from left, the yellow cylindrical block is the NaI Far sensor, the object in blue is the ^{3}He sensor, the third yellow cylindrical object is the NaI Near sensor, the orange cylindrical object is the BF_3 sensor, and finally, the block represented in green is the natural lead block.

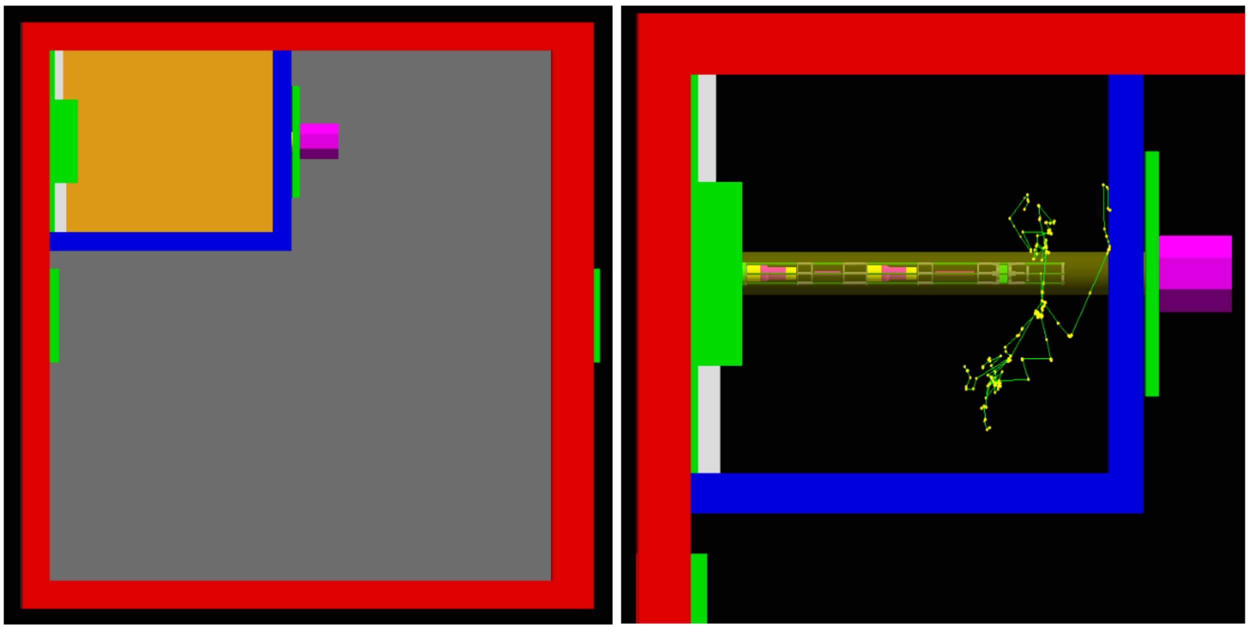

Figure 3.10: *Internal view representation of the experimental facility in Geant4. A secondary gamma-ray scattering trajectory is demonstrated in green.*

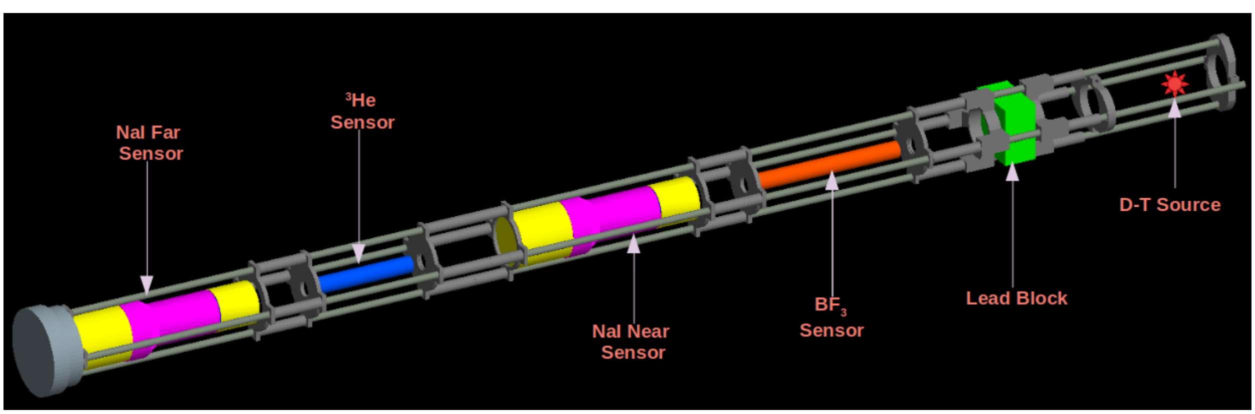

Figure 3.11: *A representation of exploration tool and sensor placement in Geant4*

Oil Well Logging Simulation Setup Summary

The entire experimental setup was successfully modeled with accurate material definitions. In Geant4, a new type of geometry was constructed, in which a combination of CAD and conventional geometry input approaches were investigated. Multiple bugs were discovered, reported, and resolved in Geant4, which led to multithreading simulation capabilities for the source code. The exploration tool was successfully modeled in Geant4 which replicated the actual setup in its entirety. Given that the neutron source was not characterized and operated below the recommended specifications, the neutron output estimates from the irradiations contained moderate disagreements, which was expected. The *QGSP_BIC_HP* reference physics list along with G4NDL[82] and G4TENDL[83] cross sections were adequate for the simulation.

3.7 Simulation Details: Trenched Microstructured Neutron Detector

Modeling is a key element in the overall design of the X-DS-MSND instrument. First, the optimal geometric design for the X-DS-MSND must be determined. This is achieved by maturing existing models of both neutron interactions and charge transport in the MSND family of sensors. The variable optimization space to be considered includes trench depth, trench width, and LiF packing fraction; these parameters will be evaluated with Monte Carlo-based radiation transport through the simulation study. Next, the current DS-MSND sensor will be modified to operate as a vertical p-i-n diode, which will be discussed in the subsequent chapters. The Geant4 toolkit was used with the high-precision binary cascade physics list (*QGSP_BIC_HP*), relevant for neutrons less than 20 MeV, to handle all necessary particles and reactions required for the DS-MSND simulations[9]. The geometry of the DS-MSND sensor device was modeled in Solidworks[26] and then imported into Geant4 with the GDML format using the same methods developed for the modeling of the oil well logging experimental setup. The simulated setup is represented in Figure 3.13. To investigate parameters in an infinite sensor geometry, a 1 cm diameter parallel beam of 25.3 meV thermal neutrons was simulated to interrogate the DS-MSND sensor.

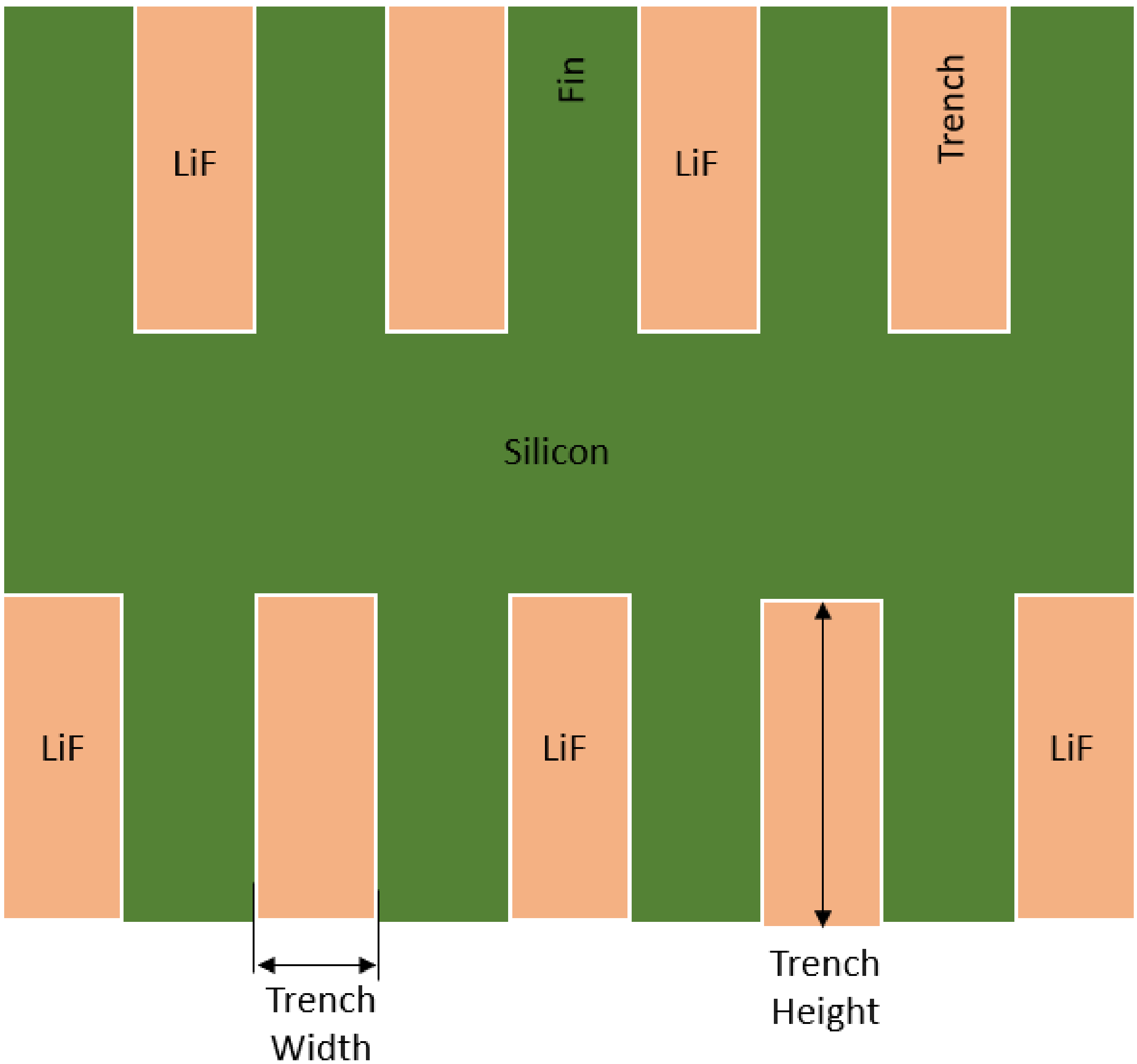

Figure 3.12: *A representative geometry for the DS-MSND sensor demonstrating parameters under investigation.*

Various trench depths were simulated to determine the minimum etching depth to achieve the target detector efficiency of 60%. As per the recommendations and results provided in previous studies[6], the simulated trench depths included 200 µm, 250 µm, 300 µm, 350 µm, 400 µm, 450 µm, and 475 µm. The interaction efficiency was defined as the percentage of ^{6}Li(n,t)α reactions per total number of incident neutron source particles.

Since a maximum trench depth of 475 µm ensures the availability of maximum neutron conver-

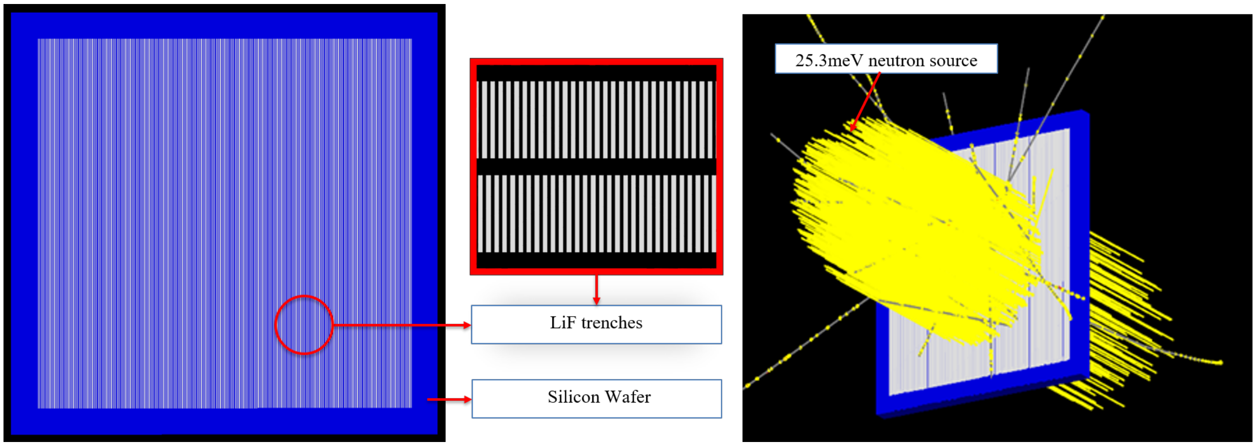

Figure 3.13: *A representation of DS-MSND sensor imported in Geant4 and the* 25.3 meV *thermal neutron source placement. This simulation setup was used for optimizing the design parameters for the DS-MSND sensor.*

sion material within the trenches, the depth of the trench was considered to be around 475 µm. The intrinsic detection efficiency was defined as the fraction of source particles that generate alpha-triton pairs that also ionize the silicon material and generate a total signal charge above the set threshold. Simulations were also conducted with a parallel beam of 662 keV gamma rays to determine the intrinsic neutron detection efficiency at a gamma ray rejection ratio of 10^{-6}. Simulations were performed with 5×10^6 source particles, and the energy deposition threshold was increased to eliminate all gamma-ray interactions. This threshold was found to be 540 keV, which was consistent with the analytical estimates for 662 keV gamma source.

The LiF is approximately 96% enriched with ^{6}Li. An energy deposited spectrum was obtained and plotted in MATLAB as shown in Figure 3.14.The simulated thermal neutron detection efficiency of the sensor after application of threshold was about 58%.

Other important parameters affecting the detection efficiency of the DS-MSND sensors are the packing fraction (PF) of the LiF inside the trenches and the trench etching width. The total pitch for one fin and one trench in the DS-MSND was exactly 55 µm as per the Timepix3 specifications. Figure 3.15 shows a detailed analysis of the effect of varying the trench width from 20 µm to 40 µm. It is observed from Figure 3.15 that as the width of the trench increases, the spectral features shift to the left (low energy region); this is because as the width of the trench increases, the LiF present in the trenches causes the neutron capture reaction products, alpha (2.05 MeV) and triton (2.73 MeV),

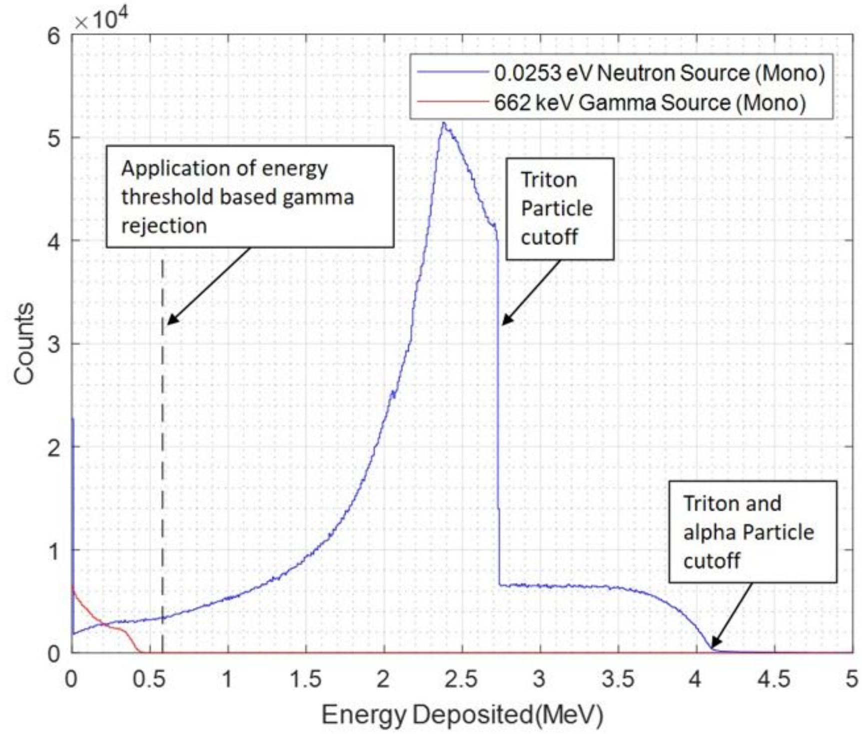

Figure 3.14: *A representation of DS-MSND spectral results obtained due to irradiations simulated with a* 25.3 meV *thermal neutron source and a* 662 keV *gamma-ray source, and an energy based threshold at* 0.54 MeV.

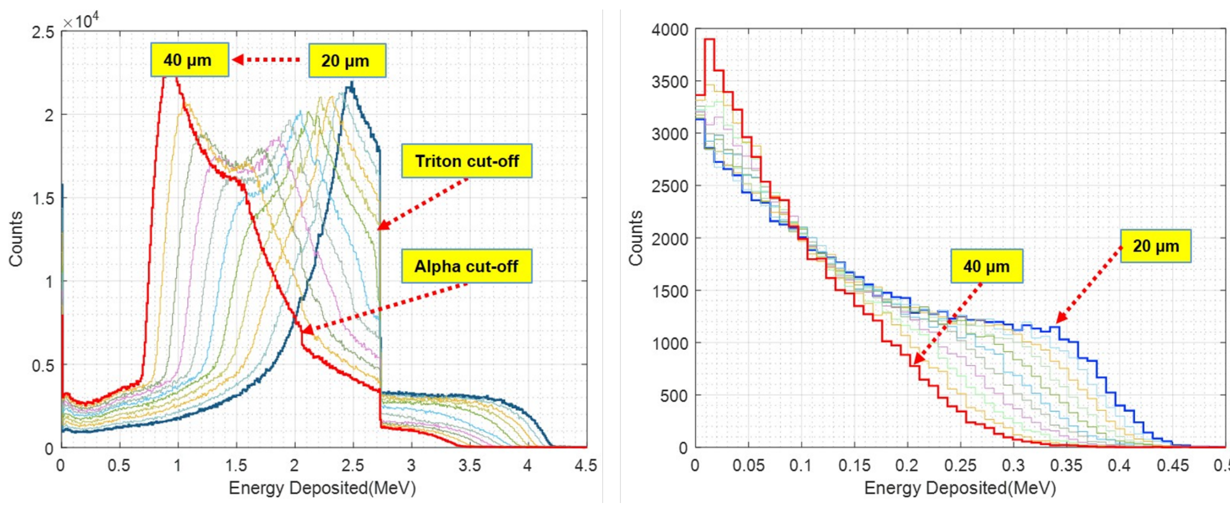

Figure 3.15: *A representation of (left) Energy deposited by neutron reaction products in the Si diode of the DS-MSND sensor; note the large signal that can be obtained over (right) gamma-ray induced signals due to the geometry of the DS-MSND-type structure and large energy reaction products.*

to undergo parasitic energy losses in the trench, which decreases the energy getting deposited in the active region of the DS-MSND sensor. These results demonstrate that the trench width and parasitic absorption of LiF in the trenches together affect the thermal neutron detection efficiency of the DS-MSND sensor. Thus, a combined parametric optimization study for LiF PF and trench width is needed to obtain an optimum solution.

For X-DS-MSND, high detection efficiency is of prime importance. To achieve this, meticulous optimizations of sensor design parameters were executed in Geant4 and the best values for trench width, trench height and LiF PF were investigated. A single, energy-based threshold was found to be around 0.5 MeV for DS-MSND, resulting in a gamma-ray rejection ratio of at least 10^{-6}. As all neutron counts between 0-0.5 MeV are ignored in this implementation, a slight decrease in neutron detection efficiency was observed. Figure 3.16 shows the effect of the variation in trench width along with LiF PF; it was observed that for trenches wider than 28 µm, effect of higher PF had a negative impact on detection efficiency due to parasitic absorption. If the trench width is less than 28 µm, then the detection efficiency will decrease significantly because the probability of neutrons streaming through Si will increase. Therefore, it was concluded that with 55 µm pixel pitch, 28 µm trench width, and 65% PF, the DS-MSND sensor was able to achieve around 60% thermal neutron detection efficiency with a gamma ray rejection ratio of 10^{-6}.

The error in the simulated results was accounted for by considering that the counts generated in the sensors are of rare events, all the detection events are independent, and the average rate of counts does not change over the period of irradiation. Relative errors (R.E.) in the simulated results were calculated considering the Poisson distribution as shown in Equation 3.7.

$$R.E.(\%) = \frac{\sqrt{(C_B)||(G)}}{(C_B)||(G)} \times 100 \tag{3.11}$$

In Equation 3.7, C_B is the counts / bin and G is the gross counts. Here, $||$ represents that this equation can be applied to C_B or G. The relative errors for each of the data points are plotted in each figure provided above and are found to be negligible.

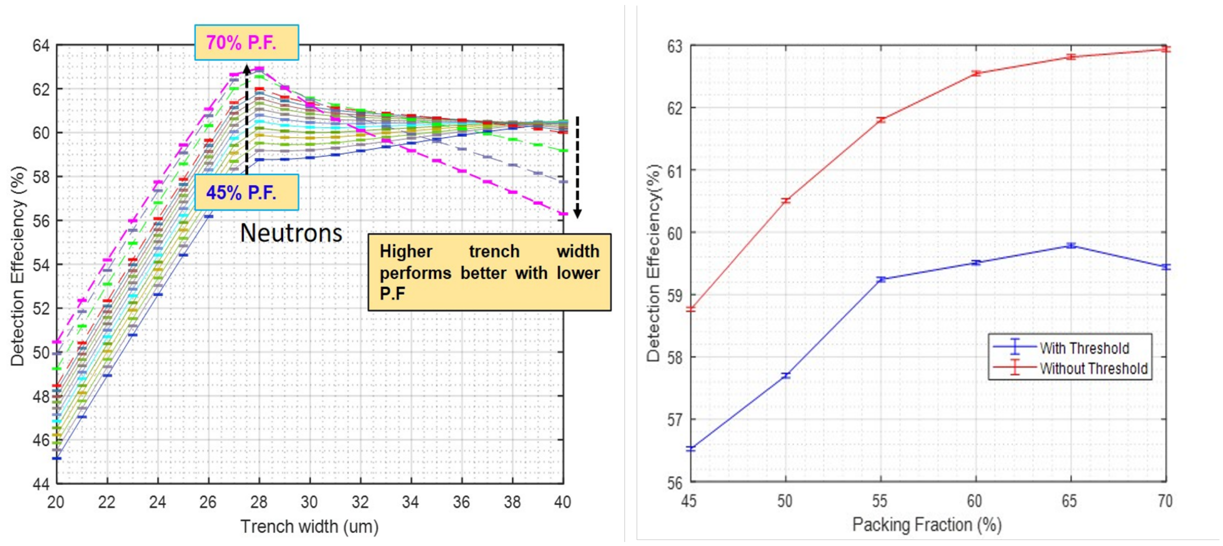

Figure 3.16: *A representation of (left) Geant4 simulation of neutron detection efficiency for various trench widths and Packing Fractions (P.F.) of the DS-MSND sensor. (right) Final Geant4 simulated neutron detection efficiencies of the X-DS-MSND with* 28 µm *trench width.*

DS-MSND Simulation Summary

Results obtained from Geant4 show that radiation detector with the trench geometry is efficient and will allow for multiple pixel hits for each neutron detection event. This provides a proof of concept for the fulfillment of the sponsor's requirement. The target gamma-ray rejection ratio of 10^{-6} was achieved along with a detection efficiency of 57.6% utilizing 475 µm **trench depth, along with a trench width of** 28 µm (**pitch was** 55 µm) **and a LiF packing fraction closer to 65%. This design will be used to develop a larger chip array device to cover a wider area and a higher imaging rate.**

Chapter 4

Semiconductor physics models of DS-MSND sensor

The space and time dependent problems in semiconductor device physics are generally expressed in terms of partial differential equations (PDE). The analysis will include solution of these PDEs across various complex geometries, doping profiles, and semiconductor materials. The solution of these PDEs is a complex, multi-variable analysis that should account for parameters like charge carrier lifetime, carrier mobility, electric field profile, fixed oxide charge, recombination rates, and leakage currents. For a vast majority of applications, these PDEs cannot be solved with basic analytical methods. Approximations to these PDEs are made using appropriate discretizations. The purpose of discretization is to convert the actual physics-based equations into numerical model-based equations that can be easily solved utilizing numerical methods. The solution of these numerical equations is an approximation to the actual solution of the PDEs. This approximation of the PDEs are calculated with the help of FEMs. COMSOL Multiphysics[11] is extensively used to determine design properties of the DS-MSND diode. COMSOL simulations were instrumental in finalizing sensor geometry and obtaining preliminary charge transport models and induced currents in the Allpix Squared[10].

4.1 COMSOL Multiphysics

The COMSOL Multiphysics Finite Element solver was used to simulate the semiconductor physics for the X-DS-MSND sensor. Various properties related to the X-DS-MSND sensor were investigated to assist the fabrication team for sensor fabrication. The semiconductor module and the default Si semiconductor material were utilized to define the X-DS-MSND FEM model in COMSOL Multiphysics. The LiF in the trenches was added in the FEM model to enhance the accuracy of the simulation results. The COMSOL semiconductor module simulates dielectric materials with the help of charge conservation node. This node adds the equations for charge conservation according to Gauss's Law for the electric displacement field. It provides an interface for defining the constitutive relation given in Equation 4.1 and its associated properties such as the relative permittivity. The *Material* input dictates how materials behave and how material properties are interpreted at mesh nodes. The material strain, material orientation, and other variables are assumed to be constant. *Solid* was selected for LiF definition.

$$D = \varepsilon_o \varepsilon_r E \tag{4.1}$$

The density of the 96% enriched ^{6}LiF is 2.54 g cm^{-3}. Further, around 50% packing fraction can be confidently ensured by the fabrication team. Thus, the relative permittivity of LiF material in the X-DS-MSND trenches was modified. The updated permittivity was calculated by Equation 4.2[84].

$$\frac{\varepsilon - 1}{\varepsilon + 2} = \frac{d}{d_o}\left[\frac{\varepsilon_o - 1}{\varepsilon_o + 2}\right] \tag{4.2}$$

where, ε is the relative permittivity of powdered LiF, ε_o is the relative permittivity of solid LiF (9)[85], d is the density of powdered LiF, and d_o is the density of solid LiF. Hence, the updated relative permittivity of the powdered LiF used to finalize the material model in COMSOL was 2.7143.

Another important aspect of the COMSOL-based semiconductor FEM simulations is the creation of an unstructured mesh. In order to quantify semiconductor properties, mathematical equations are deployed. Most of the aforementioned semiconductor properties could be obtained by solving the PDEs for simple cases. However, it is almost impossible to solve these equations for the actual cases, as there are infinite degrees of freedom present. A mesh is created over the entire sensor domain so that the geometry is separated into finite number of elements for which the solution to the PDEs can be calculated. Finally, the data are interpolated to obtain an approximated solution for the entire device.

Two types of meshing methodologies are available: structured and unstructured. For complex geometries with complex doping profiles, an unstructured mesh is preferred to save memory and simulation time, as represented in Figure 4.1. Regions 1 and 3 in Figure 4.1 are modeled with high carrier concentration gradient. Thus, a sharp change in electric field is expected and an extremely fine mesh is used to capture this change in electric field. A relatively coarser mesh is used for the rest of the model, as no sharp gradient is expected in the electric field profile. In unstructured meshes, the indices of the neighboring cells must be stored for each cell. In a structured mesh, this is not necessary since, due to the structure, the indices of neighboring cells can be easily calculated. An unstructured mesh provides the ability to perform selective refinement of mesh inside the domain, which is not possible with a structured mesh. Hence, a solution to the unstructured mesh for a complex geometry will take less time as compared to the structured mesh. Further, an extremely fine mesh would enhance the accuracy of the results at the cost of severely increased simulation times. Conversely, an extremely coarse mesh would fail to converge due to higher computational error per iteration. Thus, while solving for electrostatic fields in the presence of mobile charge carriers, it important to ensure that element size in the unstructured mesh is closer to the Debye length presented in Equation 2.5. This length is the scale over which the electric field decays in the presence of mobile carriers, so it is critically important to resolve this length scale with the user defined unstructured mesh in semiconductor models.

Substituting, k_B= $1.380\,648\,52 \times 10^{-23}\,\mathrm{kg\,m^2\,s^{-2}\,K^{-1}}$, T=293.15 K, ε_0=$8.8541 \times 10^{-12}\,\mathrm{F\,m^{-1}}$, ε_r=11.7, q=$1.602\,176\,62 \times 10^{-19}\,\mathrm{C}$, and N=$8.9163 \times 10^{17}\,\mathrm{m^{-3}}$, in Equation 2.5, the debye length (λ_d) for this device is found to be 4.28 µm. Further, the minimum element size of 0.12 µm was used at the regions of higher charge carrier gradient and maximum element size of 6 µm was used to for the bulk region of the sensor where the charge carrier concentration is roughly constant. To further optimize the simulation time, zero Neumann boundary conditions were applied such that a one-quarter pixel geometry geometry was modeled and meshed as represented in Figure 4.1. In the context of the FEM, this boundary condition provides an equation for the boundary node so that a solution can be obtained for the system of equations under investigation and hence a quarter of the DS-MSND geometry was simulated. COMSOL's default silicon material was used to model the diode. The Charge Conservation option was used to add air as a dielectric material. The

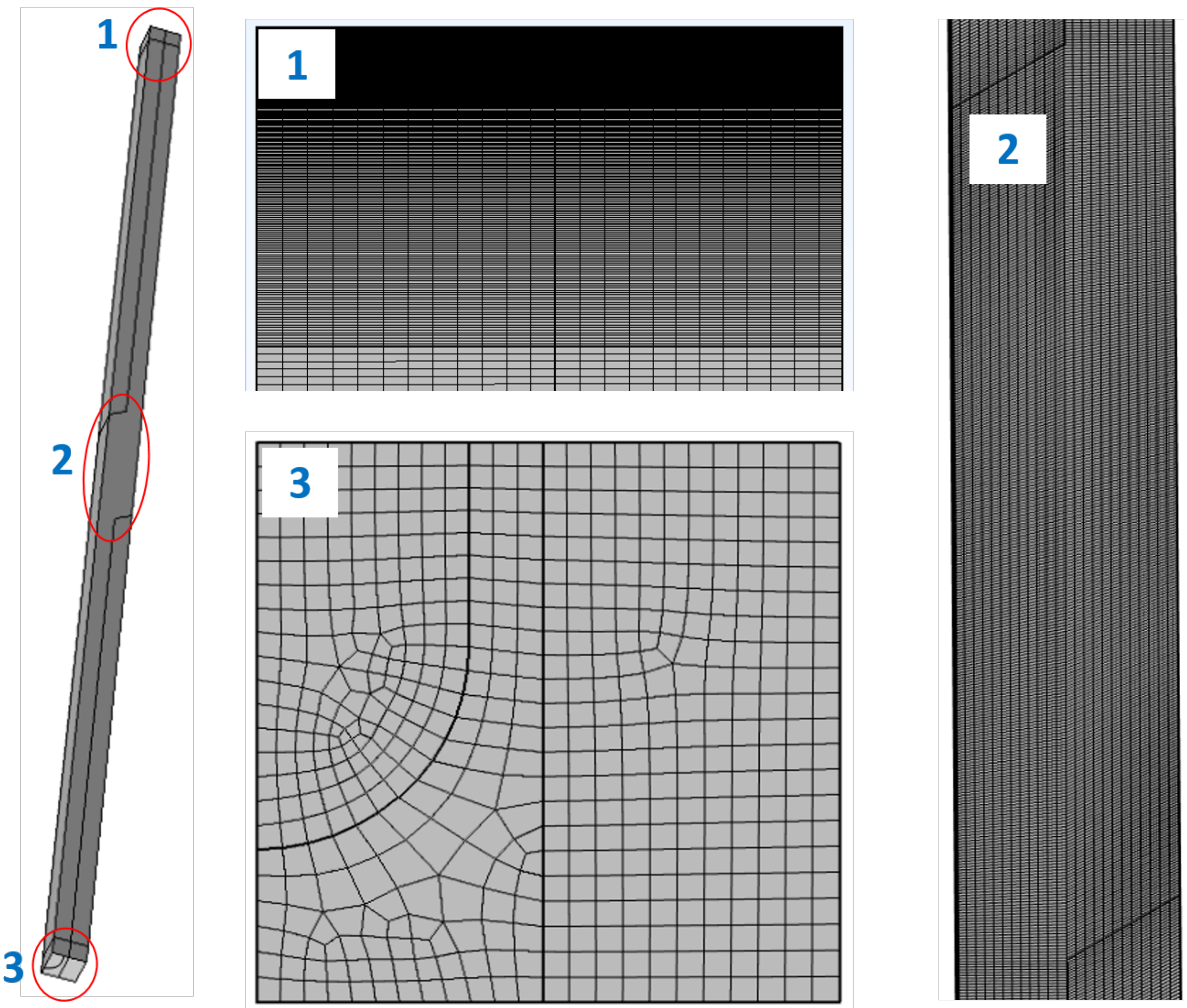

Figure 4.1: *A representation of the COMSOL FEM model (left) and the associated unstructured mesh (right) for the highlighted regions.*

high-resistivity Si substrate of 15 kΩ – cm will ensure controlled leakage current for the designed DS-MSND diode. To improve the charge collection efficiency and to counter the effects of oxide charge and traps at the Si-LiF interface, the doping scheme is *p*-type (boron) doping on the pixel side. Each pixel will be surrounded by sputtered Si_3N_4 region for pixel isolation and will have an evaporated metal contact to bond with the Timepix3. Further, the *n*-type (phosphorus) dopant will be considered for the “top” side of the sensor. The top side dopant will extend all the way to edge of fins. An insulating nitrite layer is being considered around the periphery of trenches. The *n*-type contact on fins will not be metalized. The wire bond pad for the *p*-type region (pixels) adjacent to fins will be metalized.

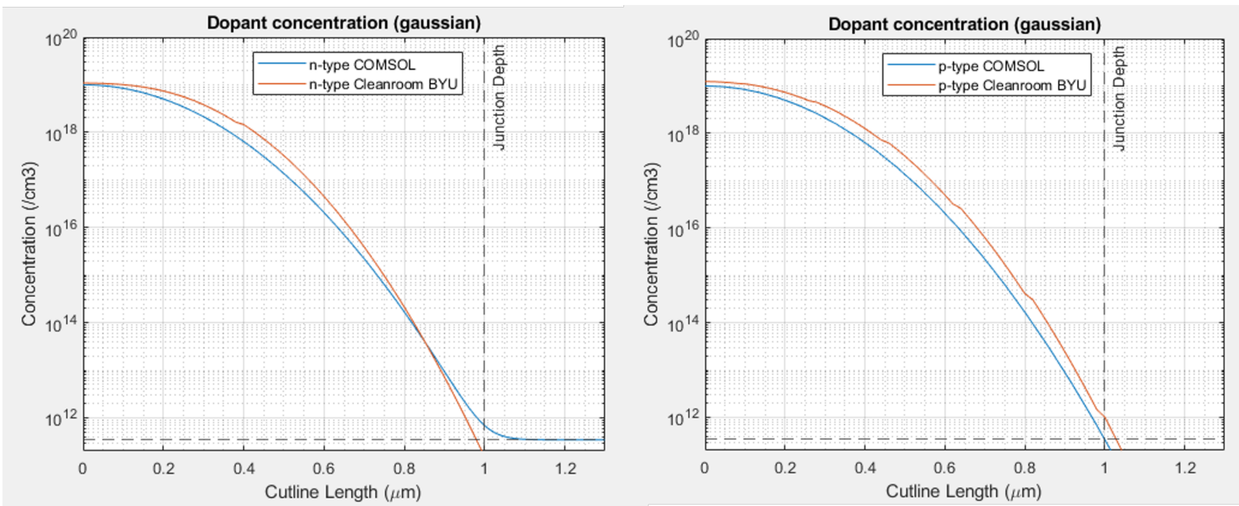

Figure 4.2: *A comparison of the peak doping profile obtained from COMSOL Multiphysics and from ion implant analytical calculation.*

An *n*-type substrate was modeled with a 1 mm thick 15 $k\Omega - cm$ resistivity, i.e., constant background doping concentration of 3.42×10^{11} cm^{-3}. The top (*n*-type) surface and bottom pixel (*p*-type) junctions of the sensor were initially modeled with peak doping concentrations of 1×10^{19} cm^{-3}; this concentration decreases with Gaussian profile with respect to depth of 1 µm, at which point the concentration was equal to the background. The junction depth is an initial value and will be finalized after further analysis, as represented in Figure 4.2. Diffusion will be done for preparing these junctions and the recipe is usually prepared by performing calculations on TCAD[86]. Good agreement between the two methods presented in Figure 4.2, suggests that the unstructured mesh is capable of resolving the steep changes in the dopant concentration profile of the sensor. As specified by the wafer manufacturer and available literature[87], a 1 ms charge carrier life time was defined for the simulated sensor model. The doping profile is presented in Figure 4.3. Ideal ohmic

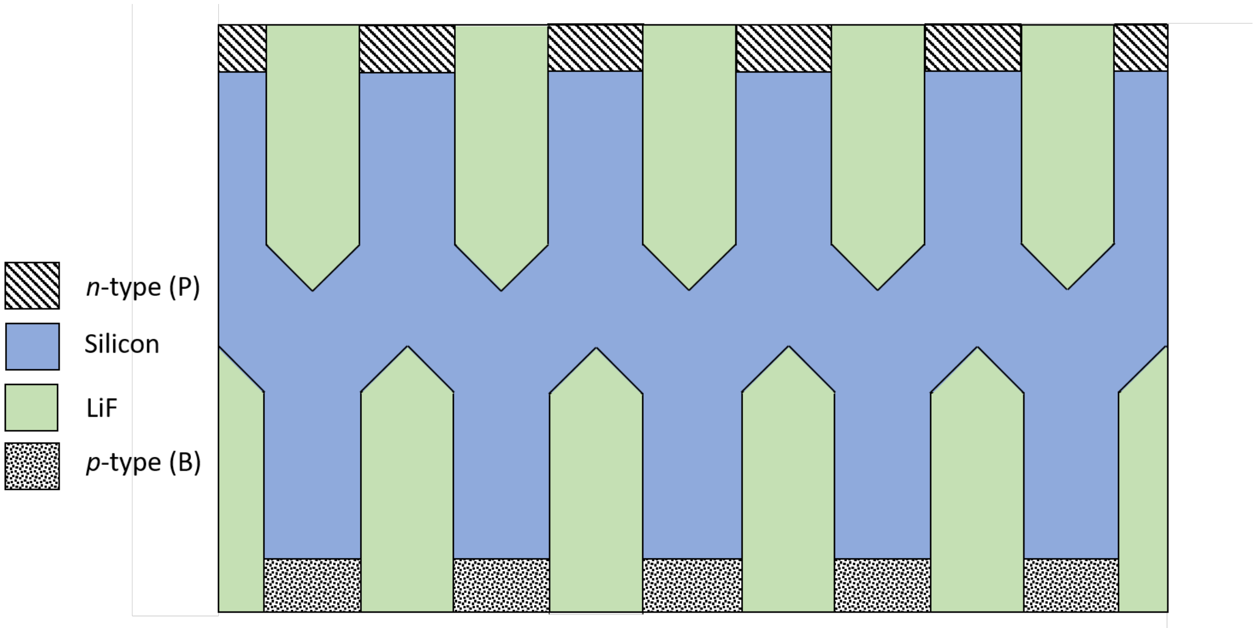

Figure 4.3: *A representation of the dual-sided trenched, DS-MSND doping profile. Dashed region represents phosphorous doped (n-type) region, dotted region represents boron doped (p-type) region, green colour represents LiF nano-powder and blue colour represents bulk high-resistive silicon. Figure is not to scale.*

metal contacts were modeled at the peak doping concentration regions to apply reverse bias and deplete the diode. Metal contact 1 (MC1) was placed on the top *n*-type doped region and positive DC voltage was applied to this contact. Metal contact 2 (MC2) was placed on the bottom *p*-type contact and was grounded. By default, a *pn* junction is formed at the bottom contact. As the positive bias is increased in small steps at the MC1, the reverse bias increases and this shifts the depletion region boundary towards the MC1. The depletion region is volume with high magnitude of electric field that forms instantaneously across the *pn*-junction of a diode. It is most easily described when the junction is in thermal equilibrium or in a steady state. For both of these cases the properties of the system do not vary in time, and they are in dynamic equilibrium. A theoretical estimation of the required reverse bias for complete depletion of the modeled X-DS-MSND diode can be found using Equation 4.3.

$$V = \frac{w^2 e N_d}{2\varepsilon_0 \varepsilon_r} \tag{4.3}$$

Equation 4.3 provides an analytical approximation of required reverse bias needed for complete depletion of a planar diode. Here, w is sensor width (1 mm), N_d is electron concentration (3.42×10^{11} cm^{-3}), e is the elementary charge (1.602×10^{-19} C), ε is the electric permittivity, ε_0 is the permittivity of the free space ($8.8541 \times 10^{-12}\,\mathrm{F\,m^{-1}}$), ε_r is the relative permittivity of Si (11.7). Substitution of these values in Equation 4.3 results in 264 V. To obtain simulated results, a stationary study was implemented and an auxiliary sweep was performed for the applied reverse bias in 1 V per step, as small steps achieve faster convergence.

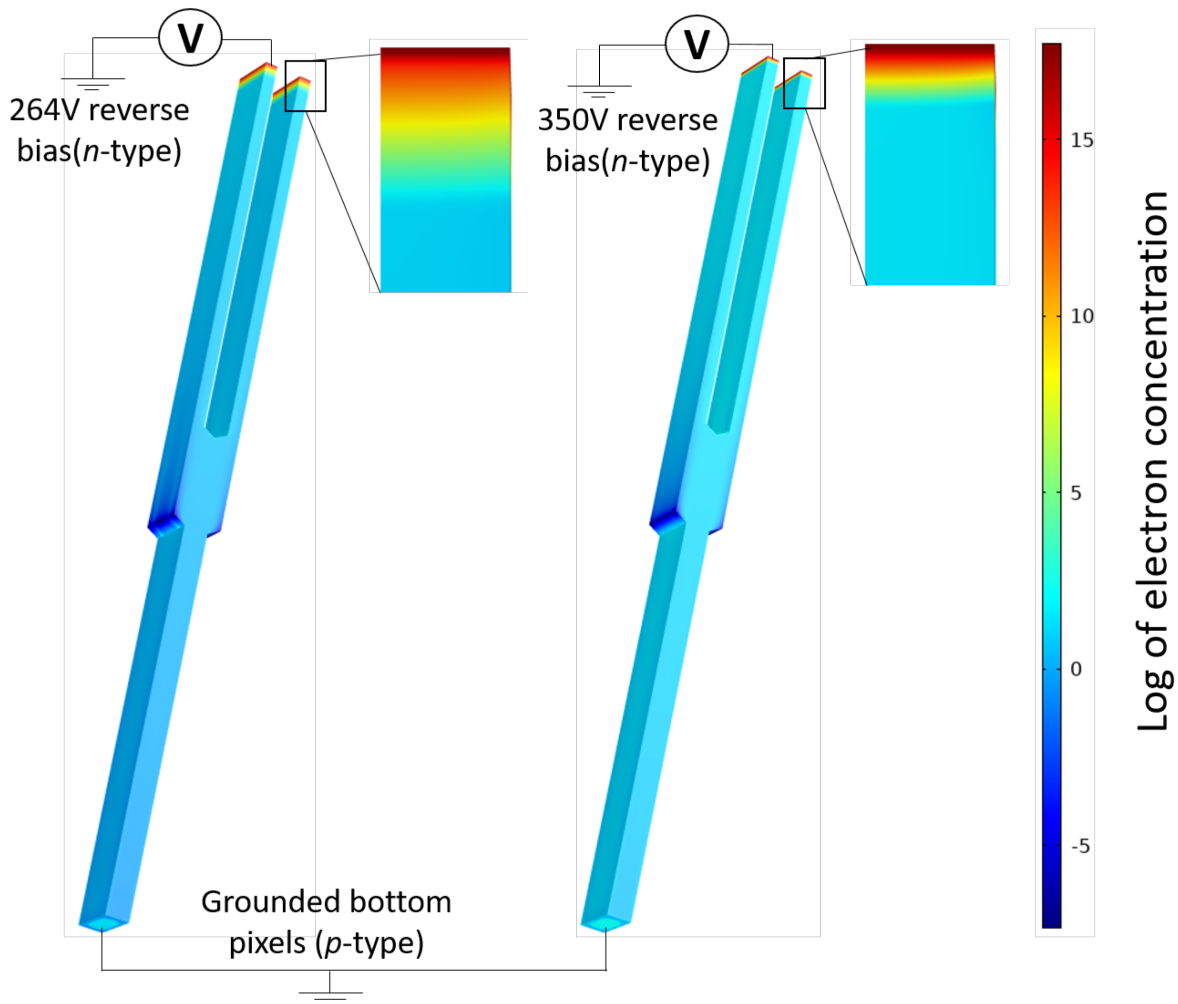

Figure 4.4: *A representation of the dual-sided trenched, X-DS-MSND depletion profiles obtained at* 264 V*(Left) and* 350 V*(right).*

It was observed from the results presented in Figure 4.4 that the diode is depleted at 264 V, and around 300 V is required for a tight depletion at the top junction. Higher voltage was needed in the COMSOL simulation to deplete around the bottom pixels because they are electrically isolated from one another. These results are demonstrated in Figure 4.4. Since most of the radiation interactions will occur at the top region of the X-DS-MSND diode, it is vitally important for the effective sensor operation that the top region is as tightly depleted as possible.

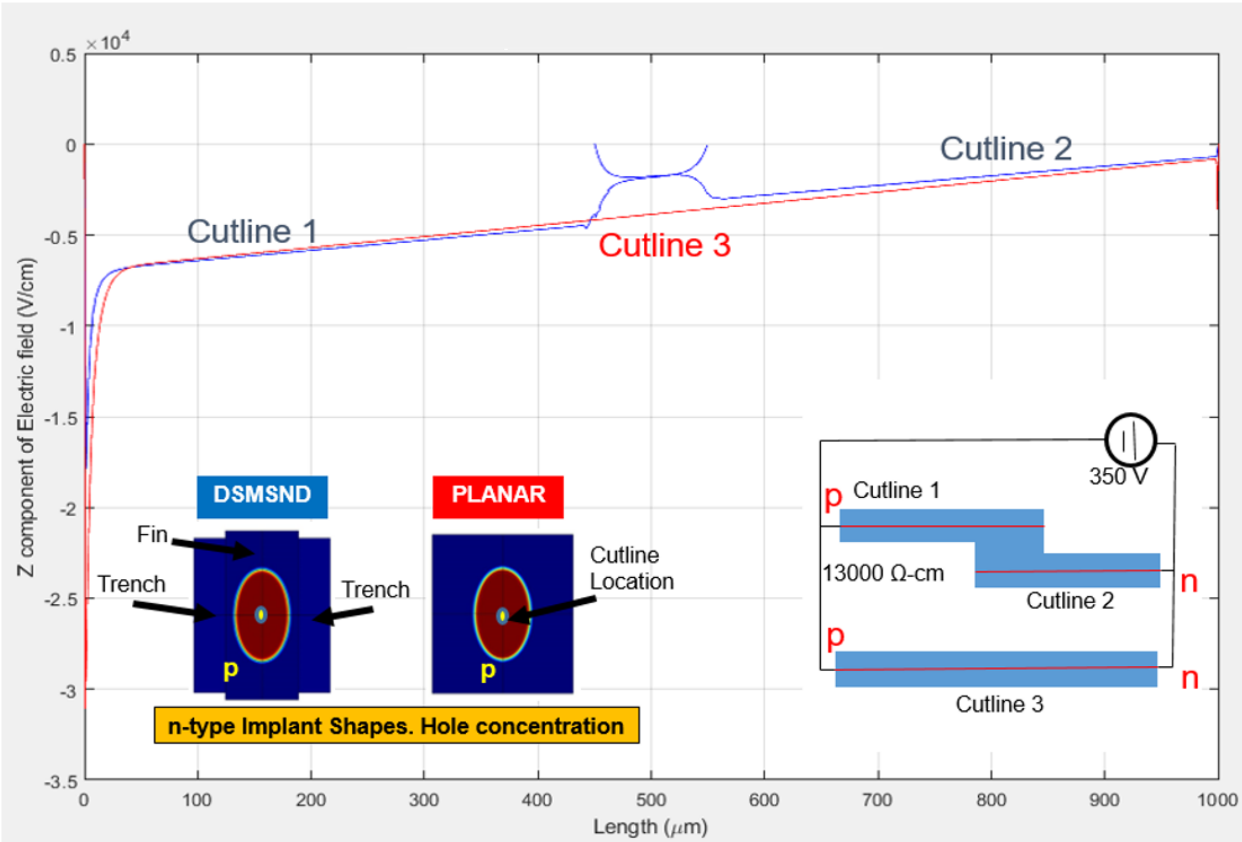

Figure 4.5: *A representation of the dual-sided trenched, DS-MSND depletion profiles obtained at* 264 V*(Left) and* 350 V*(right).*

Preliminary simulations in COMSOL were performed to understand the electric field profile of the X-DS-MSND as compared to a planar sensor. The electric field solutions for X-DS-MSND were found to be similar to that of a planar diode, except at the discontinuous region in the middle. The results presented in Figure 4.5 suggests that the electric field profiles for planar and the X-DS-MSND sensor. The only observable difference is in the bulk region of the X-DS-MSND sensor.

More simulations were executed to understand the effects of variation of the shape of the bottom implant, peak doping concentrations, and the depth of the junction on the peak electric field strength due to the presence of an external source. The design goal of these series of simulations

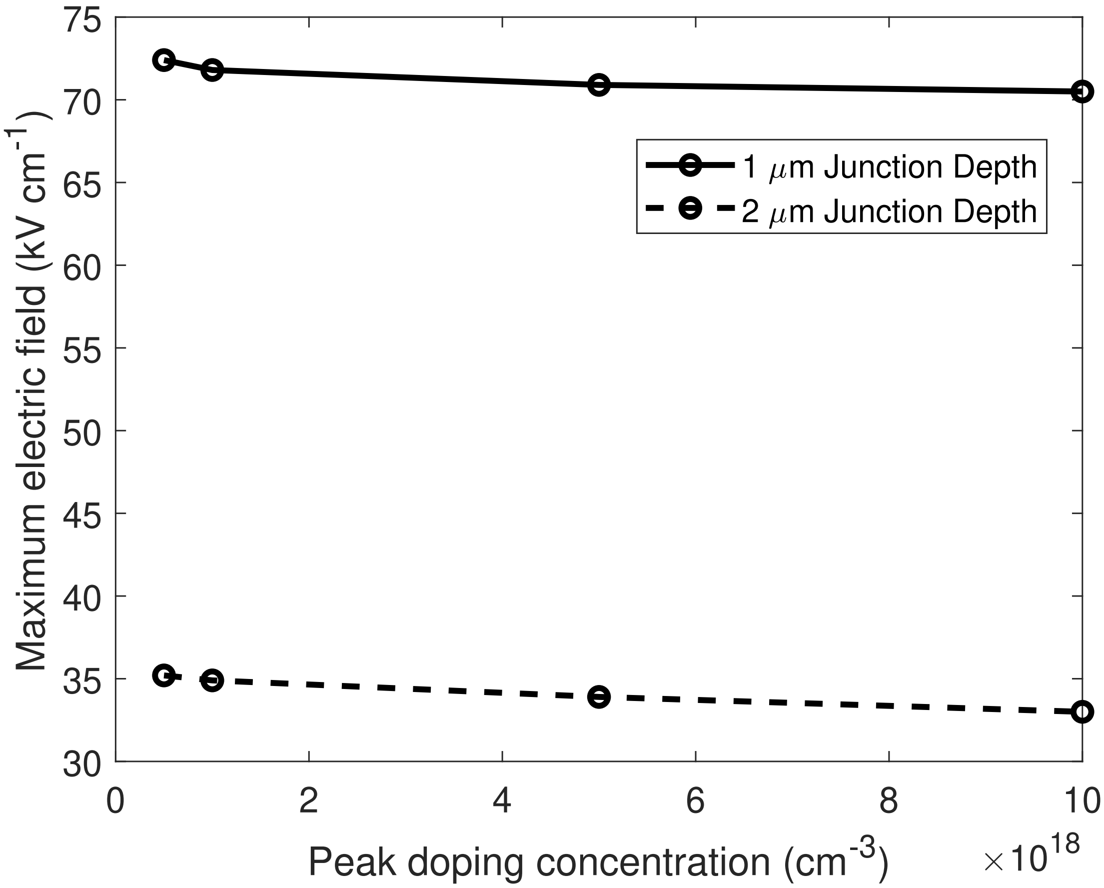

Figure 4.6: *Analysis of the effects of variation of p-type peak doping concentrations on the peak electric field magnitude present inside the device at a constant junction depth of* 1 μm.

was to analyze the behavior of the maximum electric field magnitude in the X-DS-MSND device.

Further, to enhance ease of charge transport and improve the charge carrier propagation in the sensor, modeling a pointed bottom trench was also considered. The values for the updated relative permittivity, density, and porosity were imported in the COMSOL, and the electric field solutions were obtained for both flat bottom trench and pointed bottom trench structures.

Various COMSOL simulations were also performed to finalize the essential design parameters that aid in designing an effective sensor geometry with lower peak electric field magnitude (E_{peak}) inside the active sensor volume. These parameters include, junction depth of the implants, peak dopant concentrations of the implants, and shape and size of the implants. These simulations were performed so that the peak electric field magnitude around the implant of the finalized sensor is

Table 4.1: *Peak electric field magnitude obtained for various simulated junction depths with a* 5 µm *and* 10 µm *fillet at the corners of p-type implants in COMSOL*

Fillet Radius	**Junction Depth** (µm)	**Peak Electric Field Magnitude** ($kV\,cm^{-1}$)
5 µm	0.1	200
	0.5	173
	1	83
10 µm	1	72.4
	2	35.2

lower than $50\,kV\,cm^{-1}$ for reliable operation and to keep the diode below breakdown electric field.

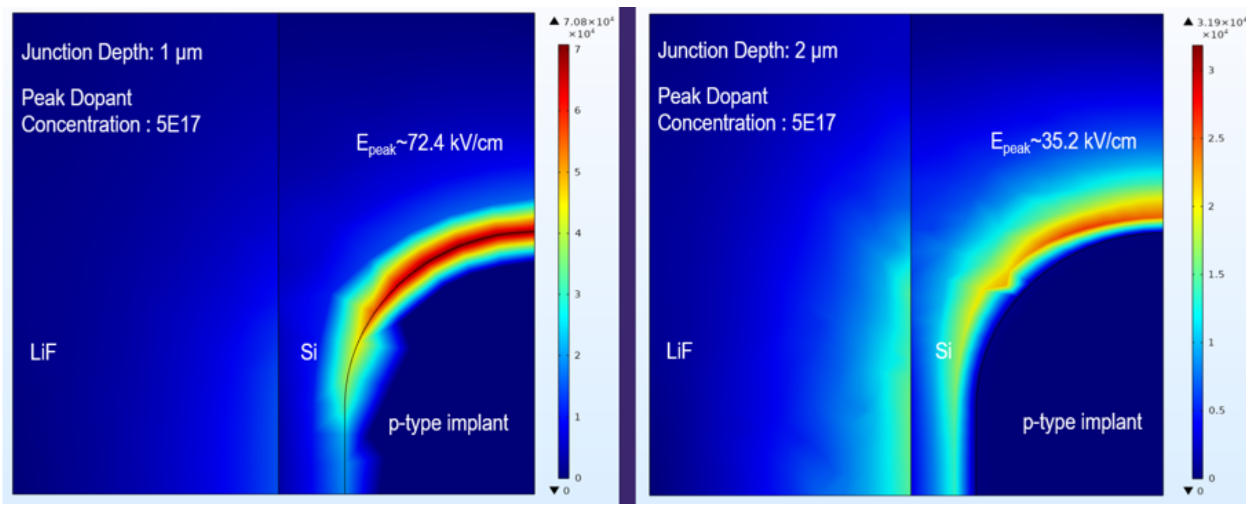

Figure 4.7: *COMSOL Simulation results to obtain peak electric field magnitude around p-type implant at (left)* 1 µm *and (right)* 2 µm *junction depth. This result is for a* 350 V *bias (complete depletion).*

In order to achieve a lower E_{peak} to finalize a junction depth and shape of the implants, various junction depths with a Gaussian profile were simulated ranging from 0.1-2 µm. Two sets of implant shapes each with a radius of 5 µm and 10 µm filleted corners were taken under consideration. The results of these simulations are summarized in Table 4.1. It was noted that 0.1 µm and 0.5 µm junction depths were found to be impractical due to very high E_{peak} values. Further, the plots of electric field profile for 1 µm and 2 µm junction depths are presented in Figure 4.7.

Four different peak doping concentrations of the *n*- and *p*-type implants (5×10^{17}, 1×10^{18}, 5×10^{18}, and $1 \times 10^{19}\,cm^{-3}$) were also considered for these simulations. No significant effect

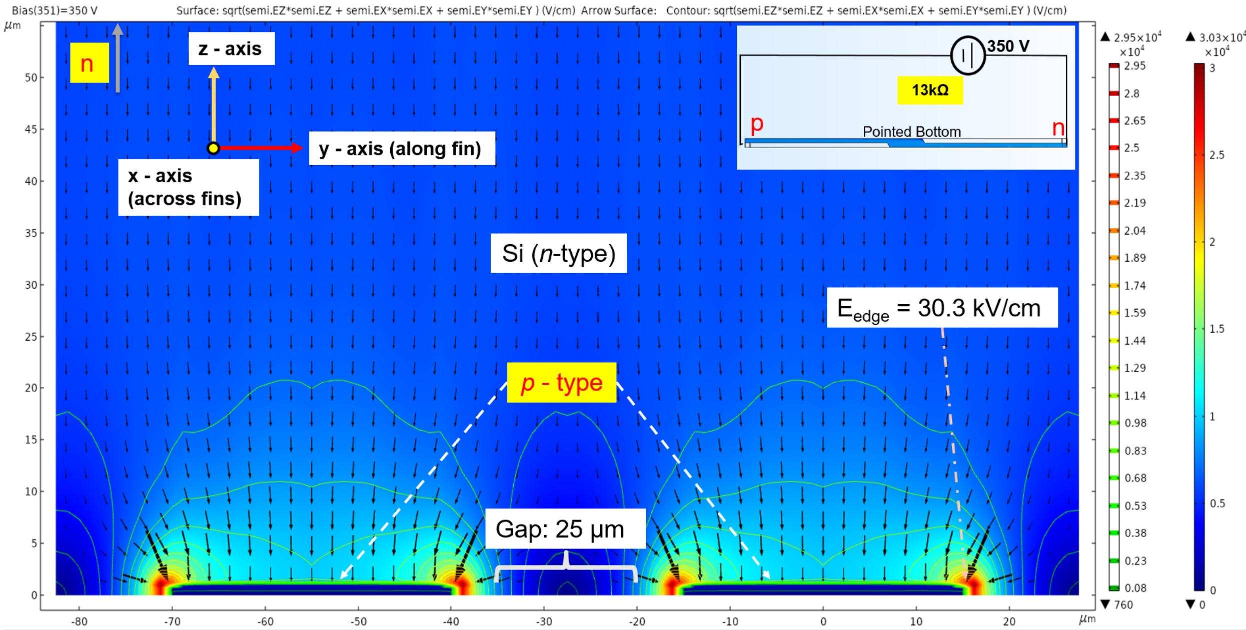

Figure 4.8: *Electric field magnitude profile for a* 25 µm *gap in between pixels in y-direction. The size of the pixel is* 20 µm*-by-*30 µm*. This result is for a 350V bias (complete depletion).*

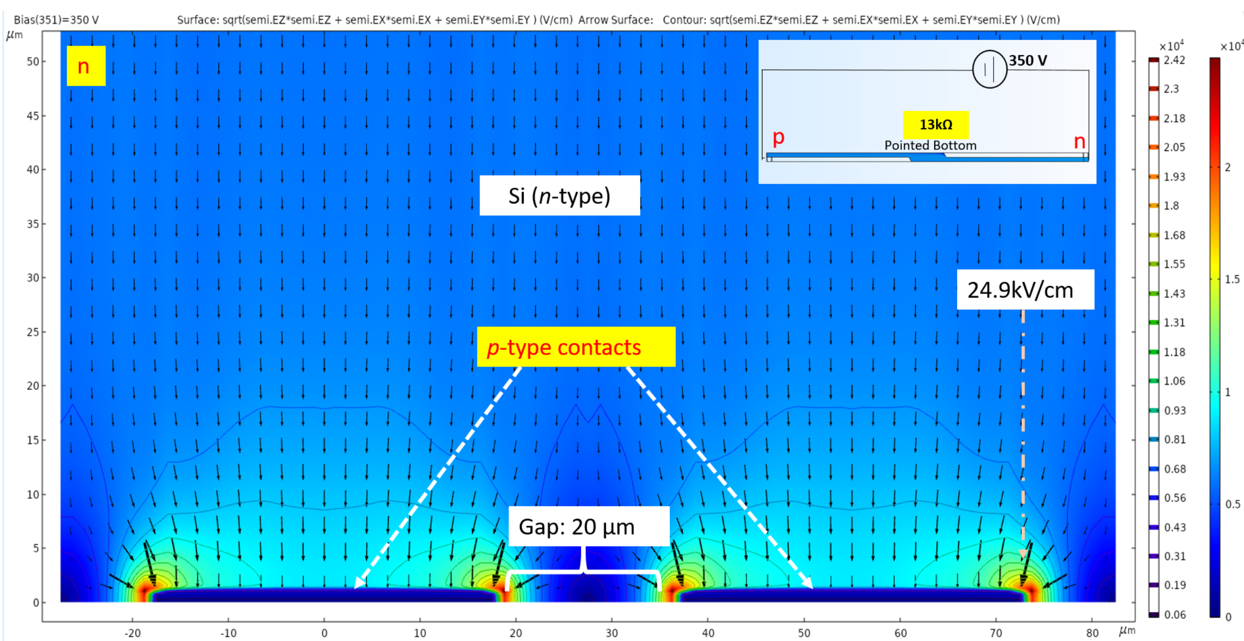

Figure 4.9: *Electric field magnitude profile for a* 20 µm *gap in between pixels in y-direction. The size of the pixel is* 20 µm*-by-*30 µm*. This result is for a 350V bias (complete depletion).*

on the E_{peak} values were observed with the variation in peak doping concentrations; thus the 5×10^{17} cm^{-3} value was used to prevent degenerative doping concentrations. Finally, the size

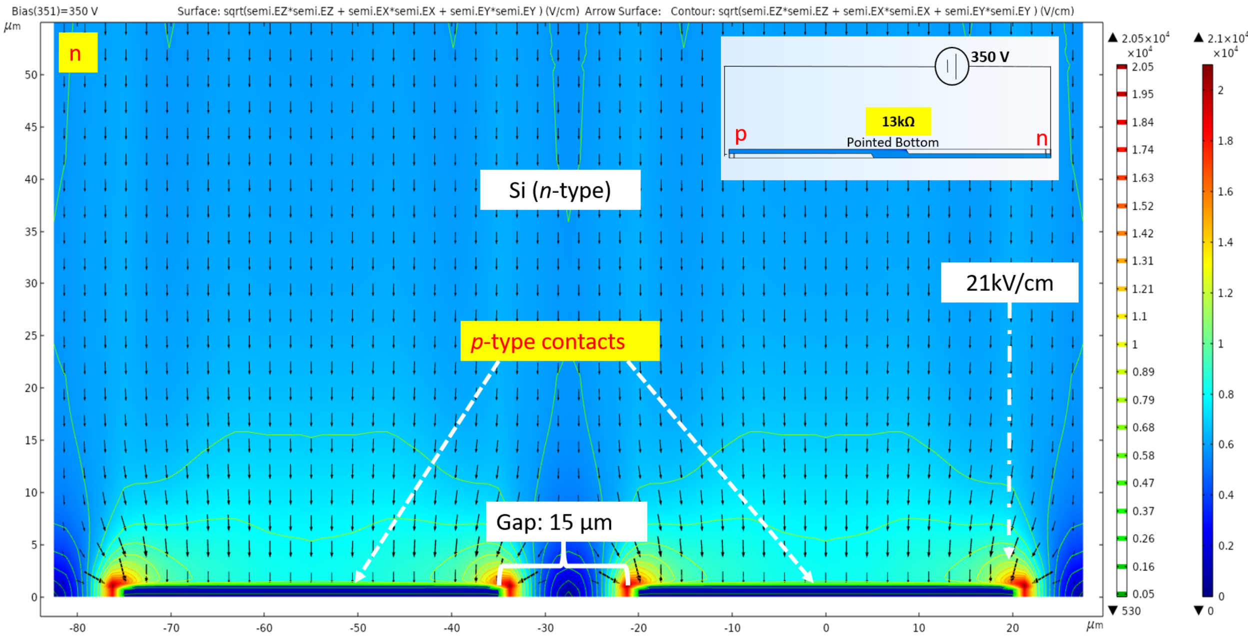

Figure 4.10: *Electric field magnitude profile for a* 15 µm *gap in between pixels in y-direction. The size of the pixel is* 20 µm*-by-*30 µm*. This result is for a 350V bias (complete depletion).*

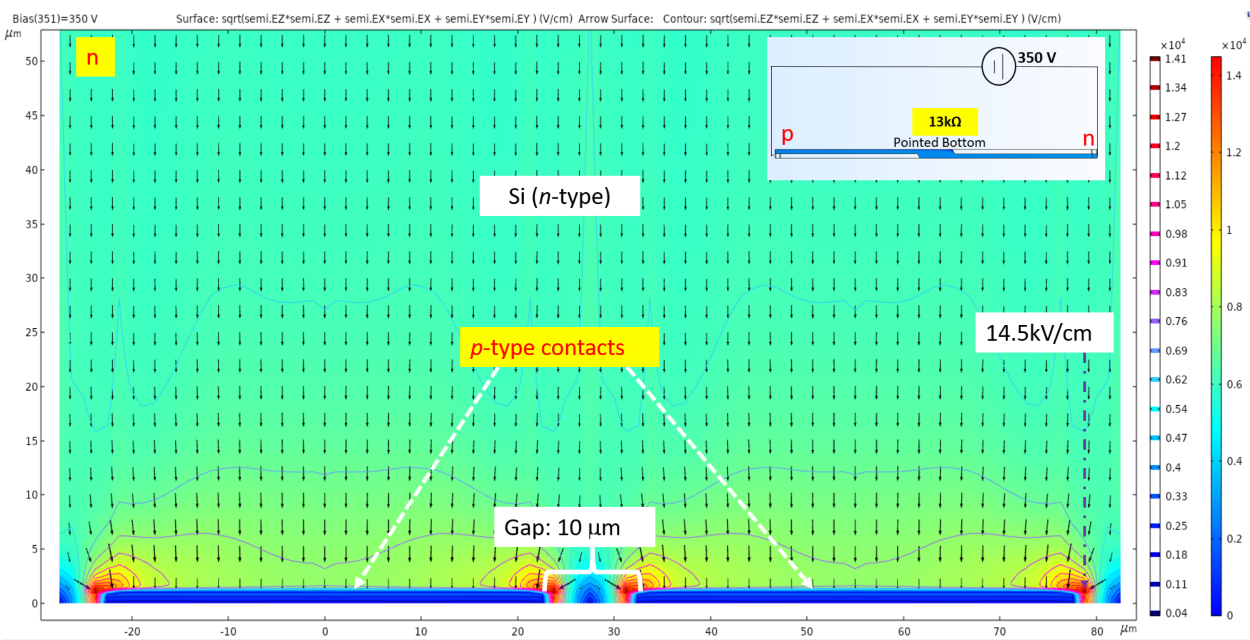

Figure 4.11: *Electric field magnitude profile for a* 10 µm *gap in between pixels in y-direction. The size of the pixel is* 20 µm*-by-*30 µm*. This result is for a 350V bias (complete depletion).*

of the *p*-type pixel was decided by simulating different pixel sizes in such a way that the gap in between the pixels in y-direction (as shown in Figures 4.8 to 4.11) was between 10-25 µm. The electric field profiles for 25 µm, 20 µm, 15 µm, and 10 µm gap are shown in Figure 4.8, Figure 4.9, Figure 4.10, and Figure 4.11, respectively. It was observed that value of highest electric field magnitude around the edges (E_{edge}) is directly proportional to the value of gap in between the pixels in y-direction. Thus, 10 µm gap had minimum value of E_{edge} of around $14.5\,kV\,cm^{-1}$, while the 25 µm gap had maximum value of E_{edge} of around $30.2\,kV\,cm^{-1}$. If the pixels are too close to each other, as shown in Figure 4.11, there is a negative effect expected on the sensor's charge collection efficiency due to charge sharing. Charge sharing is detection of one incident radiation particle in multiple pixels, this degrades the X-DS-MSND spatial resolution, as the cluster describing details of the primary neutron interaction is smeared out. However, if the pixels are too far apart, as shown in Figure 4.8, the value of E_{edge} increases. Thus, the geometry with 15 µm gap (i.e., pixel size 20 µm-by-40 µm) as shown in Figure 4.10 was finalized for the sensor geometry.

4.2 Preliminary Simulation of Induced Current Profiles from COMSOL and Allpix Squared

Allpix Squared[10] is a simulation framework for designed by CERN to simulate silicon based Timepix coupled particle trackers. The source code is prepared in C++, providing flexibility in incorporating microstructured based silicon detectors. This has been done in the past[38] for a non-conformally doped MSND diode. The goal of analysing the X-DS-MSND response with Allpix Squared framework was to obtain an initial estimation of sensor responses for with approximated boundary conditions.

Allpix Squared by default imports 3D electric field and weighting potential distributions for planar Si based sensor geometries and executes charge drift modeling for the planar sensor geometries. Ionization details were imported from interaction events in Geant4, and mobile carrier transport was simulated using the Allpix Squared Generic Propagation Module. To propagate charge carriers in the presence of electric fields, this module utilizes the fourth-order Runge-Kutta-Fehlberg method[88] with fifth-order error estimation. The diffusion of the cloud (laterally) from its centroid is accounted for by applying a Gaussian calculated with the Einstein relation:

$$\sigma = \sqrt{\frac{2KT}{q}\mu t} \tag{4.4}$$

where, K is Boltzmann's constant, T is temperature, q is the elementry charge, and t is the time step. More detiled information about the charge carrier propagation can be found in CERN's Allpix Squared Manual[10].

To simulate the 3D X-DS-MSND detector geometry, the Geometry Constructor module of Allpix Squared source code was modified to allow CAD geometry import from Solidworks in GDML format. Electric field solutions from COMSOL were imported in the Allpix Squared code after barycentric interpolation and formatting in MATLAB[89]. Allpix Squared directly interfaces with Geant4 for Monte Carlo radiation transport, and *QGSP_BIC_HP* physics list was explicitly used for simulations. Both 0.0253 eV mono-energetic neutrons and 662 keV mono-energetic gamma-rays were simulated. It was observed that gamma-rays produced clusters with mostly long electron scatter tracks. However, neutrons produced comparatively smaller tracks, which were elongated along the y-axis due to presence of fins, as illustrated in previous X-MSND work[38]. Expected results for e-h pair charge drift models for each pixel hit were successfully obtained from the simulations. Si-SiO_2 interface boundary conditions were implemented by ensuring that the charge carriers stop propagating once they reach the Si-SiO_2 interface. The results of carrier transport from a single neutron interaction is shown in Fig. 4.12.

In order to design an effective front-end readout system for a radiation detector, it is essential to determine the expected timing of the output current pulses. First, Allpix Squared code was used to address this issue. The optimum geometric structure designed was utilized in the existing models in COMSOL, Allpix Squared, and Geant4, which were updated to incorporate the suggested parametric changes. To obtain correct timing of the induced current pulses, a small amount of charge was deposited at the top of the sensor. These simulations are instrumental for optimizing the readout electronics for the finalized X-DS-MSND system for idealistic boundary conditions. The expected performance of the sensor can be predicted based on these models coupled with charge transport simulations. The default Allpix Squared source code had erroneous production of induced cur-

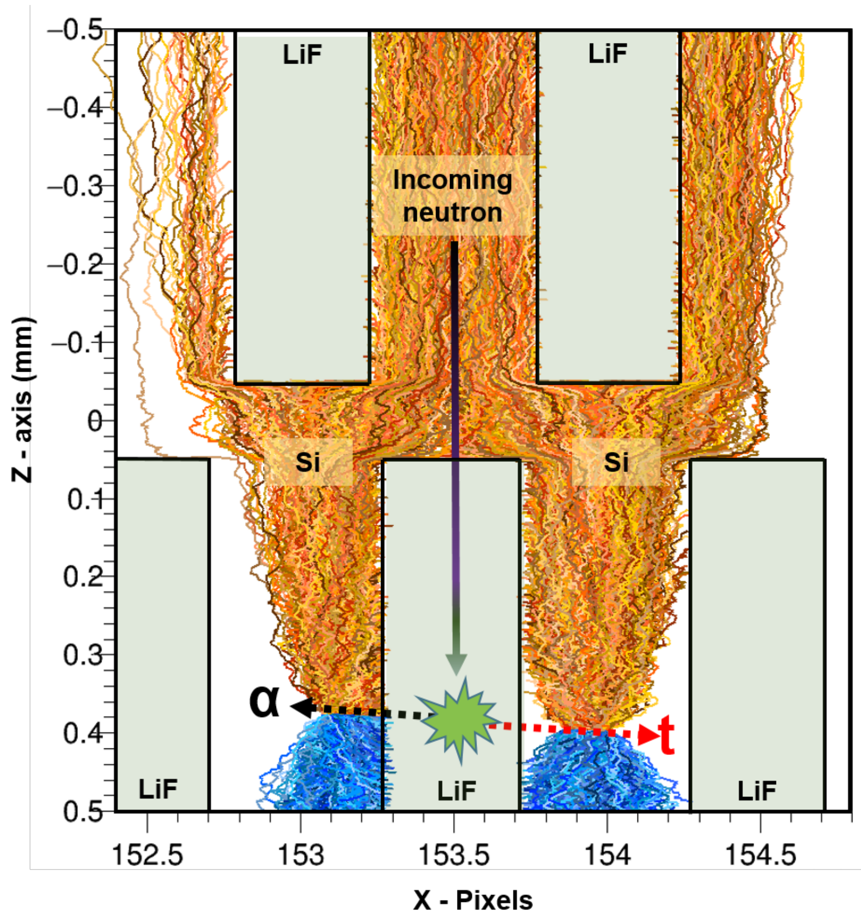

Figure 4.12: *Electron (blue)-Hole (orange) pair tracks simulated in Allpix Squared from a single neutron absorption event in a LiF-filled trench, producing ionization from an alpha particle (α) and triton (t) in silicon. Each track represents 500 individual charge carriers.*

rent plots as the currents were plotted in incorrect direction. These errors were corrected and the plots were upgraded to provide additional details like total charge deposited. An example of the induced current plot obtained for [100,100] pixel is provided in Figure 4.13. The current pulse in Figure 4.13 consists of 253,288 holes (40.5812 fC) collected in the bottom electrode.

Although Allpix Squared is an easy to use code, it is difficult to model accurate boundary conditions, which is critical in obtaining the X-DS-MSND's temporal performance. Further, Allpix Squared is unable to model particle-to-particle inter-coulombic interactions and hence the plasma effect of the injected charge cloud is not incorporated. Thus, for the development phase and to determine accurate boundary conditions, a more realistic FEM based COMSOL Multiphysics will be used to analyse the effects of Si-SiO_2 boundary conditions on the X-DS-MSND sensor.

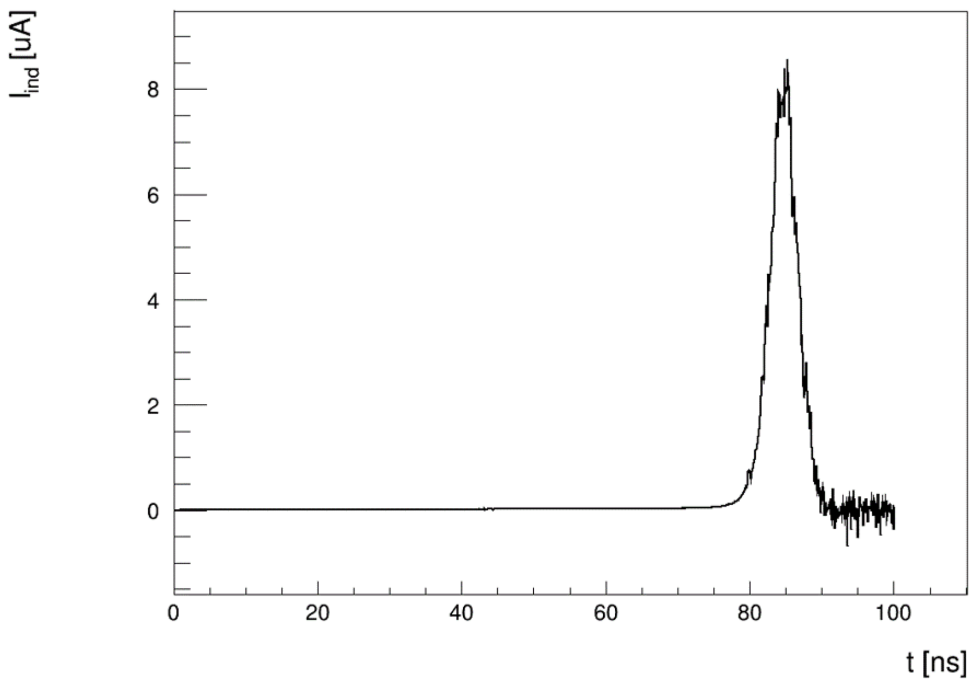

Figure 4.13: *Induced current obtained from Allpix Squared. The current pulse was extracted from bottom electrode is a case where holes and traveling downwards.*

4.3 Summary

Results obtained from COMSOL Multiphysics simulations provide critical physics based design parameters for the X-DS-MSND sensor. These results complete a multiphysics model essential to begin sensor fabrication process. At present, Allpix Squared is not capable to account for plasma effects and intercharge carrier interactions and hence COMSOL Multiphysics was utilized for detailed charge transport and Si-SiO_2 interface boundary condition analysis.

Chapter 5

Experiments and High Fidelity Simulations

The depletion characteristics of trenched microstructured devices are complicated by the introduction of trapped charges in the thermally grown oxide layer during fabrication, thus affecting the depletion region by causing a shift in the potential[53]. FOCs are of the primary interest for the sensor discussed in this dissertation in detail, as they are difficult to mitigate and can have relatively high concentrations.

A positive space charge is formed inside the oxide film due to FOCs during the thermal oxidation process. These charges induce negative image charges in the Si substrate. The accumulation of *n*-type carriers near the Si-SiO_2 interface in an *n*-type substrate decreases the resistivity of the substrate around the Si-SiO_2 interface[90], which increases the required bias to deplete the diode. FOCs are stable under moderate temperature and bias conditions and are unaffected by changes in surface potential[56]. The density of the FOC is dependent upon surface orientation of the substrate. The <111> orientation is most relevant to study the effects of FOCs on the Si-SiO_2 interface of the trench walls of a DS-MSND sensor. The negative effects of FOC are demonstrated in Figure 5.1.

To design the basic physical parameters of the X-DS-MSND sensor, ideal boundary conditions were applied where the FOC and the interface trap density were assumed to be zero, i.e., the complete depletion of the diode was achieved at the theoretically estimated reverse bias. After simulating the realistic boundary conditions with non-zero FOC and interface trap density, it was estimated that the presence of these realistic boundary conditions will have severely detrimental ef-

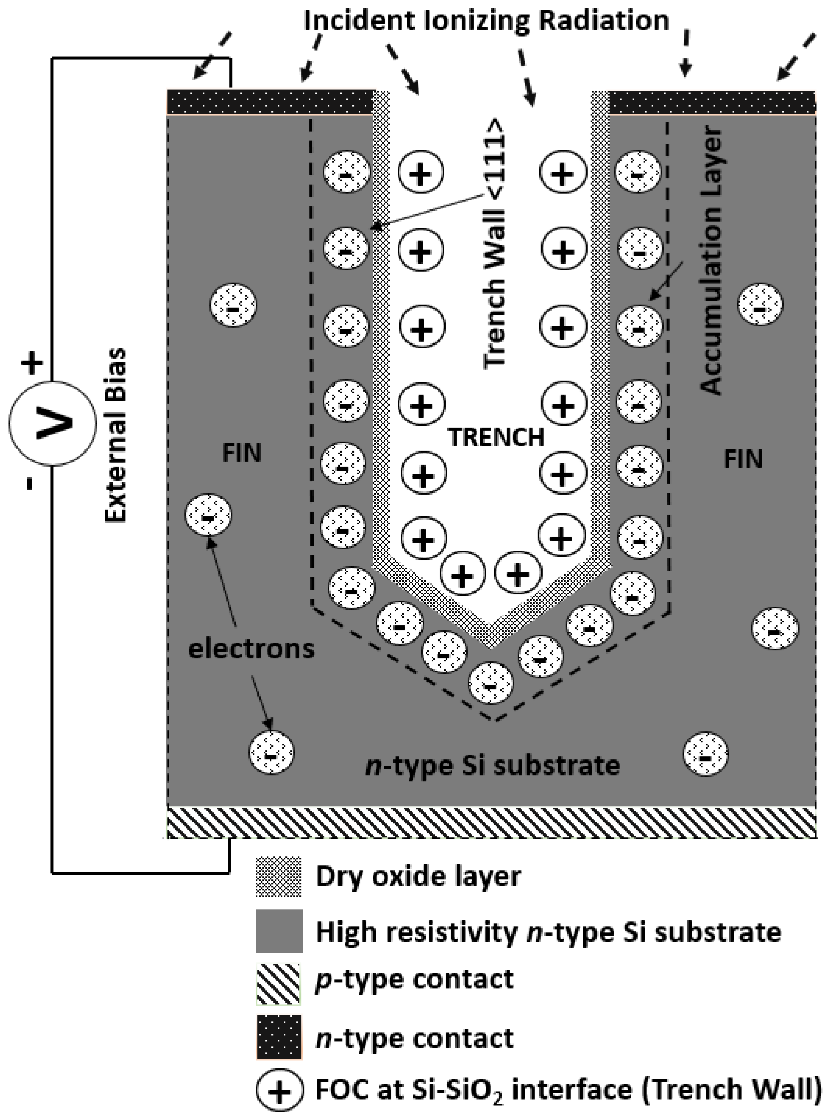

Figure 5.1: *A representation of effects of FOC on the prototype MSND device and the doping scheme used for fabrication.*

fects on the X-DS-MSND's temporal performance. Multiple simulations were performed with the X-DS-MSND device with varying realistic FOC and trap densities. An estimation of the depletion depths as a function of applied reverse bias is provided in Figure 5.2.

Previous chapters showed that under ideal conditions X-DS-MSND can fully deplete at 350 V applied reverse bias. It was observed from Figure 5.2 that the increment of both FOC and interface trap density could deteriorate the X-DS-MSNDs ability to deplete. Since this specific research subject has very limited information available through the literature, a significant amount of simulation

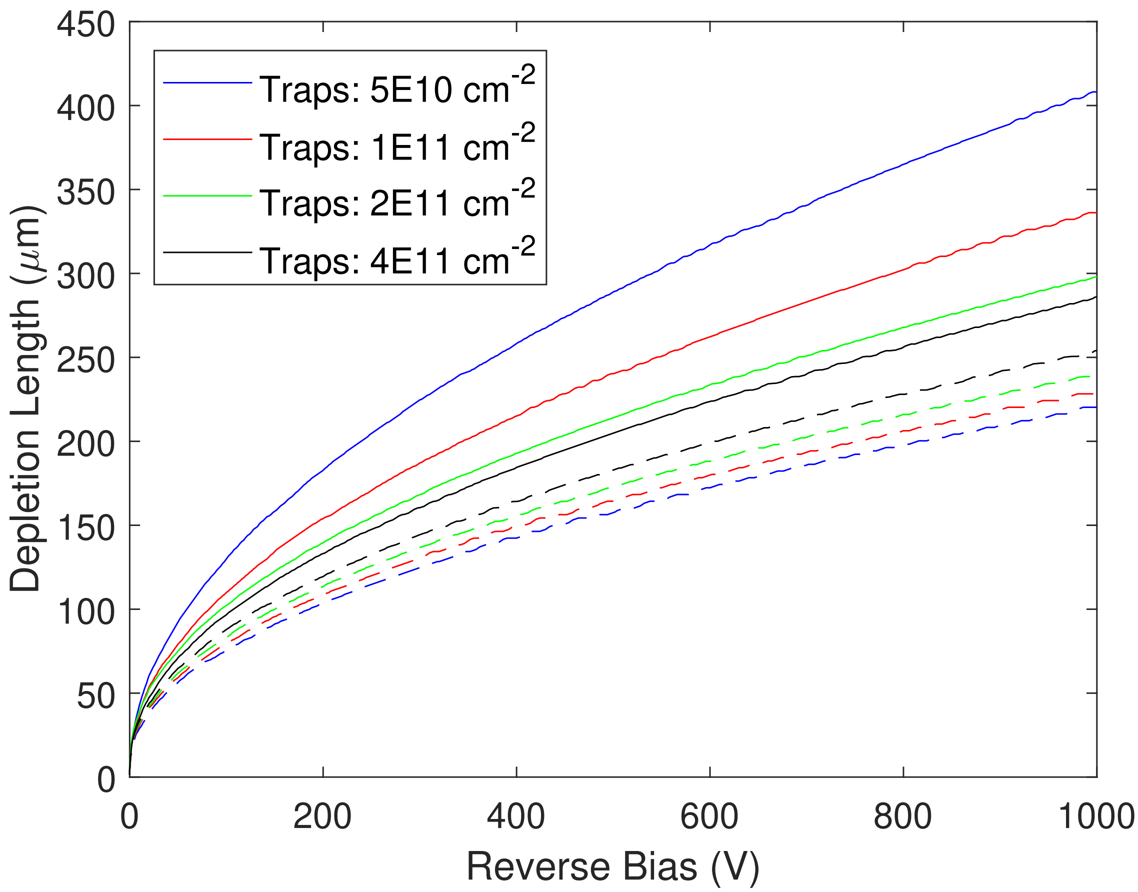

Figure 5.2: *Calculated effects of realistic boundary conditions on the depletion depths achieved for the X-DS-MSND diode. Solid lines represent values when FOC is* $5 \times 10^{9}\,\mathrm{cm}^{-2}$. *Dashed lines represent values when FOC is* $5 \times 10^{10}\,\mathrm{cm}^{-2}$

and experimentation were needed to obtain an accurate estimate of these realistic boundary conditions on the Si-SiO_2 interface. Multiple single sided reverse MSNDs were fabricated by Radiation Detection Technologies, Inc., with SiO_2 layer thicknesses of 0 nm to 250 nm. These devices were fabricated to provide empirical data for validating simulation results. They were fabricated with trenches etched through a planar *n*-type contact and have a planar *p*-type contact diffused into the backside of the diode and their IV/CV characteristics were measured.

The devices were fabricated with a 600 μm thick *n*-type wafer. A $5\,\mathrm{k\Omega - cm}$ substrate was utilized for the fabrication. The etched trenches were about 180 μm deep, resulting in fins with a width of 21 μm at the top and 27 μm at the bottom, measured by a scanning electron microscope

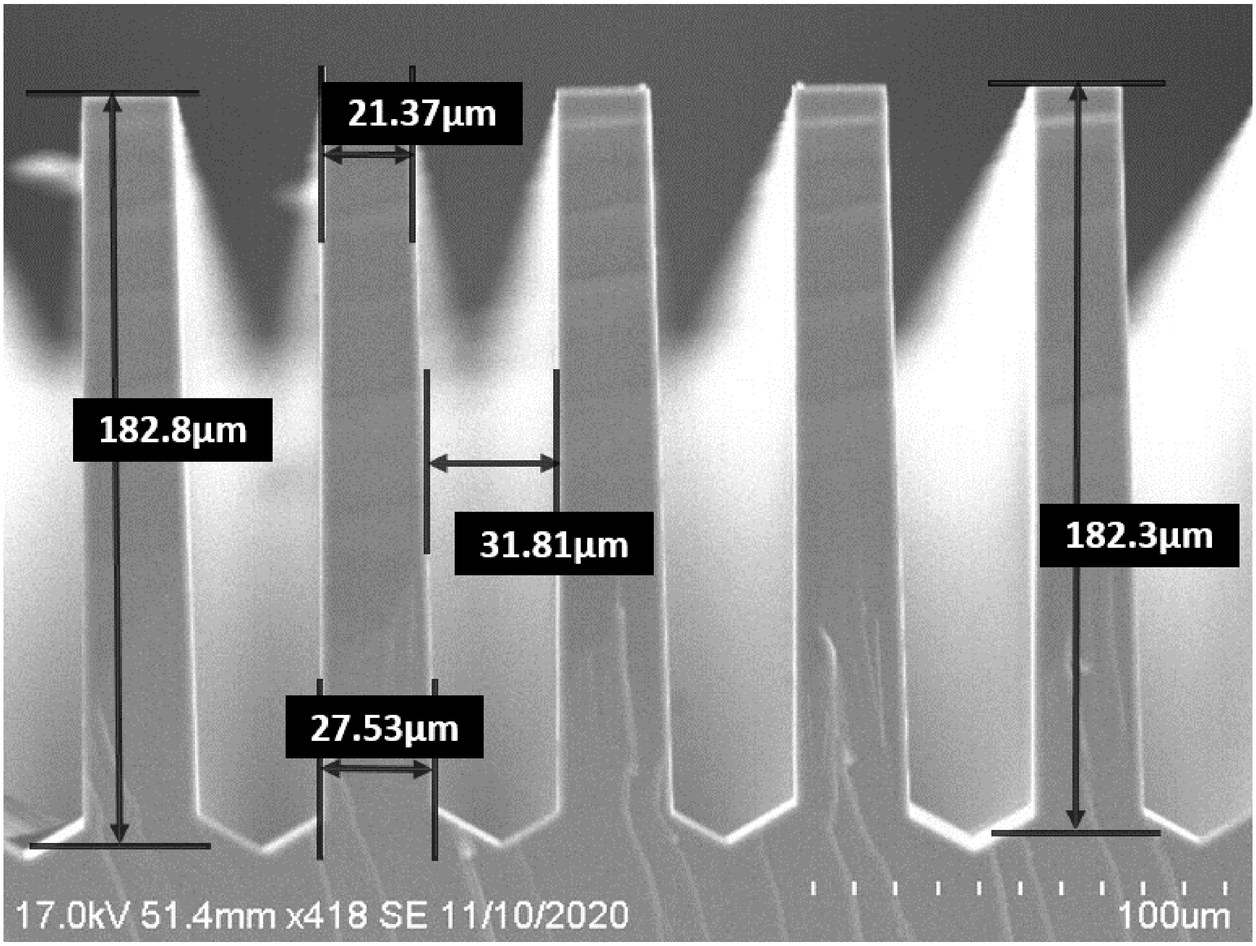

Figure 5.3: *A SEM image of the fabricated single-sided MSND device.*

(SEM) shown in Figure 5.3. The doping scheme for the device is presented in Figure 5.1. Here, the *n*-type and *p*-type contacts peak doping concentrations were both about $5 \times 10^{17}\,\mathrm{cm}^{-3}$. A 250 nm dry oxide passivation layer was found to be performing optimally, as this thickness was observed to maximize breakdown voltage while retaining relatively low leakage current below breakdown. Thicker oxides may further reduce leakage current but will negatively affect the neutron detection efficiency by reducing neutron interaction probability and reaction product escape probability.

The goal of these preliminary studies was to investigate the depletion characteristics, electric field magnitude, and spectral response of this design. COMSOL Multiphysics[11] models include FOC at the trench surface formed in a thermally grown SiO_2 passivation layer. To investigate depletion characteristics, multiple non-conformally doped reverse MSNDs were fabricated and characterized. Geant4[9] was deployed to simulate radiation interaction and ionization events and calculate spectral responses.

5.1 Fixed Oxide Charge

FOC results from dangling bonds of the Si atoms at the interface between the oxide layer and the *p*/*n* type crystal surface. One study[91] reported that the effective FOC value for the *n-type* crystal surface should be positive and similar to that of a *p*-type device. Here, the conventional CV method on a metal-oxide-semiconductor (MOS) was used to investigate oxide charge by observing the shift in the flat band voltage. One study[92] reported almost zero FOC value for very low-resistivity ($100\,\mathrm{m\Omega-m}$), Al-contaminated, *n*-type Si wafers. Other studies[54;56;93] report FOC values on order the of $10^{10}\,\mathrm{cm}^{-2}$. As per the values observed in the above mentioned literature, an FOC value of $5\times10^{10}\,\mathrm{cm}^{-2}$ is used in the present work. Further testing and simulations will be required to determine accurate value of FOC for this device.

5.2 Signal Formation

Faster signal acquisition is obtained by establishing a strong electric field in the entire device due to external bias. In this case, the motion of the charge carriers is dominated by drift instead of diffusion and the signal is fast enough to permit very high interaction rates. The presence of positive FOC on the Si-SiO_2 attracts *n*-type carriers and is expected to create an accumulation layer which decreases the resistivity of the substrate around the interface as shown in Figure 5.1. If the FOC is too high, it is hypothesized that the fins of the sensor will not achieve full depletion, and diffusion will dominate the charge carrier motion. The objective was to observe the effects of FOC on the CV curves and spectroscopy results of the radiation detector. To accomplish this, five different radiation detectors with $250\,\mathrm{nm}$ thick dry oxide were fabricated with similar design parameters. Two different experiments were conducted and later compared to the simulation results.

5.3 Experiment Details

5.3.1 CV and IV Curve Details

The capacitance of the device was measured with a Hewlett-Packard CV-curve-tracing 1 MHz system (model 4280A). The diode along with the probing station was placed in an electromagnetic shielded dark box to prevent light contamination. The capacitance C is the ratio of the charge magnitude Q on either conductor to the potential difference applied V between the those conductors:

$$C = \frac{\Delta Q}{\Delta V} \tag{5.1}$$

A simple way to obtain the capacitance (C) is by applying a small AC voltage of millivolt range to the diode under test and simultaneously measuring the resulting current. The resulting current is integrated over time to obtain charge (Q), finally calculating C from Equation 5.1. obtaining CV curves for a semiconductor device involves simultaneous application of two different voltage sources. First, an AC voltage signal (dV_{ac}) was be applied, the magnitude and frequency of the AC voltage were fixed. Second, a DC voltage (V_{dc}) was applied and this was swept in time to allow sampling of the material at different depths in the device. The AC voltage bias provides the small-signal bias so the capacitance measurement can be performed at a given depth in the device.

Leakage current is another important characteristic of the reverse-biased diodes. It is known that in the reverse-biased condition, the width of the diode's depletion region increases. Generally, this condition ensures restriction of carrier accumulation near the junction. As the majority carriers are primarily removed from the depletion region, this volume acts as an insulator. Although the majority carriers do not enter the depletion region, some amount of current is still observed when the diode is reverse biased. This current is called leakage current and is due to the motion of minority carriers. In silicon diodes used for radiation detection, the leakage current should ideally be on the order of few hundred nanoamperes for optimal operation.

A record of leakage current magnitude with respect to increasing reverse bias voltage (IV curve) was needed to obtain estimated device performance. The diode's leakage current magnitudes were recorded corresponding to the applied reverse biased voltage. It was observed from the results that two diodes out of five were the best choices for further testing as they broke down at higher reverse bias voltages of around 350 V and 540 V. The diode with breakdown voltage of 540 V was selected and its IV plot is presented in Figure 5.4. Large variations observed in the leakage current magnitudes among the diodes is attributed to variation in the quality of dry oxide passivisation with SiO_2 layer on the diode. The measured CV plot for the selected Chip 4 with 250 nm thick SiO_2 layer is presented Figure 5.5 up to a 100 V reverse bias.

5.3.2 ^{241}Am Source Spectroscopy Details

To benchmark simulated spectroscopy results, a series of alpha particle irradiations with the MSND diode were performed. The source deployed for the irradiations was a 0.1 μCi ^{241}Am alpha particle source. Most of the alpha particles generated from the source are emitted with kinetic energies of 5.388 MeV (1.4%), 5.443 MeV (12.8%), 5.485 MeV (85.2%), 5.512 MeV (0.20%), and 5.544 MeV (0.34%). A representation of the experimental setup is presented in Figure 5.6. A 5 mm-thick 3D printed polyethylene terephthalate glycol (PETG) collimator was placed on the silicon MSND diode to acquire data from alpha particles with well-known, limited angles of incidence. The top contact of the sensor was wire bonded and placed in a biasing box with BNC outlets for connection.

5.4 Modeling Methodology

5.4.1 Geant4 Radiation Transport Toolkit Simulation Details

To accurately estimate the sensor response for the experimental setup, the geometry was primarily prepared in the CAD format in Solidworks[26] and subsequently imported in Geant4 using the GDML[71] format. The raw GDML geometry file for the experimental setup contained a total of 9157 triangular facets. Out of those, 292 facets (3%) were found to be degenerate, which were skipped from the final GDML file as per the recommendation provided in the Geant4 forum[94]. *The QGSP_BIC_HP* (QGSP with binary cascade model) physics list was considered for these simulations as per results provided in available literature[75;95].

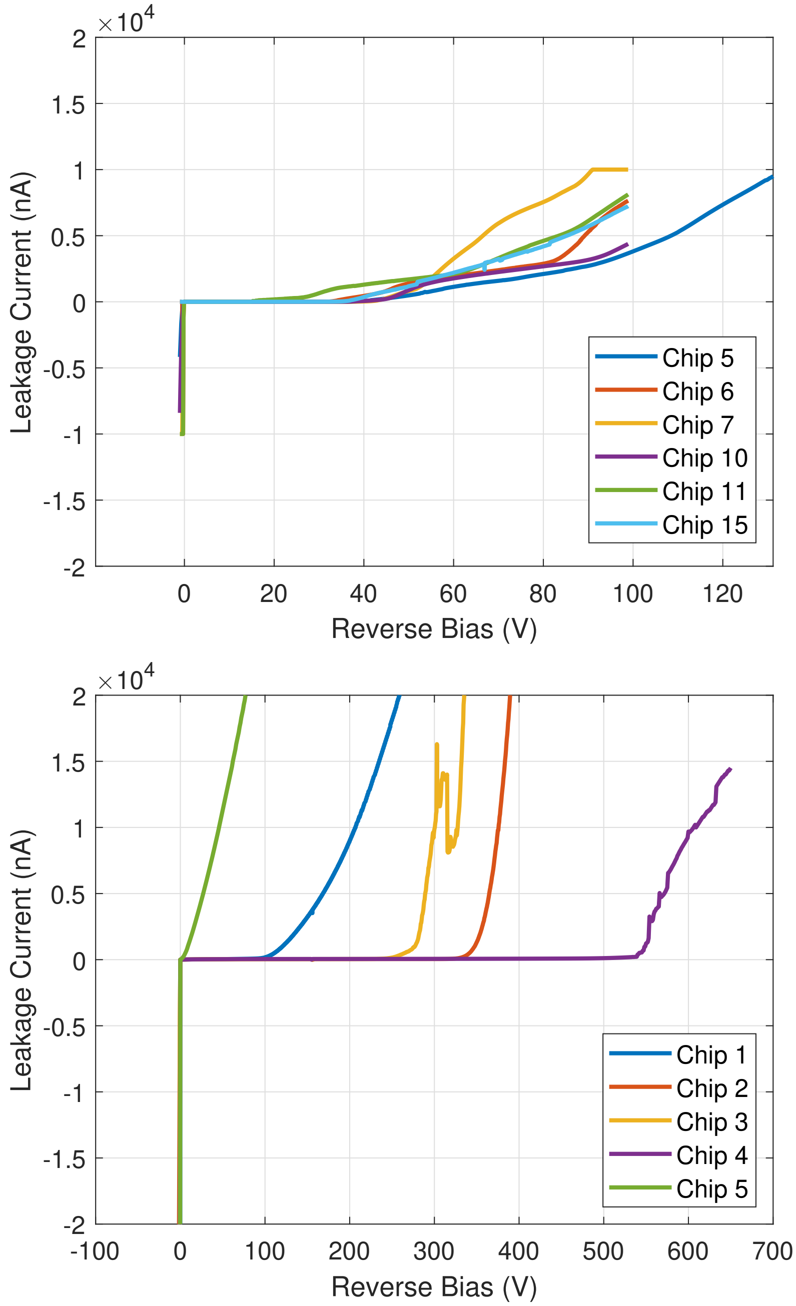

Figure 5.4: *IV curve data obtained for all the fabricated diodes. Top plot is for MSNDs with* 50 nm *thick* SiO_2 *layer. While, the bottom plot is for chips with* 250 nm *thick* SiO_2 *layer. A leakage current of* 218 nA *was observed at the breakdown voltage of* 539 V *for the best performing diode (Chip 4 with* 250 nm *thick* SiO_2 *layer). Measurements performed by Radiation Detection Technologies, Inc.*

Another important aspect of Monte-Carlo simulations is the method of particle cut-off, i.e., method of termination of history. Geant4 employs a default particle range cut-off of 0.7 mm (i.e.,

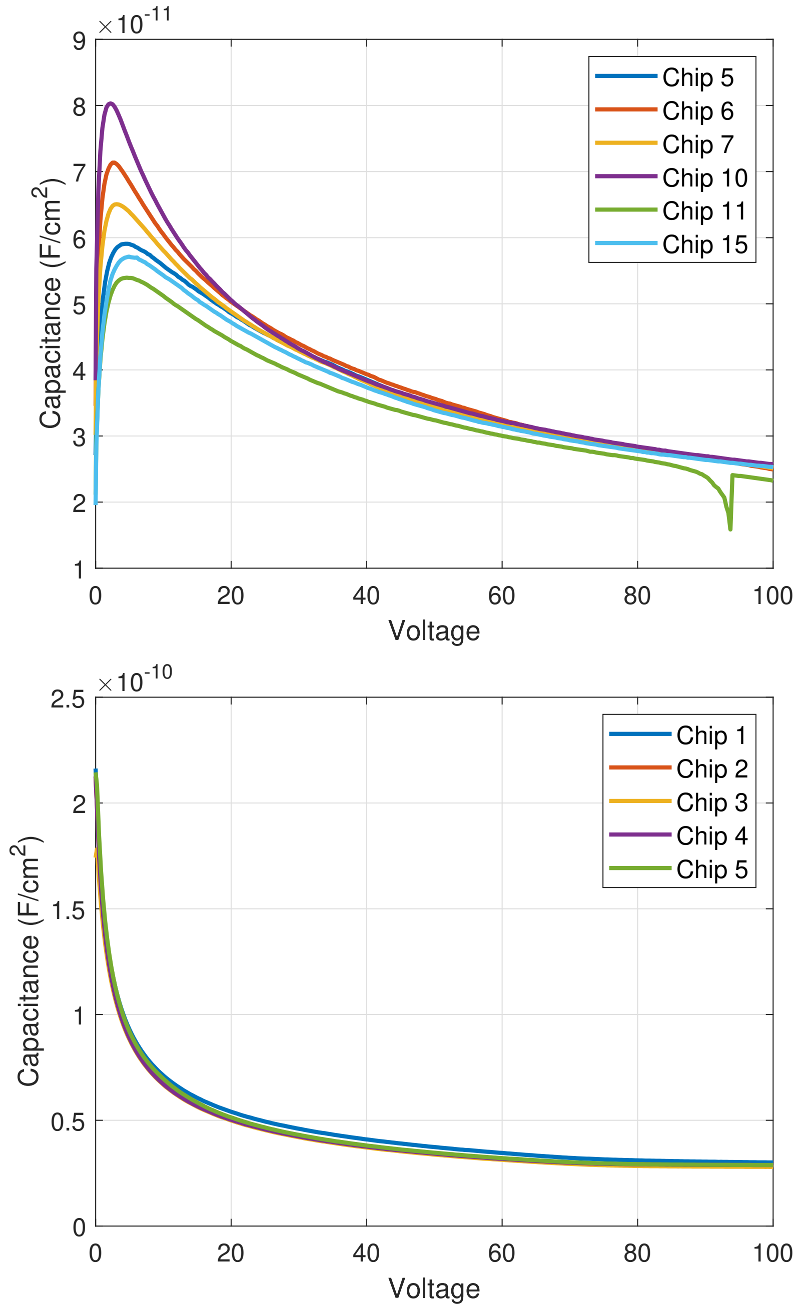

Figure 5.5: *CV curve data obtained for all the fabricated diodes. Top plot is for MSNDs with* 50 nm *thick* SiO_2 *layer. While, the bottom plot is for chips with* 250 nm *thick* SiO_2 *layer. Diodes with* 250 nm *thick oxide observes consistency in the measured data. Measurements performed by Radiation Detection Technologies, Inc.*

particle gets killed if it has insufficient energy to travel at least 0.7 mm) in any medium for electrons and gamma-rays that are produced from non-hadronic interactions like Bremsstrahlung and delta

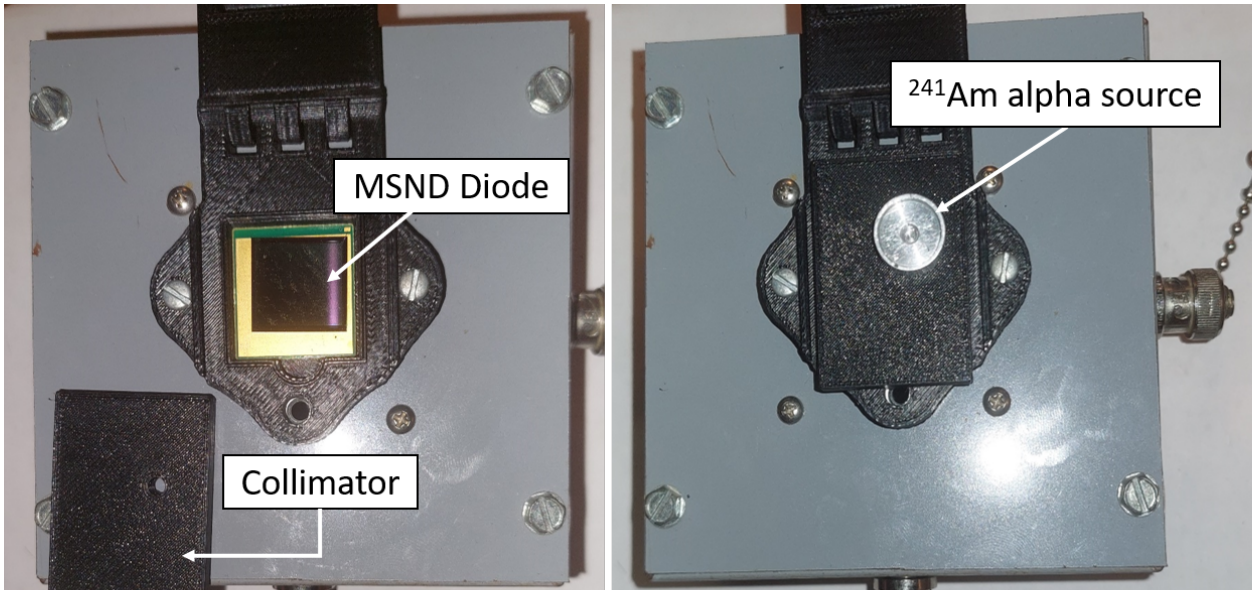

Figure 5.6: *Experimental setup to obtain alpha particle irradiation response.*

electrons. A representation of the Geant4 model is presented in Figure 5.7. The 3 mm radius source was placed 2 mm above the collimator in the model. The collimator model was 5 mm thick, had a density of 1.33 g cm^{-3}, and composed of PETG material, given by chemical formula $(C_{10}H_8O_4)_n$. The collimator had a 3 mm diameter hole in the middle. This was placed directly in between the sensor and the source as shown in Figure 5.7. The sensor was modeled with a 2.328 g cm^{-3} dense silicon material. Trenches on the sensor were modeled as per the dimensions shown in Figure 5.3.

A 4 µm thick dead layer (blue region in Figure 5.7) exists on the top of the fins that impacts the spectral results significantly. This dead layer is due the peak non-conformal doping of the top surface of the sensor. This dead layer only exists on the top of the fins and energy deposited by an incoming radiation particle in this region does not contribute to the simulated spectrum. In addition to the dead layer, a 250 nm thick and 2.65 g cm^{-3} dense SiO_2 layer was modeled covering the inner sides of the trenches. Energy deposited in the 250 nm thick SiO_2 layer does not contribute to the simulated spectrum. Finally, the entire setup was modeled in a 0.001 29 g cm^{-3} dense air environment and is represented in Figure 5.7.

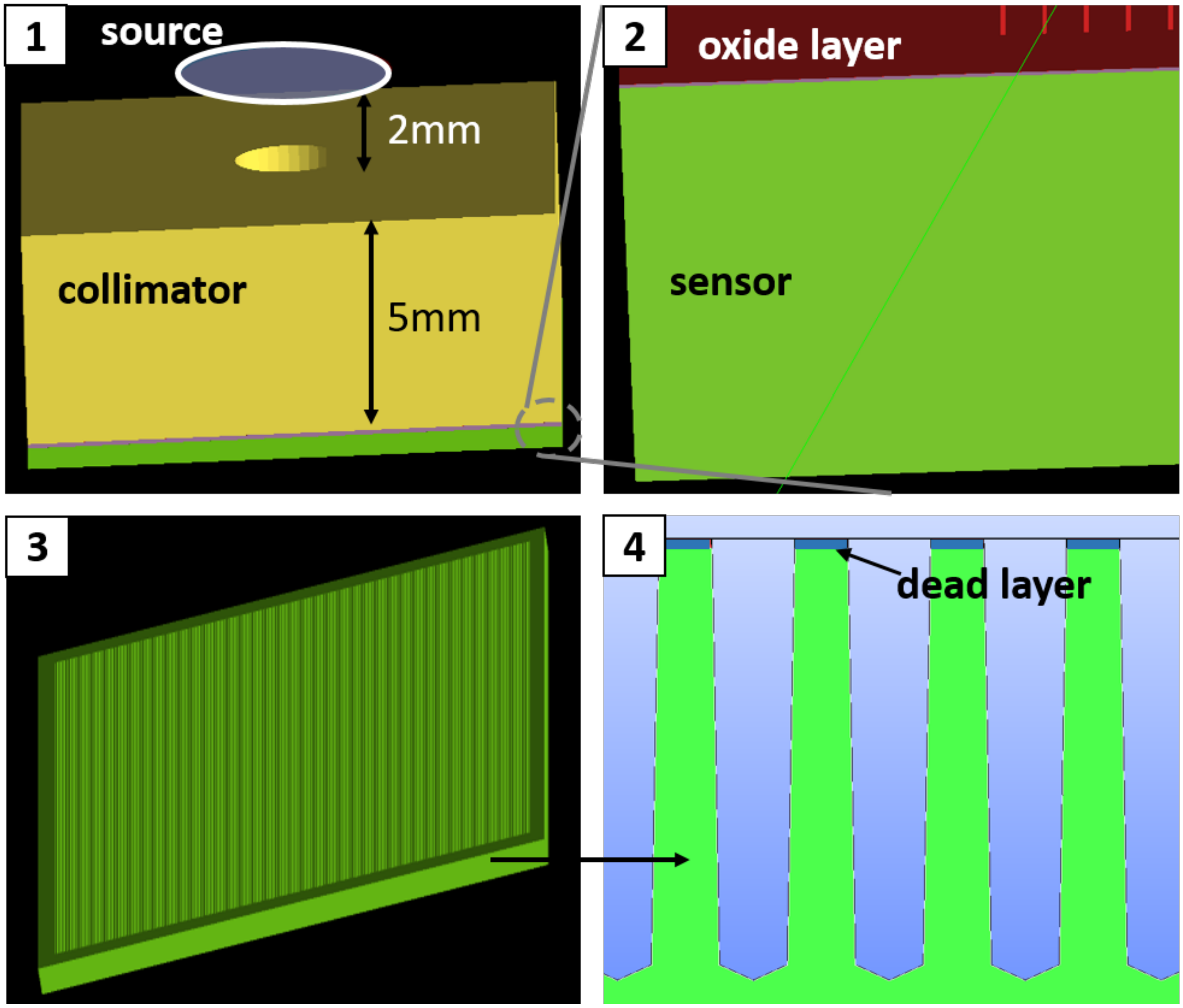

Figure 5.7: *Geant4 simulated model of the experimental setup. 1: Overall geometry; 2: zoomed view of the sensor and oxide layer; 3: entire sensor structure with the trenches; 4: zoomed view of trenches with the dead layer.*

5.4.2 COMSOL Multiphysics Models for Steady State Analysis

COMSOL Multiphysics was used to simulate semiconductor physics for investigate the effects of FOC on the trenches of the prototype MSND device. The modeling methodology for MSND devices is discussed in detail in section 2.2.6.

The optimum mesh size was decided by using Equation 2.5 and substituting, k_B = 1.38064852 $\times$ 10^{-23} JK^{-1}, T = 293.15 K, ε_0 = 8.854 187 82 $\times$ 10^{-12} Fm^{-1}, ε_r = 11.7, q = 1.602 176 62 $\times$ 10^{-19} C, and N = 8.9163 $\times$ 10^{17} m^{-3}. The debye length (λ_d) obtained for this device was 4.28 µm. Further,

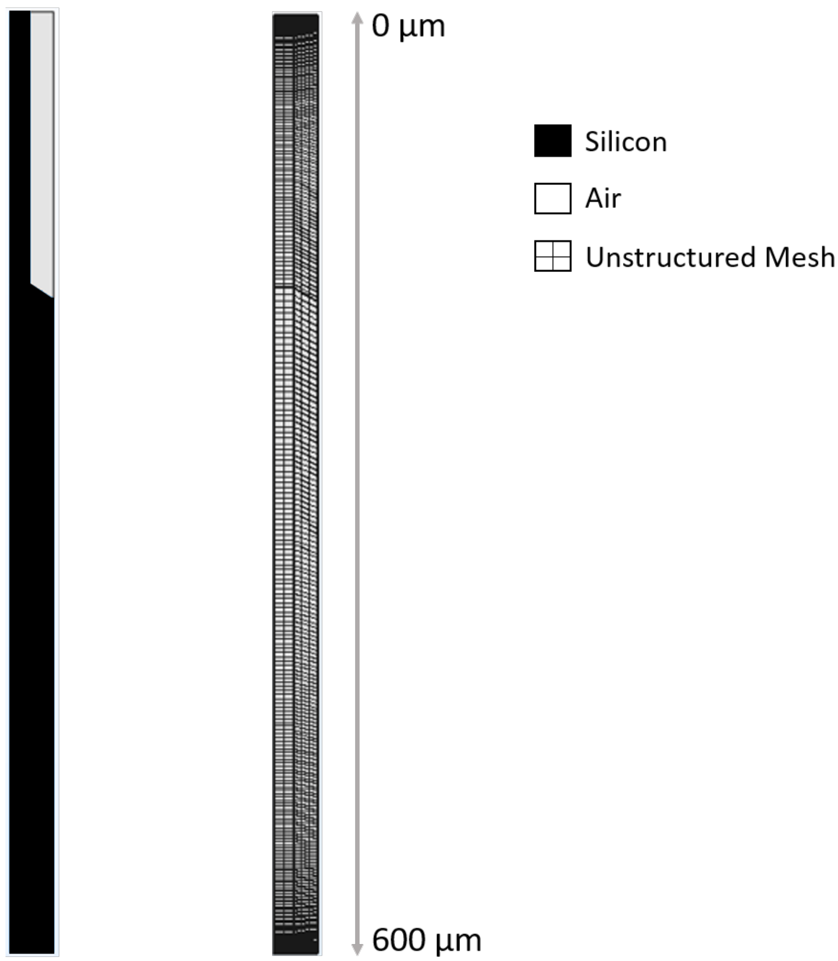

Figure 5.8: *A representation of the COMSOL FEM model (left) and the associated unstructured mesh (right).*

the minimum element size of 0.12 µm was used at the regions of higher charge carrier gradient and maximum element size of 6 µm was used at the bulk region of the sensor where the charge carrier concentration gradient is almost negligible. To further optimize the simulation time, zero Neumann boundary conditions were applied such that a one-quarter pixel geometry (27.5 µm-by-27.5 µm) was modeled and meshed as represented in Figure 5.8. COMSOL's default silicon material was used to model the diode. The Charge Conservation option was used to add air as a dielectric material.

An *n*-type substrate was modeled with a 5 kΩ − cm resistivity, i.e., constant background doping concentration of 8.9×10^{11} cm^{-3}. The top (*n*-type) and bottom (*p*-type) junctions of the sensor were modeled with peak doping concentrations of $5 \times 10^{17}\,\mathrm{cm^{-3}}$. The concentration decreases with Gaussian profile with respect to depth inside the sensor; after 2 µm the concentration becomes equal to the background. As specified by the wafer manufacturer and as per available literature[87], a 1 ms charge carrier life time was specified for the simulated sensor model. The FEM model and experimental setup was prepared to obtain steady state responses like depletion profile, CV plots, and electric field profiles from the MSND diode. Significant changes are needed in the modeling and experimental setup to analyze transient responses like charge transport models and induced current profiles.

COMSOL Multiphysics should be used to first solve for steady-state solutions before performing a transient time-dependent simulation, as an electric field needs to be established within the simulated device model for the charge carriers to drift. The transient solver utilizes the electric field solution provided by the steady state solver and then performs iterations in time to account for charge carrier motion within the semiconductor device at a specified external bias. To obtain optimum simulation performance, it is ensured that the unstructured mesh used in the finite element solver is fine enough to reduce striations. Furthermore, to ensure that COMSOL captures the accurate transition of the charge carriers within the semiconductor volume, the time steps are in the range of 0.1 ns per iteration. The default Si semiconductor material model provides accurate mobility values for the charge carriers; the value provided for electron mobility is μ_e=1400 $\mathrm{cm^2\,V^{-1}\,s^{-1}}$, and for hole mobility μ_p=450 $\mathrm{cm^2\,V^{-1}\,s^{-1}}$[96].

5.4.3 COMSOL Multiphysics Models for Transient Analysis

While performing exploratory transient simulations in COMSOL Multiphysics, it was noted that the time-dependent induced current pulse obtained by simulating a charge injection event in two-dimensional (2D) and three-dimensional (3D) geometries differed substantially. It was also observed that the electric field becomes negligible at the location of charge cloud injection. The observed differences in the induced current resulted from an absence of charge carrier diffusion in the third dimension for the 2D simulations; thus, the electric field the location of injection needed a longer time to recover to its original steady state value. While it was clear that 3D simulations were needed to appropriately represent charge carrier diffusion, a convergence study was required to optimize the size of the simulated geometry for a given injected charge inside the sensor to minimize computation times.

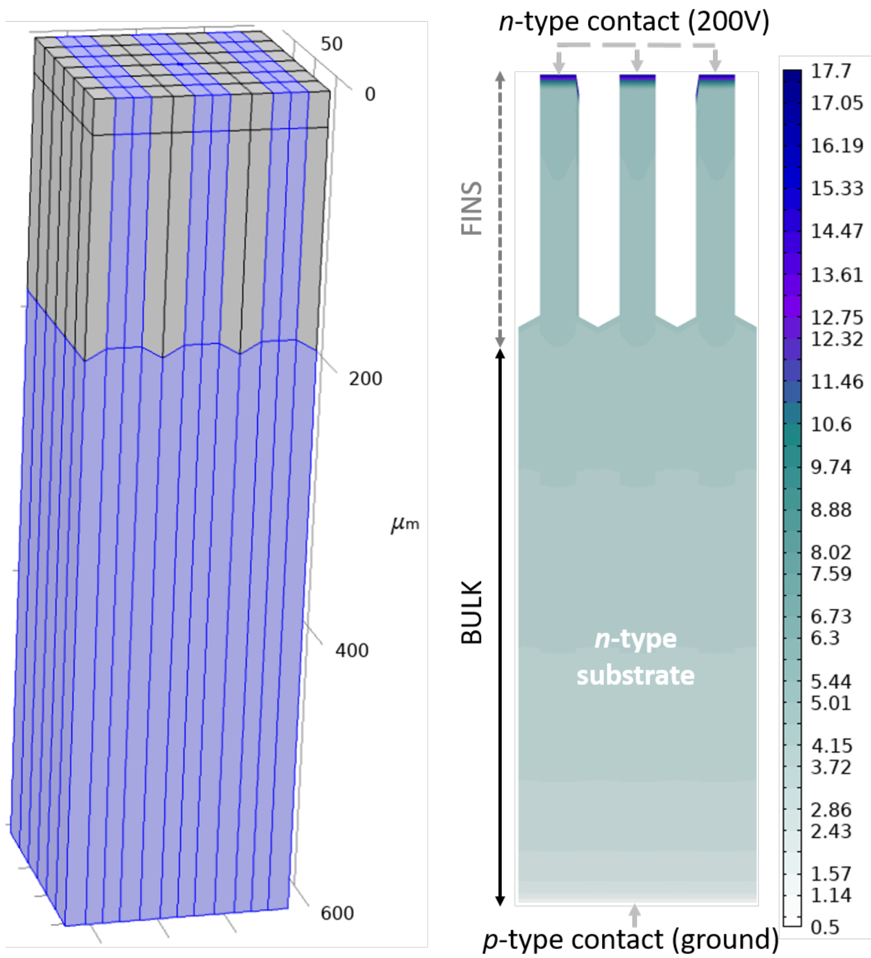

Figure 5.9: *(Left) A representation of simulated 3D geometry in COMSOL. (Right) A representation of Electron Concentration at* 200 V *reverse bias.*

A large geometry of 165 μm-by-165 μm size was simulated to ensure ample space for the charge cloud to drift and diffuse for 600 μm device length. To ensure that the simulated model represents actual fabricated diode accurate resistivity (5 kΩ − cm) and peak doping concentrations (5×10^{17} cm^{-3}) were applied to the COMSOL model and an unstructured mesh was built for the simulated structure. The simulated geometry is represented in left part of Figure 5.9.

5.5 Modeling Charge Carrier Injection

COMSOL Multiphysics provides a User Defined Generation option that is capable of generating charge carrier densities as a function of space and time.

5.5.1 Electric Fields Within the Sensor

The presence of strong electric field inside the semiconductor plays an important part in charge carrier motion and induced current response. The mobility of charge carriers within a semiconductor can be defined as the net average velocity with which the free charge carriers move towards their respective electrodes under the influence of a electric field caused due to external reverse bias,

$$\mu_{np} = \frac{V_d}{E} \tag{5.2}$$

In equation 5.2, μ is the mobility of charge carriers, V_d is the drift velocity of the charge carriers, and E is the electric field within the sensor due to an external reverse bias.

The COMSOL solution consists of millions of values for each variable spread over the entire domain of unstructured mesh of the 3D simulated geometry. To parse the dataset and obtain a simple 1D solution, a cutline was established at the center of the simulated device. The magnitude of electric field was calculated and plotted along the cutline and is represented in Figure 5.10. As per the doping profile and electric field inside the device due to external reverse bias, it is known that once the charge carriers are injected, the net velocity of the free electrons will be towards the top electrode and for holes, the net velocity will be towards bottom electrode. Furthermore, as per the data presented in Figure 5.10, the free electrons will face maximum electric field of $1988\,\mathrm{V\,cm^{-1}}$, while the free holes will face a maximum electric field strength of $7100\,\mathrm{V\,cm^{-1}}$. The maximum electric field limits for linear behavior of mobility values for charge carriers is $4000\,\mathrm{V\,cm^{-1}}$ for free electrons and $10\,000\,\mathrm{V\,cm^{-1}}$ for free holes[97]. Since the electric field strengths faced by the charge carriers inside the device is less than these values, saturation mobility models are not required for this simulation.

The charge injection is planned close to the top electrode, and so the current induced in the de-

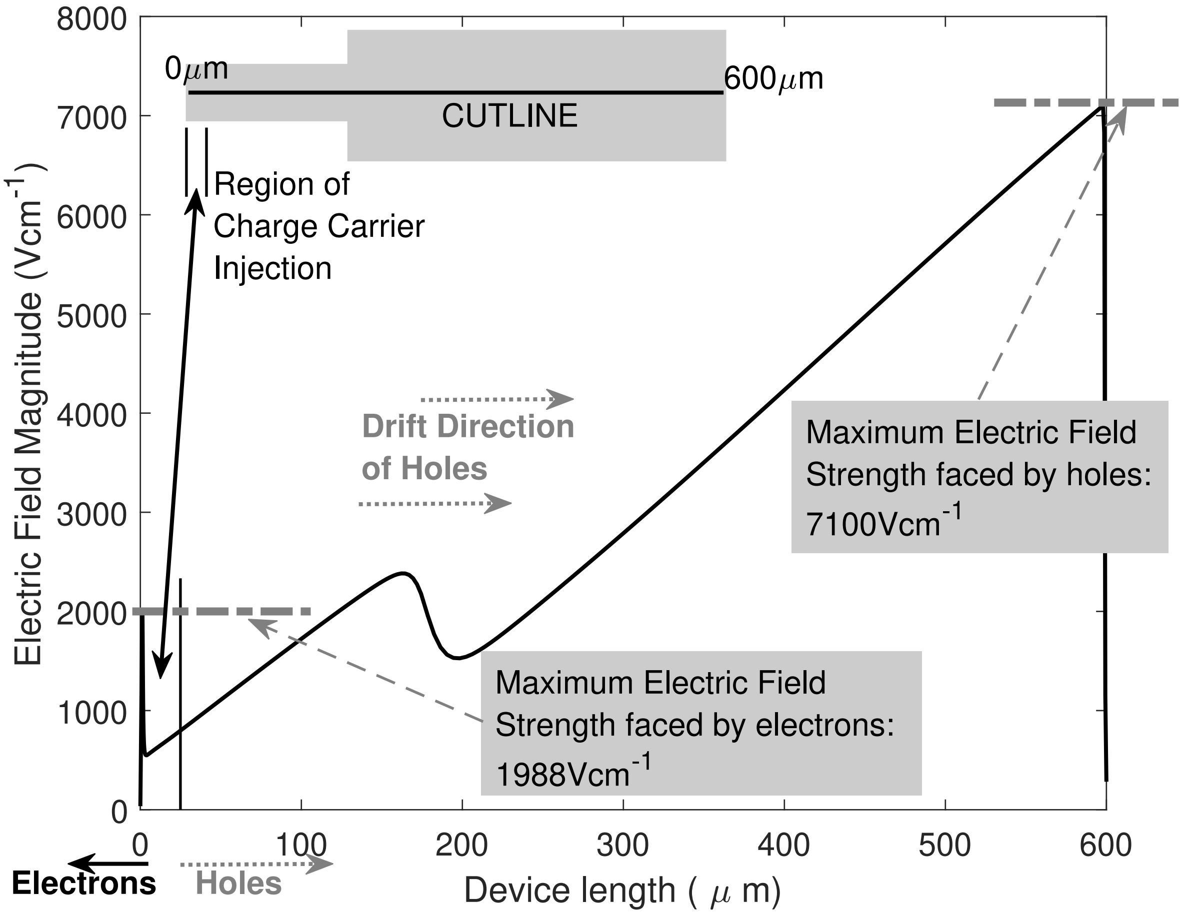

Figure 5.10: *Electric field magnitude inside the sensor along the cutline. The plot shows location of charge carrier injection and maximum electric fields faced by the 'drifting' charge carriers in motion.*

vice will be mostly due to net motion of free holes towards the bottom electrode. The contribution of free electrons for charge induction in his case will be minor as compared to that of free holes.

5.5.2 Charge Injection Method

An equation-based charge carrier injection method was used in COMSOL Multiphysics to create free charge carriers imitating energy deposition in silicon by an ^{241}Am alpha particle perpendicular to the middle of the top surface of the central fin of the modeled MSND sensor. To obtain an accurate profile of charge carrier generation in silicon due to a complete energy deposition of a

^{241}Am alpha particle, a Geant4 simulation was performed corresponding to the actual experimental setup. It was found that out of 5.48 MeV, around 4.7 MeV was deposited in the top fin of the MSND sensor. The remaining 0.78 MeV was deposited in the air. The energy deposition profile of the 4.7 MeV alpha particle can be easily obtained from SRIM[98] or Geant4 as shown in Figure 5.11.

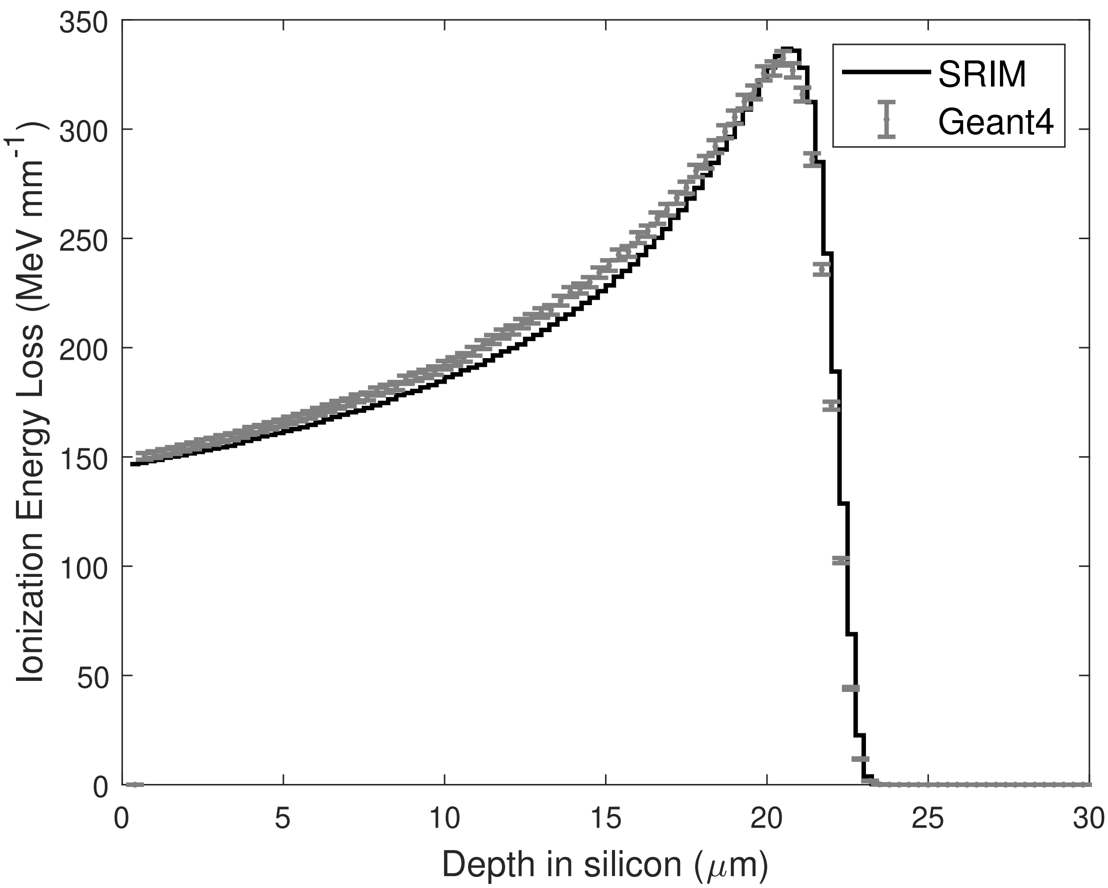

Figure 5.11: *A comparison of energy charge deposition profiles for a* 4.7 MeV *alpha particle incident perpendicularly on a Si surface, calculated from Geant4 and SRIM.*

For simplicity, it was assumed that the charge cloud has already diffused laterally for 8 ns as an initial condition and thus has a variance of 3 μm laterally as described in equation 2.6. The profile of the injected charge cloud in z-axis was imported directly from Geant4. Since 3.6 eV ionization energy loss is needed to create one thermalized electron-hole pair in silicon[99], a full ionization energy loss of 4.7 MeV will create 1,305,555 charge carriers in the the volume. The generation profile is Gaussian in time as well with mean at 8 ns and a standard deviation of 0.025 ns. The total generation profile is given by:

$$G(x,y,x,t) = e^{\left[-\frac{(x-55[\mu m])^2}{2\times Wx^2}\right]} + e^{\left[-\frac{(y-55[\mu m])^2}{2\times Wy^2}\right]} + int1(z-0.1[\mu m]) + e^{\left[-\frac{(t-8[ns])^2}{(0.1[ns])^2}\right]} \tag{5.3}$$

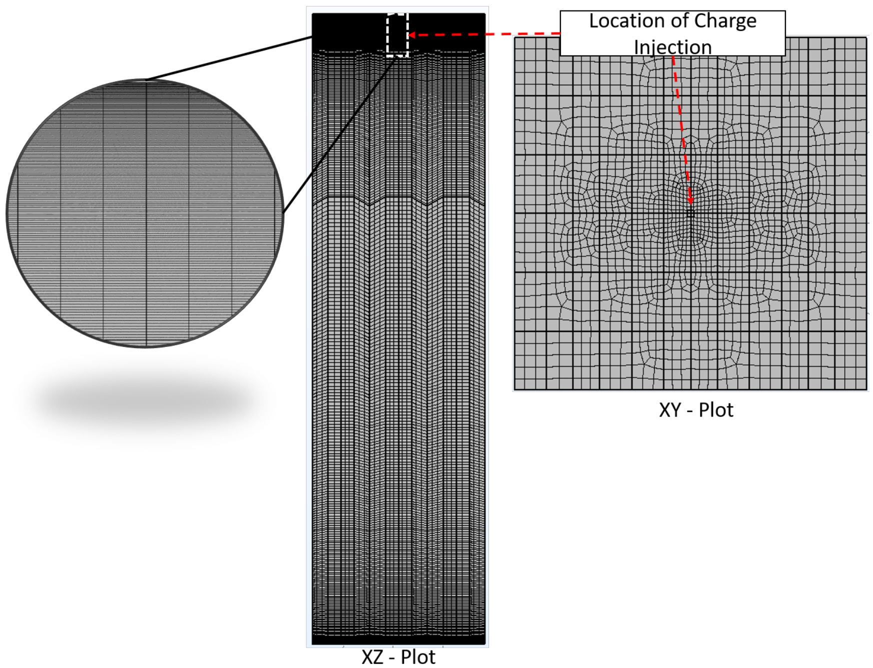

Figure 5.12: *Unstructured Mesh Profile used for calculating the solutions for the COMSOL Multiphysics model.*

Here, $G(.)$ is the generation term in $m^{-3}\,s^{-1}$, it is defined as a Gaussian distribution in space and time. The variables Wx and Wy describe the lateral location of the charge carrier injection inside the 3D domain of the sensor. An extremely fine, unstructured mesh in x, y, and z direction was employed for the 3 µm-by-3 µm-by-25 µm region of charge carrier injection in the simulated model. To accurately account for the charge carrier generation rate, extremely small time steps were considered for the duration of injection (7-9 ns). The final generation profile for a fully depleted reverse biased (200 V) MSND diode at 8 ns instant is represented in Figure 5.14. As mentioned previously, the charge injection is Gaussian with respect to time with a mean at 8 ns suggesting that the charge injection begins a bit before 8 ns and charge carriers before 8 ns have

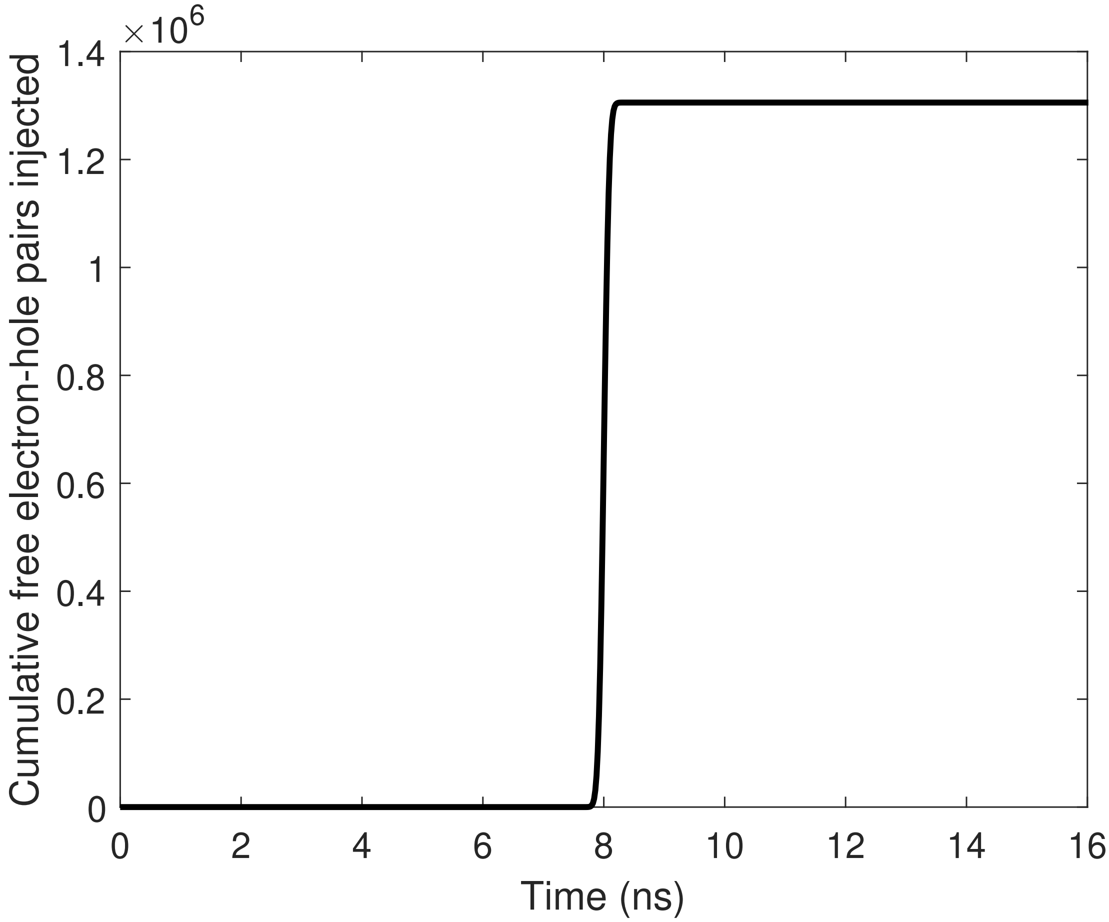

Figure 5.13: *Cumulative free electron-hole pairs injected in the simulated model with respect to time extracted from COMSOL Multiphysics.*

undergone some amount of drift and diffusion. The updated charge carrier concentration injection profile is highlighted and demonstrated in the Figure 5.14. The 2D plot in this figure provides a qualitative representation of the charge carrier injection profile. 1D plot of hole concentration has a peak within the 2 µm *n*-type junction because the net drift rate of holes outside the junction is faster as compared to the holes present within the junction. This is due to variation of electric field inside and outside the 2 µm *n*-type junction. The smoothness of the 1-D plot demonstrates that the unstructured mesh was able to resolve the sharp concentration changes in the Bragg peak of the charge injection profile used in the simulations.

Two different types of simulations are needed to understand to effects of Si-SiO_2 boundary conditions. The first type of simulation consists of geometry simulated with zero boundary condi-

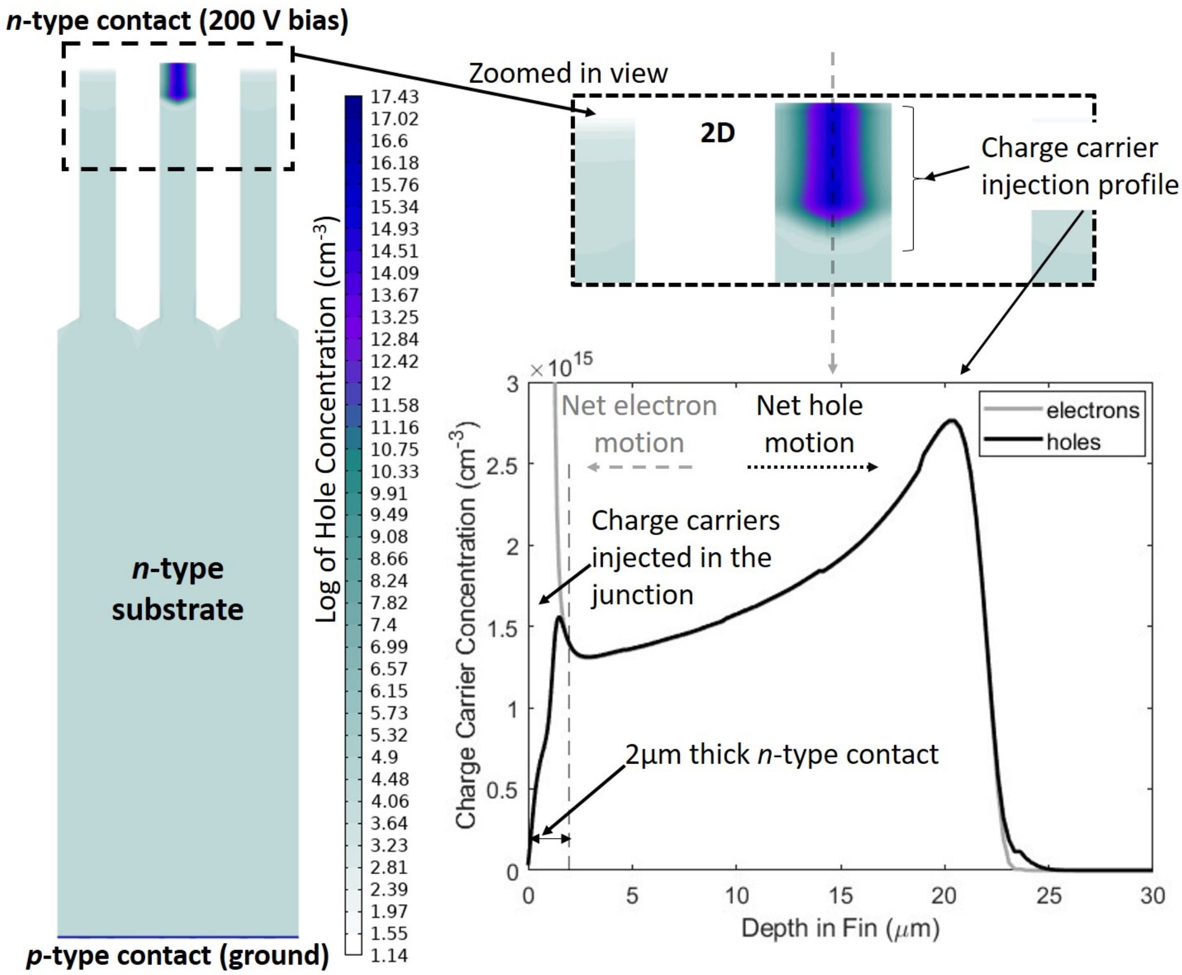

Figure 5.14: *Profile of electron-hole pairs at* 8 ns *instant in the simulated model (at 200V reverse bias) with respect to depth inside the sensor extracted from COMSOL Multiphysics.*

tion value on the trenches. These runs are not realistic but provide an estimate of an ideal device performance. The second type of simulations employed realistic boundary conditions of Si-SiO_2 interface, and will be discussed in later sections of this dissertation. The similar energy deposition profiles in Figure 5.11 and charge injection profiles in Figure 5.14 demonstrate that the charge carrier injection profile in COMSOL Multiphysics was successful in accurately replicating the energy loss data provided by Geant4 and SRIM.

5.6 Charge Cloud Motion

The electric field profile present inside the sensor dictates the net charge cloud motion inside its volume. The electric field profile for a diode simulated with zero boundary conditions is represented in Figure 5.15. Arrow plots are plotted using the x, y, and z vectors of the electric field. As mentioned in Section 5.5.1, the net electron motion will be towards top electrode and the net motion of holes will be towards bottom electrode. A 1D plot of the electric field magnitude plotted at the cutline along the line of charge carrier injection is already shown in Figure 5.10. The 1D electric field magnitude plot suggests that the displacement velocity of the charge carriers inside the fin will be much faster than in the bulk. Further, the net motion of the holes will follow the electric field arrows in the Figure 5.15. The arrow plot provides an indication of net behavior of the charge carriers within various regions of the sensor. It was noted that the electric field lines diverge while transitioning from fins to bulk. Thus, it is expected that the charge cloud would follow a similar pattern during its transition from fins to the bulk region.

Time-dependent simulations were performed in COMSOL Multiphysics to account for the effects of charge carrier motion inside the sensor. The hole drift and diffusion solutions are presented in Figure 5.16. Time step for the COMSOL transient simulation was 0.1 ns; the small time step for the simulations ensure numerical stability in the calculated charge cloud drift-diffusion models. It can be seen from Figure 5.16 that at around 25 ns, the charge cloud starts its transition from fins to the bulk region, and around this instant, the electric field profile around the bottom of the fins (shown in the arrow plot of Figure 5.15) affects the shape of the emerging cloud and the bottom electrode observes an ω shaped charge cloud emerging from the fins. Around 40 ns, the charge cloud makes the contact with the bottom electrode and holes start to get collected in the bottom electrode. At 200 ns, the charge cloud departs from fin and nearly all of the holes are collected in the bottom electrode by 215 ns. Figure 5.16 depicts a quantitative representation of the charge cloud motion inside the MSND sensor.

The data shown in Figure 5.17 quantitatively represent the charge carrier transport in the MSND detector. At 25 ns, the charge cloud can be seen departing the fin, while at around 40-50 ns, collection of charge carriers by the bottom electrode begins. It was observed that after 50 ns, the charge

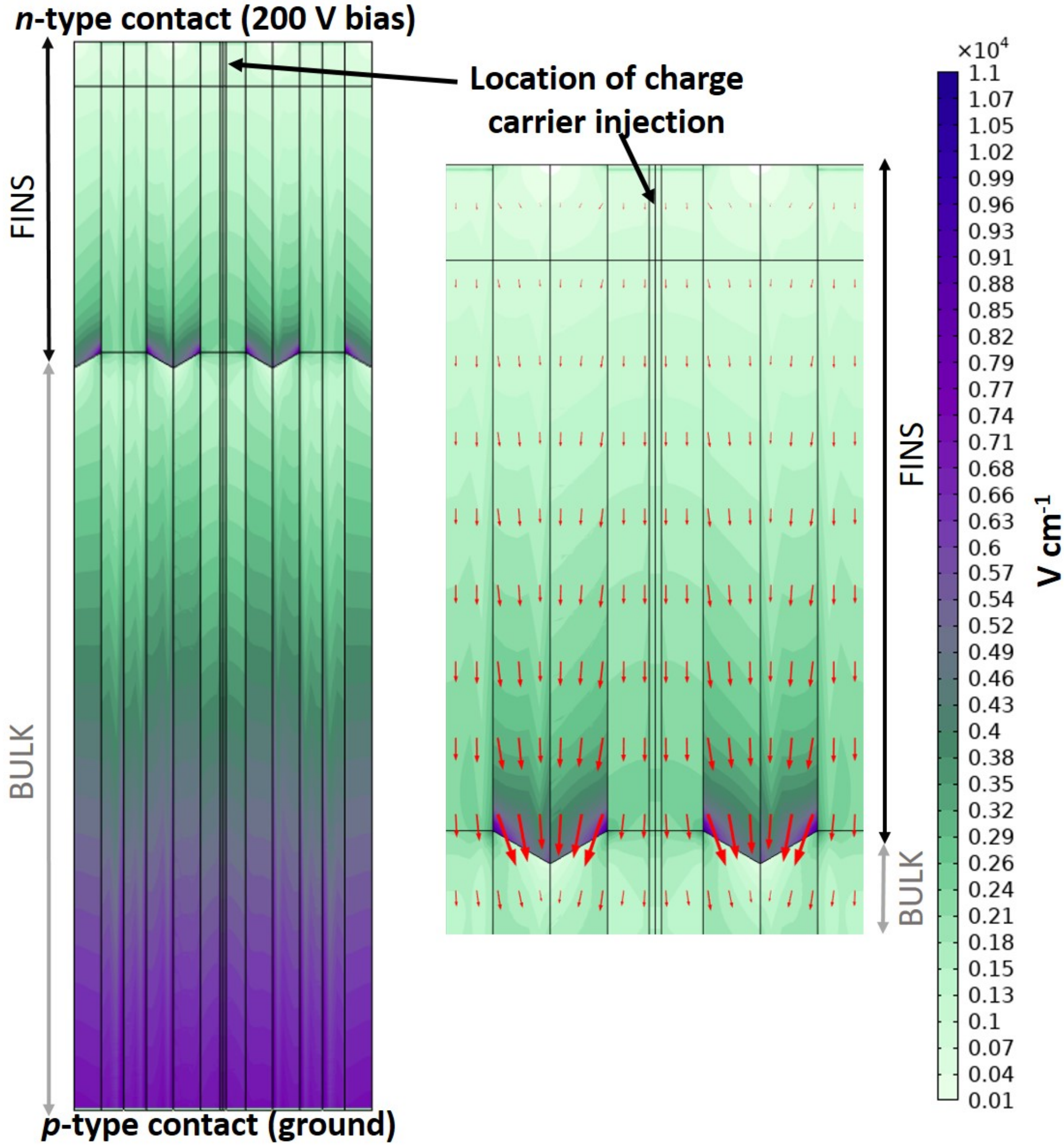

Figure 5.15: *Electric field profile within the MSND sensor at* 200 V *external bias. A zoomed-in view at the left shows an arrow plot obtained by plotting x, y, & z components of the electric field.*

collection rate by the bottom electrode is such that an almost constant level of hole concentration of around 1×10^{11} cm^{-3} was maintained throughout the cutline of the device. The charge cloud behaves like a stretched Gaussian moving along the cutline. At 175 ns, the charge cloud begins to leave the fin structure and around 200 ns, the charge cloud transitions completely to the bulk. The

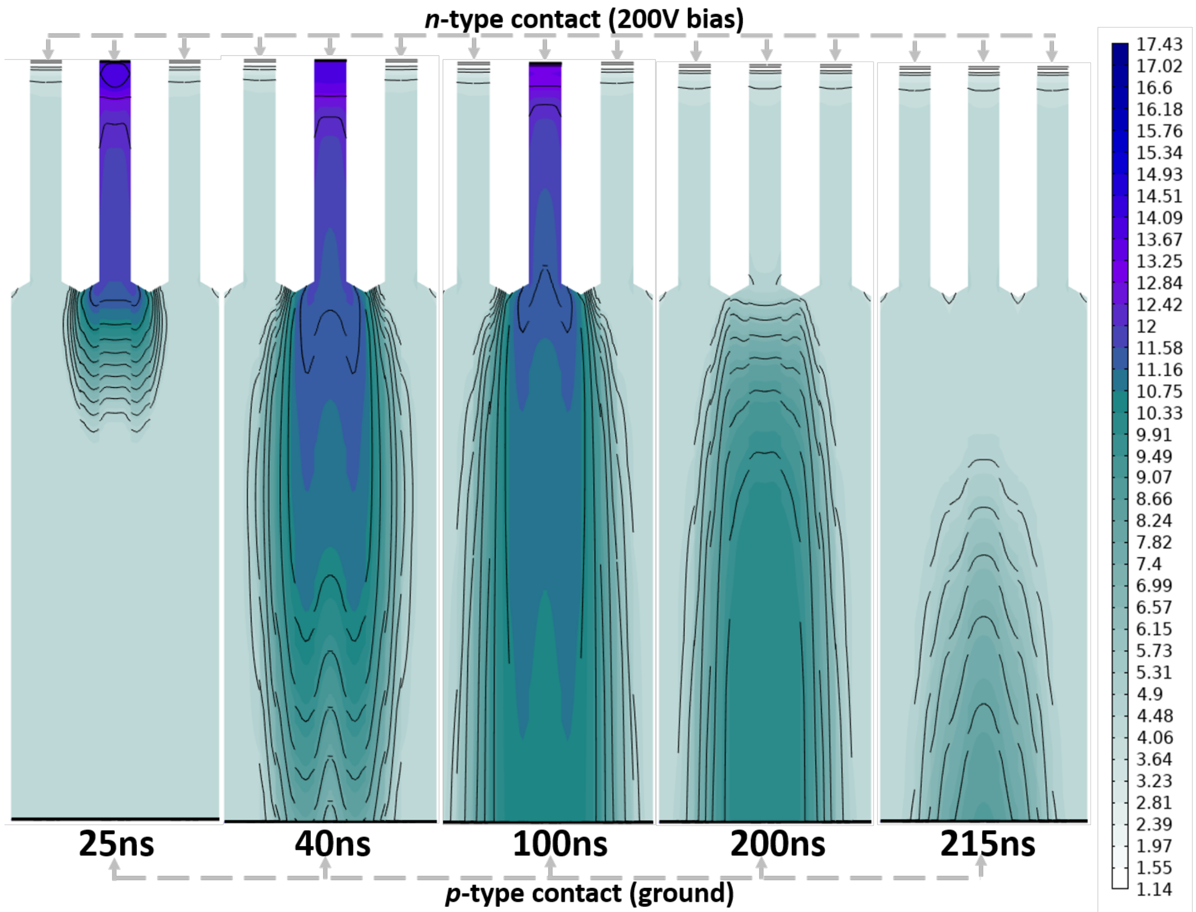

Figure 5.16: *Models for holes transport for a reverse external bias of* 200 V. *The snapshots of transient time-dependent simulations are provided for* 25 ns*,* 40 ns*,* 100 ns*,* 200 ns*, and* 215 ns

remaining carriers continue to get collected by the bottom electrode, and the complete collection of charge carriers takes slightly longer than 225 ns. At this point, the charge collection by all the electrodes is completed and an induced current profile is calculated as a post process.

5.7 Modeling Realistic Boundary Conditions

The greatest impact of the boundary conditions on the signal current would be for the case when the charge cloud is injected at the top of the fins, as the holes will travel the maximum distance around the region near Si-SiO_2 interface. To complete a response model of the trenched sensors, it is vital to determine the Si-SiO_2 interface boundary conditions. FOC and SRV are the two key parameters

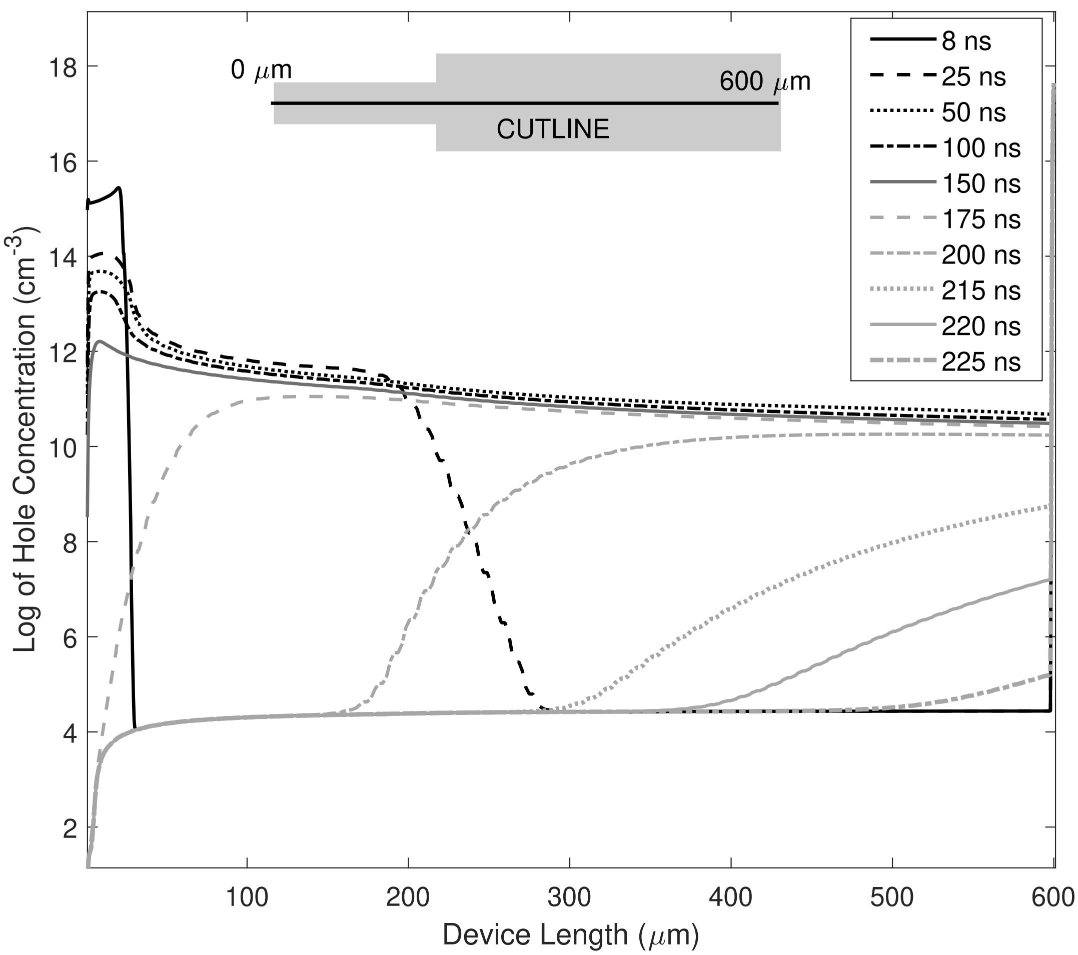

Figure 5.17: *One dimension Models for holes transport for a reverse external bias of* 200 V *plotted along the cutline within the device.*

required to complete the COMSOL model. The boundary conditions present on the trench walls due to Si-SiO_2 interface severely impact device performance. The presence of positive FOC on the Si-SiO_2 interface attracts the *n*-type carriers to the trench wall surface and an inversion layer is created. This population of increased *n*-type carriers further decreases the resistivity of the Si material around the Si-SiO_2 interface, especially inside the fins. It is estimated from the COMSOL simulations that based on the amount of FOC present at the Si-SiO_2 interface, a portion of the fin will not achieve full depletion even at 200 V bias. This effect is shown in Figure 5.18.

The net charge carrier motion within the undepleted regions (represented by purple color in

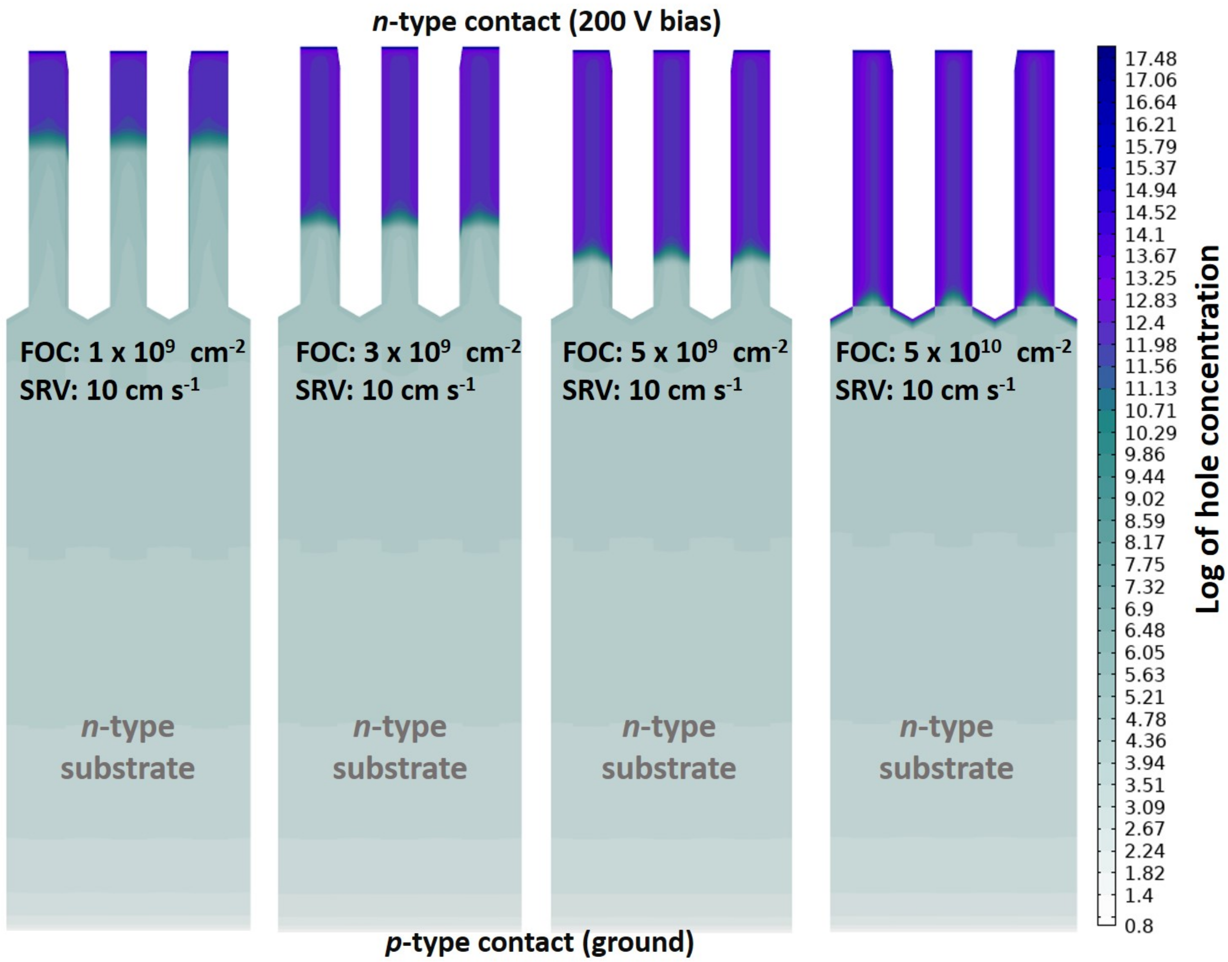

Figure 5.18: *A representation of diode's depletion depth achieved for various FOC values.*

Figure 5.18) will be dominated by diffusion governed by Fick's Law. As per the available literature[53], the expected FOC value is around $5 \times 10^{10}\,\text{cm}^{-2}$. COMSOL simulations were also performed for lower FOC values of 1×10^9 to $5 \times 10^9\,\text{cm}^{-2}$ to understand the effects of FOC on the induced current profiles emerging from the sensor. A cutline was defined at the middle of the modeled MSND diode along the charge carrier injection path. Electric field magnitude was plotted along this cutline to provide information on expected charge cloud behavior within the device. The variation of electric field magnitude inside the device due to variation in the FOC values is presented in Figure 5.19.

It is interesting to note that there is negligible electric field in the portion of the fins that is undepleted due to the presence of FOC on the Si-SiO_2 interface. These undepleted regions vary as

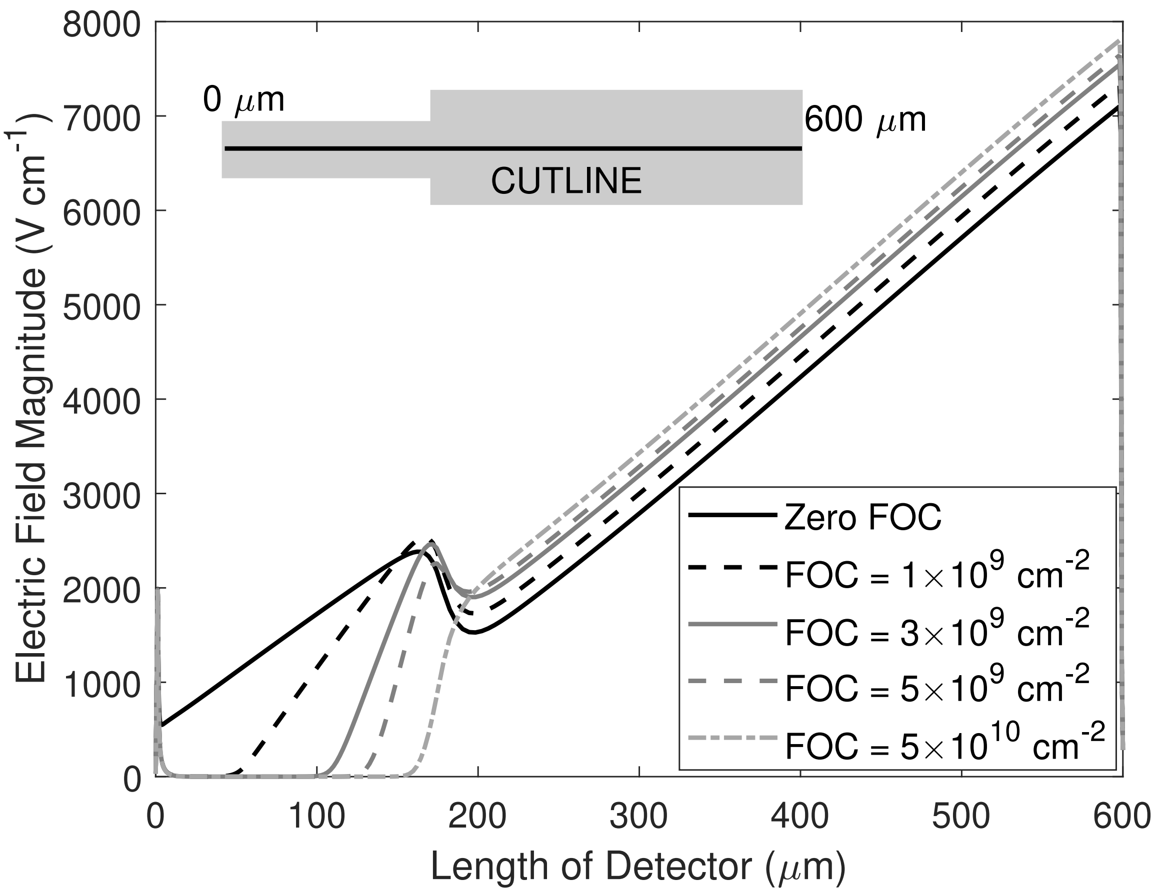

Figure 5.19: *A representation of electric field magnitude plotted along the cutline for various values of FOC in the Si-SiO_2 interface.*

a function of the FOC value and are listed in Table 5.1. Figure 5.19 suggests that the net motion of the charge carriers within the undepleted regions specified in Table 5.1 will be dominated by diffusion, thus making the response of the detector slower with respect to ideal device model, as the undepleted region width increases with the FOC value.

Table 5.1: *Updepleted regions/region with no electric field obtained for various simulated FOC values at* 200 V *reverse bias*

Sl. No.	Simulated FOC Values	Undepleted region
1	$1 \times 10^9\ \text{cm}^{-2}$	48 μm
2	$3 \times 10^9\ \text{cm}^{-2}$	100 μm
3	$5 \times 10^9\ \text{cm}^{-2}$	124 μm
4	$5 \times 10^{10}\ \text{cm}^{-2}$	157 μm

Shockley-Read-Hall's (SRH) Trap Assisted Surface Recombination[100;101] was modeled at the Si-SiO_2 interface with an SRV of $10\,\mathrm{cm\,s^{-1}}$ for both electrons and holes as per details provided in the available literature[102]. The relationship between charge carrier recombination rates ($R_{p/n}$) and the SRVs($v_{s,p/n}$) is provided by Equation 5.4.

$$R_n = R_p = \frac{np - \gamma_n \gamma_p \cdot n_{i,eff}^2}{(n+n_1)/v_{s,p} + (p+p_1)/v_{s,n}} \tag{5.4}$$

In equation 5.4, $n_{i,eff}$, n_1, and p_1 are explained in equations 5.5, 5.6, and 5.7 respectively.

$$n_{i,eff} = \sqrt{N_{c0}N_{v0}} \cdot exp(-\frac{E_g - \Delta E_g}{2V_{th}}) \tag{5.5}$$

$$n_1 = \gamma_n \cdot n_{i,eff} \cdot exp(\frac{\Delta E_t}{V_{th}}) \tag{5.6}$$

$$p_1 = \gamma_p \cdot n_{i,eff} \cdot exp(-\frac{\Delta E_t}{V_{th}}) \tag{5.7}$$

where, n and p are the electron and hole concentrations, respectively. The SRVs for holes and electrons are represented by $v_{s,p}$ and $v_{s,n}$ respectively. The $\gamma_{n/p}$ are the electron and hole degeneracy factors. $N_{c,0}$ and $N_{v,0}$ are the effective densities of states for the conduction and valence band, respectively. E_g is the band gap and ΔE_g is the the band gap narrowing energies scaled by the electron charge q (i.e. SI Unit of V). Value of V_{th} is provided below:

$$V_{th} = \frac{k_B \times T}{q} \tag{5.8}$$

where, k_B is the Boltzmann's constant and T is the temperature. The E_t is the trap energy level scaled by the electron charge with the SI unit of V. The combined SRV and FOC properties at the simulated Si-SiO_2 interface concludes a complete model for the MSND sensor with realistic boundary conditions.

A new experimental setup was prepared to perform detailed alpha-particle irradiation experiments as shown in Figure 5.23. ^{241}Am alpha source (5.48 MeV) was used along with a collimator

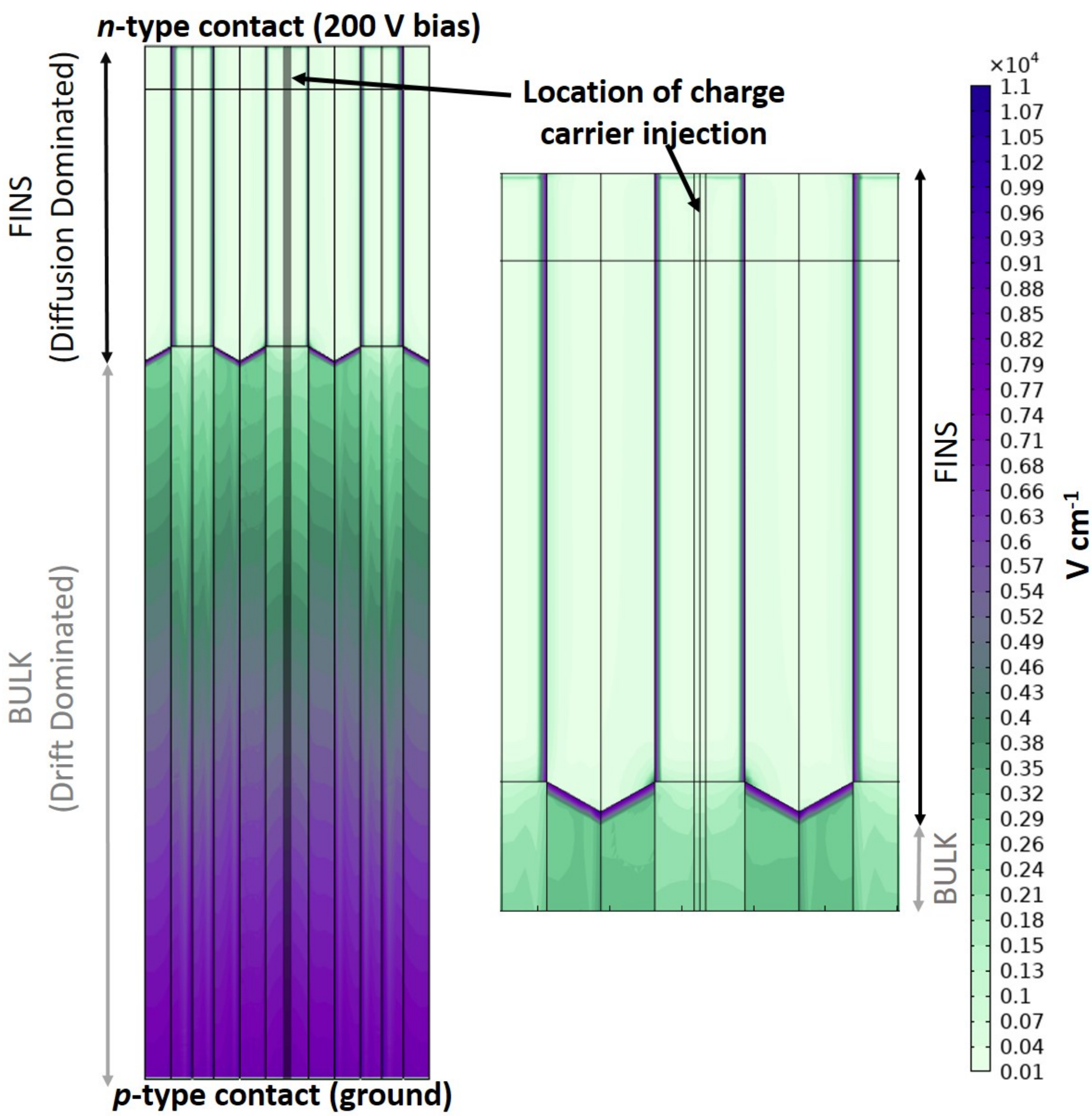

Figure 5.20: *Electric field profile within the MSND sensor at* 200 V *external bias. A zoomed-in view at the left shows an arrow plot obtained by plotting x, y, & z components of the electric field.*

to irradiate the trenches of the prototype MSND sensor. A 142A preamplifier (ORTEC) was utilized to obtain detection event pulses. The data acquisition was performed manually through a 500 MHz mixed domain oscilloscope and a DT5730 CAEN digitizer. A shielded dark box was prepared to contain the entire experimental setup. The goal of this setup was to observe the effects

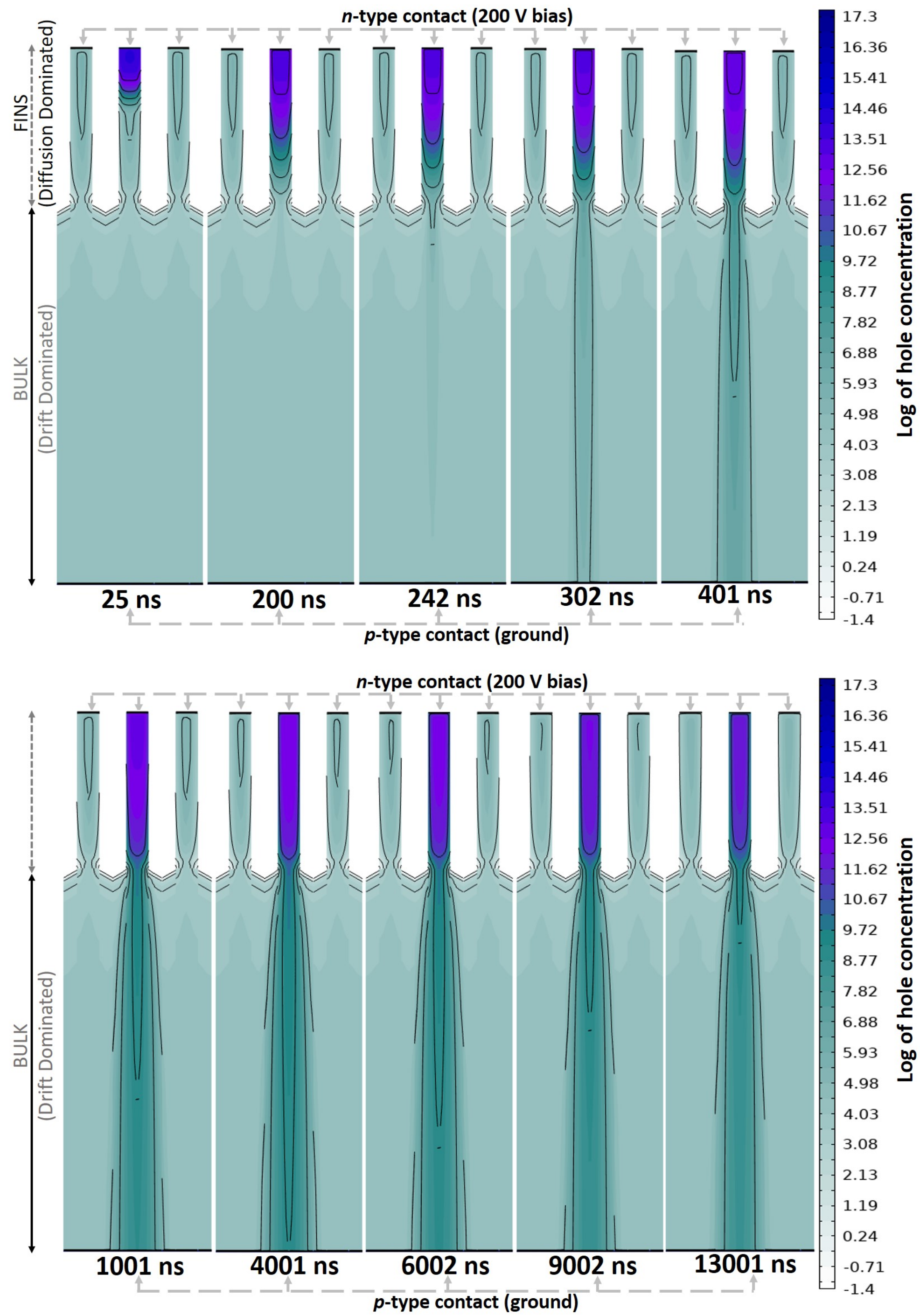

Figure 5.21: *Models for holes transport for a reverse external bias of* 200 V *on a Simulated MSND modeled with the Si-SiO_2 interface boundary condition. The snapshots of transient time-dependent simulations are provided for* 25 ns *to* 13 001 ns

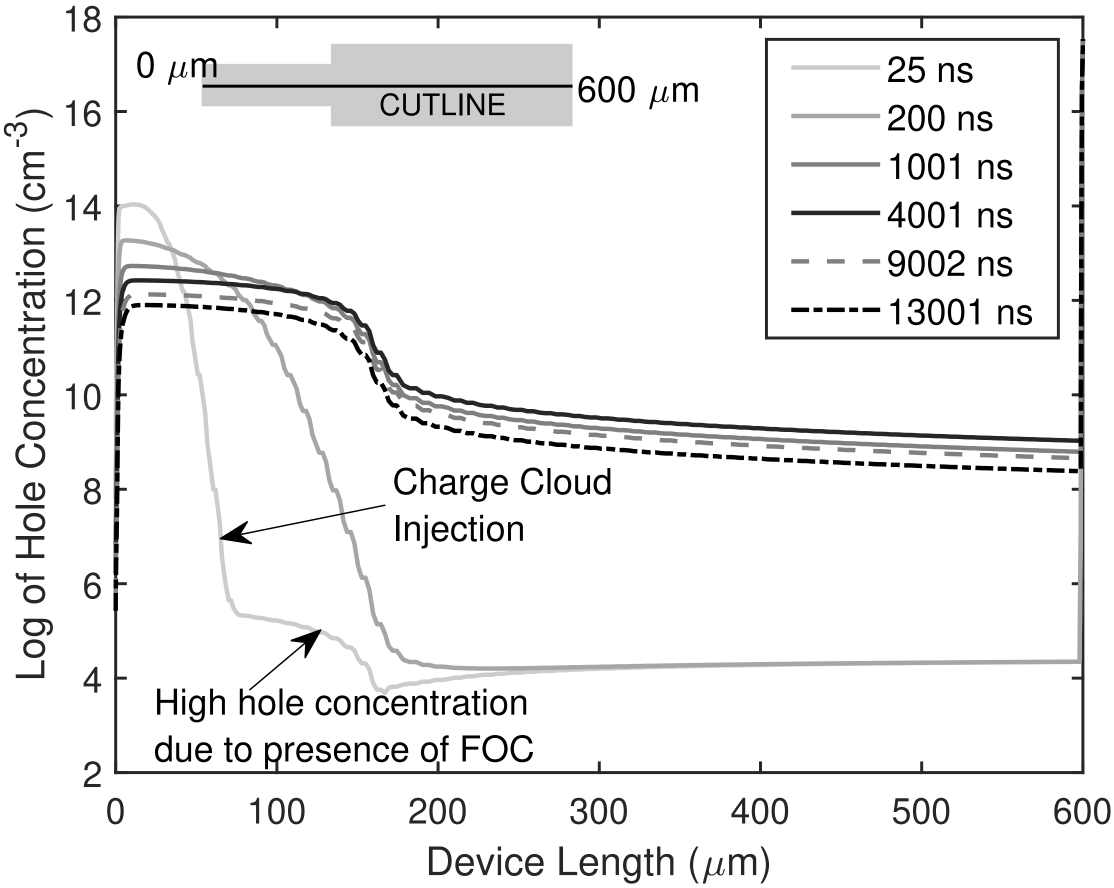

Figure 5.22: *One dimensional simulated holes transport model for a reverse external bias of* 200 V *plotted along the cutline within the MSND device modeled with Si-SiO_2 interface boundary condition.*

of the FOC and SRV at the Si-SiO_2 interface. Irradiations were performed for various reverse bias values of 40 V to 300 V. This ensured that various depletion depths inside the sensor were examined. As per COMSOL calculations, at 200 V, the MSND detector should be completely depleted assuming no negative effects due to Si-SiO_2 interface boundary conditions.

The 142A preamplifier used for these experiments was a charge-sensitive amplifier, designed for use with a room-temperature silicon detector. These preamplifiers are designed to operate over a detector input capacitance range from 0-100 pF. These devices provide an open loop gain of 40000 and a charge sensitivity of 45 mV MeV^{-1}. The collimator ensured that the impinging alpha radiation had a controlled angle of incidence on the MSND diode's trenches.

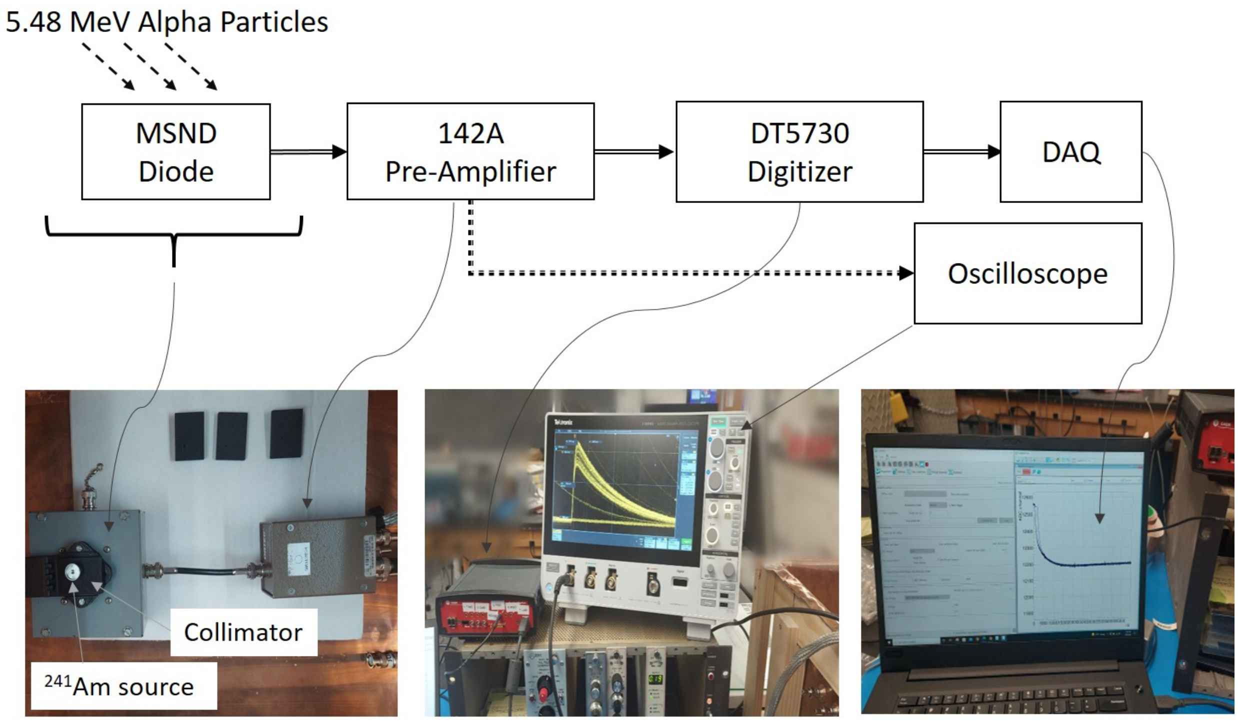

Figure 5.23: *Experimental setup to obtain alpha detection pulses from an MSND sensor.*

To investigate the effects of boundary conditions, preamplifier pulses from interaction events at two different charge injection locations inside the simulated sensor geometry were investigated:

- Location 1: At the top of the fin, i.e., near the *n*-type dopant. Holes will travel largest distance. The charge cloud injected at this location due to an alpha detection event will be most affected by Si-SiO_2 interface boundary conditions. Slower current pulses are expected for this case.

- Location 2: At the bottom of the trench. Holes will travel comparatively smaller distances. The charge cloud injected at this location due to an alpha detection event will be least affected by Si-SiO_2 interface boundary conditions. Faster current pulses are expected for this case.

The rise times (RT) of the preamplifier pulses correspond to the induced current signal duration for the MSND sensor geometry. The decay time of the preamplifier pulses was fixed around 500 µs as specified by the preamplifier manufacturer.

Section Summary

COMSOL Multiphysics software was utilized to perform steady state simulations for designing the implant shapes and sizes for the X-DS-MSND system. Multiple COMSOL Multiphysics simulation results were demonstrated to provide an estimate the junction doping profile, resistivity of the substrate, and peak electric field within the designed sensor. The details presented in this chapter were vital to begin sensor fabrication, experimental analysis, and data acquisition.

Chapter 6

Results and Discussions

This chapter is divided in to three major sections. The first section provides results and discussions for research area 1. The second section provides results and discussions for research area 2. The final section of this chapter provides analysis on how applications and detector designs from research area 2 can be implemented in research area 1.

6.1 Radiation Transport Oil Well Logging Experiments

To simulate the experimental setup for oil well logging bulk irradiation experiment, both Geant4 versions 10.5 and 10.6 were utilized for simulation and modeling. Instead of energy-based particle cuts (i.e., minimum energy below which the particle is killed) like most transport codes, Geant4 employs a default particle range cut-off of 0.7 mm (i.e., particle gets killed if it does not have enough energy to travel 0.7 mm) for both electrons and gamma rays that are produced from non-hadronic interactions like Bremsstrahlung and delta electrons. This value was kept unchanged as variation in this cut-off range had a negligible effect on the simulated results. Geant4 was installed on a high-performance computing system with libraries for both multi-threading and GDML support. Simulation for each sensor was performed for 2.5 billion histories divided equally over five nodes of 20 cores each. The total simulation time to obtain the results was approximately three days. The raw results from Geant4 were later processed in MATLAB[89] to perform Gaussian

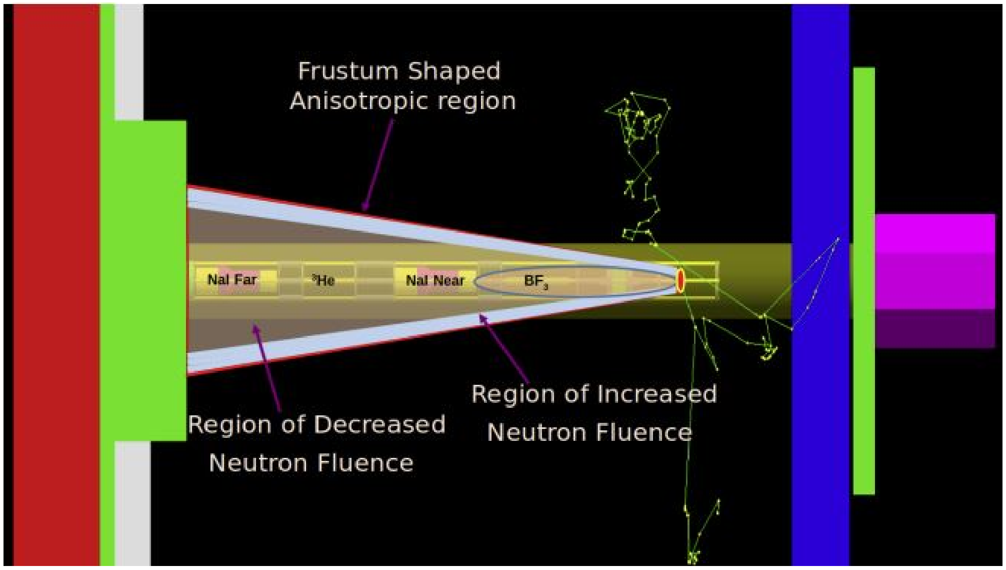

Figure 6.1: *A representation of anisotropy in the output of the D-T generator*

broadening over the entire energy spectrum.

6.1.1 Uncertainty in Source Output

The B-322 neutron generator has a region of anisotropy due to the presence of unknown components (proprietary information) present around the tritium target. As per the guidelines from the manufacturer, this anisotropy accounts for an approximately 15% decrement in D-T generator output along the axis of the generator. Further, there should be an increment of flux around this region as compensation, the distribution of which is unknown. The energy distribution of the emerging neutrons within the frustum and near the source is also unknown. The presence of low energy neutrons due to inelastic scattering from the above-mentioned components could be expected in this region, which could not be accounted for in the Monte Carlo simulations. The outer structure of the neutron generator also gives secondary gamma-ray emissions, which are also unknown and are unaccounted for in the Geant4 simulations.

6.1.2 Comparison of Simulated Results

List mode data provided the capability to select the data only when the neutron generator pulse was ON. In the past, efforts had been made to compare MCNP simulation with the data accumulated for only pulse *ON* segments of the time spectrum[103]. Although this gave acceptable results, around 90% of the generated data that included delayed gamma emission from various radionuclides were ignored. For the work presented, simulations were performed in Geant4, which addresses activation and subsequent processes by default. Geant4 utilizes *G4RadioactiveDecay()* for estimation of activation from neutron interaction. Hence, the integral spectrum that was collected from the radiation sensors for the entire 3600 s of bulk material irradiation was utilized for the comparison with the simulated data from Geant4.

The spectra obtained from simulations were in counts per simulated source particle and were scaled with a constant to match the 2.2 MeV hydrogen peak in background-subtracted and non-linearity corrected experimental spectra of the NaI Near sensor for both sand and water experiments. These constants are considered as an approximation of neutron output over a period of 3600 s. Preliminary simulations were performed with only a model of NaI(Tl) crystal instead of the whole NaI detection assembly. In the improved optimized Geant4 model, the NaI crystal was modeled along with its external components as shown in Figure 3.8, and both source and sensor locations were updated, along with cross-sections and testing materials. Energy spectra from the NaI sensors for the Preliminary model and the Optimized model are plotted in Figure 6.2. Here, it is shown that between 0-2 MeV, the optimized model fits the peak at 0.5 MeV much better. This is largely due to a 3 mm thick Pyrex^{TM} glass PMT tube model that contained approximately 4% boron by weight. An improvement in the continuum below 2 MeV is also observed, mostly due to the inclusion of the oxide layer, aluminum casing, and magnetic/light shield models in the simulations. Although bialkali dynodes were also modeled, contributions due to these structures were almost negligible due to the thickness of these being in the range of 300 nm. It is also noted from Figure 6.2 that the optimized model improves the fit for 2.2 MeV hydrogen peak. The optimized model further improves the overall fit for the spectrum up to 6 MeV. Due to the low efficiency of NaI(Tl) crystals for high energy gamma rays, a drastic decrement in counts is observed after

6 MeV. A model similar to the unoptimized Geant4 model was implemented in MCNP[104] and corresponding results are shown in Figure 6.3. Except for the peak at 0.5 MeV, almost every feature is similar in the lower energy part (< 6.1 MeV) of the comparison. As external sensor components (e.g., Pyrex™ PMT) are not present in the MCNP model, the peak at 0.5 MeV is mostly missing in MCNP spectra. This consistency in results with different transport codes further demonstrates that the neutron cross-sections and the CAD model import methods deployed in the Geant4 are appropriate for these simulations.

Comparison of Gamma Spectrometer Results

A comparison of experimental NaI spectra and scaled Geant4 NaI spectra for the water experiment is provided in Figure 6.4. All important spectral features that are present in the experimental spectra for both NaI Near and NaI Far sensors are also present in the simulated spectrum. In the region of 0-1.8 MeV, there is slight disagreement in the spectral counts where the Geant4 simulations underestimate measurement. Proper modeling of all the minor internal metal components and printed circuit boards of the NaI sensor would likely improve agreement as shown in Figure 6.2. Further, the entire NaI Far sensor simulated spectrum overestimates the count rates as compared to the experimental spectrum due to the reasons mentioned in Section 6.1.1. Here, it is hypothesized that the bulk material inside the anisotropic frustum around the NaI Far sensor is getting irradiated less from source neutrons as compared to the simulation case where the source is ideally isotropic and mono-energetic.

Similar attempts were made to benchmark the experimental NaI spectra and scaled Geant4 NaI spectra for the sand experiment as shown in Figure 6.5. In this case also, every important spectral feature that was present in the experimental spectra was also observed in the simulated spectra for both NaI Near and NaI Far sensors. For the sand results, the region of 0-1.8 MeV where a slight disagreement between the spectral counts for both simulations and measurements is observed. This could also be mitigated by proper modeling of all the minor internal metal components and printed circuit boards of the NaI sensor as mentioned in the above paragraph. It is important to note that in this case, the NaI Far sensor data show minor disagreement as seen in the case of water. This is due to the scattering nature of the sand which compensates for the anisotropic effects observed around the NaI Far sensor, that were observed in the case of water.

Table 6.1: *Analysis of neutron sensor experimental results from the sand experiment*

Time	Irradiation Number	Sensor	Geant4 Calculated Counts (C)	Experimental Counts (E)	Relative Difference in E (%)	Dead Time (%)	C/E
Day 1	1	^{3}He	821,508	675,267	1.51	2.31	1.22
Day 3	2			661,004		3.02	1.24
Day 1	1	BF_3	3,309,354	2,128,828	1.05	1.68	1.55
Day 3	2			2,097,314		1.65	1.58

Table 6.2: *Analysis of neutron sensor experimental results from the water experiment*

Time	Irradiation Number	Sensor	Geant4 Calculated Counts (C)	Experimental Counts (E)	Relative Difference in E (%)	Dead Time (%)	C/E
Day 1	1	^{3}He	301,888	289,130	1.17	12.05	1.04
Day 2	2			292,191		9.63	1.03
Day 3	3			285,439		12.96	1.06
Day 1	1	BF_3	1,638,842	2,748,238	1.83	9.98	0.59
Day 2	2			2,699,969		13.09	0.61
Day 3	3			2,683,524		12.14	0.61

Comparison of Neutron Sensor Results

Comparisons of experimental and simulated counts generated in the neutron sensors for sand and water experiments are presented in Table 6.1 and Table 6.2, respectively. The counts per neutron source in each of these cases were scaled with the same scaling factor used to scale NaI spectra for both sand and water. Since the thermal neutron population decreases as the sensor location moves further away from the neutron source, the BF_3 sensor registers a higher number of counts as compared to the ^{3}He sensor. In Table 6.1, analysis of two irradiations for sand is presented. There was a one day gap between the irradiations and fluctuation of 1.51% and 1.05% was observed in both ^{3}He and BF_3 experimental data respectively. Acceptable deadtime of 2.31-3.02% and 1.65-1.68% was also observed for ^{3}He and BF_3 experimental data respectively. Further, a comparison of scaled Geant4 counts and experimental data for the ^{3}He and BF_3 sensors is shown in Table 6.1. It was observed that Geant4 results overestimate the ^{3}He (Far) and BF_3 (Near) experimental results by 22-24% and 55-58% respectively, which suggests that the effect of anisotropy of the source is more severe at the BF_3 sensor location which is closer to the neutron source. Furthermore, the streaming of neutrons due to the porous nature of the sand is also not modeled in the Geant4 simulations. These effects diminish as the sensor moves farther away from the neutron source, i.e. at the ^{3}He sensor location.

Table 6.2 shows an analysis of three irradiations for water. Each irradiation was performed on consecutive days, and a fluctuation of 1.17% and 1.83% was observed in both ^{3}He and BF_3 experimental data respectively. An increase in deadtime was observed in the water experiments as compared to the sand experiments. For ^{3}He sensor the deadtime varied from 9.63% to 12.96%, while the deadtime for BF_3 sensor was observed to be between 9.98% to 13.09%. Further, a comparison of scaled Geant4 counts and experimental data for both ^{3}He and BF_3 sensors were performed and presented in Table 6.2. It was observed that Geant4 overestimates the ^{3}He (Far) experimental results by only 4-6% and has excellent agreement with the experimental data. However, the simulated data for BF_3 (Near) sensor underestimates the experimental data by 39-41%. This is consistent with the fact that the effect of anisotropy of the source is more severe at BF_3 sensor location nearer to the D-T neutron source. This high dead time in BF_3 and ^{3}He justifies a need to investigate a need for a replacement solid state sensor.

6.1.3 Error Analysis in Simulations

As the counts generated in the sensors are of rare events, all the detection events are independent, and the average rate of counts does not change over the period of irradiation. Relative Errors (R.E.) in simulated results were calculated considering Poisson Distribution as shown in Equation 1.

$$R.E.(\%) = \frac{\sqrt{(C_B)||(G)}}{(C_B)||(G)} \times 100 \tag{6.1}$$

In equation 1, C_B is counts/bin and G is gross counts. Here, $||$ represents that this equation can be applied to either C_B or G. Relative error per bin in calculated gamma spectra from Geant4 is represented in Figure 6.6, due to the higher number of counts, the spectra obtained from NaI

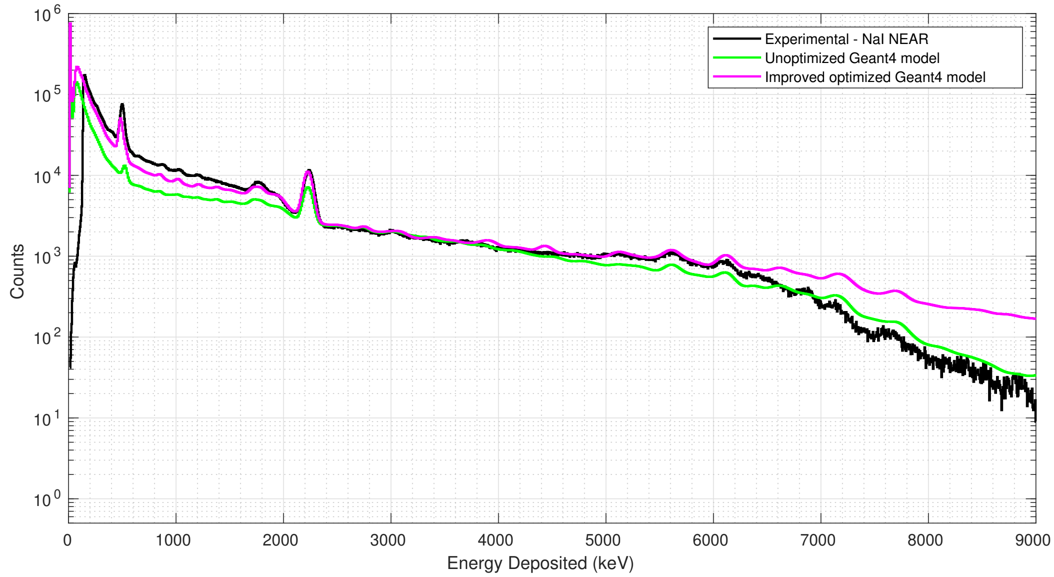

Figure 6.2: *Optimization of Geant4 results. Unoptimized Geant4 model consists of only active region of the NaI sensors. Optimized Geant4 model includes all the realistic components of the NaI detector, for e.g. PMT tube, light shield, oxide layer, etc.*

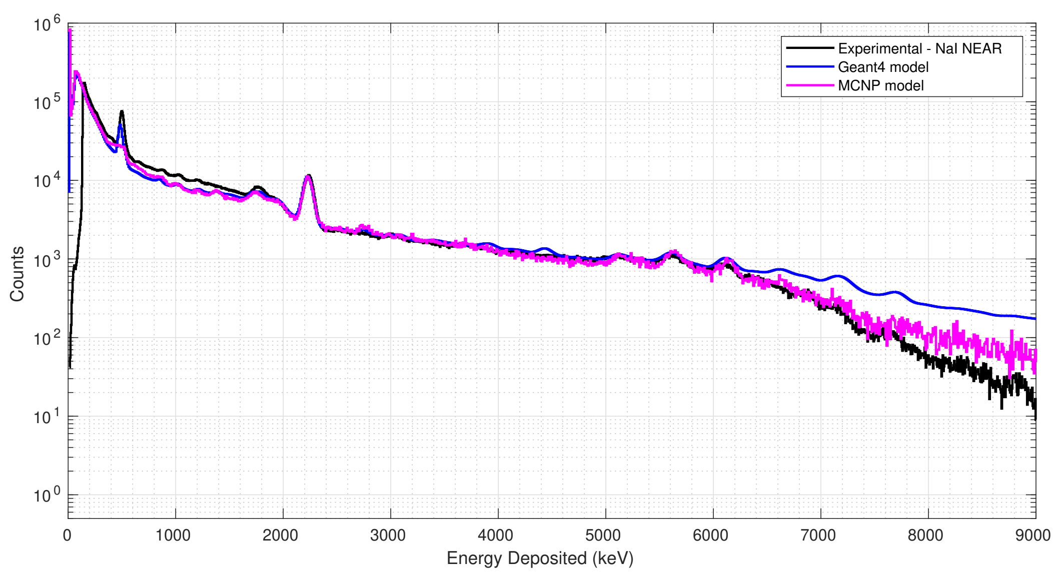

Figure 6.3: *Comparison of MCNP and Optimized Geant4 results.*

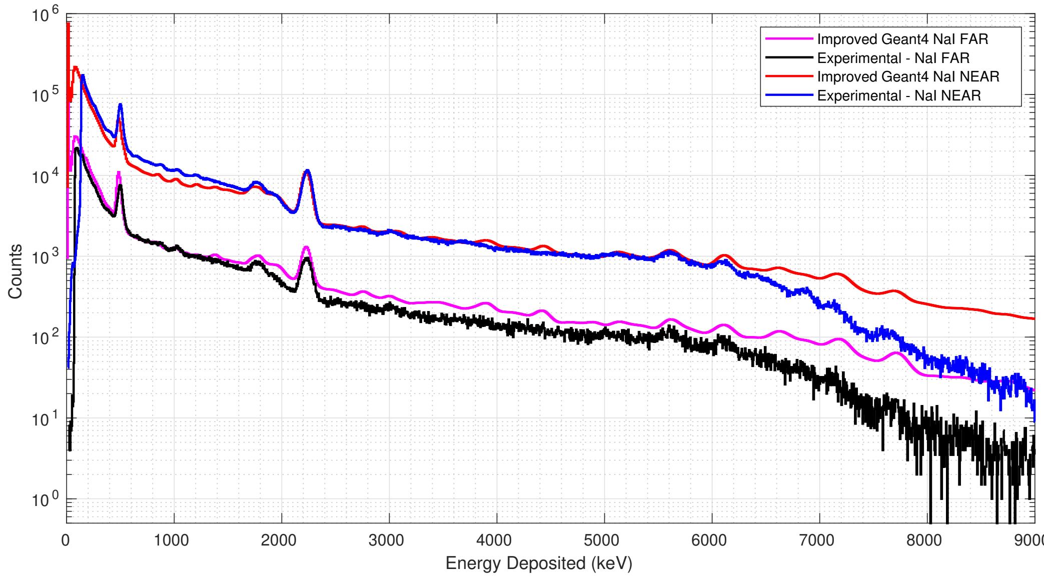

Figure 6.4: *Comparison of Geant4 and experimental results of NaI sensors with water as a testing material*

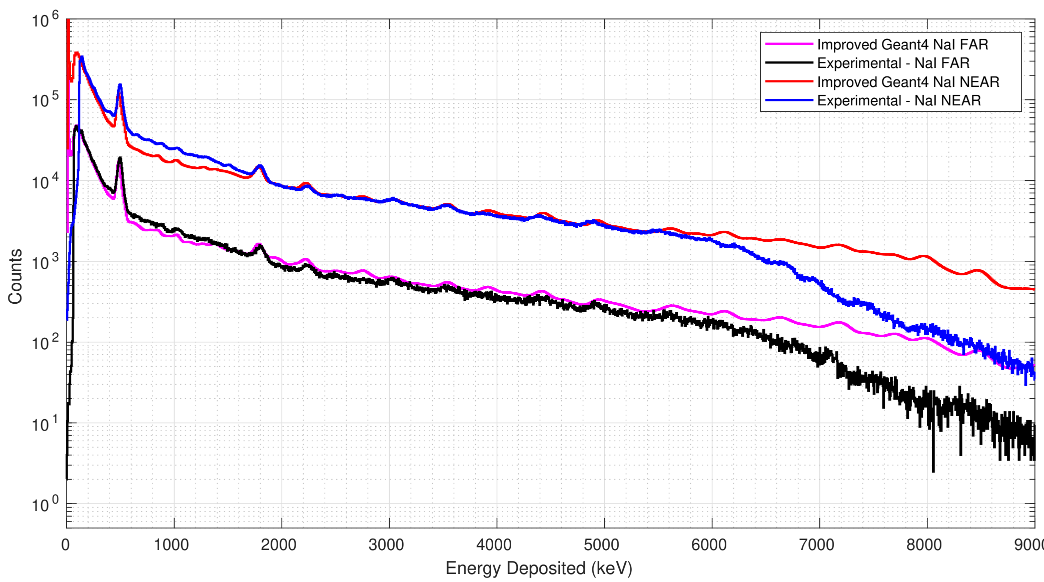

Figure 6.5: *Comparison of Geant4 and experimental results of NaI sensors with sand as a testing material*

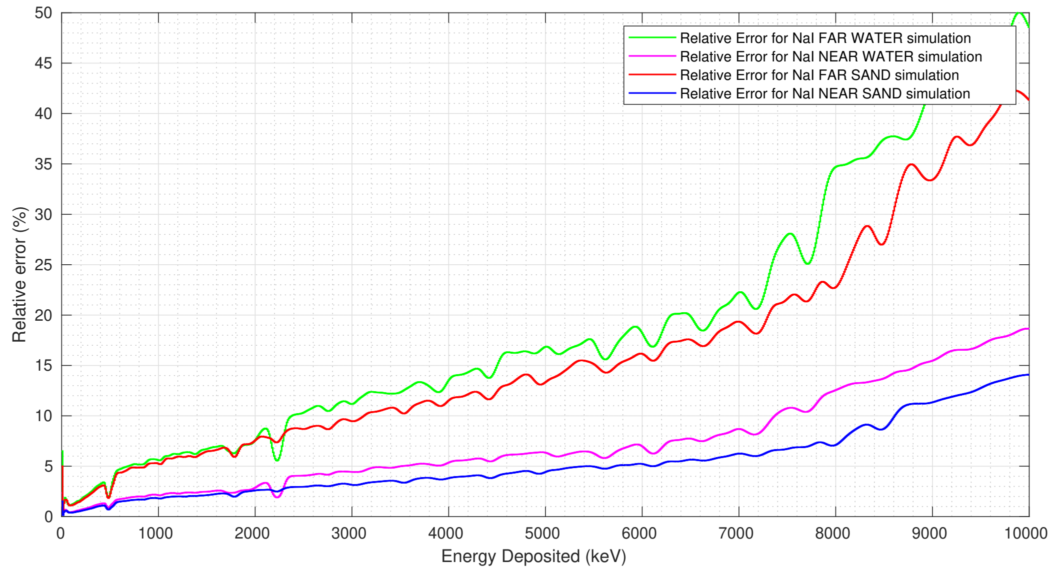

Figure 6.6: *Relative error calculated for Gamma spectra obtained from Geant4 simulations*

Near sensor for both sand and water irradiation have a lower relative error as compared to NaI Far sensors. For the NaI Far sensor, less than 15% relative error is observed at energies less than 5-6 MeV; error increases from this point to approximately around 45%. Similarly, results for NaI Near sensors are mostly reliable at energies less than 8-9 MeV. The normalized spectra were scaled with a constant that represented total neutron output for that experiment.

For the sand experiment, the neutron and gamma sensors were scaled with 1.4438×10^{10} neutrons. Hence, for sand irradiation, the neutron output was estimated by this number for a duration of one hour. In Table 6.1 the C/E value for ^{3}He is around 1.24. Similarly, for BF_3 the C/E number is around 1.55. This variation is due to the following reasons:

- The anisotropic region of the source as mentioned in Section 6.1.2.
- The density of sand is not likely to be constant throughout the large irradiated volume.
- The porous nature of the sand is not accounted for in the simulations.
- Impurities in the sand were not accounted for in the simulations.

Further, for NaI Near and NaI Far sensors, the scaling factor works very well and all the features in the experimental gamma spectrum are visible in the simulation results. This also suggests that the anisotropy of the neutron source does not have much effect on the gamma sensor results in a high scattering and low absorption medium like sand. Minor variations in the spectrum are possibly due to unaccounted chemical impurities and porosity of the medium in the simulations.

Similarly, for the water experiment, the neutron and gamma sensors were scaled with 1.0062 $\times 10^{10}$ neutrons. In Table 6.2 the C/E value for ^{3}He is around 1.05 and BF_3 is around 0.60. This suggests that:

- ^{3}He simulated results exhibit excellent agreement with the experimental data.
- The high uncertainty in C and E values for the BF_3 sensor is due to the sensor's proximity with the neutron generator.

Further, for NaI Near and NaI Far sensors, the scaling factor selected this way does not work well in an absorbing medium like water. However, all the features in the experimental gamma spectrum are visible in simulation results as well. This suggests that the effects of source anisotropy are more prominent in water.

The results presented in this section successfully demonstrate the superiority of methods developed to simulate complex CAD models in Geant4. The results obtained by these advanced methods provide better results than MCNP. Thus Geant4 was used to perform future studies related to solid state detector development as already described in Section 3.7.

6.2 Sensor Response Simulation and Analysis

6.2.1 Electric Field Calculations

Fast signal read-out requires the presence of strong electric field that can be achieved from a depletion region of a semiconductor diode. An estimation of the bias (V) at which a doped semiconductor planar diode fully depletes is given by Equation 6.2.

$$V = \frac{w^2 q N_d}{2\varepsilon} \tag{6.2}$$

where, w is sensor width (600 µm), N_d is background electron concentration ($8.9163 \times 10^{17}\,\mathrm{m}^{-3}$), q is the elementary charge ($1.6022 \times 10^{-19}\,\mathrm{C}$), ε is the electric permittivity ($(11.7) \times (8.854 \times 10^{-12}\,\mathrm{F\,m}^{-1})$). This formulation indicates that 248 V reverse bias is needed for a full planar device depletion. An MSND and a planar sensor model was prepared in COMSOL with a charge carrier life time of 1 ms and similar doping profiles. It was observed that a full MSND device depletion can be achieved at 200 V as presented in Figure 6.7. This is due to the presence of higher electric field magnitude as compared to a planar device in the fin structure of the diode as represented in Figure 6.8.

Boundary conditions representing FOC were implemented at the Si-SiO_2 interface. This was done by defining a surface charge density of $8.01 \times 10^{-5}\,\mathrm{C\,m}^{-2}$, equivalent to 5×10^{10} q cm^{-2}. SRH Trap Assisted Surface Recombination was modeled at the Si-SiO_2 interface with a SRV of $10\,\mathrm{cm\,s}^{-1}$ for both electrons and holes.

The presence of positive FOC on the trench walls attract *n*-type carriers, thus forming an *n*-type region that decreases the resistivity of the substrate of this region significantly and increases the reverse bias required to deplete the device as exhibited in Figure 6.7. It can further be noted from Figure 6.8 that the presence of FOC drastically reduces the electric field in the fins, causing charge transport in these regions to be dominated by diffusion. In a radiation detection event where all energy is deposited at the top of the fin, the formation of induced current is dominated by the downward motion of holes. Thus, a much slower detector response is expected due to the presence of FOC.

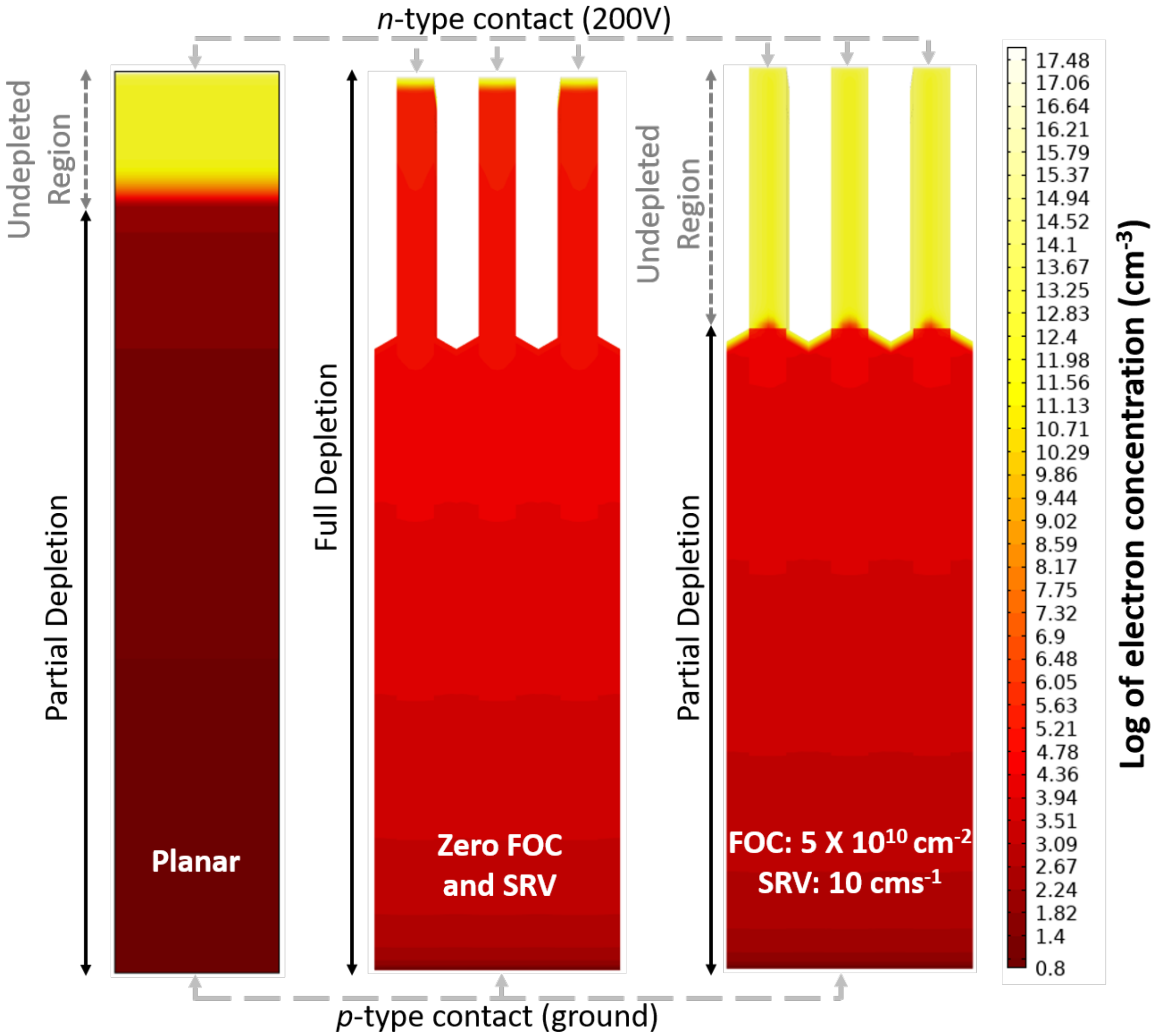

Figure 6.7: *Comparison of log of electron concentration at* 200 V *reverse bias for a planar diode (left), an MSND diode with zero FOC & SRV (middle), and an MSND diode with FOC* $= 5 \times 10^{10}\,\mathrm{cm}^{-2}$ *& SRV* $= 10\,\mathrm{cm\,s}^{-1}$ *(right).*

The accumulation layer due to FOC on the Si-SiO_2 interface counters the electric field generated by external bias (Figure 5.20). For the diode configuration investigated here, the holes will propagate towards the bottom electrode being repelled from the positively charged trench walls, preventing loss of holes in the interface oxide traps. However, once the charge carriers diffuse towards the bottom of the fin, the presence of strong electric field in the bulk will ensure that the holes drift and are collected in the bottom electrode. Since most of the energy deposited will be in

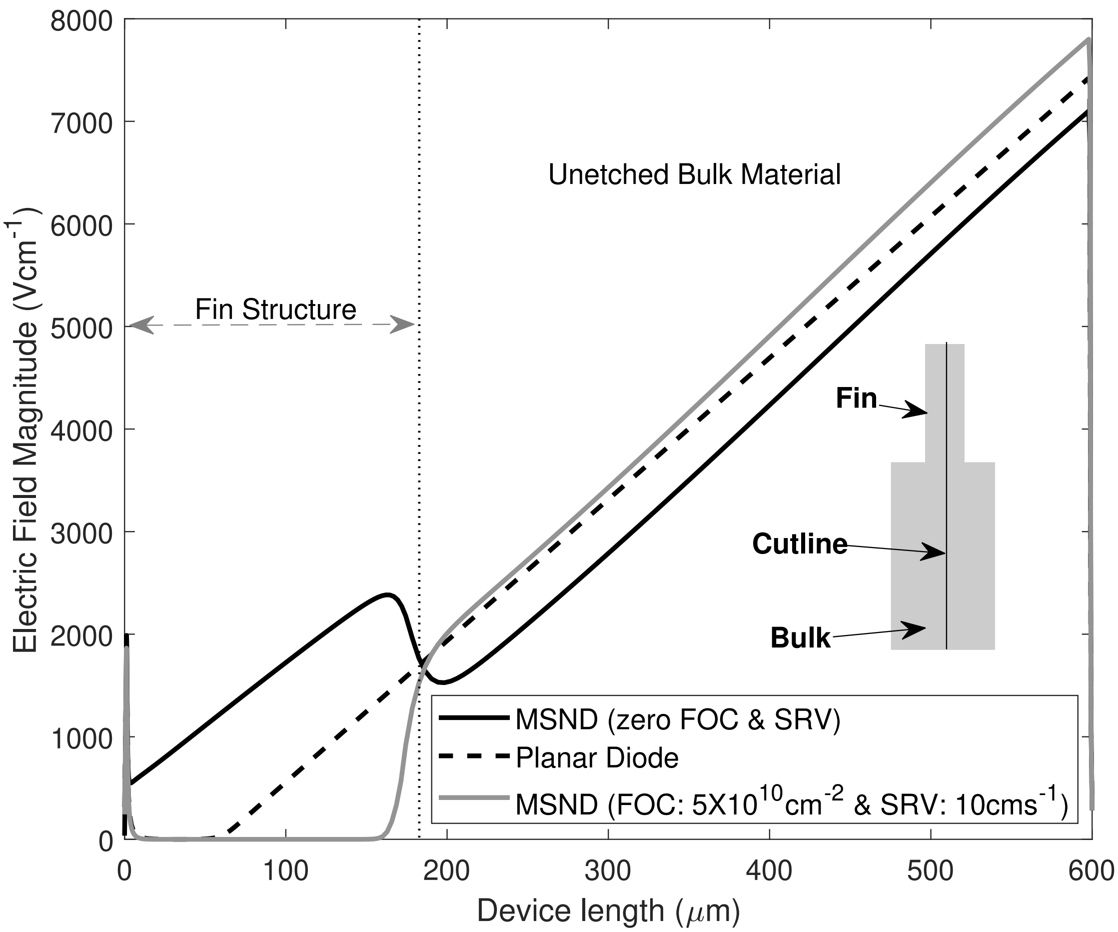

Figure 6.8: *Calculated electric field magnitude plotted along the cutline (shown in the figure) at a* 200 V *reverse bias for a planar diode and an MSND diode (with zero FOC & SRV, and with FOC* = 5×10^{10} cm^{-2} *& SRV* = 10 cm s^{-1}*).*

the top region of the sensor, holes will travel a greater distance than electrons and will dominate the induced current. Thus it is vital to maintain peak doping profiles to preserve charge collection efficiency of the sensor. Electrons, on the other hand, will be attracted towards the Si-SiO_2 interface due to positive FOC and may fall in the oxide interface traps. However, since electrons propagate a much shorter distance and toward the region of decreasing weighting potential, the impact of electron motion is essentially negligible.

6.2.2 CV Plot Calculations

In a simple MOSCAP (metal oxide semiconductor capacitor) device, the metal layer on the device is considered as one plate of the capacitor, and silicon dioxide in between is the insulator. Further, the majority charge carriers in the substrate is considered as the other plate of the capacitor. The capacitance (C), is determined as in Equation 6.3.

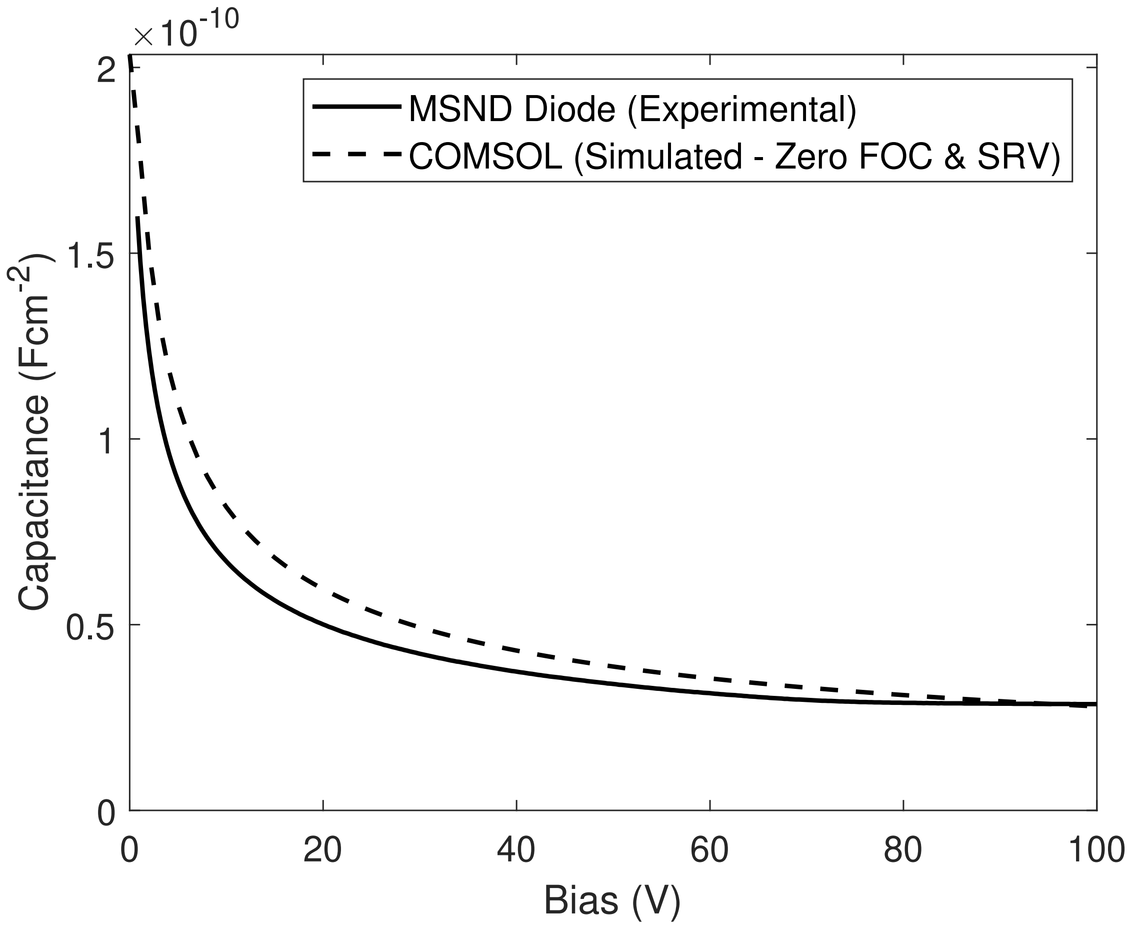

Figure 6.9: *A comparison of simulated and experimental CV curve data for an MSND diode. The y-axis is normalized for plate area to compare simulated and experimental results.*

$$C = A(\frac{k}{d}) \tag{6.3}$$

where A is the area of the capacitor, k is the dielectric constant of the oxide, and d is the separation distance between two plates of capacitor. Therefore, large values of A and k will result in

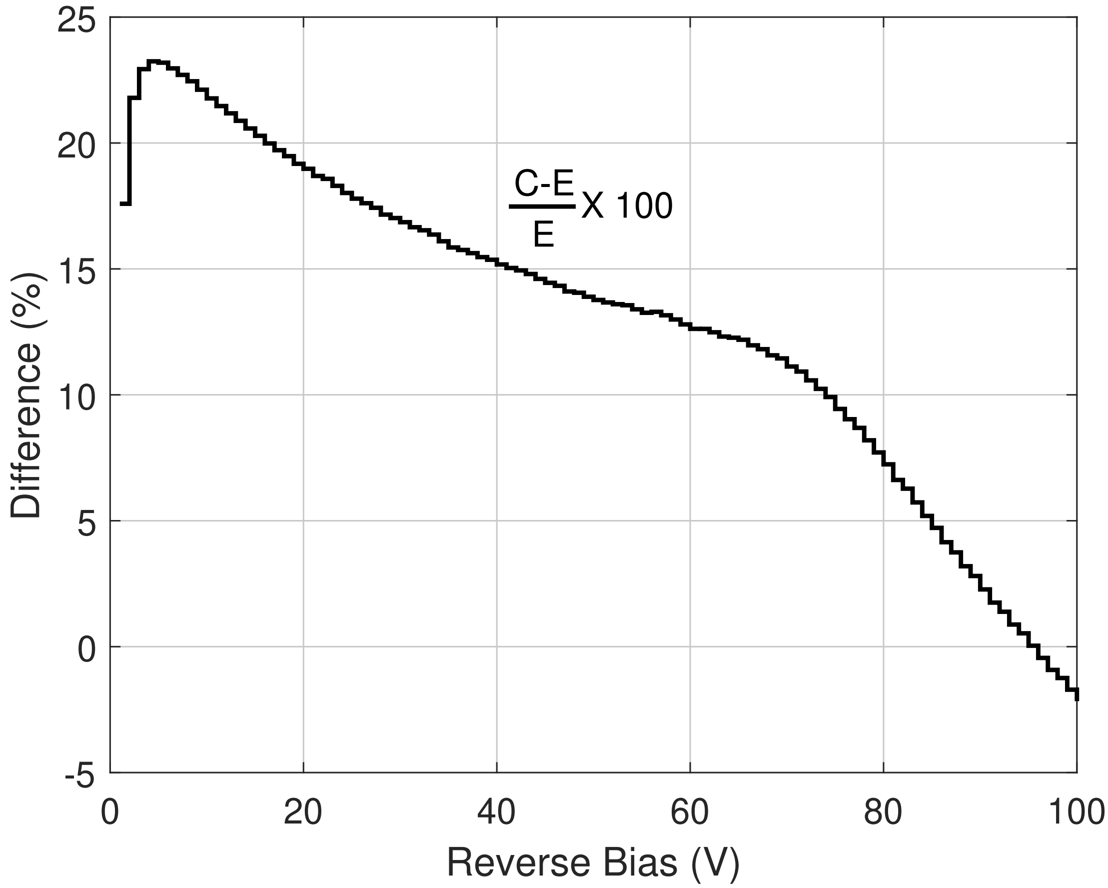

Figure 6.10: *A plot demonstrating increment in the capacitance values observed in simulated (C) values as compared to the experimental values (E).*

greater capacitance. However, for p-i-n type devices, as the reverse bias is increased, the device will deplete and the separation between the two plates d will increase, causing a decrease in the capacitance. For a radiation detector, the ability to deplete is one of the most importance properties for optimum device operation. Typically, the semiconductor detector capacitance values range from nanofarads to picofarads. Since CV measurements are actually made at Alternating Current (AC) frequencies, the capacitance for the diode is calculated with Equation 6.4.

$$C_D = \frac{I}{2\pi f V} \tag{6.4}$$

In Equation 6.4, I is the magnitude of the small AC signal through the diode, f is the frequency of the small signal, and V is the magnitude and phase angle of the measured AC voltage. The CV measurement test measures the AC impedance of the diode by applying an AC voltage and measuring the resulting AC current, AC voltage, and phase angle of the impedance between them.

Simulations show that at least 120 V reverse bias is needed for the depletion region to reach the bottom of the fins as represented in Figure 6.11. Since the equipment used in this measurement has an upper limit of 100 V reverse bias, the results obtained provided information on the depletion characteristics of the diode in the bulk region. A small signal analysis method was utilized in COMSOL to model the experimental setup and obtain the simulated CV curve result for comparison. A Harmonic Perturbation node was added to the top metal contact of the modeled diode to apply an AC signal of 30 mV. Further, a Frequency Domain Perturbation node was added in the stationary study to add a 100 MHz frequency to the small AC signal. The simulation included a 1 V per iteration step auxiliary bias sweep up to 100 V reverse bias on the top metal contact of the modeled sensor.

The simulated (C) result is presented in Figure 6.9, which agrees with the experimental (E) CV plot results, confirming that the FOC on the Si-SiO_2 trench interface has minimal impact on the depletion rate of the bulk region of the MSND diode. During post processing, the calculated capacitance from COMSOL was normalized with the simulated metal plate area, as the simulated device size and the experimental device size are different. The experimental results presented in Figure 6.9 are also normalized with the actual measured metal plate area to perform accurate benchmark of the measured data. Around 20% overestimation of capacitance values at very low reverse bias are expected from device edge effects that were not present in the simulated geometry that basically consisted only a central section of the device. This difference decreases rapidly as the reverse bias is increased and the depletion region reaches deep inside the bulk material. As the depletion region approaches the bottom of the trenches at around 95 V reverse bias, COMSOL starts underestimating the capacitance values, because the COMSOL simulated model does not have FOC conditions implemented and keeps on depleting the diode, while in an actual diode the depletion rate becomes slower due to the presence of FOC on the Si-SiO_2 interface.

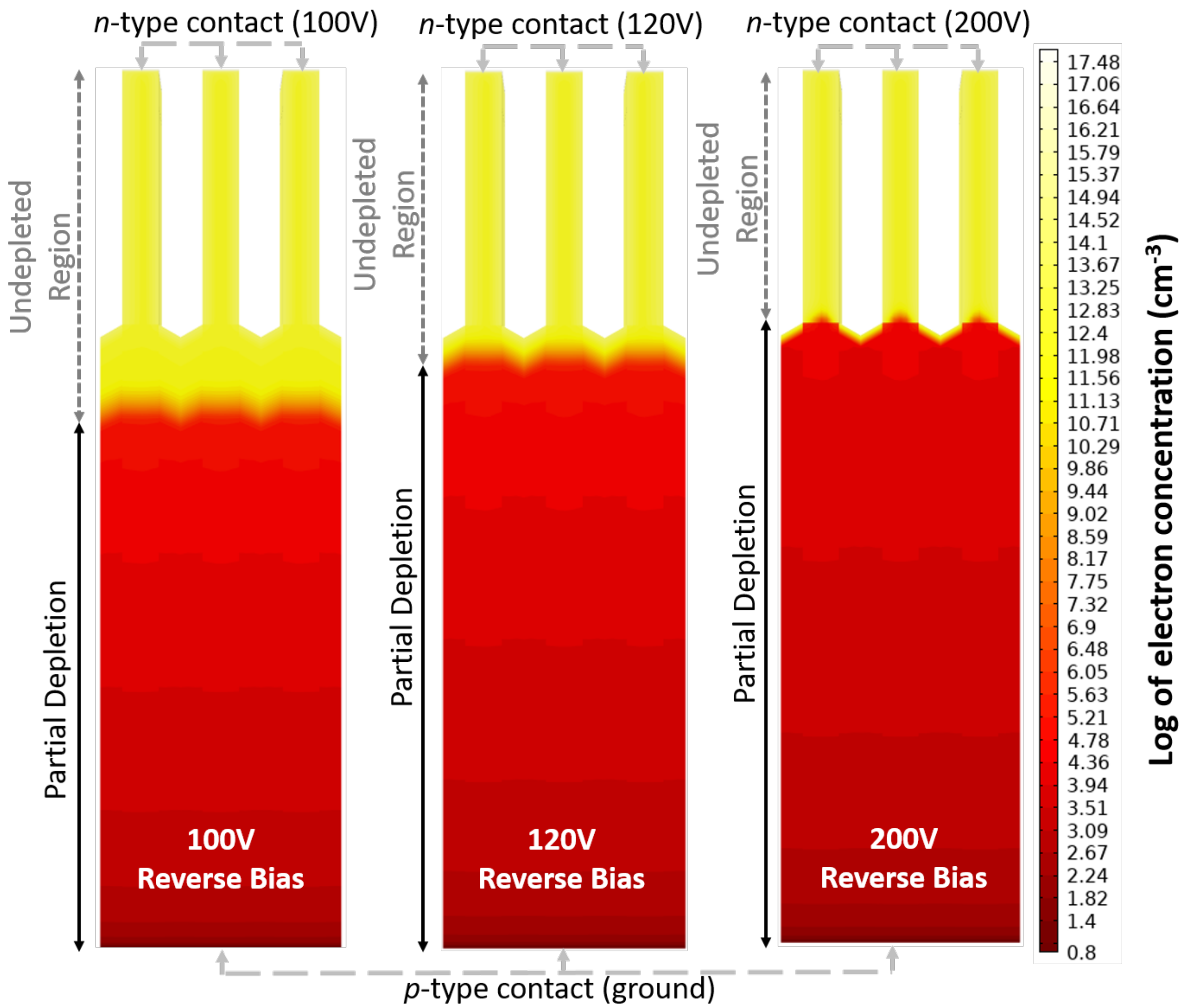

Figure 6.11: *A plot of log of electron concentration representing the depletion region widths achieved at* 100 V, 120 V, *and* 200 V *external reverse bias.*

6.2.3 Spectral Data Calculations

A detailed representation of the simulated geometry is presented in Figure 5.7. A 3 mm radius disk shaped ^{241}Am source was simulated and 5 million decay events provided provided good results with acceptable statistics. To efficiently simulate the decay in Geant4, the Radioactive Decay Module was used. Further, a controlled nuclei decay was needed to be simulated for eliminating unwanted decays, so the *grdm* module was used to simulate a controlled decay scheme. All the detector features were incorporated sequentially and the spectral features were analyzed for each of these cases. The purpose of these simulations was to explain the cause of the three peaks in experimental alpha spectrum from the MSND diode as shown in Figure 6.12. The final simulation incorporated all the physical features of the detector as shown in Figure 5.7 and the resultant output is represented in Figure 6.13.

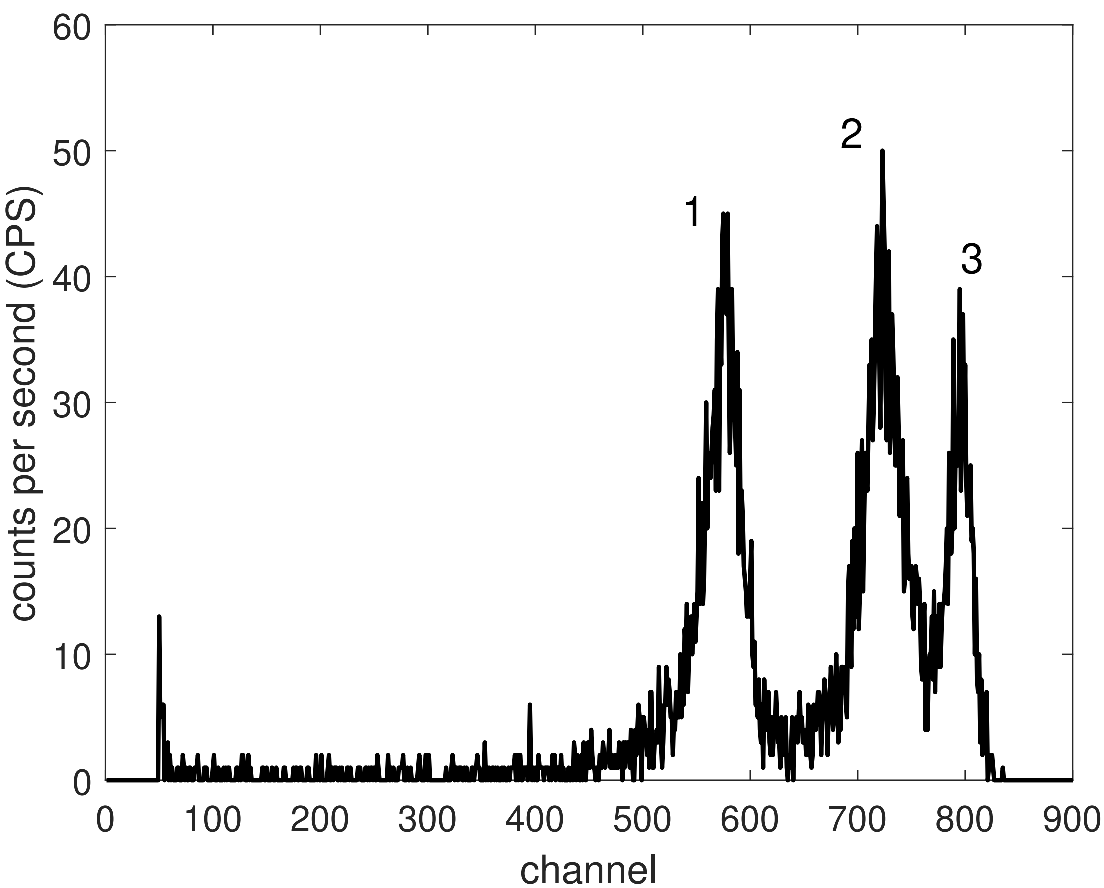

Figure 6.12: *Experimental spectral data obtained from the alpha irradiation of the fabricated MSND detector.*

Multiple simulations with different physical parameters provide sufficient evidence to conclude that in Figures 6.12 and 6.13:

- Peak 1 at 4.1 MeV originates from the alpha particles that deposit energy in the top part of the Si fin after losing energy in air, the oxide layer, and then the dead layer of the MSND sensor. This section of the geometry is represented in Figure 6.14.

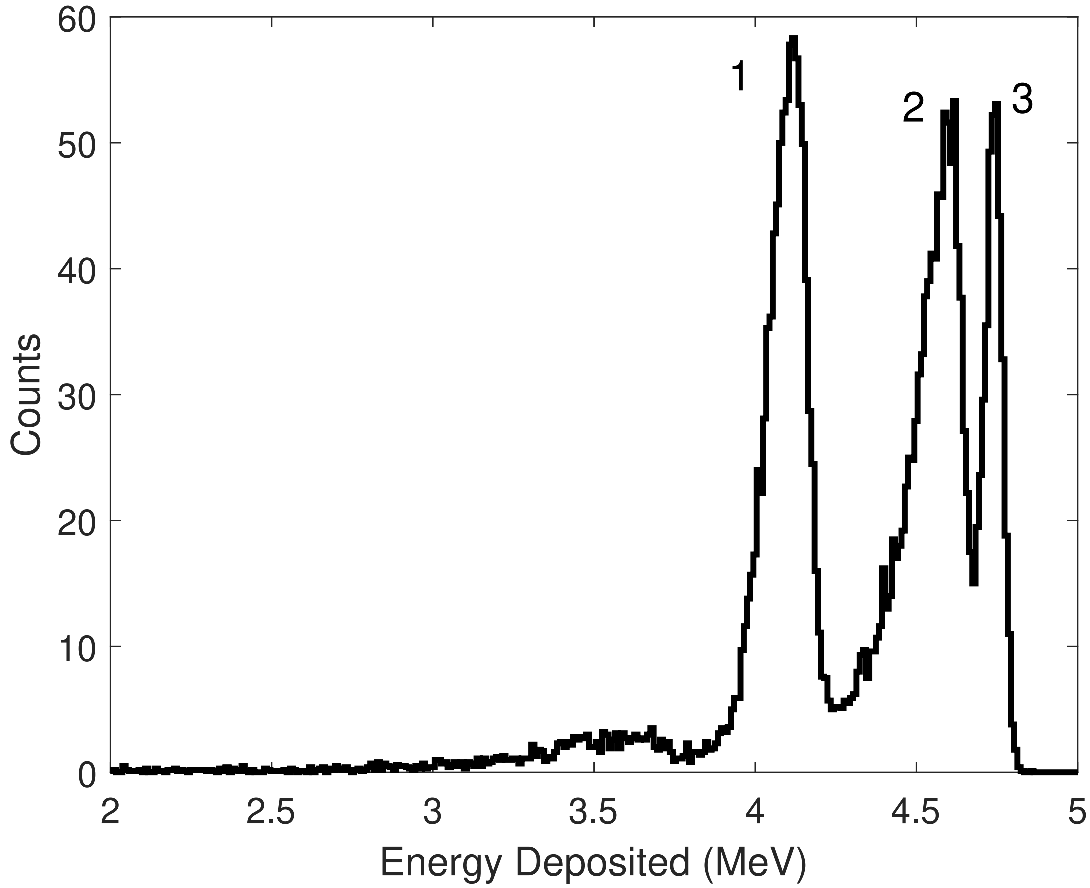

Figure 6.13: *Particle energy deposition in the MSND device's active volume from simulating the alpha irradiation experiment in Geant4.*

- Peak 2 at 4.6 MeV originates from the alpha particles that deposit energy on the slanted sides of the Si fin after losing energy in air and then the oxide layer. It should be noted that due to the angular feature of the fin's side wall, the average track length of the alpha particle in the SiO_2 layer is larger than those penetrating the region corresponding to peak 1. This section of the geometry is represented in Figure 6.14.

- Peak 3 at 4.7 MeV originates from the alpha particles that deposit energy on the bottom of the MSND trench after losing energy in air and then the oxide layer. The average track length of the of the incoming alpha particle in the SiO_2 layer for this case is similar to the region corresponding to peak 1.

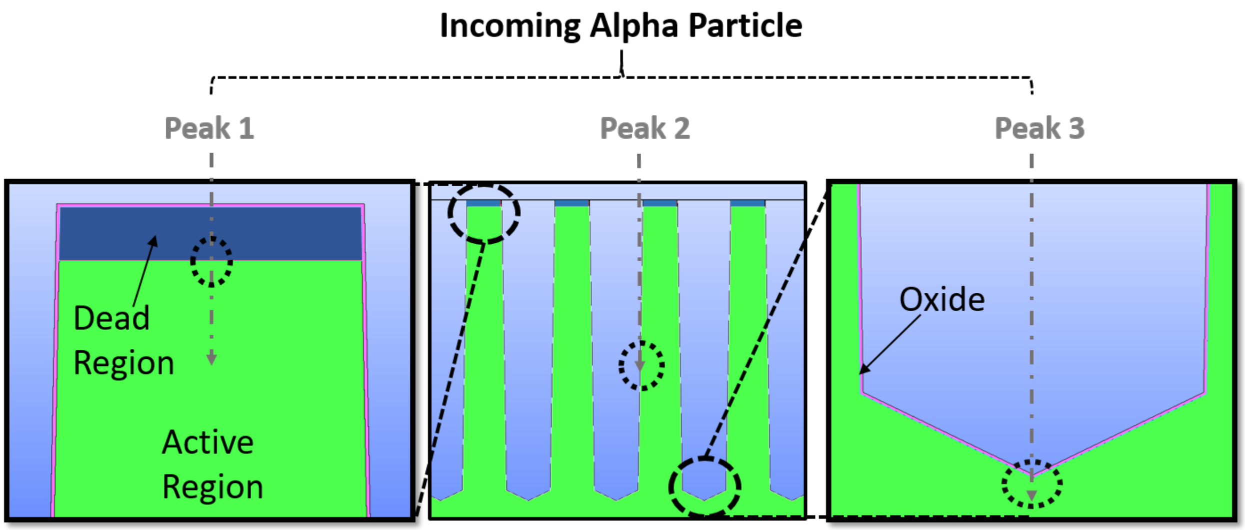

Figure 6.14: *A representation of regions of interest for the explanation of three distinct peaks in the alpha energy spectrum.*

The discrepancies in the three distinct peak heights for Experimental and Simulated results in Figures 6.12 and 6.13 likely result from losses in the charge collection efficiency due to presence of oxide interface traps at the Si-SiO_2 interface, which cannot be modeled in Geant4. Interface traps affect the charge collection efficiency as a function of location of energy deposited in the sensor.

All major features in the experimental spectrum are represented through the Geant4 simulations. These results suggests that the presence of FOC and SRV do not significantly deteriorate spectral features observed in Monte Carlo radiation transport simulations.

6.2.4 Electric Field Solutions

While simulating the charge carrier injection, it was noted that the presence of this dense region of free charge carriers greatly depresses the electric field in that region, causing plasma effects[41;42] in the charge cloud. This happens because the high density charge cloud behaves as a conductor temporarily. The time taken by the sensor to recover this electric field governs the ability of electrode to quickly collect all the holes. In order to obtain a faster induced current, it is vital that this electric field is recovered in the region of injection as fast as possible. One way to do this is by increasing the applied external reverse bias. The effect of charge carrier injection on the electric field magnitude for MSND sensor modeled with ideal boundary conditions is shown in Figure 6.15. As expected, at 0 ns, the electric field magnitude is linear as a function of device length. However, due to the sudden injection of high density charge, a large disruption can be observed at 8 ns, where a dip is observed in electric field magnitude up to a depth of 20 µm. The shape of this dip follows the inverse of the imported Bragg peak charge density profile and is accompanied by an abrupt spike in the field magnitude, which occurs for balancing the space charge within the device. A complete recovery of the electric field profile was observed at around 200 ns, which corresponds to complete collection of holes by the bottom electrode.

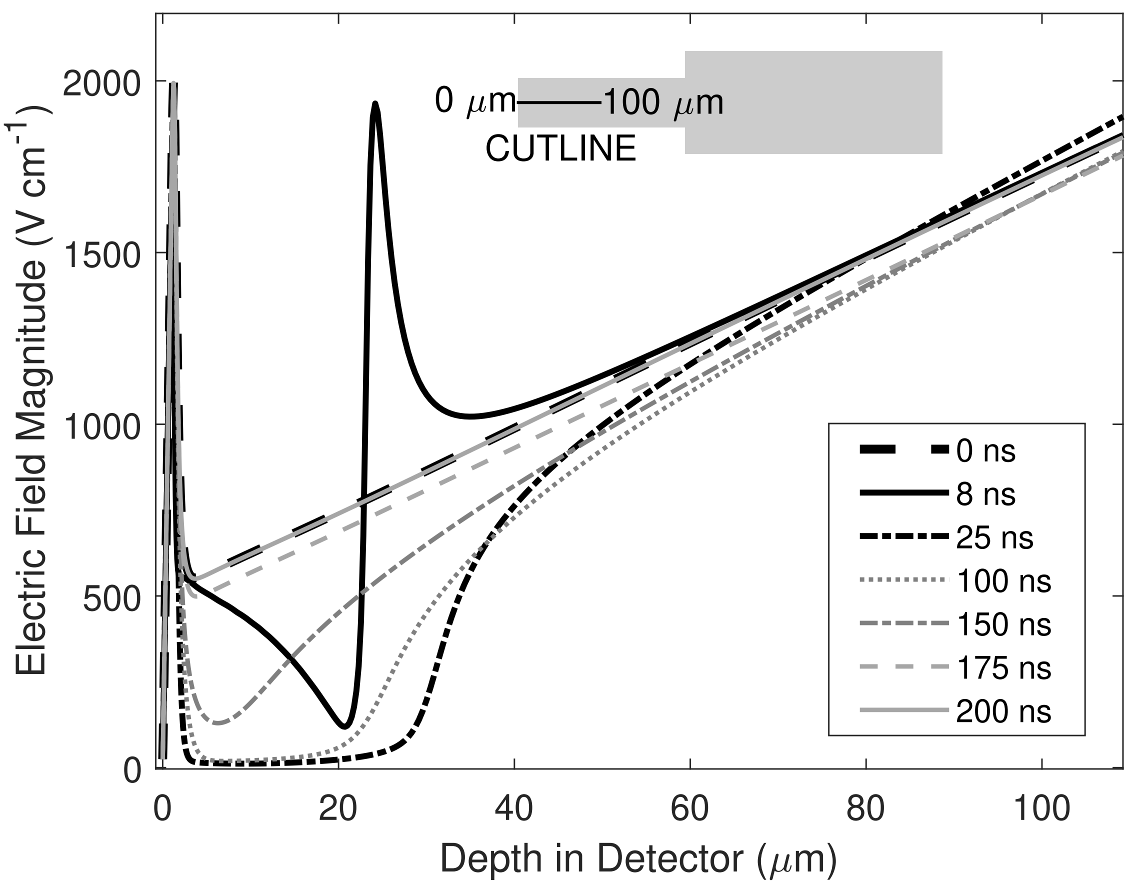

Figure 6.15: *Variation of electric field magnitude along the line of charge injection at various times.*

6.2.5 Induced Current Profile

For the these types of analyses, it is important that the study is separated into simulation results with two types of boundary conditions: ideal boundary conditions and realistic boundary conditions. The ideal boundary conditions will address the case where FOC and SRV is kept zero for simulated Si-SiO_2 interface. Realistic boundary conditions address the case where FOC and SRV are non-zero for simulated Si-SiO_2 interface. The charge cloud evolution inside the device starts immediately from beginning of injection due to the presence of attractive and repulsive Coulombic forces in the charge cloud and electric field inside the sensor due to external reverse bias. Furthermore, it is known that any motion of charge carriers in the presence of external electric field inside the sensor volume induces current at the electrode[105;106], so the shape of the simulated charge cloud could plays a vital role in obtaining an accurate induced current pulse from the sensor geometry.

The available literature[107–110] related to the simulation of charge cloud evolution inside the semiconductor geometry generally assumes either spherical or elliptical shape with a Gaussian distribution in the charge cloud density. For comparison, another COMSOL simulation was performed where a spherical shaped charge cloud was simulated with a Gaussian distribution of the charge carrier density amounting to same number of charge carriers. The Gaussian distribution for this case had a spatial standard deviation of 4 µm and a temporal standard deviation of 0.025 ns. The possibility of a coarser mesh was entertained for the Gaussian approximation of the charge carrier distribution, making the simulations comparatively faster. However, a comparison of the induced currents obtained for both the cases exhibits observable differences in the induced current profiles as shown in Figure 6.16. The difference in the induced current profile in Figure 6.16 mainly is due to the difference in the simulated density profiles of the charge clouds. A higher density of injected free charge carriers causes a greater depression of electric field magnitude inside the device, and this field takes longer to recover, resulting in a slightly longer charge collection time for the free carriers and hence a slower induced current pulse. The difference presented in these two cases is further expected to increase if a comparatively larger number of charge carriers are being simulated, since the recovery of electric field magnitude will take longer.

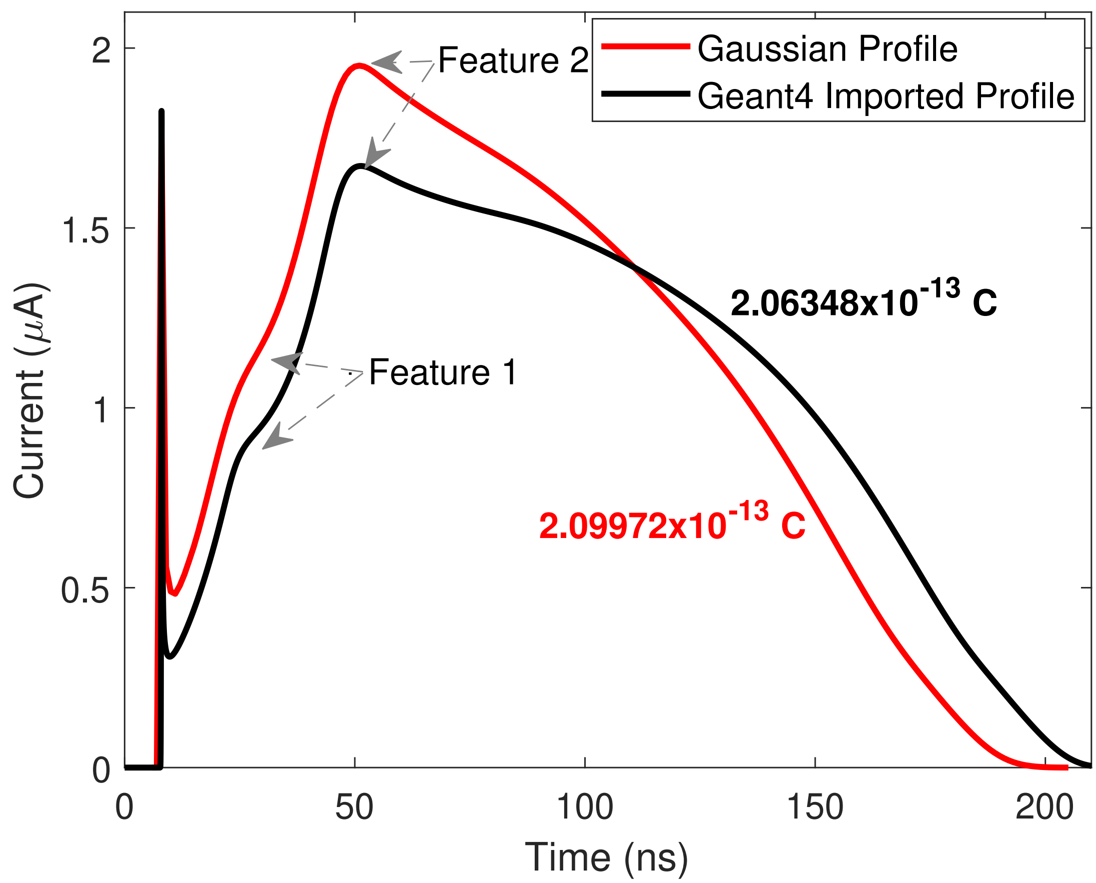

Figure 6.16: *A comparison between the induced currents (at* 200 V *reverse bias) when the simulated charge cloud is in a generalized Gaussian profile and an imported profile with Bragg distribution. The figure further shows the amount of total induced charge in the bottom electrode.*

The induced current represented in the Figure 6.16 has two main features in the profiles.

- Feature 1: This is a decrement of slope in the induced current profile observed at 25 ns. As per Figures 5.17 and 5.16, this feature occurs when the charge cloud begins transitioning from the fin to the bulk region, where the charge carriers face a sudden decrease in the electric field strength, and as per Equation 5.2, this causes a decrement in the drift velocity of the carriers and a corresponding decrement of the induced current magnitude.

- Feature 2: This feature corresponds to the "Peak Time" (T_P), as described in previous work[44], of the resultant simulated induced current and was observed at about 50 ns. As per Figures 5.17 and 5.16, this feature occurs when the charge collection by the bottom electrode obtains a constant level of hole concentration of around $1 \times 10^{11}\,\text{cm}^{-3}$. This level of charge transfer is maintained when all the charge carriers in the injected charge cloud starts to move under the influence of an electric field due to an external reverse bias. The bottom electrode continues to collect the holes after 50 ns at a nearly constant rate and the number of charge carriers in motion decreases in the device, which further decreases the induced current.

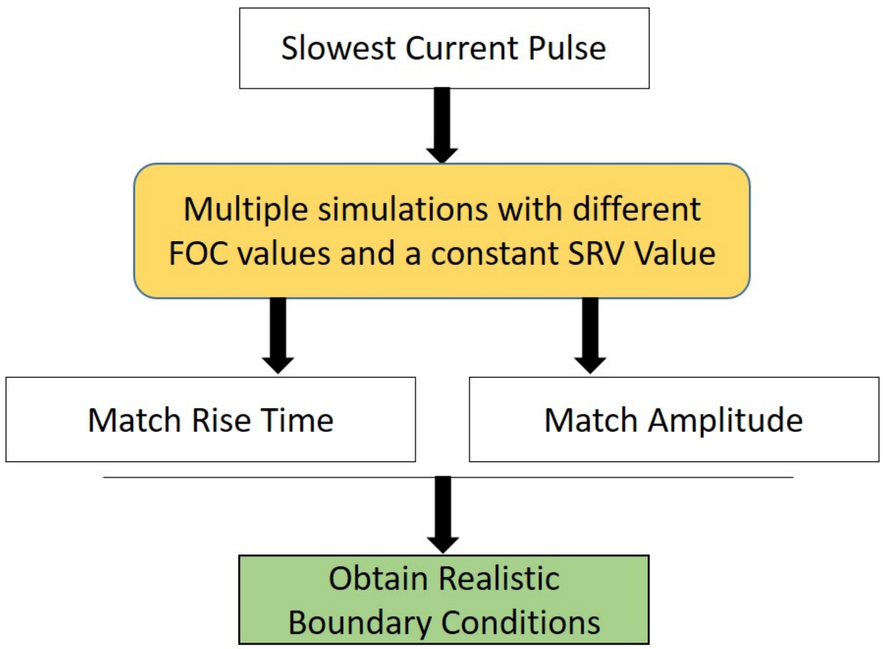

Figure 6.17: *Methodology to determine realistic Si-SiO_2 boundary conditions.*

The results presented in Figure 6.16 demonstrate that simulating an accurate profile of charge carrier injection is important for obtaining more realistic induced current pulse shapes from the simulated radiation sensor in an FEM-based multiphysics software. To determine a high fidelity response model of these microstructured sensors, it is vital to provide accurate numerical approximation of the realistic Si-SiO_2 boundary conditions. Experimental data were utilized to prepare a robust plan of action represented in Figure 6.17.

Among the three group of pulses encountered in the Figure 6.12, the slowest ones were selected for investigation. The slowest pulses are caused when the location of injection is at the top of the fins, at this location the charge cloud is most affected by the Si-SiO_2 boundary conditions. As shown in Figure 6.17, the first step was to perform multiple simulations in COMSOL to match the rise times and the amplitudes of the preamplifier pulses, since the rise time corresponds to the current signal duration. Multiple COMSOL simulations were performed, where FOC was varied from $1 \times 10^9\,\mathrm{cm}^{-2}$ to $5 \times 10^{10}\,\mathrm{cm}^{-2}$ and SRV was kept constant at $10\,\mathrm{cm\,s}^{-1}$, as it was noted that the variation in SRV value around $10\,\mathrm{cm\,s}^{-1}$ has a negligible effect on the induced current profiles. Depletion profiles obtained for these simulations are provided in Figure 5.18 and the corresponding electric fields are presented in Figure 5.19.

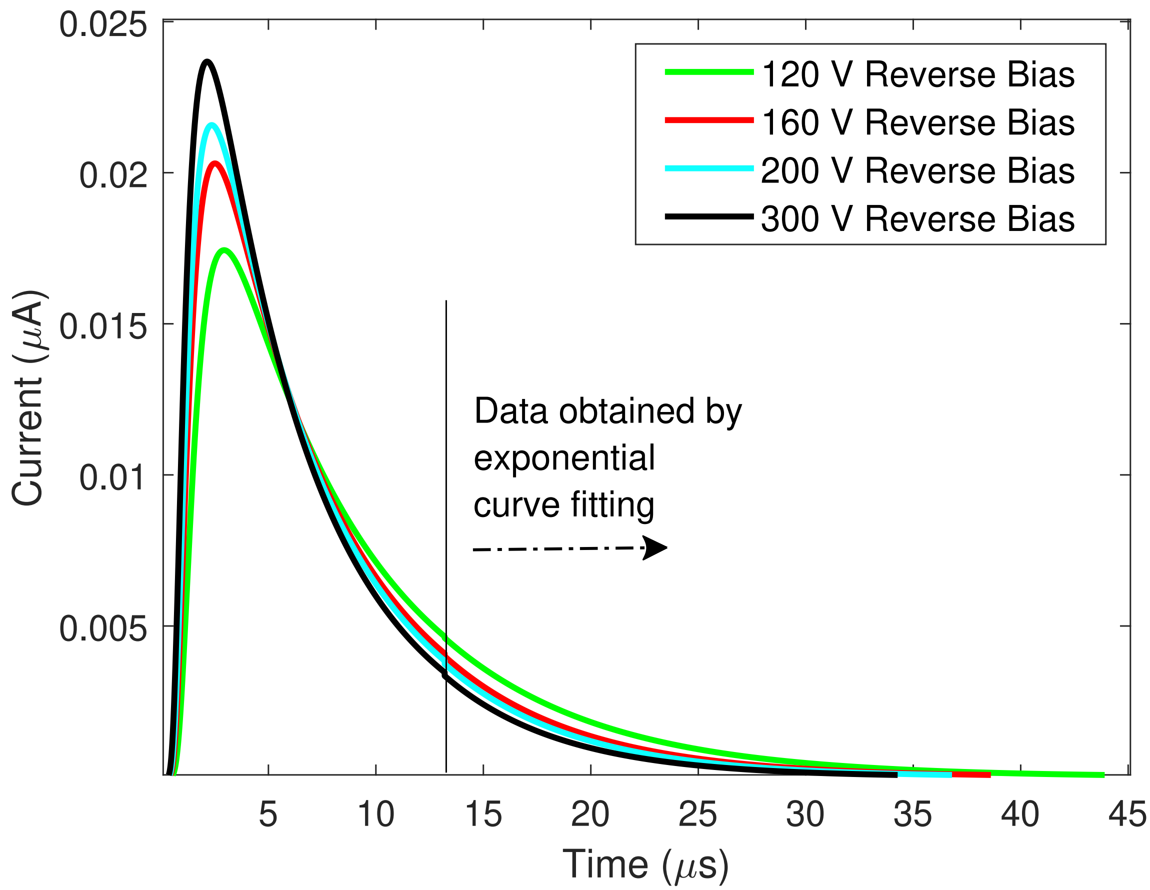

Figure 6.18: *A comparison between the simulated induced currents for an MSND device modeled with Si-SiO_2 interface obtained for various reverse bias values. A artificial cutoff is implemented as the simulations are resource and time expensive. No current is induced initially for a few hundred nanoseconds as the charge carriers are diffusing in all the directions inside the fins, cancelling each other's effects. The artificial cutoff for the induced currents from COMSOL was removed and replaced with extrapolated values for processing in LTspice 142A preamplifier model.*

Figure 6.18 shows the raw induced current profiles obtained from COMSOL Multiphysics simulations, which were performed for 13 000 ns of simulated time and with realistic boundary conditions on the Si-SiO_2 trench interfaces. Charge carriers experience diffusion and recombination inside the undepleted region of the fin at first, so no net current is induced at the bottom electrode due to compensating effects of charge motion in different directions in the very weak electric field. The current becomes substantially positive as soon as the holes transition from the undepleted region to the depleted region, which occurs around 240 ns for an FOC value of 5×10^{10} cm^{-2}, as per Figure 5.21. A 1D quantitative representation of the charge cloud motion is shown in Figure 5.22. Assuming constant values of FOC in the simulations, the rate of escape of holes from the undepleted region increases as the charge cloud undergoes diffusion. The peak of the induced current occurs when the maximum rate of hole transfer from undepleted to depleted region is achieved. Subsequently, the current decreases in an exponential fashion. These simulations are extremely time consuming and hence it was decided to perform extrapolation using exponential curve fitting for times greater than 13 µs.

6.2.6 Experimental Results and Analysis

It was observed from the experimental results that signal pulses occurred in three distinct groups of rise times and pulse heights. These differences are directly related to the interaction of alpha particles at different locations in the MSND sensor as shown in Figure 6.19. This effect was first observed from the oscilloscope's persistence trace plot presented in Figure 6.20 and then the detailed intensity plot of rise times and pulse heights from the digitizer as presented in Figures 6.21 and 6.22. It was observed from COMSOL simulations that at 120 V the depletion region will reach the bottom of the fins. The intensity plots presented in Figure 6.21 describes the mutation of correlation between pulses heights and rise times for the preamplifier's pulses collected from one hour of alpha particle irradiation at 40 V, 50 V, 60 V, 70 V, 80 V, and 120 V reverse bias. The cause of mutation these figures will be analyzed with respect to the depth of undepleted region (DUR) below bottom of the trench (Location 2). As per Figure 6.21 following observations are made:

- At 40 V Reverse Bias: The DUR value is 192 µm, and the effect of the microstructures is not visible on the correlation. A small number of slow pulses were accumulated. The correlation appears as a single nearly gaussian blob on the intensity plot.

- At 50 V Reverse Bias: The DUR value is 167 µm, and the effect of the microstructures is slightly visible on the correlation. An elongation is observed due to events depositing energy at Location 2.

- At 60 V Reverse Bias: The DUR value is 142 µm, and the effect of the microstructures starts to dominate the correlation. Slight separation is observed for pulses arriving from different parts of the microstructures.

- At 70 V Reverse Bias: The DUR value is 117 µm, and the effect of the microstructures becomes significant. Clear separation is observed for pulses arriving from three distinct regions of the microstructures as shown in Figure 6.19.

- At 80 V Reverse Bias: The DUR value is 92 µm. Three groups are clearly visible. Even though the range of the ^{241}Am alpha particle in Si is around 20 µm, these three groups are evident at DUR equal to 92 µm because a charge cloud injected at Location 2 will reach the drift region faster that a charge cloud injected at Location 1.

- At 120 V Reverse Bias: The pulse heights are improved and the rise times are faster than for previously presented reverse bias voltages.

If ideal boundary conditions are assumed, the diode will achieve full depletion at 200 V reverse bias. However, as per Figure 6.22, this does not happen. In Figure 6.22, the Group 3 pulses originate from the bottom of the trenches, where charge is injected at a location where there is negligible impact of the FOC. The charge carriers have a smaller probability of recombination as compared to other groups, since injection occurs in the presence of a strong electric field. Thus, Group 1 pulses exhibit the greatest pulse heights.

As the charge injection location begins moving towards the sidewalls of the fin, recombination increases and the pulse height decreases to around 400 ADC Value. Each charge injection location on the 183 µm long fin side wall[111] results in a greater rise time and smaller pulse heights for the Group 2 pulses as compared to Group 3 pulses. Different rise times are expected for pulses corresponding to different interaction locations along the fin side wall, which manifests as a band of pulses presented in Figure 6.22.

Interestingly, Group 1 pulses originating from the top of the fins demonstrate a further decrement in pulse height. This is because the incoming alpha particle loses some of its energy in the dead layer of the sensor as represented in Figure 6.19. Charge carriers generated in this dead layer do not contribute towards induced current generation. The rise times of the Group 1 pulses do not vary as much as those of Group 2 pulses, since all the pulses in Group 1 are originating from a common fin location.

The marginal histograms of the 2D intensity plot in Figure 6.22 are presented in Figure 6.23. These figures support the hypothesis that the presence of FOC and surface traps impacts the injected charge cloud evolution based on its location inside the fin of the MSND. If the charge is injected at the top of the fin, then the preamplifier pulse corresponding to that event will have the slowest rise time (i.e., slowest current pulse) and smallest pulse height. Similarly, if the charge is injected at the bottom of the trench, then then the preamplifier pulse corresponding to that event will have fastest rise time and largest peak magnitude.

Although the qualitative representation of the experimental data provides sufficient evidence of the expected charge cloud behavior, a comparison with the high fidelity physics models is required to benchmark and validate the detector responses. The SRH recombinations of charge carriers impacts the magnitude of the preamplifier pulses, while the undepleted region created by the presence of FOCs impacts the rise times of the preamplifier pulses. A detection event injecting charge at the top of the fin, corresponding to Group 1, will have the resultant charge cloud most impacted by the Si-SiO_2 boundary conditions, so validating the Group 1 pulses will enable the best approximation for the FOC value.

An analysis and comparison of pulses from Group 1 and Group 3 will assist in understanding the effects of Si-SiO_2 interface boundary conditions on the signal pulses. Further, a detailed analysis of the pulses originating from slower Group 1 is done to investigate whether the slow pulses get faster as a function of detector bias. The results obtained from this analysis will provide information on detector depletion characteristics. If the the pulses get faster significantly, it means that

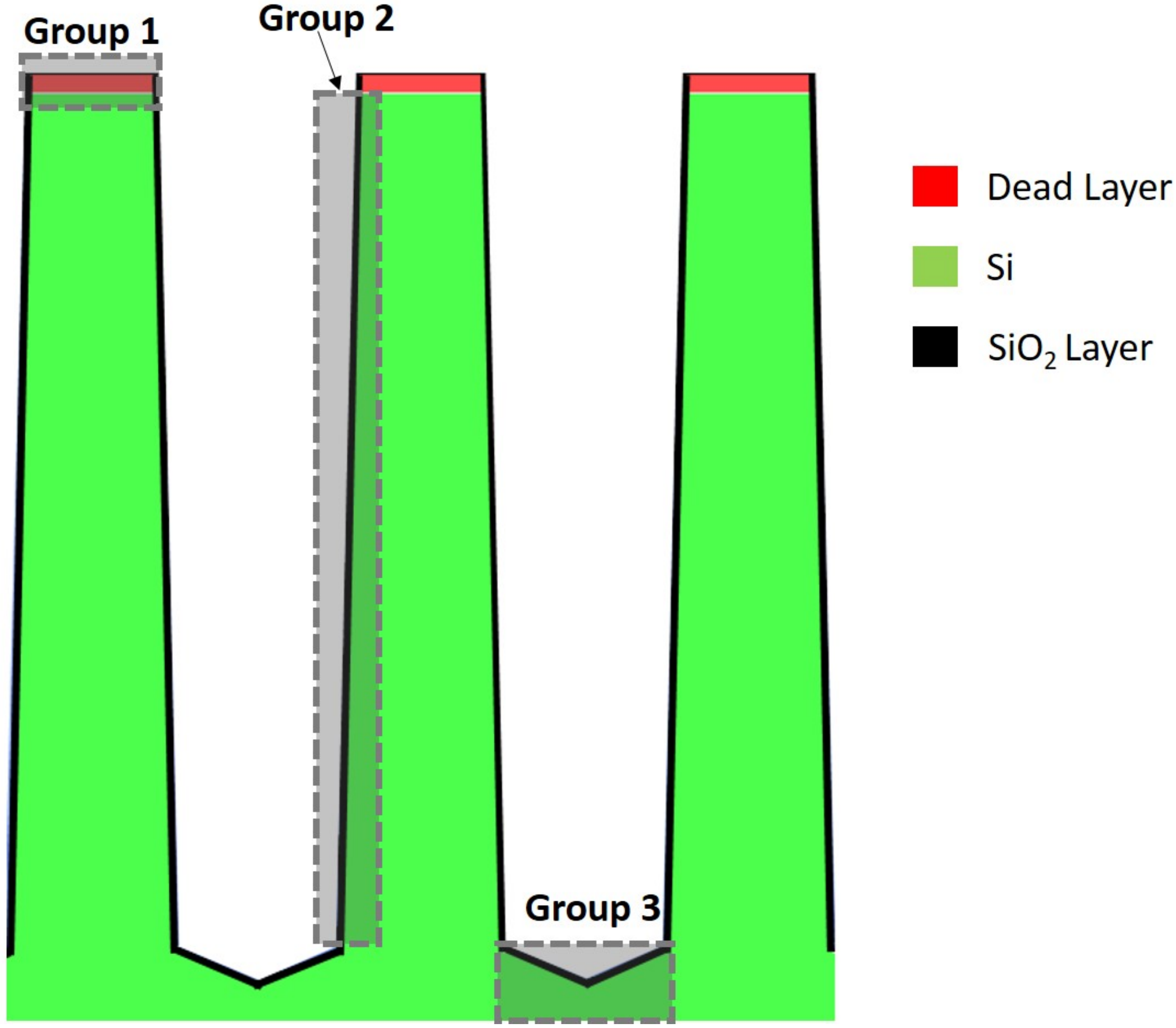

Figure 6.19: *A representation of regions of interest for the explanation of three distinct group of pulses observed in the experimental data.*

the Si-SiO_2 interface boundary conditions have little to no effect on the diode's depletion profile and the induced current profile.

A detailed analysis of the rise times is done by splitting the fast (RT $< 100\,$ns) and slow (RT $> 1000\,$ns) pulses represented in Figure 6.23. Detailed curve fitting was performed using MATLAB[89] to extract significant parameters from the rise time distributions. The shape of the histogram obtained for the Group 1 pulses was observed to be a skewed Gaussian. A sample of the fit is presented in Figure 6.24. Here, a reverse log normal distribution was used to fit the entire distribution with a coefficient of correlation (R^2 value) of 0.9923. The peak of this distribution

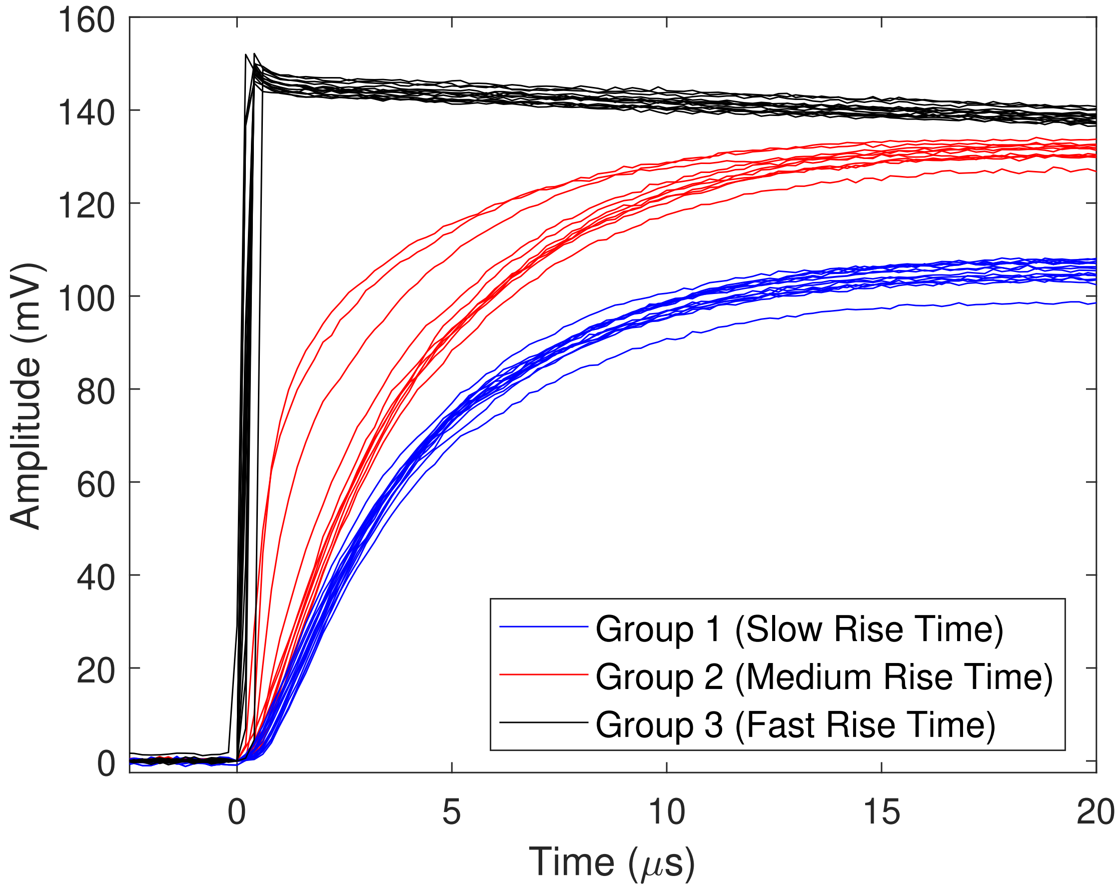

Figure 6.20: *Experimental pulses observed from oscilloscope's persistence mode. The pulses emerge from 142A preamplifier due to alpha particle irradiation at* 200 V *detector bias.*

corresponds to the largest number of slow pulses originating from the top of the fins (Group 1). This value will be used for comparison with the rise times of the simulated pulses. Similar fits were performed to characterize a complete response of the MSND sensor, shown in Figure 6.24.

Figure 6.24 also shows the rise time distribution of the all groups at various reverse biases, from 160 V to 300 V. For a fully depleted sensor, the rise time should be on the order of around 40-50 ns. The reverse bias of this sensor was increased to 300 V in an attempt to overdeplete the MSND diode[44]. Figure 6.24 shows that the peak value of the all the plotted distributions occurs at same spot for increasing reverse biases; the pulses in Group 1 are not getting faster as a function of applied reverse bias, indicating that the fins will not deplete.

To benchmark the preamplifier signals, an exponential curve fitting was performed to extrapo-

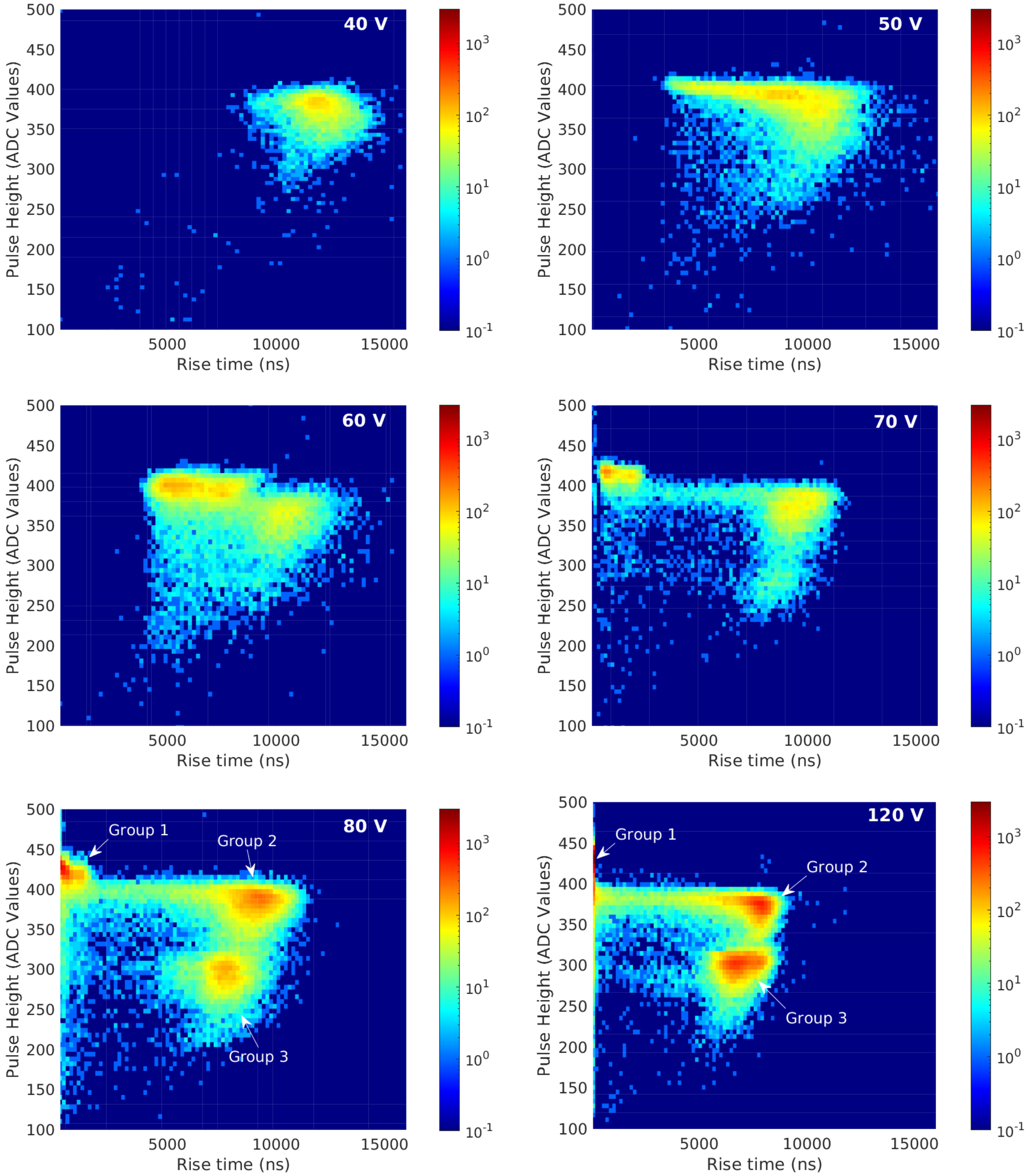

Figure 6.21: *Intensity plots demonstrating the mutation of correlation between pulses heights and rise times for the preamplifier's pulses collected from one hour of alpha particle irradiation at* 40 V*,* 50 V*,* 60 V*,* 70 V*,* 80 V*, and* 120 V *reverse bias.*

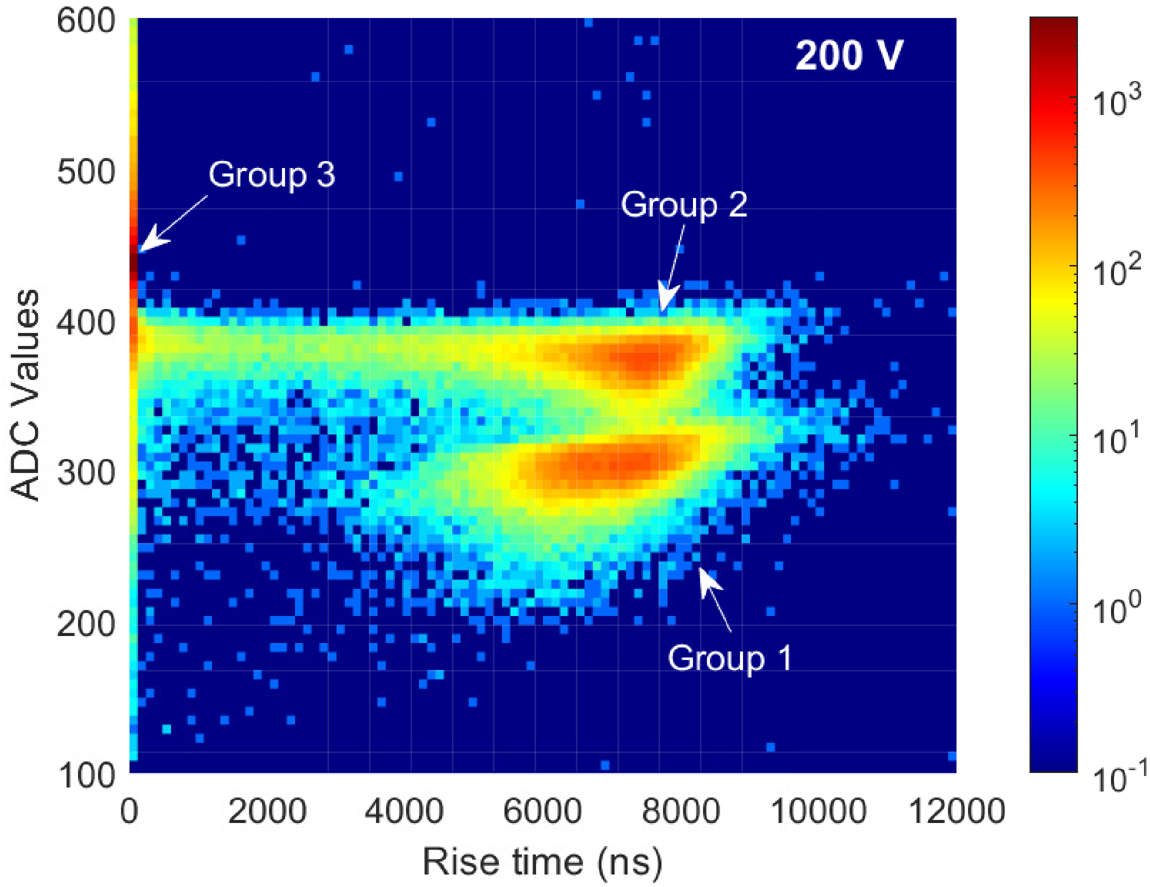

Figure 6.22: *Intensity plot for one hour irradiation obtained from analysis of preamplifier pulses at* 200 V *external reverse bias.*

late the missing portions of the simulated induced currents, shown in Figure 6.18. Readout electronics were simulated in LTspice[112]. A model for the Ortec 142A preamplifier is represented in Figure 6.25. The component details for the preamplifer were obtained from the manufacturer[113]. It should be noted that this model is approximate, as the manufacturer could not provide accurate details due to proprietary issues. The diode in this model was represented by a parallel connection of a current source I_D (signal current); R_D is the detector resistance and C_D is the detector capacitance. Here, the current pulses obtained from COMSOL were imported in as I_D to get the final result at the *E* of the LTspice model. A1 is the generic ideal op-amp with an open-loop gain of 40,000 was utilized to complete the simulated preamplifer model. A transient simulation was performed for 50 µs to obtain the simulated voltage pulses for comparison. Although the man-

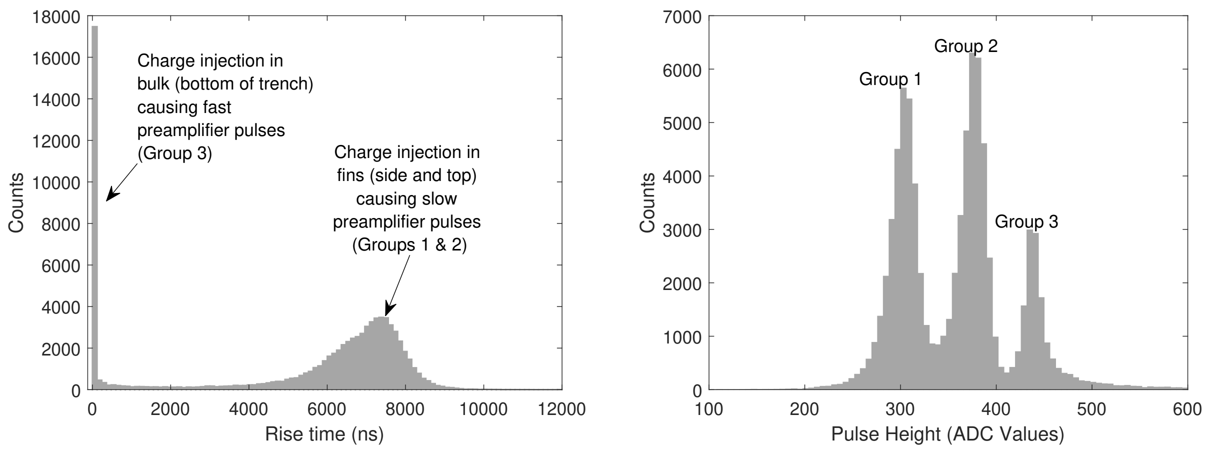

Figure 6.23: *(LEFT) Rise time histogram obtained from alpha irradiation of an MSND diode reverse biased at* 200 V *reverse bias. (RIGHT) Pulse height spectrum obtained from alpha irradiation of an MSND diode reverse biased at* 200 V *reverse bias.*

ufacturer has specified a charge conversion gain of 45 mV MeV^{-1}, a calibration with tail pulse generator provided a charge conversion gain of 31.63 mV MeV^{-1}.

The capacitance of the device was measured with a Hewlett-Packard CV-curve-tracing 1 MHz system (model 4280A). This equipment has an upper limit of 100 V in reverse bias application. At 100 V, the device capacitance was found to be 67 pF. It was found in previous work[111] that at around 100 V reverse bias, the depletion region is close to the bottom of the trenches. Decrease in capacitance of the diode is directly linked to the depletion width of the diode[114]. The simulated electric field results presented in Figures 5.19 and 5.20, and the analysis of measured pulse responses presented in Figures 6.20, 6.22, and 6.24, show that the device will not deplete further with increased reverse bias. It is thus appropriate to assume that the detector capacitance (C_D) at a reverse bias magnitude higher than 100 V will have capacitance values very close to 67 pF. The detector resistances R_D was found to be 2920 MΩ, 3747 MΩ, 4525 MΩ, and 6289 MΩ for an applied external reverse bias of 120 V, 160 V, 200 V, and 300 V, respectively[111]. The I_D was modeled as a current source where the extrapolated induced current from COMSOL (Figure 6.18) was directly imported as a piecewise linear (PWL) text file in LTspice. The resulting output was then adjusted for accurate charge conversion gain and then compared with the oscilloscope traces. A comparison of simulated pulse with measured Group 1 pulses is presented in Figure 6.26. Fur-

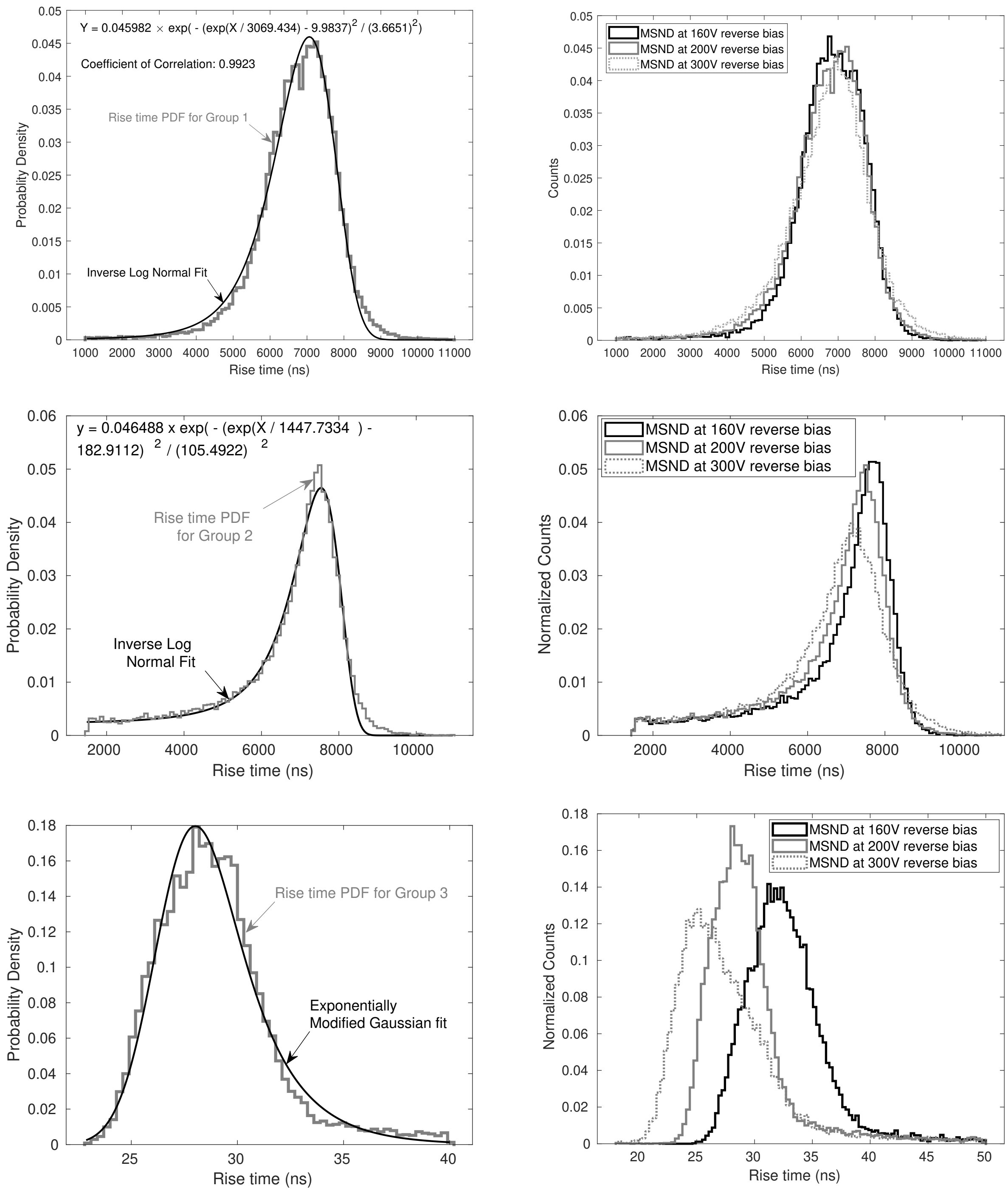

Figure 6.24: *(LEFT) Curve fit performed on rise time histogram obtained from alpha irradiation of an MSND diode reverse biased at 200 V reverse bias for Group 1, 2, and 3 pulses. (RIGHT) Rise time distribution of measured pulses in Group 1, 2, and 3 pulses obtained from alpha particle irradiation of reverse MSND at different reverse biases.*

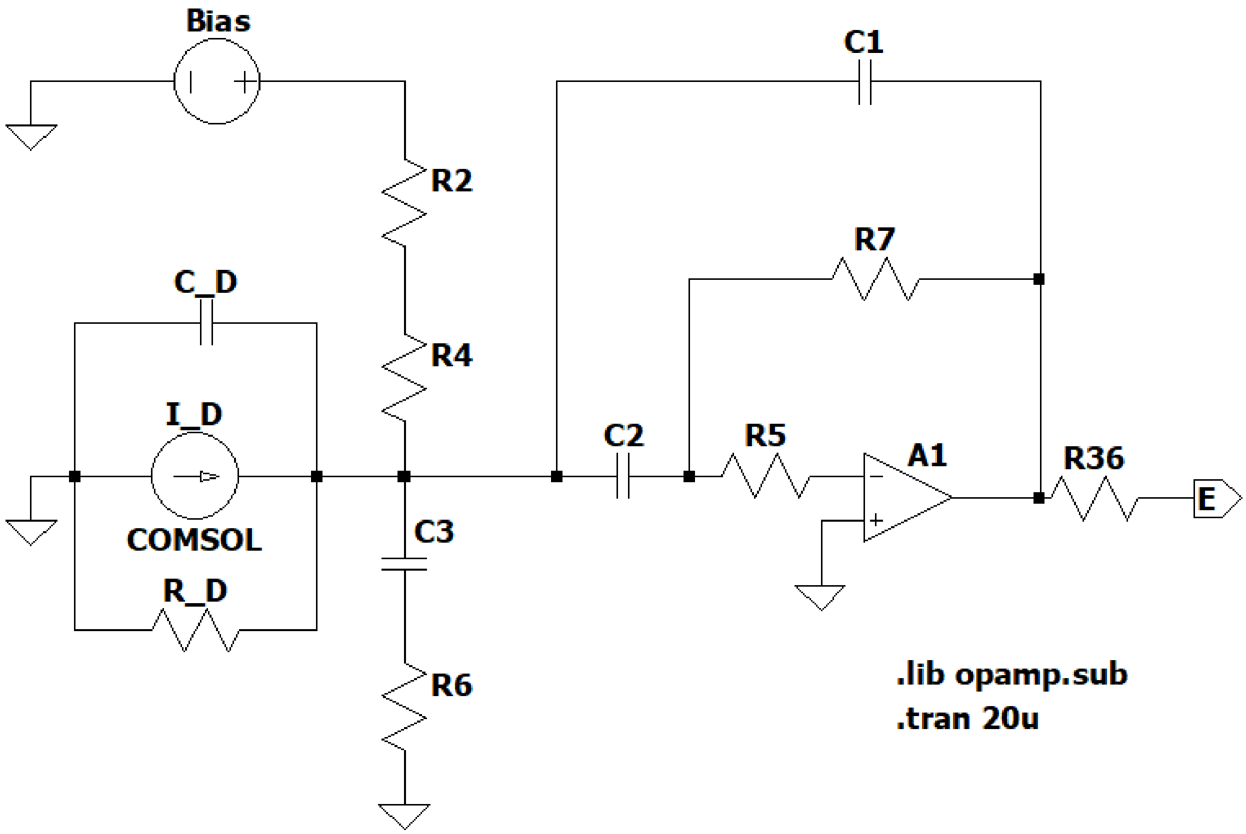

Figure 6.25: *LTspice model of the Ortec 142A preamplifier.*

ther, a comparison of simulated pulse with measured Group 3 pulses is presented in Figure 6.27. Very good qualitative agreement is observed in between simulated and measured pulses for both the cases. These results demonstrate that the COMSOL Multiphysics MSND model with a constant FOC value of $5 \times 10^{10}\,\mathrm{cm}^{-2}$ and a constant SRV value of $10\,\mathrm{cm\,s}^{-1}$ provides an acceptable approximation for the actual MSND device performance. The discrepancies in the simulated and experimental responses could be due to the fact that the values of FOC and SRV in actual devices are not constant along the trench surfaces.

The simulated rise time and amplitude of the preamplifier pulse at 200 V was 11.5 µs and 109 mV respectively. However, the experimental pulses of Group 1 show an average amplitude of 107.8 mV and according to Figure 6.24 the rise time of the Group 1 pulses can be anywhere in between 4-11 µs, with a maximum probability around 7 µs. This source of disagreement could be due to the fact that the value of FOC at the Si-SiO_2 interface in the actual device has an unknown

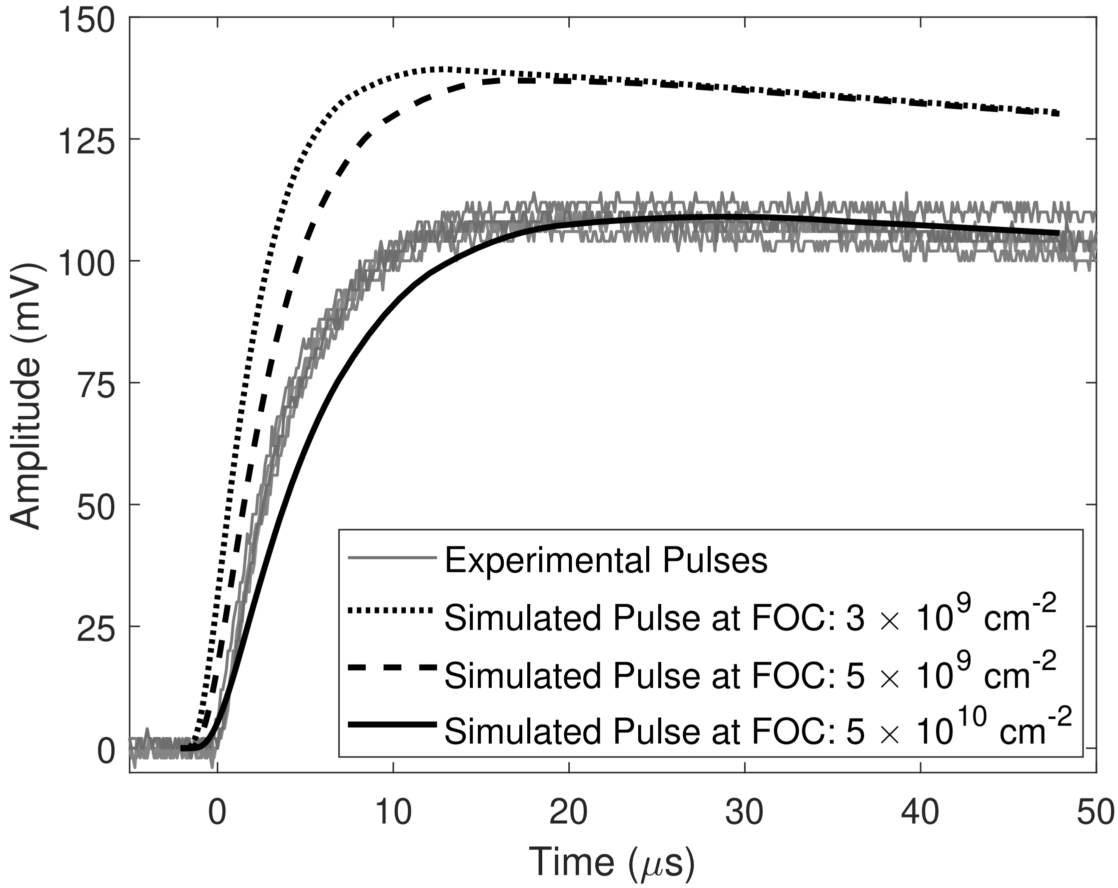

Figure 6.26: *A visual representation of comparison of simulated and experimental pulses of Group 1, obtained from the MSND at* 200 V *reverse bias.*

distribution and varies along length of the fin. Secondly, the 165 μm restricted length of the simulated fin in y-axis in not sufficient to incorporate entire diffusion of the charge cloud in the absence of electric field. The charge carriers are not able to diffuse realistically, causing the simulated induced currents to be artificially slow. The simulated size of fins in y direction is limited due to time and memory requirements. Finally, the missing proprietary circuit component details of the 142A preamplifier SPICE model could also be a potential source of disagreement.

Further analysis of magnitude and rise times of simulated and experimental scope traces confirm that an approximate FOC value of $5 \times 10^{10}\,\mathrm{cm}^{-2}$ and an approximate SRV value of $10\,\mathrm{cm\,s}^{-1}$ provides an acceptable model for an otherwise complicated device. Three major groups of preamplifier pulses were identified. Group 1 pulses were the slowest pulses with smallest magnitudes,

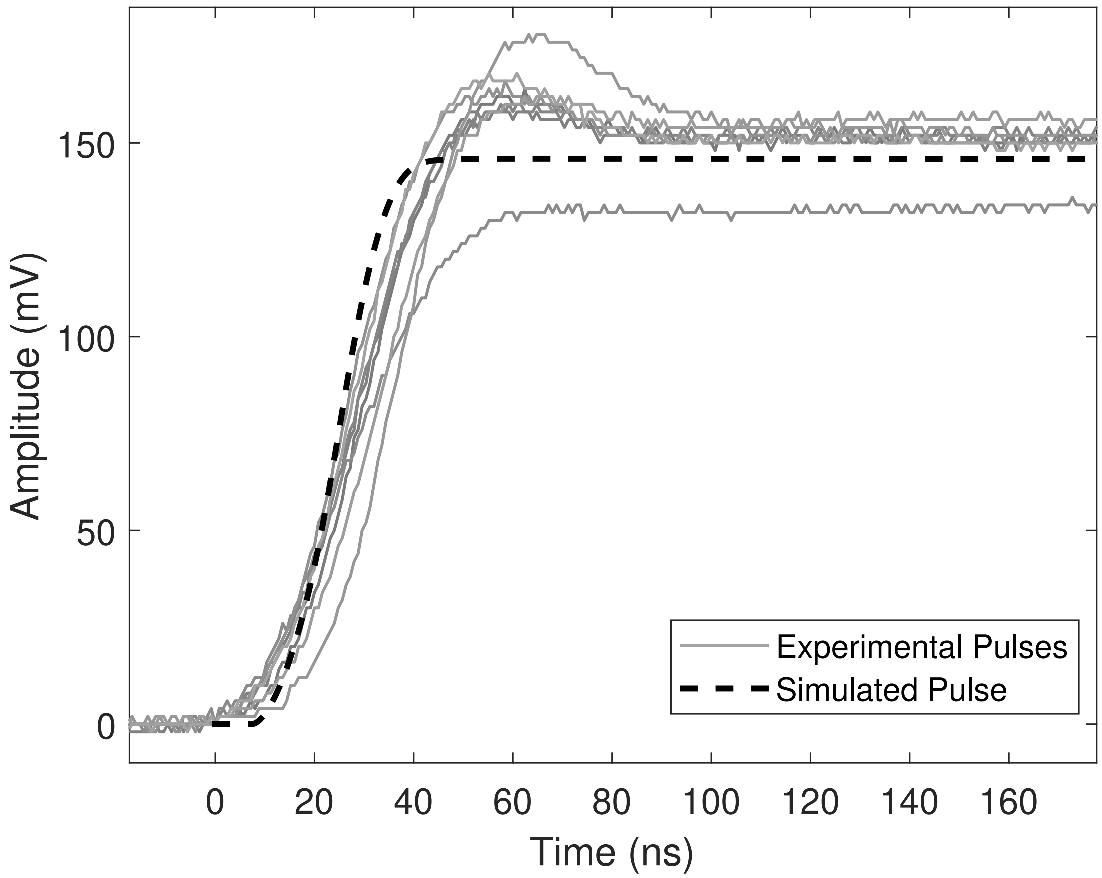

Figure 6.27: *A visual representation of comparison of simulated and experimental pulses of Group 3, obtained from MSND at* 200 V *reverse bias.*

radiation interaction location was at the top of the fins. Holes are most affected by the Si-SiO_2 interface boundary conditions such as fixed oxide charge and surface traps. Group 2 pulses, where the alpha particle interaction location was at the side walls of the fins. The charge cloud is moderately affected by the Si-SiO_2 interface boundary conditions such as FOC and surface traps. Finally, Group 3 were the fastest pulses with largest magnitudes, alpha particle interaction location was at the bottom of the trench. Holes are least affected by the Si-SiO_2 interface boundary conditions such as FOC and surface traps.

The results provide strong evidence that the presence of high density FOC is extremely detrimental to fast operation of the X-DS-MSND. It should be noted that these results are for single sided devices. Based on the results above, it can be confidently concluded that the dual sided sensors will have almost no pulses in Group 3, i.e., no fast pulses. Further, almost all the pulses will be extremely slow as compared to MSND sensors considering that DS-MSND sensors will have trenches on both sides and hence almost no depletion region. Simulations show that electric field lines points towards the bulk silicon region. The electric field lines at the bottom of the top trenches are in opposite direction to the electric field lines on the top of the bottom trenches, creating additional complexities for the charge carrier motion inside the sensor.

If the polarities of the doped junctions are reversed, almost 90% of the DS-MSND sensor will still be undepleted. The induced current will be mostly due to electrons moving downwards. Electrons will undergo more recombinations as they also recombine at the Si-SiO_2 interface due to presence of positive FOCs. Hence, in this case, the magnitude of the induced current will be much smaller than for the present doping conditions.

6.3 Application of X-DS-MSND sensor as a neutron radiation counter

Many physical features were found to be important to accurately construct a Monte Carlo radiation transport model of the microstructured Si based detectors. Features like the 4 µm dead layer, trench shape, and 250 nm thick SiO_2 layer were found to be accurate during the alpha spectroscopy characterization. This information was previously not well characterized. These features were incorporated and the Monte Carlo model of the updated X-DS-MSND with all these features was irradiated with 0.0253 eV thermal neutrons and 662 keV gamma-rays in Geant4.

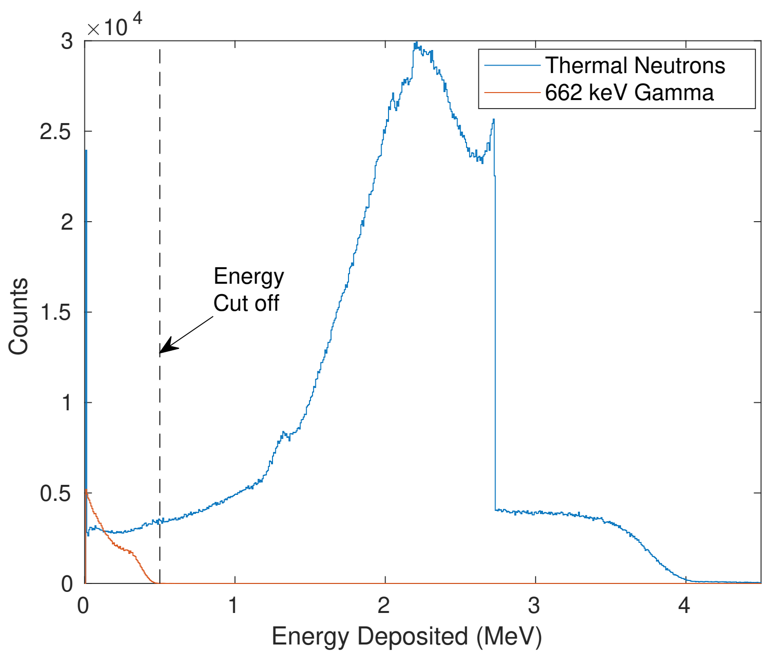

Figure 6.28: *Spectral response from a realistic DS-MSND model.*

The updated X-DS-MSND spectral response for thermal neutrons (blue) and gamma-rays (orange) are presented in Figure 6.28. Here, an energy based threshold was placed at 0.5 MeV. To obtain an optimum gamma-ray rejection, all neutron and gamma-ray counts were ignored between 0-0.5 MeV while accounting for the thermal neutron detection efficiency. It was found that the updated model had 57% thermal neutron detection efficiency without gamma-ray rejection and around 54.5% thermal neutron detection efficiency with gamma-ray rejection ratio higher than

10^{-6}. These results demonstrate that X-DS-MSND may be an excellent replacement for conventional thermal neutron detectors used in large neutron interrogation experiments.

The ^3He detector sensor was modeled with its aluminum casing to accurately account for gamma-ray scattering. Neutron capture and gamma-ray spectra were calculated with Geant4 and are represented in Figure 6.29. Here a energy based cut off was placed at 80 keV to reject any counts achieved due to gamma rays. The neutron spectra demonstrated escape peaks for proton (191 keV) and triton (573 keV) along with a full energy peak at 764 keV. The simulated count rate observed for the ^3He detector was around 80 cps without gamma-ray discrimination. When an energy cut off is applied at 80 keV, the ^3He detector count rate decreases to 40 cps.

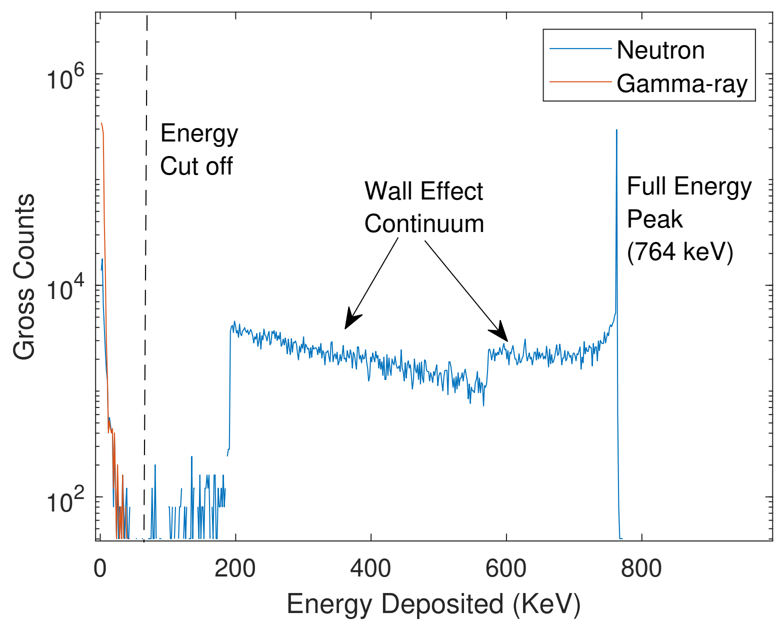

Figure 6.29: *Neutron and Gamma-ray spectrum obtained from ^3He detector in oil well logging setup with water as a testing material.*

The main objective of the STTR project was to fabricate a tiled 2-by-2 X-DS-MSND system[12] (i.e., four X-DS-MSNDs per tile). In order to achieve higher count rate, six such tiles were modeled in place of ^3He sensor in the oil well logging irradiation setup as represented in Figure 6.30.

Figure 6.31 represents the X-DS-MSND's simulated neutron energy spectrum obtained from Geant4. As per Section 6.1.3, the total neutron fluence used for scaling the water experimental

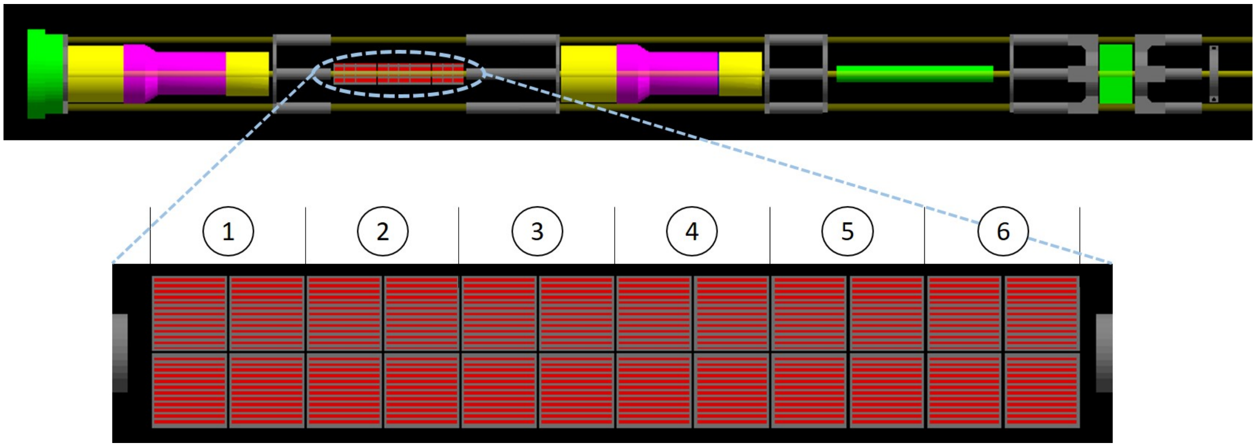

Figure 6.30: *Six 2-by-2 X-DS-MSND tiles placement in oil-well logging experiment.*

results was 1.0062×10^{10} neutrons for one hour irradiation, providing an expected count rate of 76 cps for X-DS-MSND. When an energy based cut off is applied to account for gamma-ray rejection, the X-DS-MSND count rate decreases to 30 cps.

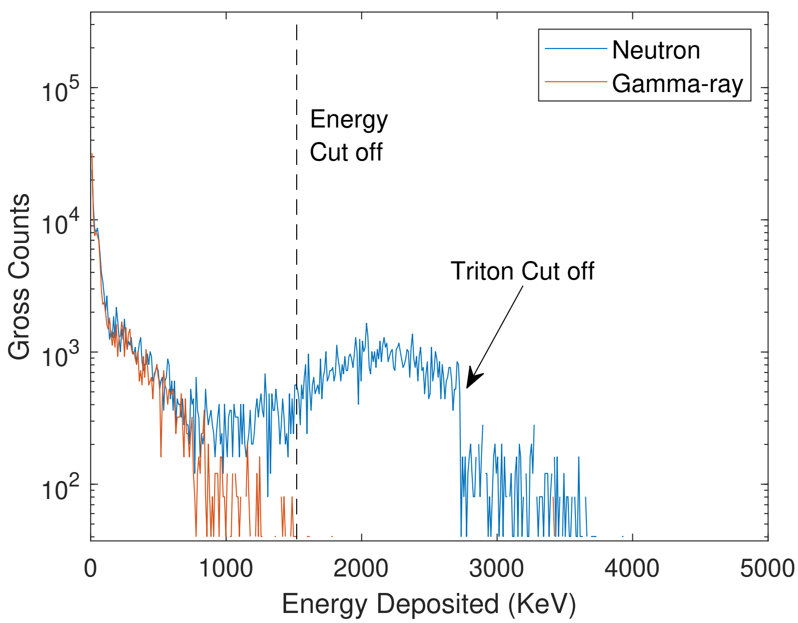

Figure 6.31: *Neutron and Gamma-ray spectrum obtained from X-DS-MSND as a replacement of ^{3}He detector in oil well logging setup with water as a testing material.*

The 30 cps count rate in the X-DS-MSND system can be further improved as compared to the ^{3}He detector's 40 cps, with the implementation of cluster morphology analysis. A proof of concept was prepared and presented in this dissertation as a reference for future study. A source code was developed in MATLAB to discriminate the clusters as a function of total charge, area, circularity, and extent as described in Figure 6.32. Based on these features, each cluster is provided a cumulative shape feature score. A shape feature score of 100 determines that the cluster was generated by a neutron interaction event. Known clusters were accumulated from Allpix Squared simulations and were used as a training data set and were processed in the machine learning source code.

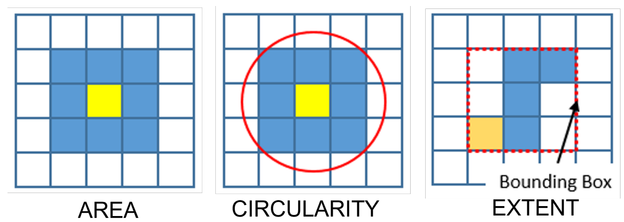

Figure 6.32: *Shape features used to perform cluster morphological analysis.*

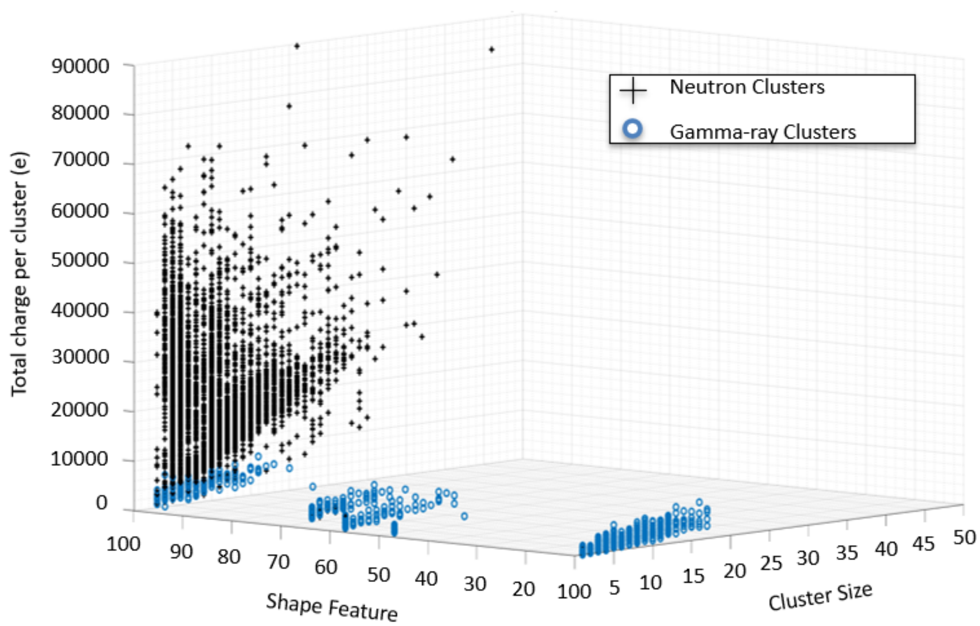

Figure 6.33: *Proof of concept describing results for machine learning processing of simulated training data.*

The initial result of the cluster morphological analysis of the source code is presented in Figure 6.33. The result presented here demonstrates that the source code was successful in discriminating majority (57%) of the gamma-ray clusters from neutron clusters, on the basis of three shape features. If more shape features are incorporated, this developed source code could improve the expected count rates from an X-DS-MSND detection system. This would not be possible with a ^{3}He detector.

The temperature at the oil well logging sites can be between 150-380 °C[115], while the operating temperature range for Si based detectors is -30 to 25 °C. An increase in the operation temperature reduces the bandgap of the Si sensor. Due to this, an increment in temperature will result in an increment in the electron-hole pairs generated thermally within the active volume of the sensor increasing noise in the signal. Thus, a cryogenic system is needed to keep the temperature within the warranted operating range.

Chapter 7

Conclusions

The research presented in this dissertation successfully combined two different research topics, i.e., radiation transport (RA1) and charge transport (RA2). RA 1 concluded that the spectral features in the gamma spectrum obtained from Geant4 for both irradiations show good agreement with experimental results. Small discrepancy between experimental and simulated gamma spectrum from 0-2 MeV was due to the lack of gamma scattering in the missing Geant4 models of electrical cables and smaller components inside the sensor. The exploration tool was modeled in Geant4 and the results from various sensors were benchmarked. Given that the neutron source was not characterized and was operated below the recommended specifications, the neutron output estimates from the irradiations contained moderate disagreements, which was expected. The *QGSP_BIC_HP* reference physics list along with G4NDL and G4TENDL cross-sections were adequate for validating the spectral features in the experimental spectra. The spectral results from experiments and simulations were successful in characterizing and identifying the irradiation material with acceptable statistics. The import tools presented improved the existing Geant4 source code by identifying bugs and will continue to allow the community to run CAD models on a mutltithreaded machines. These methods were then used in analysis of complex microstructured sensors.

RA 2 further demonstrated good agreement between experimental and simulated results, exhibiting the ability to simulate the MSND device response using COMSOL Multiphysics and Geant4 with high accuracy. The analysis provided a better understanding of all the modeling components and their importance in obtaining an accurate sensor response. The effects of positive FOC and interface traps on the depletion profile within sensor were confirmed by the experimental data. CV measurements and alpha particle irradiation measurements further confirmed the effects of FOC and interface traps on the MSND's depletion profile. An experimental validation is further needed to benchmark the effects of Si-SiO_2 interface boundary conditions on the electric field profile within the sensor. This validation required statistical analysis of the preamplifier pulses emerging due to radiation interactions around different parts of the microstructured sensor and was discussed in the proceeding section of the dissertation. A detailed analysis and experimental validation of the event pulses from the preamplifier can benchmark the parametric values of boundary conditions.

COMSOL Multiphysics simulations were found to be extremely complicated and time consuming. The above results were proceeded by detailed information on an ideal (zero FOC and SRV) and realistic (non-zero FOC and SRV) non-conformally doped MSND device performance. A 5.48 MeV ^{241}Am source was used for the test irradiations. It was found that the actual device behavior was significantly different from ideal. A detailed study was then presented to develop methods for accurate charge injection profiles and obtain expected induced current response. It was found that observable improvement in the current profiles could be expected by simulating the accurate Bragg distribution in the charge cloud injection profiles. Electric field profiles were analyzed for various FOC values and ideal case. It was found that due to the presence of FOC, the electric field strength in the fin becomes negligible. Detailed analysis of rise times from slow group confirmed this hypothesis. Further analysis of magnitude and rise times of simulated and experimental scope traces confirm that a constant FOC value of $5 \times 10^{10}\,\mathrm{cm}^{-2}$ and a constant SRV value of $10\,\mathrm{cm\,s}^{-1}$ provides an acceptable approximate FEM model for an otherwise complicated device. Three major groups of preamplifier pulses were identified, Group 1 pulses were the slowest pulses with smallest magnitudes (charge injection occurs at the top of the fin). Holes are most affected by the Si-SiO_2 interface boundary conditions such as fixed oxide charge and surface traps. Group 2 pulses were of moderate duration (charge injection occurs at the side walls of the fin). The charge cloud is moderately affected by the Si-SiO_2 interface boundary conditions such as FOC and surface traps. Finally, Group 3 pulses were the fastest pulses with largest magnitudes (charge injection occurs at the bottom of the trench). Holes are least affected by the Si-SiO_2 interface boundary conditions such as FOC and surface traps. Future studies will include multi-bias experiments to characterize depletion rate inside the fin. The scope of the study of different passivation methods is based on an attempt to reduce the deteriorating effects of FOC. The benchmarks presented in this dissertation were novel, as the methods and the results are found to be desirable in the field of advanced semiconductor radiation detector development. An attempt could also be made to neutralize the positive FOC by intentionally contaminating the side walls of the fins with aluminum[116].

The research area 3 provides promising results for a tiled X-DS-MSND system which could be used as an effective replacement for a ^{3}He sensor. Lower count rates in the X-DS-MSNDs are largely due to the smaller active volume of X-DS-MSND sensor as compared to the ^{3}He sensor. The cluster morphological analysis of the X-DS-MSND data obtained from Allpix Squared demonstrated a promising proof of concept to provide better gamma-ray discrimination with the help of complex machine learning algorithms. Three basic shape features were used to perform morphological analysis of the simulated data. More shape features can be incorporated in future to obtain better discrimination. It was discussed that the temperature at the oil well logging sites can be much greater than recommended Si device operating temperatures. An increment in temperature results in an increment in the number of electron-hole pairs generated thermally within the active volume of the sensor, increasing noise in the sensor signal. Thus, a cryogenic system is needed to keep the temperature within the warranted operating range.

The work presented provides an approximation of device performance with a constant FOC value. However, the actual FOC present on the Si-SiO_2 interface in not necessarily constant; more research is needed to investigate the FOC profile as a function of trench depth. Another significant research area is trapped charge buildup at the Si-SiO_2 interface. Significant research is needed at the fabrication end to investigate methods for reducing the FOC value to ensure imaging capabilities for X-DS-MSND sensor. Transient COMSOL runs with accurate boundary conditions, are time and memory expensive. Hence, Allpix Squared source code needs to be upgraded as an alternate simulation methodology to account for real Si-SiO_2 interface boundary conditions and plasma times. There is tremendous scope in fabrication based research to reduce FOC value for making the device faster, so the X-DS-MSND could possibly have imaging properties. To use X-DS-MSND as a neutron counter readout electronics with larger integration time needs to be considered, i.e., older Timepix chips.

Bibliography

[1] M.B. Chadwick, M. Herman, P. Obložinský, M.E. Dunn, Y. Danon, A.C. Kahler, D.L. Smith, B. Pritychenko, G. Arbanas, R. Arcilla, R. Brewer, D.A. Brown, R. Capote, A.D. Carlson, Y.S. Cho, H. Derrien, K. Guber, G.M. Hale, S. Hoblit, S. Holloway, T.D. Johnson, T. Kawano, B.C. Kiedrowski, H. Kim, S. Kunieda, N.M. Larson, L. Leal, J.P. Lestone, R.C. Little, E.A. McCutchan, R.E. MacFarlane, M. MacInnes, C.M. Mattoon, R.D. McKnight, S.F. Mughabghab, G.P.A. Nobre, G. Palmiotti, A. Palumbo, M.T. Pigni, V.G. Pronyaev, R.O. Sayer, A.A. Sonzogni, N.C. Summers, P. Talou, I.J. Thompson, A. Trkov, R.L. Vogt, S.C. van der Marck, A. Wallner, M.C. White, D. Wiarda, and P.G. Young. Endf/b-vii.1 nuclear data for science and technology: Cross sections, covariances, fission product yields and decay data. *Nuclear Data Sheets*, 112(12):2887–2996, 2011. ISSN 0090-3752. doi: https://doi.org/10.1016/j.nds.2011.11.002. URL https://www.sciencedirect.com/science/article/pii/S009037521100113X. Special Issue on ENDF/B-VII.1 Library.

[2] National Institute of Standards and Technology. Security requirements for cryptographic modules. Technical Report Federal Information Processing Standards Publications (FIPS PUBS) 140-2, Change Notice 2 December 03, 2002, U.S. Department of Commerce, Washington, D.C., 2001.

[3] D.S. McGregor, W.J. McNeil, S.L. Bellinger, T.C. Unruh, and J.K. Shultis. Microstructured semiconductor neutron detectors. *Nuclear Instruments and Methods in Physics Research Section A: Accelerators, Spectrometers, Detectors and Associated Equipment*, 608(1):125–131, 2009. ISSN 0168-9002. doi: https://doi.org/10.1016/j.nima.2009.06.031. URL https://www.sciencedirect.com/science/article/pii/S016890020901239X.

[4] Ryan G. Fronk, Steven L. Bellinger, Luke C. Henson, Taylor R. Ochs, Colten T. Smith,

J. Kenneth Shultis, and Douglas S. McGregor. Dual-sided microstructured semiconductor neutron detectors (DSMSNDs). *Nuclear Instruments and Methods in Physics Research Section A: Accelerators, Spectrometers, Detectors and Associated Equipment*, 804:201 – 206, 2015. ISSN 0168-9002. doi: https://doi.org/10.1016/j.nima.2015.09.040.

[5] R. G. Fronk. *Dual-side etched microstructured semiconductor neutron detectors*. PhD thesis, Mechanical and Nuclear Engineering, Kansas State University, Manhattan, Kansas, 2017. URL https://krex.k-state.edu/dspace/handle/2097/35426.

[6] Taylor R. Ochs. *Advanced dual-sided microstructured semiconductor neutron detectors and instrumentation*. PhD thesis, Mechanical and Nuclear Engineering, Kansas State University, Manhattan, Kansas, 2020. URL https://krex.k-state.edu/dspace/handle/2097/40545.

[7] T. Poikela, J. Plosila, T. Westerlund, M. Campbell, M. De Gaspari, X. Llopart, V. Gromov, R. Kluit, M. Van Beuzekom, F. Zappon, V. Zivkovic, C. Brezina, K. Desch, Y. Fu, and A. Kruth. Timepix3: a 65K channel hybrid pixel readout chip with simultaneous ToA/ToT and sparse readout. *Journal of Instrumentation*, 2014. ISSN 17480221. doi: 10.1088/1748-0221/9/05/C05013.

[8] T. Goorley. Mcnp6.1.1-beta release notes. *LA-UR-14-24680*, 2014.

[9] S. Agostinelli, J. Allison, K. Amako, J. Apostolakis, H. Araujo, P. Arce, M. Asai, D. Axen, S. Banerjee, G. Barrand, F. Behner, L. Bellagamba, J. Boudreau, L. Broglia, A. Brunengo, H. Burkhardt, S. Chauvie, J. Chuma, R. Chytracek, G. Cooperman, G. Cosmo, P. Degtyarenko, A. Dell'Acqua, G. Depaola, D. Dietrich, R. Enami, A. Feliciello, C. Ferguson, H. Fesefeldt, G. Folger, F. Foppiano, A. Forti, S. Garelli, S. Giani, R. Giannitrapani, D. Gibin, J. J. Gomez Cadenas, I. Gonzalez, G. Gracia Abril, G. Greeniaus, W. Greiner, V. Grichine, A. Grossheim, S. Guatelli, P. Gumplinger, R. Hamatsu, K. Hashimoto, H. Hasui, A. Heikkinen, A. Howard, V. Ivanchenko, A. Johnson, F. W. Jones, J. Kallenbach, N. Kanaya, M. Kawabata, Y. Kawabata, M. Kawaguti, S. Kelner, P. Kent, A. Kimura, T. Kodama, R. Kokoulin, M. Kossov, H. Kurashige, E. Lamanna, T. Lampen, V. Lara, V. Lefebure,

F. Lei, M. Liendl, W. Lockman, F. Longo, S. Magni, M. Maire, E. Medernach, K. Minamimoto, P. Mora de Freitas, Y. Morita, K. Murakami, M. Nagamatu, R. Nartallo, P. Nieminen, T. Nishimura, K. Ohtsubo, M. Okamura, S. O'Neale, Y. Oohata, K. Paech, J. Perl, A. Pfeiffer, M. G. Pia, F. Ranjard, A. Rybin, S. Sadilov, E. di Salvo, G. Santin, T. Sasaki, N. Savvas, Y. Sawada, S. Scherer, S. Sei, V. Sirotenko, D. Smith, N. Starkov, H. Stoecker, J. Sulkimo, M. Takahata, S. Tanaka, E. Tcherniaev, E. Safai Tehrani, M. Tropeano, P. Truscott, H. Uno, L. Urban, P. Urban, M. Verderi, A. Walkden, W. Wander, H. Weber, J. P. Wellisch, T. Wenaus, D. C. Williams, D. Wright, T. Yamada, H. Yoshida, and D. Zschiesche. GEANT4 - a simulation toolkit. *Nuclear Instruments and Methods in Physics Research, Section A: Accelerators, Spectrometers, Detectors and Associated Equipment*, 2003. ISSN 01689002. doi: 10.1016/S0168-9002(03)01368-8.

[10] S. Spannagel, K. Wolters, D. Hynds, N. Alipour Tehrani, M. Benoit, D. Dannheim, N. Gauvin, A. Nürnberg, P. Schütze, and M. Vicente. Allpix^2: A modular simulation framework for silicon detectors. *Nuclear Instruments and Methods in Physics Research, Section A: Accelerators, Spectrometers, Detectors and Associated Equipment*, 2018. ISSN 01689002. doi: 10.1016/j.nima.2018.06.020.

[11] COMSOL Multiphysics® v. 5.6. https://www.comsol.com/.

[12] X-DSMSND: A Dual-Sided Microstructured Semiconductor Neutron Detector with Integrated Pixel Read-Out. https://www.sbir.gov/sbirsearch/detail/1620659.

[13] William L. Dunn and J. Kenneth Shultis. 1 - introduction. In William L. Dunn and J. Kenneth Shultis, editors, *Exploring Monte Carlo Methods*, pages 1–20. Elsevier, Amsterdam, 2012. ISBN 978-0-444-51575-9. doi: https://doi.org/10.1016/B978-0-444-51575-9.00001-4. URL https://www.sciencedirect.com/science/article/pii/B9780444515759000014.

[14] R. Oswald, E. Kasper, and K.H. Gaukler. A multiple scattering theory of elastic electron backscattering from amorphous surfaces. *Journal of Electron Spectroscopy and Related Phenomena*, 61(3):251–274, 1993. ISSN 0368-2048. doi: https://doi.org/10.1016/

0368-2048(93)80019-I. URL https://www.sciencedirect.com/science/article/pii/036820489380019I.

[15] Ying Liang, Wazir Muhammad, Gregory Hart, and Bradley Nartowt. A general-purpose Monte Carlo particle transport code based on inverse transform sampling for radiotherapy dose calculation. *Scientific Reports*, 10, 2020. ISSN 2045-2322. doi: 10.1038/s41598-020-66844-7. URL https://doi.org/10.1038/s41598-020-66844-7.

[16] I Kawrakow, DWO Rogers, E Mainegra-Hing, F Tessier, RW Townson, and BRB Walters. Egsnrc toolkit for monte carlo simulation of ionizing radiation transport. doi:10.4224/40001303 [release v2021], 2000.

[17] Nuclear Energy Agency. *PENELOPE 2018: A code system for Monte Carlo simulation of electron and photon transport*. 2019. doi: https://doi.org/https://doi.org/10.1787/32da5043-en. URL https://www.oecd-ilibrary.org/content/publication/32da5043-en.

[18] S. Incerti, I. Kyriakou, M. A. Bernal, M. C. Bordage, Z. Francis, S. Guatelli, V. Ivanchenko, M. Karamitros, N. Lampe, S. B. Lee, S. Meylan, C. H. Min, W. G. Shin, P. Nieminen, D. Sakata, N. Tang, C. Villagrasa, H. N. Tran, and J. M. C. Brown. Geant4-dna example applications for track structure simulations in liquid water: A report from the geant4-dna project. *Medical Physics*, 45(8):e722–e739, 2018. doi: https://doi.org/10.1002/mp.13048. URL https://aapm.onlinelibrary.wiley.com/doi/abs/10.1002/mp.13048.

[19] Paolo Dondero, Alfonso Mantero, Vladimir Ivanchencko, Simone Lotti, Teresa Mineo, and Valentina Fioretti. Electron backscattering simulation in geant4. *Nuclear Instruments and Methods in Physics Research Section B: Beam Interactions with Materials and Atoms*, 425: 18–25, 2018. ISSN 0168-583X. doi: https://doi.org/10.1016/j.nimb.2018.03.037. URL https://www.sciencedirect.com/science/article/pii/S0168583X18302301.

[20] V.M. Grichine. Integral cross-sections of light nuclei in the glauber-gribov representation. *Nuclear Instruments and Methods in Physics Research Section B: Beam Interactions with*

Materials and Atoms, 427:60–62, 2018. ISSN 0168-583X. doi: https://doi.org/10.1016/j.nimb.2018.04.044. URL https://www.sciencedirect.com/science/article/pii/S0168583X18302957.

[21] J. Barylak, A. Barylak, T. Mrozek, O. Grimm, A. Howard, P. Podgórski, and M. Steślicki. Simulation of charge sharing in the caliste-so detector. *Nuclear Instruments and Methods in Physics Research Section A: Accelerators, Spectrometers, Detectors and Associated Equipment*, 903:234–240, 2018. ISSN 0168-9002. doi: https://doi.org/10.1016/j.nima.2018.05.062. URL https://www.sciencedirect.com/science/article/pii/S0168900218306818.

[22] P Lazarakis, S Incerti, V Ivanchenko, I Kyriakou, D Emfietzoglou, S Corde, A B Rosenfeld, M Lerch, M Tehei, and S Guatelli. Investigation of track structure and condensed history physics models for applications in radiation dosimetry on a micro and nano scale in geant4. *Biomedical Physics &amp Engineering Express*, 4(2):024001, feb 2018. doi: 10.1088/2057-1976/aaa6aa. URL https://doi.org/10.1088/2057-1976/aaa6aa.

[23] National Research Council. *Radiation Source Use and Replacement: Abbreviated Version*. The National Academies Press, Washington, DC, 2008. ISBN 978-0-309-11014-3. doi: 10.17226/11976. URL https://www.nap.edu/catalog/11976/radiation-source-use-and-replacement-abbreviated-version.

[24] UNITED-STATES-NUCLEAR-REGULATORY-COMMISSION. Well logging. https://www.nrc.gov/docs/ML1122/ML11229A017.pdf, 2011.

[25] Long Vo, Aaron Hellinger, Maria Pinilla, William Dunn, Amir Bahadori, and Walter McNeil. Development of test facilities for studies relevant to replacing dangerous radiological sources. *AIP Conference Proceedings*, 2160(1):50001, 2019. doi: 10.1063/1.5127693. URL https://aip.scitation.org/doi/abs/10.1063/1.5127693.

[26] SOLIDWORKS. https://www.solidworks.com/, 2017.

[27] J. Allison, K. Amako, J. Apostolakis, et al. Recent developments in Geant4. *Nuclear Instruments and Methods in Physics Research Section A: Accelerators, Spectrometers, Detectors and Associated Equipment*, 835:186 – 225, 2016. ISSN 0168-9002. doi: https://doi.org/10.1016/j.nima.2016.06.125. URL http://www.sciencedirect.com/science/article/pii/S0168900216306957.

[28] T.R. Ochs, R.G. Fronk, S.L. Bellinger, and D.S. McGregor. Design and performance considerations for dual-sided microstructured semiconductor neutron detectors. *Nuclear Instruments and Methods in Physics Research Section A: Accelerators, Spectrometers, Detectors and Associated Equipment*, 951:163006, 2020. ISSN 0168-9002. doi: https://doi.org/10.1016/j.nima.2019.163006. URL http://www.sciencedirect.com/science/article/pii/S0168900219313774.

[29] R. G. Fronk, S. L. Bellinger, L. C. Henson, D. Huddleston, T. R. Ochs, C. T. Smith, T. J. Sobering, C. J. Rietcheck, R. D. Taylor, J. K. Shultis, and D. S. McGregor. Development of the dual-sided microstructured semiconductor neutron detector. In *2014 IEEE Nuclear Science Symposium and Medical Imaging Conference (NSS/MIC)*, pages 1–4, Nov 2014. doi: 10.1109/NSSMIC.2014.7431247.

[30] T.R. Ochs, S.L. Bellinger, R.G. Fronk, L.C. Henson, R.M. Hutchins, and D.S. McGregor. Improved manufacturing and performance of the dual-sided microstructured semiconductor neutron detector (DS-MSND). *Nuclear Instruments and Methods in Physics Research Section A: Accelerators, Spectrometers, Detectors and Associated Equipment*, 2018. ISSN 0168-9002. doi: https://doi.org/10.1016/j.nima.2018.12.011. URL http://www.sciencedirect.com/science/article/pii/S0168900218318096.

[31] R. G. Fronk, S. L. Bellinger, L. C. Henson, D. E. Huddleston, T. R. Ochs, C. J. Rietcheck, C. T. Smith, J. K. Shultis, T. J. Sobering, and D. S. McGregor. Advancements on dual-sided microstructured semiconductor neutron detectors (dsmsnds). In *2015 IEEE Nuclear Science Symposium and Medical Imaging Conference (NSS/MIC)*, pages 1–4, Oct 2015. doi: 10.1109/NSSMIC.2015.7582287.

[32] S. L. Bellinger, W. J. McNeil, T. C. Unruh, and D. S. McGregor. Characteristics of 3d micro-structured semiconductor high efficiency neutron detectors. *IEEE Transactions on Nuclear Science*, 56(3):742–746, 2009. doi: 10.1109/TNS.2008.2006682.

[33] D.S. McGregor, S.L. Bellinger, W.J. McNeil, and T.C. Unruh. Micro-structured high-efficiency semiconductor neutron detectors. 2009. doi: 10.1109/nssmic.2008.4775204.

[34] Steven L. Bellinger, Ryan G. Fronk, Luke C. Henson, Taylor R. Ochs, Timothy J. Sobering, and Douglas S. McGregor. Microstructured semiconductor neutron detector (MSND)-based Helium-3 Replacement technology. In *2014 IEEE Nuclear Science Symposium and Medical Imaging Conference, NSS/MIC 2014*, 2016. ISBN 9781479960972. doi: 10.1109/NSSMIC.2014.7430745.

[35] Sanchit Sharma, Diego Laramore, Steven Bellinger, Walter J. McNeil, and Amir A. Bahadori. Simulation of signal formation and imaging in a dual-sided micro-structured semiconductor neutron detector. In *2019 IEEE Nuclear Science Symposium and Medical Imaging Conference (NSS/MIC)*, pages 1–3, 2019. doi: 10.1109/NSS/MIC42101.2019.9059683.

[36] Diego Laramore, Sanchit Sharma, Steven L. Bellinger, Amir A. Bahadori, and Walter J. McNeil. Simulation of charge carrier transport in pixelated micro-structured semiconductor neutron detectors. In *2019 IEEE Nuclear Science Symposium and Medical Imaging Conference (NSS/MIC)*, pages 1–3, 2019. doi: 10.1109/NSS/MIC42101.2019.9060059.

[37] Diego Laramore, Sanchit Sharma, Kaitlyn C. Smallfoot, Steven L. Bellinger, Luke C. Henson, Taylor R. Ochs, Douglas S. McGregor, Amir A. Bahadori, and Walter J. McNeil. Simulation of charge drift in surface doped, pixelated micro-structured semiconductor neutron detectors. *Nuclear Instruments and Methods in Physics Research Section A: Accelerators, Spectrometers, Detectors and Associated Equipment*, 978:164351, 2020. ISSN 0168-9002. doi: https://doi.org/10.1016/j.nima.2020.164351. URL https://www.sciencedirect.com/science/article/pii/S0168900220307488.

[38] Diego Laramore. *Simulation and validation of charge carrier drift in pixelated microstruc-*

tured semiconductor neutron detectors. Doctoral Thesis. PhD thesis, Kansas State Univeristy, 2020.

[39] Walter McNeil. *Perforated Diode Neutron Sensors. Doctoral Thesis.* PhD thesis, Kansas State Univeristy, 2010.

[40] Diego Laramore, Sanchit Sharma, Steven L. Bellinger, Luke C. Henson, Taylor R. Ochs, Douglas S. McGregor, Lawrence Pinsky, Amir A. Bahadori, and Walter J. McNeil. Advancements in modeling conformally doped x-msnd radiation imagers. *Nuclear Instruments and Methods in Physics Research Section A: Accelerators, Spectrometers, Detectors and Associated Equipment*, page 166799, 2022. ISSN 0168-9002. doi: https://doi.org/10.1016/j.nima.2022.166799. URL https://www.sciencedirect.com/science/article/pii/S0168900222002984.

[41] G. L. Miller, W. L. Brown, P. F. Donovan, and I. M. Mackintosh. Silicon p-n junction radiation detectors. *IRE Transactions on Nuclear Science*, 7(2/3):185–189, 1960. doi: 10.1109/TNS2.1960.4315762.

[42] P.A. Tove and W. Seibt. Plasma effects in semiconductor detectors. *Nuclear Instruments and Methods*, 51(2):261–269, 1967. ISSN 0029-554X. doi: https://doi.org/10.1016/0029-554X(67)90012-2. URL https://www.sciencedirect.com/science/article/pii/0029554X67900122.

[43] W. Seibt, K.E. Sundström, and P.A. Tove. Charge collection in silicon detectors for strongly ionizing particles. *Nuclear Instruments and Methods*, 113(3):317–324, 1973. ISSN 0029-554X. doi: https://doi.org/10.1016/0029-554X(73)90496-5. URL https://www.sciencedirect.com/science/article/pii/0029554X73904965.

[44] Raymond N. Williams and Ewan M. Lawson. The plasma effect in silicon semiconductor radiation detectors. *Nuclear Instruments and Methods*, 120(2):261–268, 1974. ISSN 0029-554X. doi: https://doi.org/10.1016/0029-554X(74)90044-5. URL https://www.sciencedirect.com/science/article/pii/0029554X74900445.

[45] Anton S. Tremsin, W. Bruce Feller, and R. Gregory Downing. Efficiency optimization of microchannel plate (mcp) neutron imaging detectors. i. square channels with 10b doping. *Nuclear Instruments and Methods in Physics Research Section A: Accelerators, Spectrometers, Detectors and Associated Equipment*, 539(1):278–311, 2005. ISSN 0168-9002. doi: https://doi.org/10.1016/j.nima.2004.09.028. URL https://www.sciencedirect.com/science/article/pii/S0168900204021850.

[46] A.S. Tremsin, M. Morgano, T. Panzner, E. Lehmann, U. Filgers, J.V. Vallerga, J.B. McPhate, O.H.W. Siegmund, and W.B. Feller. High resolution neutron imaging capabilities at boa beamline at paul scherrer institut. *Nuclear Instruments and Methods in Physics Research Section A: Accelerators, Spectrometers, Detectors and Associated Equipment*, 784:486–493, 2015. ISSN 0168-9002. doi: https://doi.org/10.1016/j.nima.2014.09.026. URL https://www.sciencedirect.com/science/article/pii/S0168900214010274. Symposium on Radiation Measurements and Applications 2014 (SORMA XV).

[47] A.S. Tremsin, J.V. Vallerga, J.B. McPhate, and O.H.W. Siegmund. Optimization of high count rate event counting detector with microchannel plates and quad timepix readout. *Nuclear Instruments and Methods in Physics Research Section A: Accelerators, Spectrometers, Detectors and Associated Equipment*, 787:20–25, 2015. ISSN 0168-9002. doi: https://doi.org/10.1016/j.nima.2014.10.047. URL https://www.sciencedirect.com/science/article/pii/S0168900214012042. New Developments in Photodetection NDIP14.

[48] A.S. Tremsin and J.V. Vallerga. Unique capabilities and applications of microchannel plate (mcp) detectors with medipix/timepix readout. *Radiation Measurements*, 130:106228, 2020. ISSN 1350-4487. doi: https://doi.org/10.1016/j.radmeas.2019.106228. URL https://www.sciencedirect.com/science/article/pii/S1350448719305141.

[49] Andrei Nomerotski. Imaging and time stamping of photons with nanosecond resolution in timepix based optical cameras. *Nuclear Instruments and Methods in Physics Research*

Section A: Accelerators, Spectrometers, Detectors and Associated Equipment, 937:26–30, 2019. ISSN 0168-9002. doi: https://doi.org/10.1016/j.nima.2019.05.034. URL https://www.sciencedirect.com/science/article/pii/S0168900219306667.

[50] Elan Herrera, Daniel Hamm, Ashley Stowe, Jeffrey Preston, Brenden Wiggins, Arnold Burger, and Eric Lukosi. Neutron imaging with timepix coupled lithium indium diselenide. *Journal of Imaging*, 4(1), 2018. ISSN 2313-433X. doi: 10.3390/jimaging4010010. URL https://www.mdpi.com/2313-433X/4/1/10.

[51] R Biagi, V Corradini, G Bertoni, C Mariani, U del Pennino, and MG Betti. Single-particle and collective excitations of a two-dimensional electron gas at the cs/inas(110) surface. *PHYSICAL REVIEW B*, 64(19), NOV 15 2001. ISSN 1098-0121. doi: 10.1103/PhysRevB.64.195407.

[52] NE HAKIKI and MD BELO. Semiconductor study in the fermi-dirac statistic - application to passive films. *COMPTES RENDUS DE L ACADEMIE DES SCIENCES SERIE II*, 320(9, 1):463–469, MAY 4 1995. ISSN 1251-8069.

[53] *Oxide and Interface Trapped Charges, Oxide Thickness*, chapter 6, pages 319–387. John Wiley and Sons, Ltd, 2005. ISBN 9780471749097. doi: https://doi.org/10.1002/0471749095.ch6. URL https://onlinelibrary.wiley.com/doi/abs/10.1002/0471749095.ch6.

[54] Emil Arnold. Determination of oxide fixed charge at the top and bottom si/sio2 interfaces of silicon insulator devices. *Applied Physics Letters*, 66(22):3027–3029, 1995. doi: 10.1063/1.114266. URL https://doi.org/10.1063/1.114266.

[55] N Woods and Stephen Hall. Self-aligned cobalt disilicide/silicon schottky barrier contacts: Fabrication, materials and electrical characterization. *Semiconductor Science and Technology*, 11:1103, 01 1999. doi: 10.1088/0268-1242/11/7/023.

[56] S. I. Raider and A. Berman. On the nature of fixed oxide charge. 125(4):629–633, apr 1978. doi: 10.1149/1.2131513. URL https://doi.org/10.1149/1.2131513.

[57] Helmuth Spieler. Semiconductor detector systems. *Oxford University Press*, 2005. doi: https://doi.org/10.1093/acprof:oso/9780198527848.001.0001. URL https://oxford.universitypressscholarship.com/view/10.1093/acprof:oso/9780198527848.001.0001/acprof-9780198527848. Oxford Scholarship Online, 2007.

[58] ThermoFisher. B-320 Neutron Generator. https://www.thermofisher.com/order/catalog/product/1510431A?SID=srch-srp-1510431A#/1510431A?SID=srch-srp-1510431A, 0.

[59] Santhosh M. Malkapur and Mattur C. Narasimhan. 10 - virgin and waste polymer incorporated concrete mixes for enhanced neutron radiation shielding characteristics. In Fernando Pacheco-Torgal, Jamal Khatib, Francesco Colangelo, and Rabin Tuladhar, editors, *Use of Recycled Plastics in Eco-efficient Concrete*, Woodhead Publishing Series in Civil and Structural Engineering, pages 215–247. Woodhead Publishing, 2019. ISBN 978-0-08-102676-2. doi: https://doi.org/10.1016/B978-0-08-102676-2.00010-4. URL https://www.sciencedirect.com/science/article/pii/B9780081026762000104.

[60] Magdi Ragheb. *University of Illinois, Urbana Champaign*. Neutron Cross Sections, 2011. URL https://www.coursehero.com/file/7252795/0409-Neutron-Cross-Sections/.

[61] *Nuclear Reactor Engg., 4e Vol. II : Reactor Systems Engineering*. Nuclear Reactor Engineering. CBS Publishers & Distributors, 2004. ISBN 9788123906485. URL https://books.google.com/books?id=oH95tgAACAAJ.

[62] P Rinard. Neutron interactions with matter. *Passive nondestructive assay of nuclear materials*, (375-377), 1991.

[63] WM Deuchars and GP Lawrence. Interaction of 14-mev. neutrons with a silicon semiconductor nuclear particle detector. *Nature (London)*, 191(4792), 1961.

[64] J.L. Autran and D. Munteanu. Electronics reliability assessment of future power fusion machines: Neutron interaction analysis in bulk silicon. *Microelectronics Reliability*, 126:114223, 2021. ISSN 0026-2714. doi: https://doi.org/10.1016/j.microrel.2021.114223. URL https://www.sciencedirect.com/science/article/pii/S002627142100189X. Proceedings of ESREF 2021, 32nd European Symposium on Reliability of Electron Devices, Failure Physics and Analysis.

[65] D.A. Brown, M.B. Chadwick, R. Capote, A.C. Kahler, A. Trkov, M.W. Herman, A.A. Sonzogni, Y. Danon, A.D. Carlson, M. Dunn, D.L. Smith, G.M. Hale, G. Arbanas, R. Arcilla, C.R. Bates, B. Beck, B. Becker, F. Brown, R.J. Casperson, J. Conlin, D.E. Cullen, M.-A. Descalle, R. Firestone, T. Gaines, K.H. Guber, A.I. Hawari, J. Holmes, T.D. Johnson, T. Kawano, B.C. Kiedrowski, A.J. Koning, S. Kopecky, L. Leal, J.P. Lestone, C. Lubitz, J.I. MÃ¡rquez DamiÃ¡n, C.M. Mattoon, E.A. McCutchan, S. Mughabghab, P. Navratil, D. Neudecker, G.P.A. Nobre, G. Noguere, M. Paris, M.T. Pigni, A.J. Plompen, B. Pritychenko, V.G. Pronyaev, D. Roubtsov, D. Rochman, P. Romano, P. Schillebeeckx, S. Simakov, M. Sin, I. Sirakov, B. Sleaford, V. Sobes, E.S. Soukhovitskii, I. Stetcu, P. Talou, I. Thompson, S. van der Marck, L. Welser-Sherrill, D. Wiarda, M. White, J.L. Wormald, R.Q. Wright, M. Zerkle, G. Å½erovnik, and Y. Zhu. Endf/b-viii.0: The 8th major release of the nuclear reaction data library with cielo-project cross sections, new standards and thermal scattering data. *Nuclear Data Sheets*, 148:1–142, 2018. ISSN 0090-3752. doi: https://doi.org/10.1016/j.nds.2018.02.001. URL https://www.sciencedirect.com/science/article/pii/S0090375218300206. Special Issue on Nuclear Reaction Data.

[66] A. Pais. Einstein and the quantum theory. *Rev. Mod. Phys.*, 51:863–914, Oct 1979. doi: 10.1103/RevModPhys.51.863. URL https://link.aps.org/doi/10.1103/RevModPhys.51.863.

[67] Arthur H. Compton. A quantum theory of the scattering of x-rays by light elements. *Phys. Rev.*, 21:483–502, May 1923. doi: 10.1103/PhysRev.21.483. URL https://link.aps.org/doi/10.1103/PhysRev.21.483.

[68] C. Canali, M. Martini, G. Ottaviani, and A. Alberigi Quaranta. Measurements of the average energy per electron-hole pair generation in silicon between 5-320°k. *IEEE Transactions on Nuclear Science*, 19(4):9–19, 1972. doi: 10.1109/TNS.1972.4326778.

[69] S. Agostinelli, J. Allison, K. Amako, et al. Geant4 a simulation toolkit. *Nuclear Instruments and Methods in Physics Research Section A: Accelerators, Spectrometers, Detectors and Associated Equipment*, 506(3):250 – 303, 2003. ISSN 0168-9002. doi: https://doi.org/10.1016/S0168-9002(03)01368-8. URL http://www.sciencedirect.com/science/article/pii/S0168900203013688.

[70] J. Allison, K. Amako, J. Apostolakis, et al. Geant4 developments and applications. *IEEE Transactions on Nuclear Science*, 53(1):270–278, Feb 2006. ISSN 0018-9499. doi: 10.1109/TNS.2006.869826.

[71] R. Chytracek, J. Mccormick, W. Pokorski, and G. Santin. Geometry description markup language for physics simulation and analysis applications. *IEEE Transactions on Nuclear Science*, 53(5):2892–2896, Oct 2006. ISSN 0018-9499. doi: 10.1109/TNS.2006.881062.

[72] CERN. Problem 2156 - GDML export shows segmentation fault in multithreading, but runs fine in sequential. https://bugzilla-geant4.kek.jp/show_bug.cgi?id=2156, 2019.

[73] CERN. Geant4 10.5 - patch-01 release notes. http://geant4-data.web.cern.ch/geant4-data/ReleaseNotes/Patch4.10.5-1.txt, 2019.

[74] Dennis Wright. A short guide to choosing a physics list. *Geant4 Tutorial at Marshall Space Flight Center*, 2012.

[75] CERN. *Reference Physics Lists*, 2009. https://geant4.web.cern.ch/node/155.

[76] Robin Tesse, Frédéric Stichelbaut, Nicolas Pauly, Alain Dubus, and Jonathan Derrien. GEANT4 benchmark with MCNPX and PHITS for activation of concrete. *Nuclear Instruments and Methods in Physics Research Section B: Beam Interactions with Materials and Atoms*, 416:68 – 72, 2018. ISSN 0168-583X. doi: https://doi.org/10.1016/

j.nimb.2017.12.006. URL http://www.sciencedirect.com/science/article/pii/S0168583X17310066.

[77] S Aini, U Nizar, A NST, and J Efendi. Identification and purification of nyalo river silica sand as raw material for the synthesis of sodium silicate. *IOP Conference Series: Materials Science and Engineering*, 335:012025, 04 2018. doi: 10.1088/1757-899X/335/1/012025.

[78] MIRION. *802 Scintillation Detectors*, 0. https://mirion.s3.amazonaws.com/cms4_mirion/files/pdf/spec-sheets/csp0232_802_super_spec_2.pdf?1557861234.

[79] Klea Dhimitri. Personal communication. KDhimitri@hamamatsu.com, 2019.

[80] Sam Barron. Personal communication. sam.barron@saint-gobain.com, 2019.

[81] Jim Simpson. Personal communication. jim.simpson@thermofisher.com, 2019.

[82] Mendoza E. and Cano-Ott D. Update of the Evaluated Neutron Cross Section Libraries for the Geant4 Code (see also INDC(NDS)-0612) (INDC(NDS)–0758). *International Atomic Energy Agency (IAEA)*, 2018. URL https://inis.iaea.org/search/search.aspx?orig_q=RN:50006622.

[83] A.J. Koning, D. Rochman, J.-Ch. Sublet, N. Dzysiuk, M. Fleming, and S. van der Marck. Tendl: Complete nuclear data library for innovative nuclear science and technology. *Nuclear Data Sheets*, 155:1–55, 2019. ISSN 0090-3752. doi: https://doi.org/10.1016/j.nds.2019.01.002. URL https://www.sciencedirect.com/science/article/pii/S009037521930002X. Special Issue on Nuclear Reaction Data.

[84] PREM SWARUP and R. P. ARORA. Dielectric constant of powders. *Nature Letters*, 201, March 1964. doi: https://doi.org/10.1038/2011018a0. URL https://www.nature.com/articles/2011018a0#citeas.

[85] Lithium Fluoride. https://princetonscientific.com/materials/substrates-wafers/lithium-fluoride/.

[86] Silvaco® (2016) atlas™ user's manual. https://dynamic.silvaco.com/dynamicweb/jsp/downloads/DownloadManualsAction.do?req=silentmanuals&nm=atlas, 2016.

[87] Stefano Meroli. The minority carrier lifetime in silicon wafer. https://meroli.web.cern.ch/lecture_lifetime.html.

[88] E. Fehlberg. Some old and new runge-kutta formulas with stepsize control and their error coefficients. *Computing*, 34:265–270, 2005.

[89] Mathworks. MATLAB® Primer. https://www.mathworks.com/products/matlab.html, 2019.

[90] J. T. Walton and F. S. Goulding. Silicon radiation detectors with oxide charge state compensation. *IEEE Transactions on Nuclear Science*, 34(1):396–400, 1987. doi: 10.1109/TNS.1987.4337370.

[91] Z. Y. Cheng and C. H. Ling. A model for minority carrier lifetime variation in the oxide silicon structure following 253.7 nm ultraviolet irradiation. *Journal of Applied Physics*, 83(10):5289–5294, 1998. doi: 10.1063/1.367353. URL https://doi.org/10.1063/1.367353.

[92] C. Munakata and Hirofumi Shimizu. Fixed oxide charge in n-type silicon wafers studied by ac surface photovoltage technique. *Semiconductor Science and Technology - SEMICOND SCI TECHNOL*, 15:40–43, 01 2000. doi: 10.1088/0268-1242/15/1/307.

[93] N.P. Maity, R.R. Thakur, Reshmi Maity, R.K. Thapa, and S. Baishya. Analysis of interface charge using capacitance-voltage method for ultra thin hfo2 gate dielectric based mos devices. *Procedia Computer Science*, 57:757–760, 2015. ISSN 1877-0509. doi: https://doi.org/10.1016/j.procs.2015.07.470. URL https://www.sciencedirect.com/science/article/pii/S1877050915019997. 3rd International Conference on Recent Trends in Computing 2015 (ICRTC-2015).

[94] Gabor Galgoczi. Warning: Facet is too small or too narrow. *Geant4*

Forum, Sep 2021. URL https://geant4-forum.web.cern.ch/t/warning-facet-is-too-small-or-too-narrow/6182.

[95] Sanchit Sharma, Long Vo, Michael P. Pfeifer, William L. Dunn, Walter J. McNeil, and Amir A. Bahadori. Bulk material interrogation experimental results and validation with geant4 for replacement of dangerous radiological sources in oil-well logging industries. *Applied Radiation and Isotopes*, 170:109602, 2021. ISSN 0969-8043. doi: https://doi.org/10.1016/j.apradiso.2021.109602. URL https://www.sciencedirect.com/science/article/pii/S0969804321000178.

[96] New Semiconductor Materials. Biology systems. Characteristics and Properties. Nsm archive - physical properties of semiconductors. www.matprop.ru.

[97] *Physics and Properties of Semiconductors-A Review*, pages 5–75. John Wiley & Sons, Ltd, 2006. ISBN 9780470068328. doi: https://doi.org/10.1002/9780470068328.ch1. URL https://onlinelibrary.wiley.com/doi/abs/10.1002/9780470068328.ch1.

[98] James F. Ziegler, M.D. Ziegler, and J.P. Biersack. Srim – the stopping and range of ions in matter (2010). *Nuclear Instruments and Methods in Physics Research Section B: Beam Interactions with Materials and Atoms*, 268(11):1818–1823, 2010. ISSN 0168-583X. doi: https://doi.org/10.1016/j.nimb.2010.02.091. URL https://www.sciencedirect.com/science/article/pii/S0168583X10001862. 19th International Conference on Ion Beam Analysis.

[99] Jingtian Fang, Mahmud Reaz, Stephanie L. Weeden-Wright, Ronald D. Schrimpf, Robert A. Reed, Robert A. Weller, Massimo V. Fischetti, and Sokrates T. Pantelides. Understanding the average electron–hole pair-creation energy in silicon and germanium based on full-band monte carlo simulations. *IEEE Transactions on Nuclear Science*, 66(1):444–451, 2019. doi: 10.1109/TNS.2018.2879593.

[100] W. Shockley and W. T. Read. Statistics of the recombinations of holes and electrons. *Phys.*

Rev., 87:835–842, Sep 1952. doi: 10.1103/PhysRev.87.835. URL https://link.aps.org/doi/10.1103/PhysRev.87.835.

[101] Robert Noel Hall. Recombination processes in semiconductors. 1959.

[102] Ruy S. Bonilla and Peter R. Wilshaw. On the c-si/sio2 interface recombination parameters from photo-conductance decay measurements. *Journal of Applied Physics*, 121(13):135301, 2017. doi: 10.1063/1.4979722. URL https://doi.org/10.1063/1.4979722.

[103] M.I. Pinilla, A. Hellinger, L.K. Vo, W.L. Dunn, W. McNeil, and A. Bahadori. Design studies using MCNP6® for an oil well logging prototype tool and a test facility. *Radiation Physics and Chemistry*, 167:108393, 2020. ISSN 0969-806X. doi: https://doi.org/10.1016/j.radphyschem.2019.108393. URL http://www.sciencedirect.com/science/article/pii/S0969806X18313677. Special issue dedicated to the 14th International Symposium on Radiation Physics.

[104] Christopher John Werner, Jeffrey S. Bull, C. J. Solomon, Forrest B. Brown, Gregg Walter McKinney, Michael Evan Rising, David A. Dixon, Roger Lee Martz, Henry G. Hughes, Lawrence James Cox, Anthony J. Zukaitis, J. C. Armstrong, Robert Arthur Forster, and Laura Casswell. MCNP version 6.2 release notes. *OSTI.GOV*, 2 2018. doi: 10.2172/1419730.

[105] W. Shockley. Currents to conductors induced by a moving point charge. *Journal of Applied Physics*, 9(10):635–636, 1938. doi: 10.1063/1.1710367. URL https://doi.org/10.1063/1.1710367.

[106] Simon Ramo. Currents induced by electron motion. *Proceedings of the IRE*, 27:584–585, 1939.

[107] J. Segal, J. Plummer, and C. Kenney. Simulation of charge cloud evolution in silicon drift detectors. In *1996 IEEE Nuclear Science Symposium. Conference Record*, volume 1, pages 558–562 vol.1, 1996. doi: 10.1109/NSSMIC.1996.591061.

[108] M Kolstein, G Ariño, M Chmeissani, and G De Lorenzo. Simulation of charge transport in pixelated CdTe. *Journal of Instrumentation*, 9(12):C12027–C12027, dec 2014. doi: 10.1088/1748-0221/9/12/c12027. URL https://doi.org/10.1088/1748-0221/9/12/c12027.

[109] Mathieu Benoit and L.A. Hamel. Simulation of charge collection processes in semiconductor cdznte Î³-ray detectors. *Nuclear Instruments and Methods in Physics Research Section A: Accelerators, Spectrometers, Detectors and Associated Equipment*, 606(3):508–516, 2009. ISSN 0168-9002. doi: https://doi.org/10.1016/j.nima.2009.04.019. URL https://www.sciencedirect.com/science/article/pii/S0168900209007864.

[110] Manfred Krammer et al. Silicon detectors. *Institute of High Energy Physics, Vienna, Austria*, 2011.

[111] Sanchit Sharma, Diego Laramore, Taylor Ochs, Douglas S. McGregor, Steven L. Bellinger, Walter J. McNeil, and Amir A. Bahadori. Preliminary benchmarks and analysis of boundary conditions in a trenched microstructured silicon radiation detector. *Journal of Applied Physics*, 131(13):134503, 2022. doi: 10.1063/5.0087397. URL https://doi.org/10.1063/5.0087397.

[112] Analog devices - ltspice simulator. https://www.analog.com/en/design-center/design-tools-and-calculators/ltspice-simulator.html, 2022.

[113] John Barncord. Personal communication. john.barncord@ametek.com, 2019.

[114] A Poyai, C Claeys, and E Simoen. Improved extraction of carrier concentration and depletion width from capacitance-voltage characteristics of silicon n(+)-p-well junction diodes. *APPLIED PHYSICS LETTERS*, 80(7):1192–1194, FEB 18 2002. ISSN 0003-6951. doi: 10.1063/1.1435809.

[115] Benedikt Steingrímsson. Geothermal well logging: Temperature and pressure logs. Technical report, ISOR – Iceland GeoSurvey, ICELAND, 2018.

[116] C. Munakata and Hirofumi Shimizu. Fixed oxide charge in n-type silicon wafers studied by ac surface photovoltage technique. *Semiconductor Science and Technology - SEMICOND SCI TECHNOL*, 15:40–43, 01 2000. doi: 10.1088/0268-1242/15/1/307.